Modular, Low-Cost Point-of-Care System for Metabolomics Applications

Ataollah Mohammad Ali Abdullah Saleh Tajabadi

Submitted in fulfilment of the requirements for the
Degree of Doctor of Philosophy

School of Engineering
College of Science and Engineering
University of Glasgow

February 2025

Contents

List of Tables

List of Figures

Acknowledgements

There are many people who have played a part in the last four years, helping me navigate the herculean challenge that is a doctoral degree.

First and foremost, I owe a deep gratitude to my parents. Not only did they feed, raise, and educate me, but they also funded the multiple degrees necessary for me to stay in this country. I am forever grateful for their boundless foresight and unwavering support, which ultimately steered me onto this path.

I would also like to thank Darya Shulakova for bringing me to Glasgow, only to leave promptly as soon as I arrived. Dasha, I'm not mad; I just wish you had taken me with you!

To my incredible labmates, Parisa, Dani, Vaithi, Hongli, Raghad, and Harry, thank you for making sure no day passed without entertainment nor incident. I will never forget the times I was nearly asphyxiated, immolated, intoxicated, offered as a ritualistic sacrifice to the Pagan Gods, exposed to airborne carcinogens, or simply maimed just by existing in that basement. You are the most wild and wonderful group of colleagues I could have asked for, and I couldn't have chosen a better bunch to suffer through a PhD with. Also, a huge thanks to the amazing folks at MELAB, whose kindness and generosity, especially in sharing their food and their equipment, helped make this journey smoother (and tastier).

Finally, I would like to extend my heartfelt thanks to the individuals who made this PhD a reality. Dr. Hasan Abbas, I know this project wasn't always easy to supervise, and I'm grateful that you supported me through it until the end. Professor Hadi Heidari, thank you for that first meeting and for convincing Professor Roy to take me on as a student. Professor Roy Vellaisamy, your support made this PhD possible despite the many hurdles it presented along the way. And finally, my sincerest thanks to Professor Muhammed Imran for securing the continued funding behind my PhD. I could literally not have done this without all of you!

List of Abbreviations

Abbreviation	Definition
ADS	Advanced Design System
AI	Artificial Intelligence
ALD	Atomic Layer Deposition
Al_2O_3	Aluminium Oxide
ANN	Artificial Neural Network
ARW	Angular Random Walk
ASIC	Application Specific Integrated Circuit
BPF	Bandpass Filter
CE-MS	Capillary Electrophoresis-MS
CMOS	Complementary Metal-Oxide-Semiconductor
CSF	Cerebrospinal Fluid
DAD	Diode-Array Detection
DART	Direct Analysis in Real Time
DESI	Desorption Electrospray Ionisation
DFT	Discret Fourier Transform
DMF	Digital Microfluidics
DNP	Dynamic Nuclear Polarisation
DOSY	Diffusion-Ordered Spectroscopy
EMF	Electromotive Force
ESR	Electron Spin Resonance
FID	Free Induction Decay
FEM	Finite Element Method
FTIR	Fourier Transform Infrared Spectroscopy
FWHM	Full Width at Half Maximum
GA	Genetic Algorithm
GC-MS	Gas Chromatography-MS
GOx	Glucose Oxidation
HERMES	Hetero-nuclear Resonance Multichannel Electronic System
HMRS	HP Micromagnetic Resonance Spectrometer

HMQC	Heteronuclear Multiple QC
HP	Hyperpolarized
HP-MRS	HP Magnetic Resonance Spectroscopy
HPLC	High-Performance LC
HSQC	Heteronuclear Single Quantum Coherence
INR	International Normalized Ratio
LC-MS	Liquid Chromatography-MS
LL	Lenz Lens
LL_1	Lenz Lens Design 1
LL_2	Lenz Lens Design 2
LM	Liquid Metal
LNA	Low-Noise Amplifier
LO	Local Oscillator
LOD	Limit of Detection
LPF	Lowpass Filter
MEMS	Micro-Electro-Mechanical Systems
MRI	Magnetic Resonance Imaging
MS	Mass Spectrometry
nLOD	Normalized LOD
NMR	Nuclear Magnetic Resonance
NV	Nitrogen Vacancy
ODNP	Overhauser Dynamic Nuclear Polarisation
PA	Power Amplifier
PCB	Printed Circuit Board
PDMS	Polydimetilsiloxane
PHIP	Parahydrogen-Induced Polarisation
photo-CIDPN	photochemically induce DNP
PoC	Point-of-Care
PMMA	Poly(methyl methacrylate)
Pre-LNA	Low-Noise Preamplifier
PTSD	Post-Traumatic Stress Disorder
RAT	Rapid Antigen Test
RF	Radio Frequency
Rx	Receive
S3L	Stripline-based Lenz Lens
SABRE	Signal Amplification by Reversible Exchange
SNR	Signal-to-Noise Ratio
TBI	Traumatic Brain Injury

Tx	Transmit
UHPLC	Ultra-HPLC
VNA	Vector Network Analyser
VSWR	Voltage Standing Wave Ratio

List of Publications

1. Ataollah M. A. A. S. Tajabadi, Parisa Dehghani, Dani S. Assi, Vaithinathan Karth-ikeyan, Chen-Bin Huang, Senior Member, IEEE, Hasan T. Abbas, Senior Member, IEEE, and Vellaisamy A. L. Roy, "Compact Magnetic Field Amplification by Tuned Lenz Lens," *IEEE Sensors Journal*, 2023.

2. Parisa Dehghani, Vaithinathan Karthikeyan, Ataollah M. A. A. S. Tajabadi, Dani S. Assi, Hongli Huang, Anthony Catchpole, John Wadsworth, Hing Y. Leung, and Vellaisamy A. L. Roy, "Rapid Near-Patient Impedimetric Sensing Platform for Prostate Cancer Diagnosis," *ACS Omega*, 2024.

3. Parisa Dehghani, Mostafa Salehirozveh, Ataollah M. A. A. S. Tajabadi, Hing Y. Leung, Sajjad Hussain, and Vellaisamy A. L. Roy, "MIP-Enhanced EGFET Sensor for Ultra-Sensitive Detection of Urinary Spermine in Prostate Cancer," submitted to *ACS Sensors*, 2024.

Abstract

This thesis presents the design, development, and validation of a modular, low-cost NMR system tailored for point-of-care diagnostics, with an emphasis on enabling early detection of prostate cancer. This application imposes specific requirements on the system, including the ability to detect low-concentration metabolic biomarkers in microlitre-scale biological fluids, maintain a compact footprint suitable for bedside or outpatient use, and deliver sufficient sensitivity despite the limitations of low-field operation. To meet these needs, two high-sensitivity NMR probes were developed, each incorporating Lenz lenses to focus magnetic flux and enhance signal detection. The system architecture was designed for compatibility with small-volume samples and scalability for integration into portable diagnostic platforms.

The first probe iteration demonstrated a 40.6-fold increase in received power, confirming the effectiveness of Lenz lenses in amplifying local magnetic fields. However, alignment and robustness issues led to a second iteration optimised for field uniformity, achieving a 3.8-fold improvement while maintaining return losses below -10 dB at 28.566 MHz. Experimental validation confirmed impedance accuracy, with minor deviations highlighting component sensitivity.

Supporting NMR electronics were developed and characterised for efficient signal generation, amplification, and detection. A modular approach ensured accessibility, with impedance matching circuits validated via Smith charts and Monte Carlo simulations, maintaining return losses below -10 dB across 28–29.2 MHz. The system amplified signals down to 45 nV with a 12 dB signal-to-noise ratio (SNR), achieving a spin sensitivity of 5.07×10^{15} spins$/\sqrt{\text{Hz}}$ and a concentration sensitivity of 4.77 M$/\sqrt{\text{Hz}}$. Free induction decay signals were acquired, distinguishing water and oil based on transverse relaxation, with T_2^* values of 0.489 ms and 0.412 ms, respectively. Broad linewidths indicated magnetic field inhomogeneities requiring further refinement.

Compared to other low-cost NMR systems, this design offers improved energy efficiency and a modular architecture that supports customisation for a range of diagnostic applications. While this work is not yet suitable for metabolomics or clinical use in prostate cancer detection, it lays important groundwork for future development. The system demonstrates how high sensitivity can be achieved using microlitre-scale samples in a compact, low-cost platform, and its flexible design can be adapted to accommodate other sample formats or integrated into larger

diagnostic workflows. With further advancements in spectral resolution, stability, and signal-to-noise performance, this platform has the potential to evolve into a practical point-of-care tool for early disease detection and biochemical analysis.

Chapter 1

Introduction

1.1 Point-of-Care Diagnostics

Point-of-care (PoC) diagnostics refers to testing conducted near the patient at the point of need, providing real-time, rapid, and accurate results without requiring a centralised laboratory. While often considered a modern advancement, PoC testing has historical roots dating back to ancient medical practices. Early physicians performed bedside diagnostic tests, particularly using urine, due to its ease of collection and observable characteristics. One of the earliest recorded diagnostic tests, developed by Indian physicians around 3000 BCE, identified illnesses based on the presence of sweet-tasting urine that attracted insects [1]. Millennia later, Hippocrates of Kos theorised that disease resulted from an imbalance of the body's four humours and proposed that urine characteristics could reflect these imbalances, making it a valuable diagnostic tool [2]. Although the humoral theory has long been abandoned, the fundamental concept of using biological samples for disease diagnosis remains central to modern medicine. The need for systematic urine analysis led to the development of diagnostic instruments, such as the matula and urine wheel, which were used to assess the physical properties of urine samples [3].

PoC devices now encompass a wide spectrum, ranging from simple dipsticks for urinalysis to handheld glucose meters and advanced molecular analysers capable of detecting infectious diseases. These innovations have played a critical role in addressing global health challenges, particularly in densely populated and resource-limited regions where the need for rapid disease detection is most pressing [4].

The evolution of PoC testing has been driven by the increasing demand for rapid diagnostics across diverse clinical settings, particularly in primary care and emergency medicine. For the past two centuries, diagnostic testing has predominantly relied on centralised laboratories [5], where accuracy and reliability have been prioritised above all else [6]. However, this reliance comes at the cost of prolonged turnaround times, which can be significant depending on the urgency of the condition and the time-sensitive nature of treatment decisions [7]. As a result, clinical biochemistry testing for acute conditions such as myocardial infarction remained largely

unavailable for immediate patient care until more recent advancements in PoC technology [8]. The development of PoC testing has since enabled a broad range of acute and chronic diagnostic applications [9], expanding accessibility from clinical settings to remote and field-based locations [10], [11].

One of the primary advantages of PoC diagnostics is their ability to reduce dependency on centralised laboratories, thereby strengthening healthcare systems by making diagnostic testing more equitable. This is particularly beneficial in underserved or resource-limited areas, where access to centralised infrastructure is scarce. In such settings, PoC devices allow healthcare providers to deliver essential diagnostic services, helping to bridge critical gaps in global health. Their portability and rapid turnaround times also make them indispensable in emergency departments and intensive care units, where immediate test results can directly inform life-saving treatment decisions [12]. In primary care, PoC testing reduces unnecessary referrals, enhances treatment planning, and reassures patients by providing rapid rule-out diagnostics [13].

Over the past five decades, the development and commercialisation of PoC diagnostic systems have significantly transformed healthcare, enabling rapid disease diagnosis in diverse environments ranging from hospitals to resource-poor regions [14]–[30]. The COVID-19 pandemic further underscored their importance, as rapid, sensitive, and accessible diagnostic tools became essential for outbreak management. The widespread use of rapid antigen test (RAT) kits during the pandemic exemplified the impact of PoC testing by facilitating decentralised screening and reducing hospital visits. Despite their moderate accuracy, RAT kits played a crucial role in alleviating healthcare burdens and curbing viral transmission in domestic settings. These developments highlight how PoC diagnostics accelerate disease detection and enable timely treatment, particularly for infectious diseases where rapid intervention can save lives.

Beyond acute care and resource-limited settings, PoC diagnostics have become seamlessly integrated into routine healthcare. Consumer electronics, such as smartwatches, now incorporate heart rate sensors and pulse oximeters, bringing diagnostic capabilities directly to individuals. Widely used PoC tests, including home pregnancy [31], hemoglobin [32], fecal occult blood [33], and rapid strep tests [34], further illustrate their accessibility and convenience in both clinical and domestic settings. These applications underscore the versatility of PoC technology in addressing a broad spectrum of healthcare needs.

The rapid advancement of technologies such as artificial intelligence has further expanded the capabilities of PoC diagnostics. These innovations are driving the field toward intelligent, labor-free solutions that provide high-quality diagnostics with minimal user intervention. This progress has accelerated the global adoption of PoC testing, positioning it as a cornerstone of modern healthcare and a rapidly expanding market [35], [36]. Ultimately, the transformative potential of PoC diagnostics lies not only in their ability to deliver rapid results but also in their adaptability across diverse healthcare environments. By offering decentralised, patient-centered testing, PoC diagnostics play a critical role in enabling timely and effective medical decision-

making.

1.2 Metabolomics

Introduction

Metabolomics is the study of metabolites, small molecular weight compounds that are the downstream products of biological processes. Collectively, these metabolites form the metabolome, which encompasses all low molecular weight compounds present in a biological sample, such as blood, urine, or tissue extracts [37]–[39]. By systematically identifying and quantifying these compounds, metabolomics provides a comprehensive snapshot of the biochemical state of a biological system. This approach offers insights that extend beyond traditional diagnostic methods, making it a valuable tool in modern diagnostics and treatment planning [40].

As shown in Fig. 1.1, metabolomics occupies the lowest layer of the "-omics" hierarchy and was initially conceived as a complementary tool to genomics. However, it has since evolved into an independent discipline with distinct applications in biomedical research and clinical diagnostics. Traditional methods for assessing metabolic changes focused on measuring individual metabolites or hormones, often relying on imaging modalities or standard laboratory tests. In contrast, metabolomics provides a comprehensive and systematic profiling of metabolic networks and pathways, capturing metabolic signatures that reflect a patient's health status and uncovering associations with physiological conditions, disease states, and responses to treatment [38]–[40].

These advances have significantly expanded the utility of metabolomics, enabling it to assess disease risk, support early detection, refine diagnoses, and monitor the effects of therapeutic interventions [41], [42]. It has played pivotal role in biomarker discovery for diseases such as rheumatoid arthritis, cardiovascular conditions, and Alzheimer's disease [43]–[50]. In oncology, metabolomics supports cancer diagnosis, prognosis, and treatment monitoring [50]. The field has also been instrumental in identifying drug targets, uncovering oncogenic mechanisms, and evaluating treatment effects [51], [52]. Beyond disease-focused applications, metabolomics has been used to assess metabolic disturbances in response to severe injury and to explore environmental interactions that influence health. Additionally, metabolomics has extended beyond Earth's boundaries through its application in space biology studies, including NASA's twin study [53], [54].

By offering a detailed snapshot of biochemical activity at a molecular level, metabolomics bridges the gap between genotype and phenotype, providing crucial insights into the mechanisms underlying health and disease. This ability to dynamically track metabolic fluctuations makes metabolomics a powerful tool in precision medicine, where it can guide treatment decisions and improve patient outcomes. Through its capacity to analyze metabolic signatures,

metabolomics allows for early disease detection, personalised treatment strategies, and more effective monitoring of therapeutic responses.

However, the complexity of metabolic signatures presents significant challenges for routine clinical implementation. These signatures often consist of subtle concentration variations that require sophisticated statistical techniques, such as the biosigner algorithm [42], to identify meaningful patterns and translate them into actionable clinical insights. The variability in metabolic profiles, influenced by factors such as genetics, environment, and lifestyle, further complicates standardisation efforts. Despite these obstacles, the field of metabolomics is experiencing rapid growth, as evidenced by the increasing number of studies published each year (Fig. 1.2).

To bridge the gap between research and clinical application, initiatives such as the establishment of Phenome Centres in the United Kingdom have been introduced, enabling large-scale diagnostics and personalised therapies [42]. These efforts are crucial for integrating metabolomics into routine clinical workflows, where its potential to enhance disease detection, patient monitoring, and treatment strategies can be fully realised. As research continues to refine analytical techniques and improve standardisation, metabolomics is poised to become an essential tool in modern healthcare, supporting the transition toward precision medicine and more individualised therapeutic interventions.

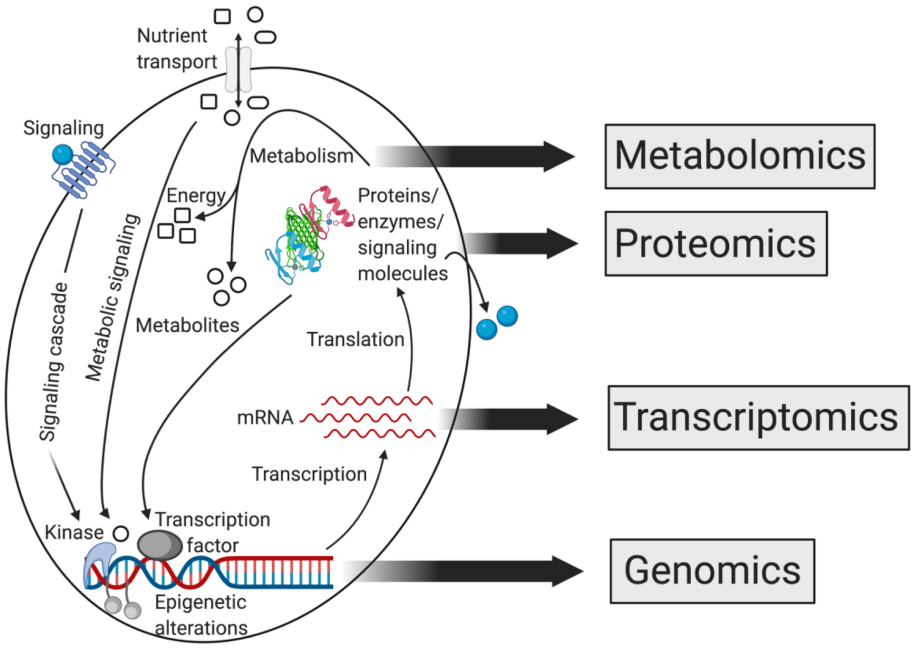

Figure 1.1: Various levels of "-omics" disciplines. Reproduced with permission from [55].

1.2.1 Metabolomics for Point-of-Care Diagnostics

Many studies (Fig. 1.2) have shown that metabolomics plays a critical role in identifying disease biomarkers for early detection, which is one of the most effective ways to improve clinical out-

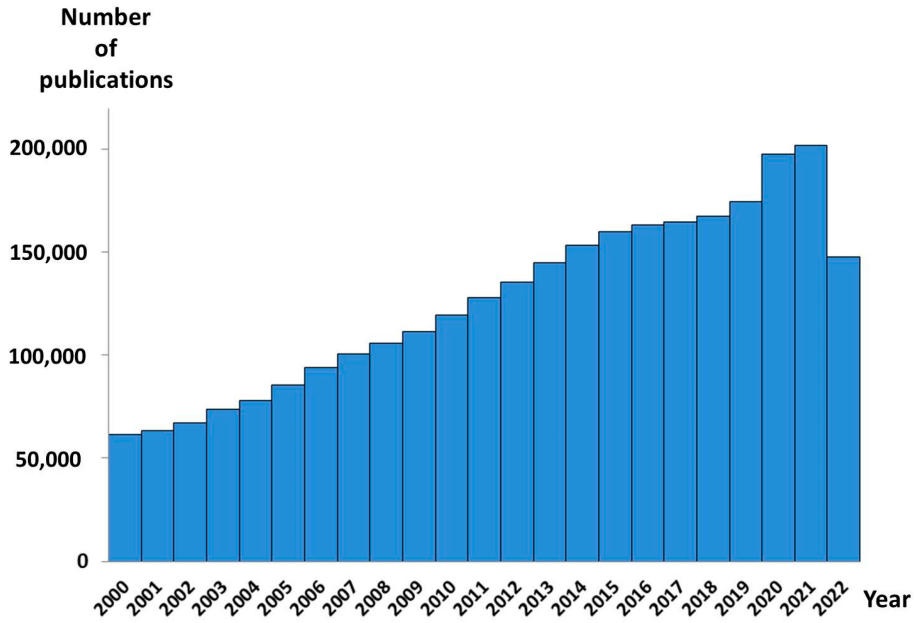

Figure 1.2: Number of metabolomics-related publications from 2000 to 2022. Reproduced with permission from [56].

comes. Many diseases induce characteristic changes in metabolite profiles of body fluids before the appearance of clinical symptoms. This sensitivity to early-stage conditions enables the development of personalised therapies and preventive care strategies. For instance, metabolomic profiling can detect changes in the circulating metabolome within 10 minutes of coronary occlusion, demonstrating its rapid responsiveness and potential for real-time diagnostics [57]–[59].

By focusing on easily accessible body fluids such as blood, serum, and urine, metabolomics supports the development of minimally invasive diagnostic tools that offer speed, sensitivity, and specificity. The analysis of volatile organic compounds in exhaled breath further illustrates the potential for rapid PoC diagnostics. These capabilities are particularly valuable for creating affordable, simple, and adaptable diagnostic tools suited for diverse environments, including resource-limited and remote areas [53], [54], [60]–[64]. These attributes position metabolomics as an ideal approach for PoC diagnostics that must function effectively outside of traditional clinical settings [65].

Cancer research has significantly benefited from the study of metabolic alterations (Fig. 1.3), which provide unique insights into tumour biology. By analysing small molecules in biological samples, researchers can identify metabolic drivers of disease, enabling earlier detection, more precise diagnosis, and personalised treatment strategies. This approach also facilitates the monitoring of treatment efficacy, allowing therapies to be tailored to the metabolic characteristics of individual cancers [66].

Consistent metabolic changes have been observed across various cancers, including lung, gastric, colorectal, breast, and prostate cancers, when compared with sex- and age-matched controls [67]. These alterations not only indicate the presence of disease but also reveal its

underlying biological mechanisms. For example, elevated lactate levels in lung cancer tissue and serum suggest that lactate may serve as a marker of disease aggressiveness [68]–[73]. In breast cancer, specific serum metabolites have been identified that distinguish patients from healthy individuals, with recent studies highlighting their potential in detecting recurrence [74]–[76]. Similarly, metabolic profiling has proven useful in differentiating pancreatic cancer from chronic pancreatitis, aiding in complex diagnoses [77].

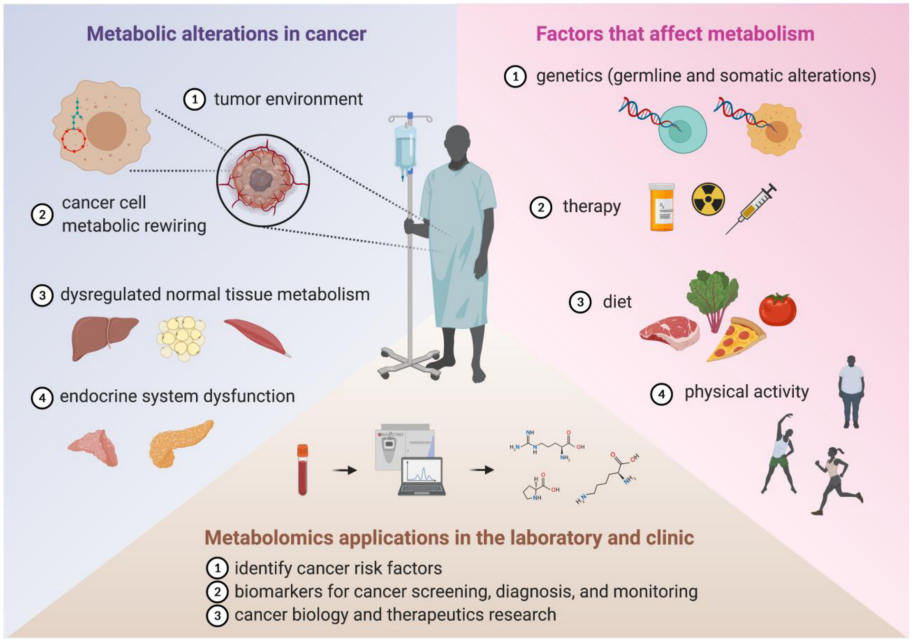

Figure 1.3: Different ways metabolomics aids cancer diagnostics and treatment. Reproduced with permission from [55].

Innovative approaches are expanding the role of metabolic analysis in diagnostics. For instance, the study of volatile organic compounds in exhaled breath has shown promise in distinguishing patients with non-small cell lung cancer from non-cancer controls, offering a noninvasive diagnostic tool [62]–[64]. Additionally, the classification of tumour versus non-involved tissues has become possible through serum analysis, as demonstrated in the detection of epithelial ovarian cancer [78]. Biomarker studies in both serum and urine have also successfully distinguished lung cancer patients from healthy controls [60], [61].

These techniques provide also valuable insights into treatment response. For example, metabolic differences in tumours following neoadjuvant chemotherapy have been linked to breast cancer survival outcomes, demonstrating their potential in refining therapeutic strategies [79]. Understanding how tumours metabolically respond to treatment offers a pathway to more personalised and effective care. The study of cancer-related metabolic changes is proving to be a powerful tool in diagnostics and treatment. By enabling earlier detection, guiding therapeutic decisions, and improving our understanding of tumour biology, metabolomics continues to transform cancer diagnostics and management, with significant implications for patient outcomes.

Metabolomics is increasingly being explored as a tool for understanding and diagnosing conditions such as traumatic brain injury (TBI), severe trauma, and burns. The primary objective of these studies is to identify metabolic fingerprints specific to each condition that can be tracked over time, highlighting the immense potential of metabolomics in trauma research. In the case of TBI, the disruption of physiological homeostasis is believed to result in a metabolic crisis, which is reflected in the metabolome [80]–[87]. Urine analysis has identified approximately 2,500 molecules affected by TBI [88], while cerebrospinal fluid (CSF) serves as another significant source of metabolomic data. CSF analysis is particularly relevant in clinical settings where intracranial monitoring and extraventricular drains are often required for patient care [89]–[95].

Research has demonstrated that metabolomics can distinguish between TBI and post-traumatic stress disorder (PTSD) [96]–[98], assess TBI severity, and predict patient outcomes [99]. Additionally, metabolomic profiling has been used to differentiate TBI patients with cognitive impairment from those without, as well as from healthy controls [100]. Beyond TBI, metabolomics has provided significant insights into trauma-related conditions such as hemorrhagic shock and organ failure, both of which are associated with distinct metabolic changes [101]–[103]. Certain metabolic phenotypes may even serve as predictive markers for sepsis risk in trauma patients, offering a critical opportunity for early intervention [104].

In burn injuries, metabolomics and proteomics have demonstrated considerable prognostic value [105]–[108]. Early-stage burns are characterised by significant metabolic disturbances [109], and metabolomics has shown potential in distinguishing between septic and non-septic burn patients, a crucial differentiation for optimising treatment strategies [110]. These findings collectively underscore the versatility and promise of metabolomics in addressing a wide range of trauma-related conditions, reinforcing its potential as a powerful tool for improving diagnosis, prognosis, and therapeutic decision-making in critical care settings.

1.2.2 Current Limitations of Metabolomics

Advancements in analytical techniques have been critical to the growth of metabolomics. The field relies on powerful platforms such as mass spectrometry (MS) and nuclear magnetic resonance (NMR) spectroscopy. MS offers high sensitivity and specificity and is often coupled with separation techniques such as gas chromatography (GC-MS), liquid chromatography (LC-MS), or capillary electrophoresis (CE-MS) to analyze complex biological samples [111]–[113]. NMR spectroscopy, on the other hand, is valued for its minimal sample processing, nondestructive analysis, and unbiased metabolite detection, making it highly robust and well-suited for quantitative analysis [114], [115]. Additional methods, including high-performance liquid chromatography (HPLC) and ultra-high-performance liquid chromatography (UHPLC), further enhance the analytical capabilities of metabolomics [116]–[123]. However, no single platform currently provides comprehensive metabolome coverage, necessitating the integration of multiple technologies to capture the full complexity of biological systems [62], [124].

Each of these instruments is expensive, bulky, and complex, making them impractical for use outside centralised laboratory facilities. For instance, modern MS systems, including GC MS and LC MS, range in cost from $200,000 to $800,000, while high field NMR instruments may exceed $800,000 [62], [125], [126]. These financial burdens, coupled with recurring maintenance costs, make such systems inaccessible to many institutions, particularly in resource limited settings.

Beyond financial and logistical constraints, technical challenges further limit the utility of these techniques. In NMR, overlapping signals between high and low concentration metabolites complicate spectral analysis, while in MS, low annotation rates, where fewer than five percent of detected features can be confidently identified, reduce the interpretability of results [127], [128]. These limitations highlight the need for continued advancements in analytical techniques to improve the feasibility and clinical applicability of metabolomics.

Efforts to address these limitations are underway. Advances in NMR technology, including improvements in magnet shielding, electronics, and cryotechnology, promise smaller, more affordable, and accessible instruments [57]. However, achieving the high sensitivity and resolution required for comprehensive metabolomics remains challenging, and translating these technical advancements into routine diagnostics will require further innovation and investment [127], [129]. Despite rapid progress in metabolomics technologies, widespread implementation in PoC diagnostics will depend on overcoming the technical, analytical, and translational barriers outlined above. Addressing these challenges will enable metabolomics to revolutionise personalised medicine and facilitate real time disease diagnosis and monitoring in clinical settings.

In addition to NMR and MS, several emerging technologies have been proposed to expand the analytical toolbox available for metabolomics. These platforms aim to address specific limitations related to sensitivity, cost, sample throughput, or suitability for point-of-care settings. For instance, CE-MS offers high separation efficiency for charged and polar metabolites in small sample volumes. Its minimal sample preparation and suitability for low-volume biofluids make it especially promising for clinical and single-cell applications.

Vibrational spectroscopy techniques, such as Fourier transform infrared (FTIR) [130] and Raman spectroscopy [131], have also been explored for metabolomics. These methods are rapid, label-free, and non-destructive, allowing for the fingerprinting of complex biological mixtures. Although they generally offer lower sensitivity and molecular specificity compared to MS or NMR, they can be valuable in high-throughput screening, quality control, and real-time monitoring contexts.

Other approaches include direct injection (DI) strategies [132] that allow rapid sample introduction into mass spectrometers without chromatographic separation, and diode-array detection (DAD) [133], which captures UV-visible absorbance spectra for metabolite identification. While these methods trade off some specificity and sensitivity, they offer increased speed and simplic-

ity in workflows where these factors are critical.

Finally, emerging microfluidic and lab-on-a-chip systems [134] are pushing the boundaries of miniaturised metabolomics. These platforms aim to reduce sample and reagent consumption while increasing automation and integration, potentially making metabolomics more compatible with portable and decentralised diagnostic devices. Additionally, ambient ionisation techniques such as desorption electrospray ionisation (DESI) [135] and direct analysis in real time (DART) [136] are expanding MS capabilities by enabling direct sample analysis with minimal preparation.

These alternative platforms complement traditional NMR and MS approaches and collectively broaden the range of metabolomics applications. As technical maturity increases, they may offer viable routes to making metabolomics more accessible, especially in time-sensitive or resource-limited clinical environments [137].

To align with the requirements of PoC diagnostics, metabolomics tools must balance accessibility, affordability, and diagnostic power. While no single platform can comprehensively identify all metabolites in a sample, technologies such as NMR and panels of multimetabolite markers show significant promise. These tools enable simultaneous measurements, regular screening, and disease monitoring, which are essential for time sensitive and routine care settings. Such advancements highlight the potential of metabolomics to transform healthcare delivery, particularly by creating rapid and cost effective diagnostic solutions [138]–[149].

1.2.3 Prostate Cancer and the Role of Metabolomics in Early Diagnosis

Prostate cancer (PCa) is the second most commonly diagnosed cancer in men worldwide, with more than 1.4 million new cases reported in 2020 alone [150]. It primarily affects men over the age of 60 and often progresses without noticeable symptoms in the early stages, which makes timely detection a significant challenge. The most widely used diagnostic tools, prostate-specific antigen (PSA) testing and digital rectal examination (DRE), are limited by low specificity and sensitivity. Elevated PSA levels can result from benign conditions such as prostatitis or benign prostatic hyperplasia, which leads to unnecessary biopsies and overtreatment. On the other hand, aggressive cases of PCa may not cause a noticeable increase in PSA, resulting in missed or delayed diagnoses [151].

These limitations have driven interest in developing more accurate, non-invasive methods for early detection. Metabolomics has emerged as a promising approach in this context. It is the comprehensive study of small molecules within biological systems and provides a direct reflection of cellular activity and metabolic state. Since metabolic reprogramming is a well-established feature of cancer progression, metabolomic profiling can capture subtle biochemical changes associated with disease onset and development [152].

In PCa, metabolic pathways such as citrate and polyamine metabolism are disrupted during

the transition from normal to malignant cells. These changes are reflected in the concentrations of specific metabolites that can be measured in biological fluids such as blood, urine, and seminal plasma [153]. Several studies have shown that prostate tumours exhibit distinct metabolic signatures. For example, elevated sarcosine levels have been proposed as a potential biomarker for PCa progression, while reduced citrate levels are commonly observed in malignant prostate tissue [154], [155].

Recent advances in metabolomics technologies have further enabled the identification of clinically relevant biomarkers. Large cohort studies using mass spectrometry and NMR have demonstrated that metabolomic profiling can distinguish between prostate cancer and benign conditions with high accuracy [155]. Furthermore, metabolomics is compatible with non-invasive sample collection and lends itself to integration with point-of-care platforms, which makes it well suited for early detection and patient monitoring outside traditional hospital settings [156].

Given its high prevalence and often silent progression, prostate cancer represents a compelling target for point-of-care diagnostics. Early-stage disease is highly treatable, yet many patients are only diagnosed after progression due to the limitations of current screening tools such as PSA testing. PoC systems have the potential to shift diagnosis closer to the patient by enabling rapid, non-invasive assessments outside traditional laboratory settings. Metabolomics is particularly well suited for this purpose. By capturing disease-specific biochemical changes in accessible biofluids such as urine or blood, metabolomics offers a route to sensitive and specific diagnostics that can be miniaturised and integrated into portable systems. Applying metabolomics at the point of care could significantly improve early prostate cancer detection, reduce unnecessary biopsies, and enable real-time monitoring of disease progression.

1.3 Thesis Objective

To fully realise these advancements in clinical practice, a suitable vehicle is needed to translate cutting edge metabolomics technologies into routine healthcare. While research continues to expand the scope and precision of metabolomics, its integration into diagnostics depends on the development of accessible, scalable, and reliable platforms. Without a practical means to implement these technologies in real world settings, their impact will remain limited to specialised laboratories rather than benefiting broader patient populations. The challenge, therefore, lies not only in refining metabolomic techniques but also in creating diagnostic tools that can deliver these innovations to clinicians in a way that is cost effective, rapid, and easy to use.

One of the most promising analytical platforms for metabolomics, particularly in PoC settings, is NMR spectroscopy. Unlike MS-based approaches, which require extensive sample preparation and are susceptible to ion suppression effects, NMR is non-destructive, requires minimal preprocessing, and is highly reproducible and automatable. These attributes make it particularly suited for rapid, routine diagnostics. Moreover, NMR can detect a broad range of metabolites, including sugars, alcohols, and highly polar molecules, many of which are chal-

lenging to analyze with LC-MS [114], [115], [127], [157], [158]. The simplicity, speed, and scalability of NMR further strengthen its potential for resource limited environments, making it a promising technology for integrating metabolomics into PoC applications [157].

Despite these advantages, existing NMR platforms remain largely confined to research laboratories and centralised clinical facilities due to their high cost and infrastructure requirements. PoC NMR metabolomics is an evolving field, with ongoing research continuously advancing its capabilities. Currently, most NMR systems used for metabolomics are general-purpose instruments optimised for research applications, where they provide detailed metabolic data but require significant technical expertise to operate. These systems are not designed for clinical use, where nurses and doctors need diagnostic tools that are easy to use and integrate into routine workflows.

At this stage, the ideal clinical system for PoC NMR metabolomics has not yet been established. More research is needed to determine how best to balance sensitivity, ease of use, and cost-effectiveness for real-world healthcare settings. To enable this research to progress efficiently, researchers require an adaptable, low-cost system that allows them to set up experiments quickly, test new ideas, and refine designs without the financial and logistical barriers of custom-built instrumentation. The goal of this work is to develop a system that is flexible, accessible, and easy to deploy, allowing more researchers to contribute to shaping the future of PoC NMR metabolomics.

This thesis seeks to design, develop, and validate a modular, low-cost NMR platform tailored to the unique demands of PoC applications. By addressing existing limitations and proposing practical solutions, this work aims to bridge the gap between cutting-edge metabolomics research and real-world clinical implementation. The proposed platform is expected to not only expand access to advanced diagnostics but also drive innovation in personalised medicine by enabling real-time metabolic profiling in diverse healthcare environments. Ultimately, this research highlights the potential of metabolomics in PoC diagnostics, providing a foundation for improving healthcare outcomes on a global scale.

Chapter 2

Enhancing Sensitivity in Nuclear Magnetic Resonance

2.1 NMR Physics

NMR is a phenomenon that arises from the interaction between nuclear magnetic moments and an external magnetic field. At the core of NMR is the concept of nuclear spin, which is an intrinsic quantum property of certain atomic nuclei. Nuclei with a non-zero spin quantum number, such as hydrogen-1 (^{1}H), carbon-13 (^{13}C), nitrogen-15 (^{15}N), fluorine-19 (^{19}F), and phosphorus-31 (^{31}P), possess a magnetic moment ($\vec{\mu}$), illustrated in Fig. 2.1a, that enables interaction with an external magnetic field ($\vec{B_0}$). These isotopes are commonly studied in NMR due to their natural abundance, magnetic properties, and relevance to biological and chemical systems. Among these, ^{1}H is the most frequently measured nucleus because of its high natural abundance and strong signal sensitivity.

When placed in a static magnetic field, such nuclei precess at a characteristic frequency known as the Larmor frequency, given by:

$$\omega_0 = \gamma B_0 \tag{2.1}$$

where ω_0 is the angular precession frequency, γ is the gyromagnetic ratio of the nucleus, and B_0 is the strength of the external magnetic field. For example, at a magnetic field strength of approximately 0.67 T, the Larmor frequency of ^{1}H is 28.6 MHz, which serves as the operational frequency of the system described in this work. This choice reflects the design target based on the field strength of the permanent magnet used. Other nuclei have different Larmor frequencies at the same field strength, such as 7.2 MHz for ^{13}C and 11.3 MHz for ^{31}P, but these are not the focus of the current system.

In the absence of $\vec{B_0}$, nuclear magnetic moments are randomly oriented, producing no net

magnetization (Fig. 2.1b). When the sample is placed in a magnetic field, these magnetic moments align with or against the field, resulting in discrete energy levels. This is known as the Zeeman effect, and for spin-$\frac{1}{2}$ nuclei, it gives rise to two energy states separated by:

$$\Delta E = \hbar\omega_0 = \hbar\gamma B_0 \tag{2.2}$$

where ΔE is the energy difference between the spin states and $\hbar$ is the reduced Planck constant. The slight excess population in the lower energy state leads to a net magnetization, $\vec{M}$, along the direction of $\vec{B}_0$ (Fig. 2.1c). The degree of spin polarization, and thus the strength of the NMR signal, is governed by the Boltzmann distribution:

$$\frac{N_\uparrow}{N_\downarrow} = \exp\left(\frac{-\Delta E}{kT}\right) \tag{2.3}$$

where $N_\uparrow$ and $N_\downarrow$ are the populations in the lower and upper spin states, k is the Boltzmann constant, and T is the absolute temperature. Typically the population difference is minute, which makes ΔE very small under laboratory conditions leading to inherently low signal strengths, thus making NMR one of the less sensitive spectroscopic techniques. The sensitivity is primarily determined by the magnitude of the external magnetic field $\vec{B}_0$, the temperature T, and the gyromagnetic ratio γ of the nucleus being observed. Higher magnetic fields increase ΔE and improve polarization, while lower temperatures reduce thermal agitation, both contributing to better signal-to-noise ratios. Additionally, nuclei with higher gyromagnetic ratios, such as ^{1}H, yield stronger signals.

To perturb this equilibrium, an external radiofrequency (RF) magnetic field ($\vec{B}_1$) is applied perpendicular to $\vec{B}_0$. When $\vec{B}_1$ oscillates at the Larmor frequency, it induces a torque on the net magnetization vector, tipping it away from the z-axis. The extent of this tilting depends on both the amplitude and duration of the RF pulse, allowing precise manipulation of the magnetization vector. By selecting appropriate pulse parameters, specific flip angles such as 90 or 180 degrees can be achieved, forming the basis for many NMR pulse sequences used in spectroscopy and imaging.

Following the RF excitation, the system returns to equilibrium through relaxation processes (Fig. 2.1d). The transverse component of the magnetization vector precesses in the xy-plane at the Larmor frequency, generating an oscillating magnetic flux that induces a voltage in a nearby coil. This time-dependent signal, which can be seen in Fig. 2.1e, is known as free induction decay (FID) and is recorded during the NMR experiment. In NMR, relaxation times describe how the net magnetization vector returns to equilibrium following excitation. Two distinct relaxation mechanisms are observed: spin-lattice relaxation and spin-spin relaxation, characterised by the time constants T_1 and T_2, respectively. The spin-lattice relaxation time

T_1 describes the recovery of the longitudinal magnetization component along the z-axis due to energy exchange between the nuclear spins and their surrounding lattice. In contrast, the spin-spin relaxation time T_2 characterises the loss of phase coherence among spins in the transverse plane, leading to a decay of the transverse magnetization without any net loss of energy from the system. These two processes are independent, and typically $T_2 \leq T_1$ for a given sample.

Measurement of T_1 is commonly performed using an inversion-recovery pulse sequence, which involves a 180-degree pulse to invert the magnetization, followed by a variable delay and a 90-degree pulse to detect recovery. The signal intensity is plotted as a function of delay time to extract the T_1 value. T_2, on the other hand, is typically measured using a spin-echo or Carr–Purcell–Meiboom–Gill (CPMG) sequence, which applies a 90-degree excitation pulse followed by a train of 180-degree refocusing pulses. This sequence refocuses static inhomogeneities in the magnetic field and isolates the decay due to spin–spin interactions. Understanding and accurately measuring T_1 and T_2 is critical for both quantitative analysis and the optimisation of pulse sequences in NMR experiments.

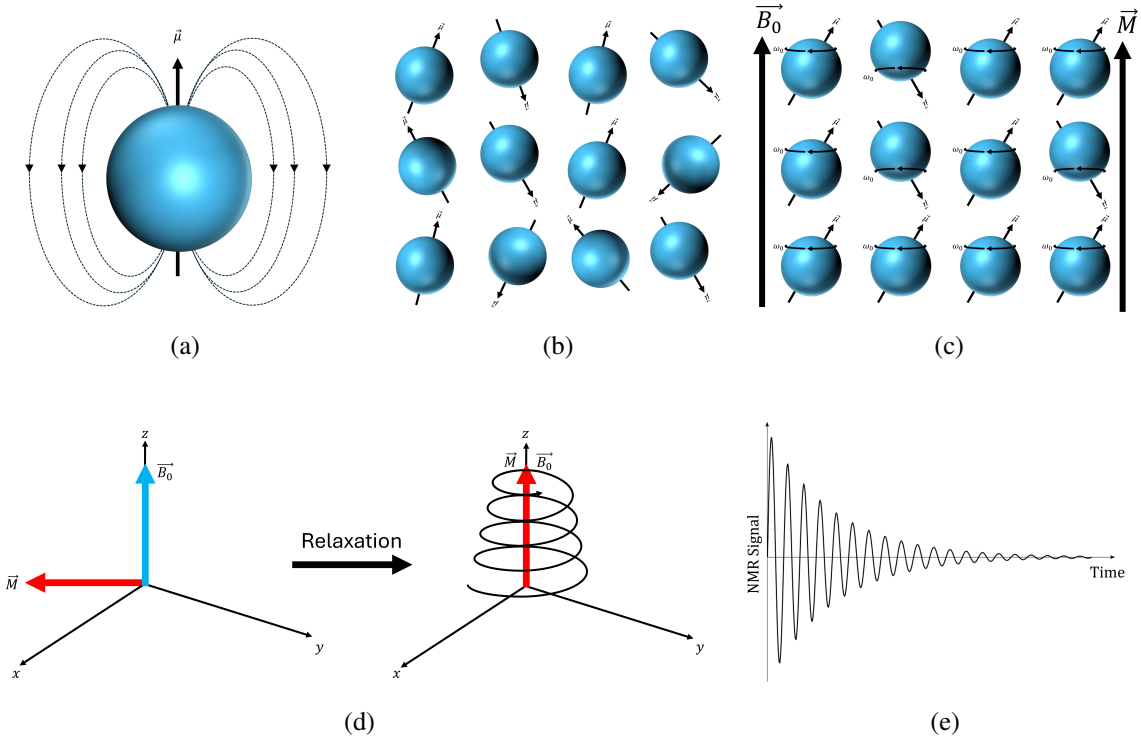

Figure 2.1: (a) Magnetic moment $\vec{\mu}$ and field lines of a nucleus. (b) Orientation of $\vec{\mu}$ in the absence of an external magnetic field $\vec{B}_0$. (c) Induced a net magnetization vector $\vec{M}$ and Larmor precession ω_0 in the presence of $\vec{B}_0$. Exciting the nuclei tilts $\vec{M}$ into the XY-plane (d), and the free induction decay signal (e) is recorded as they relax.

In addition to analysing the FID in the time domain [159], a Fourier transform can be applied to yield a one-dimensional NMR frequency spectrum [160]. This spectrum reveals peaks corresponding to resonance frequencies of the nuclei, providing information on chemical structure,

molecular dynamics, and spatial relationships between atoms.

More details on the fundamentals of NMR can be found in Appendix A and in resources like Malcolm Levitt's Spin Dynamics: Basics of Nuclear Magnetic Resonance [161].

2.2 NMR Hardware

A functional NMR system consists of a set of coordinated hardware components that perform the tasks of excitation, detection, signal conditioning, and data acquisition. These blocks must be carefully integrated to ensure minimal noise, sufficient power handling, and accurate timing. Fig. 2.2 presents the core architecture of the low-field NMR system developed in this work, which was designed with modularity and accessibility in mind.

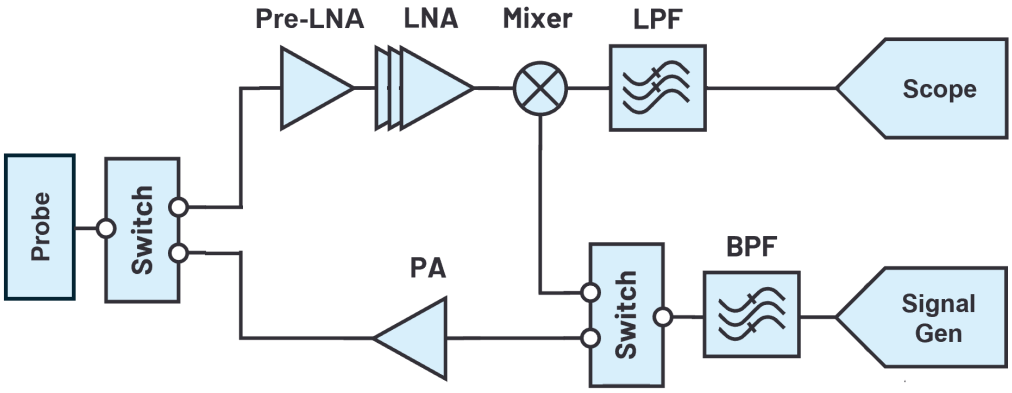

Figure 2.2: NMR electronic system diagram. BPF: bandpass filter, IF Amp: intermediate frequency amplifier, LNA: low-noise amplifier, LPF: lowpass filter, PA: power amplifier, Signal Gen: signal generator, Scope: oscilloscope.

At the heart of the system is the probe, which contains the RF coil and holds the sample. The coil has a dual function: during transmission, it generates the oscillating magnetic field that excites the nuclear spins in the sample, and during reception, it acts as a sensitive detector, converting the precessing magnetic moment of the nuclei back into a voltage signal. Because the signal induced during detection is extremely weak, typically in the nanovolt range, it is essential to isolate and protect the receiver circuitry during high-power transmission. This is achieved using an RF switch, which toggles the signal path between the transmit and receive chains with fast timing control.

The transmit chain begins with a signal generator, which produces an RF carrier at the Larmor frequency of the nuclei being measured. A band-pass filter (BPF) is used immediately after the generator to eliminate harmonics and out-of-band noise, which could otherwise distort the excitation pulse or generate spurious signals during detection. The filtered signal is then passed

through a power amplifier (PA) to boost its strength to the required transmit power level, which must be sufficient to tip the nuclear magnetization by the desired flip angle. A second switch directs the output of the PA to the probe during transmission and isolates the transmit path during reception.

On the receive side, the NMR signal returning from the probe is first passed through a pre-low-noise amplifier (Pre-LNA), which provides initial amplification with minimal added noise. This stage is critical because any noise introduced here cannot be removed downstream. The amplified signal is then passed to the main low-noise amplifier (LNA), which further boosts the signal level while preserving signal integrity. After amplification, the signal is mixed with a local oscillator in a mixer to convert it from the carrier frequency down to an intermediate frequency (IF) or baseband. This makes it easier to digitise and process. A low-pass filter (LPF) then removes high-frequency mixing products and any residual RF noise. The resulting signal is fed into a digital oscilloscope or data acquisition system, where it is digitised, stored, and processed to extract frequency, amplitude, and phase information.

One of the most important factors influencing spectral resolution and sensitivity in NMR is the uniformity of the static magnetic field across the sample volume. Inhomogeneities in the field cause the nuclear spins to precess at slightly different Larmor frequencies, resulting in broadened resonance lines and reduced ability to distinguish closely spaced spectral peaks. This effect can obscure small metabolic changes, especially in low-concentration samples or complex mixtures.

To correct for these inhomogeneities, a process known as shimming is employed. Passive shimming involves placing small pieces of ferromagnetic material around the magnet bore in specific positions to correct spatial variations in the magnetic field. This method is low-cost and often used in permanent magnet systems where simplicity is essential, although it lacks flexibility once set. Active shimming, by contrast, uses a set of orthogonal shim coils driven by precisely controlled currents to produce corrective magnetic fields. These fields can be dynamically adjusted during the experiment to optimise field homogeneity. Active shimming is standard in high-field NMR systems and is often automated using field mapping techniques. It allows for fine-tuning of the field down to sub-parts-per-million (ppm) variations and is essential for applications requiring high spectral resolution or large sample volumes. While this system does not incorporate active shimming, the hardware was designed with the potential for passive field optimization during magnet alignment and coil placement.

Although the fundamental principles of NMR are well established, the realisation of a sensitive and practical detection system requires careful attention to hardware design. Key components such as the magnet, RF coils, matching networks, and receiver electronics must be optimised to preserve signal integrity and minimise losses. However, even with ideal hardware, the intrinsic low sensitivity of NMR remains a significant challenge, particularly for small sample volumes. To address this, recent research has increasingly focused on microlitre-scale NMR

technologies that enhance signal detection by improving the filling factor, reducing noise, and concentrating the magnetic field at the region of interest. The following section reviews the current state-of-the-art in microlitre NMR, highlighting how advanced probe geometries, microcoils, and passive field focusing techniques are being used to overcome the limitations of conventional NMR hardware.

2.3 State-of-the-Art in Microlitre NMR

One of the key advancements in NMR technology has been the development of microcoils, which enable the analysis of mass-limited and volume-restricted samples with enhanced sensitivity. Microcoil cells were initially prone to severe $\vec{B}_0$ field inhomogeneities, primarily due to the proximity of the coil windings to the sample. However, thanks to a much better filling factor compared to standard 5 mm tubes, microcoils can achieve significantly lower limits of detection (LODs). A breakthrough was made when susceptibility mismatches were mitigated using inert liquids such as Fluorinert FC-43 around the coil, which minimised magnetic field disturbances and enabled high-resolution spectra acquisition with line widths of approximately 11 Hz at 300 MHz [162], [163].

Traditionally, microcoils have been fabricated using manual techniques such as hand-winding insulated copper wire around non-magnetic formers, often under a microscope to ensure precision. More advanced techniques include using micromachined substrates or lithographic processes, especially for planar microcoils. While these methods can yield high-performance coils, they are typically time-consuming, require operator skill, and can be challenging to reproduce consistently. Sweedler et al. demonstrated that a solenoid microcoil with a 1 mm length and a 5 nL sample volume, shown in Fig. 2.3, could achieve LODs as low as 1 ng in under one minute of acquisition time. Since then, a plethora of new designs and fabrication techniques have emerged to further improve sensitivity and reproducibility [164].

Advanced Fabrication Techniques for 3D NMR Microcoils

A critical factor in the broader adoption of microcoil technology is the ability to fabricate these coils in a way that is both cost effective and accessible to a wider range of laboratories. While early microcoil designs demonstrated impressive gains in sensitivity and resolution, their implementation was often constrained by the complex and expensive fabrication processes required to produce them. Modern manufacturing techniques have played a crucial role in overcoming these cost and accessibility barriers. Advanced methods such as 3D printing have significantly simplified the development of complex three dimensional geometries that previously required custom machinery. By leveraging these innovations, researchers have developed scalable fabrication approaches that maintain the high performance required for NMR applications. These advancements also enable greater customization and reproducibility, ensuring that microcoil technology

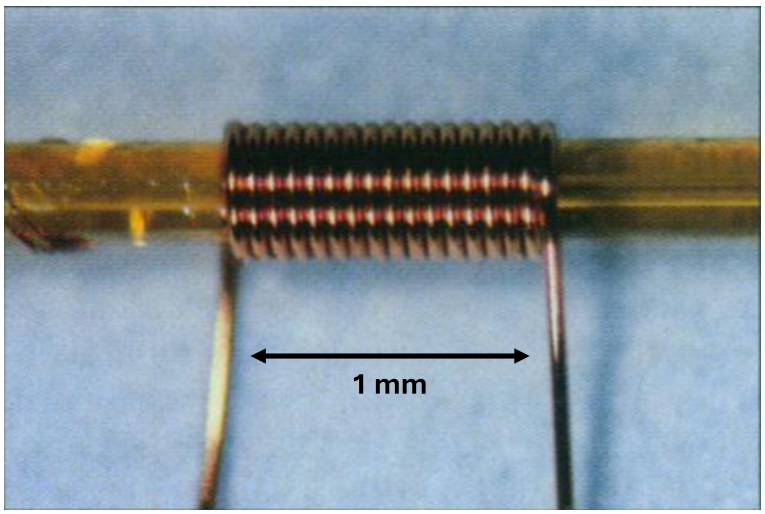

Figure 2.3: NMR microcoil developed by Olson. Reproduced with permission from [162].

can be more widely adopted across various research and clinical settings.

3D printing can be used to manufacture coils in various ways. Dohi et al. reported the design, fabrication, and application of a bicone-shaped microcoil (Fig. 2.4a) with low resistance and parasitic capacitance for magnetic resonance imaging (MRI) [165]. The microcoil was fabricated using vacuum evaporation and electroplating of copper onto a stepped helical structure developed by a 3D printer. The innovative manufacturing method opens doors to all forms of 3D structures that can be optimised based on its specific applications.

The fabrication process involved 3D printing stepped helical structures, followed by vacuum evaporation of copper to create the coil wiring. Copper was selectively deposited on the upper surfaces of the structure while the device was fixed on a rotary-tilted stage, allowing precise control of the coil geometry. Electroplating was then used to increase the thickness of the copper wiring, further reducing resistance. This approach enabled the creation of coils with wire thicknesses of 1.0 mm, 1.5 mm, and 2.0 mm and 8, 10, or 12 turns, tailored for different applications.

The results demonstrated that increasing the linewidth significantly reduced resistance, which correlated with improved signal-to-noise ratio (SNR). The fabricated coils achieved SNR values of up to 154 at 4.7 T MRI systems with a voxel size of $50 \times 50 \times 100\ \mu m^3$. High-resolution MRI images of small samples, such as berries, were acquired, clearly resolving internal structures. These results validated the coil's performance, with reduced resistance and parasitic capacitance below 0.6 pF, ensuring compatibility with MRI systems operating at 202 MHz.

Xie et al. took it one step further and introduced a method that combined using 3D printing and liquid metal (LM) infusion techniques [166]. They created highly customizable and precise MR probes (Fig. 2.4b), by embedding conductive liquid metal coils within 3D-printed substrates. These probes are tailored for various applications, including small-sample NMR spectroscopy, in situ electrochemical monitoring, and MRI of small objects. The 3D-printed

probes achieved high precision and flexibility, allowing for the integration of tailored sample chambers and complex coil geometries. Experimental testing demonstrated that these probes delivered comparable performance to conventional designs, with optimised SNR and effective magnetic field homogeneity. Additionally, the study highlighted the use of liquid metal pastes infused with gold microparticles to enhance coil conductivity, achieving stable performance across a range of temperatures and MR operating conditions. Specific applications, such as in situ monitoring of ethanol oxidation and reaction kinetics in microfluidic systems, showcased the practicality and versatility of the new probes.

For more advanced designs, fabrication methods like photolithography can be necessary, which require cleanrooms and are prohibitively expensive for many laboratories; however, computer numerical control (CNC) machining and laser etching are more affordable alternatives. Moxley-Paquette et al. [167] aimed to develop a cost-effective solution for producing customizable NMR microcoils to enhance the sensitivity and adaptability of NMR systems, particularly for applications involving small biological or environmental samples that traditional NMR hardware isn't ideal for.

In their work (Fig. 2.4c), they applied CNC micromilling and laser etching to fabricate complex three-dimensional NMR microcoils designed for mass-limited samples. The researchers engaged these high-resolution machines to achieve the precision needed for microcoil production. Several copper-coated dielectric materials were turned into microcoils that showed excellent results, among those poly(methyl methacrylate) (PMMA) and copper-coated glass proved to be a superior material.

PMMA-based coils produced with CNC micromilling exhibited excellent SNR and line shape, making them well-suited for larger sample volumes. Laser-etched glass microcoils demonstrated even greater sensitivity and were capable of handling smaller sample sizes, with their performance significantly exceeding that of PMMA coils. A large PMMA solenoid coil achieved a 6.6× improvement in signal area compared to a standard commercial NMR probe, showcasing its effectiveness for mass-limited samples. Additionally, laser-machined coils enabled the detailed analysis of metabolites in algae extracts and copepod egg sacs, further highlighting their potential for advancing biological and environmental research.

The fabrication method for microcoil significantly impact their design, especially in the case of three-dimensional designs. Traditional probe fabrication is labor-intensive, lacks design flexibility, and struggle with miniaturization. 3D printing is a way to circumvent those challenges and create probes with complex geometries and integrated components, thereby improving the efficiency of fabrication and the adaptability of to specific experimental requirements.

3D fabrication has always been more difficult than 2D; however, Noor et al. showed that a combination of 2D fabrication with 3D assembly could help reduce the challenge [168]. They created self-assembling coils (Fig. 2.4d) that were fabricated using advanced micro-electromechan-ical systems (MEMS) technology and assembled throygh origami-inspired tech

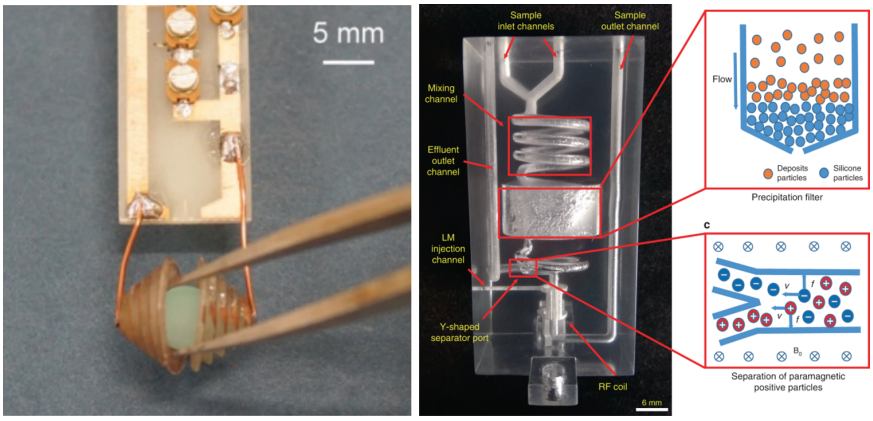

(a) (b)

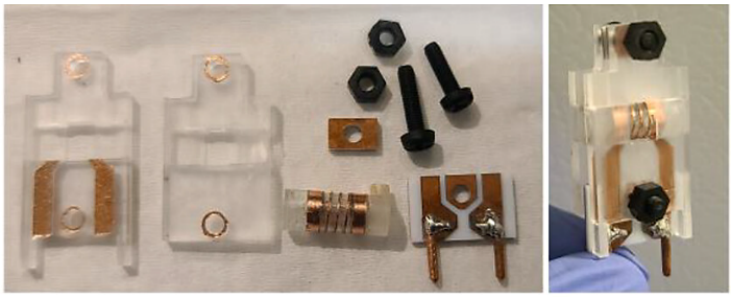

(c)

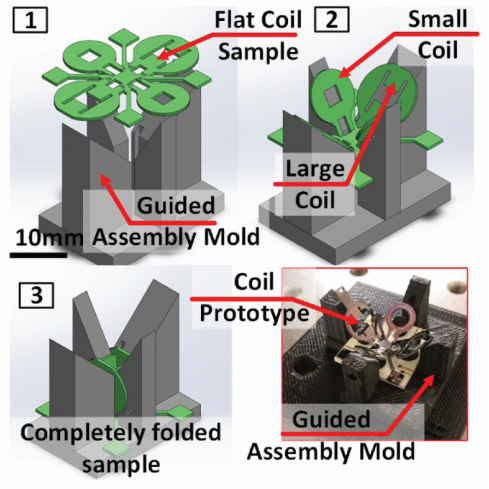

(d)

Figure 2.4: (a) Bi-cone MRI probe. Reproduced with permission from [165]. (b) Continuous-flow separation probe. Reproduced with permission from [166]. (c) Individual (left) and assembled (right) components of NMR microprobe. Reproduced with permission from [167]. (d) Assembly process for foldable MEMS NMR atomic sensor. Reproduced with permission from [168].

niques. This extended the reliable and scalable two-dimensional MEMS method into the third dimension to create high-performance Helmholtz coils and other critical components. This can reduce the size, weight, and cost of NMR atomic sensors while maintaining or improving their

sensitivity and accuracy.

The manufacturing of the coils involved a combination of photolithography and electroplating techniques. The coils were designed as folded Helmholtz configurations, enabling precise alignment and compact integration with the sensor system. The MEMS fabrication process allowed for the creation of multiple coil layers, enhancing magnetic field uniformity while minimising the device footprint. The origami-like folding approach further simplified the assembly process, ensuring accurate coil alignment without the need for complex manual adjustments.

Experimental results confirmed the effectiveness of the fabricated coils. The folded Helmholtz coils exhibited high magnetic field uniformity and stability, critical for accurate NMR measurements. Analytical models predicted that the coils, when integrated into the sensor system, could achieve an angular random walk (ARW) of $0.1^{\circ}/\sqrt{hr}$ and a magnetic field sensitivity of 10 fT/$\sqrt{Hz}$. These results demonstrate the feasibility of using MEMS technology for manufacturing high-performance coils for NMR sensors.

Application of Artificial Intelligence in NMR Design

Conventional methods require extensive iterations to analyze the complex interactions between design parameters, such as geometry, substrate material properties, and operating frequency. There may, however, be a solution in artificial intelligence (AI). By leveraging AI, Bernardo et al. showed that it is possible use AI to accelerate this optimization process and improve prediction accuracy for microprobe performance [169]. Specifically, they demonstrated that an Artificial Neural Network (ANN)-based model trained on a dataset generated through extensive electromagnetic simulations could be a great solution. The dataset included various predictors, such as geometric parameters, and substrate material properties, and target variables, like quality (Q) factor and resistance. The ANN model was designed to map these inputs to the desired performance outputs, enabling efficient evaluation of design variations. The training involved optimising the ANN's architecture, including the number of hidden layers, neurons, and activation functions, to achieve the best trade-off between simplicity and accuracy.

Using their method, they created several types of coils (Fig. 2.5a). The ANN model achieved high prediction accuracy, with a test precision of 99.67% for the Q-factor and 91.34% for resistance. The model significantly reduced computation times, providing predictions in just two minutes compared to 15 hours required by traditional simulations. The use of the ANN model also guided the design of optimised microprobe prototypes, which were later fabricated and characterised.

NMR is inherently a low sensitivity technique and often requires extensive signal averaging and lengthy scan times to improve signal quality. To increase sensitivity, several approaches are typically employed. One common method is cryogenic cooling of the RF detection circuitry, which reduces thermal noise and significantly improves signal to noise ratio. Other strategies include the use of high field magnets, optimised probe geometries, and preamplifiers with ultra

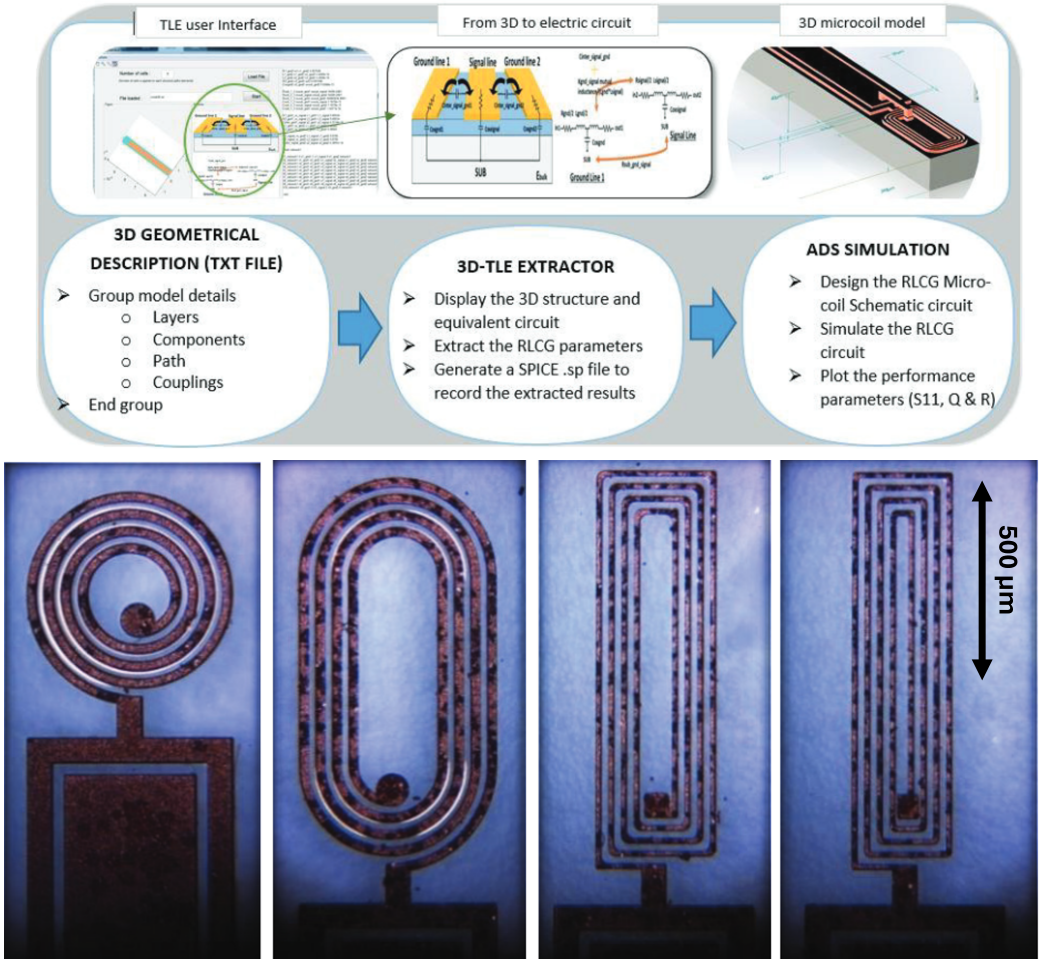

(a)

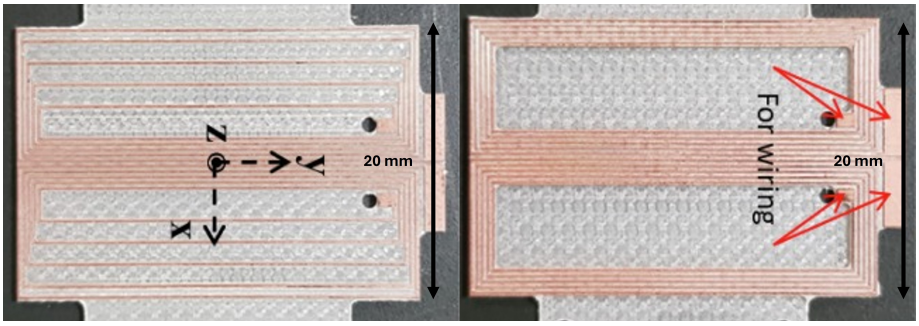

(b)

Figure 2.5: (a) Process and results of microcoils produced using ANN model. Coil geometries are 500 x 500 μm^2 (circular), 1000 x 500 μm^2 (ellipsoidal), 1000 x 300 μm^2 (rectangular left), 1000 x 250 μm^2 (rectangular right). Reproduced with permission from [169]. (b) Fabricated coils on FR-4 circuit board using GA-optimised (left) and traditional (right) approaches. Both coil dimensions are 20 mm x 30 mm. Reproduced with permission from [170].

low noise figures. Despite these advances, extensive signal averaging remains necessary in many low field or small volume systems. However, prolonged acquisition times introduce new challenges, most notably system drift. This includes thermal drift in the magnet or electronics and

gradual changes in the sample itself, all of which can distort spectral resolution and compromise quantitative accuracy.

By focusing on RF coil geometry, Tritrakarn et al. developed a simulation method that utilises a genetic algorithm to identify optimal coil configurations for various sample shapes and conditions [170]. Where Bernardo et al. fed their artificial neural network physical parameters from coils themselves, Tritrakarn et al. showed that the models could be extended to incorporate the Bloch equations, accounting for NMR specific parameters such as spin relaxation times, thereby ensuring more realistic fitness evaluations.

They applied the optimization method to substrate coils designed for single-sided NMR systems (Fig. 2.5b). The optimised coils were evaluated through simulations and experiments, with results indicating a 10% improvement in signal intensity compared to non-optimised designs. This enhancement corresponded to a 20% reduction in required scan time for achieving the same signal-to-noise ratio. The method also demonstrated strong agreement between simulated and experimental data, with errors below 5%, confirming its reliability.

Nuclear Polarization

Dynamic nuclear polarization (DNP) is a technique used to enhance NMR signal sensitivity by transferring spin polarization from unpaired electron spins, which have a much larger magnetic moment, to nuclear spins. This is typically achieved using microwave irradiation at frequencies corresponding to electron spin transitions, dramatically increasing nuclear spin polarization and hence signal strength. While DNP can offer enhancements of several orders of magnitude, its implementation generally requires high-frequency microwave sources and cryogenic cooling to maintain the necessary electron spin conditions. These technical demands lead to bulky, energy-intensive, and costly setups, making DNP unsuitable for low-field or portable NMR systems. For this reason, DNP was not included in the designs presented in this thesis, which prioritise accessibility, modularity, and ease of use. Instead, sensitivity improvements were pursued through strategies better aligned with compact hardware, such as integrating microcoils with microfluidic channels. This method increases the filling factor and boosts detection efficiency for microlitre samples while significantly simplifying the system architecture.

Gomez et al. aimed to simplify the RF circuitry, reduce hardware costs, and achieve high sensitivity for small samples by utilising a planar spiral microcoil in an untuned circuit integrated into a microfluidic chip [171]. Through this platform, shown in Fig. 2.6a, they combined multinuclear NMR spectroscopy with photo chemically induced dynamic nuclear polarization (photo-CIDNP). The combination with photo-CIDNP hyperpolarization further enhances sensitivity and potentially reduce the need costly high-field magnets or cryogenic setups. The chip integrates RF, optical, and fluidic components, enabling advanced 1D and 2D experiments on sub-microliter sample volumes. The microcoil's broadband capabilities allow for simultaneous detection of different nuclei, while photo-CIDNP hyperpolarization significantly boosts signal

intensity, addressing the low sensitivity often associated with traditional NMR systems.

Results demonstrated significant advancements in sensitivity and versatility. The system achieved a mass sensitivity in the picomole range for ^{19}F, ^{13}C, and ^{1}H nuclei, with a normalised LOD (nLOD) as low as 0.01 nmol/$\sqrt{\text{Hz}}$ for hyperpolarised ^{19}F. The untuned microcoil enabled simultaneous multinuclear experiments, including 1D and 2D heteronuclear correlation spectroscopy, without the need for frequency tuning. The photo-CIDNP enhancement allowed rapid detection of target molecules, with a 230× increase in signal intensity for certain compounds. The system's small sample volume and efficient optical design also mitigated common challenges such as photodegradation of photosensitisers.

Hyperpolarised (HP) magnetic resonance spectroscopy (HP-MRS) is another technique that looks to boost the sensitivity of NMR spectroscopy. However, it requires separate dissolutions for each sample which is a resource-intensive process that introduces variability, and limits throughput. Using a vertical micro-reservoir, that enabled rapid sample loading and unloading, Lees et al. microcoil system allows for multiple measurements in a high-throughput manner, thus significantly improving efficiency compared to traditional methods [172].

They used their method (Fig. 2.6b) to measure HP pyruvate-to-lactate metabolic flux in multiple melanoma cell samples using a single hyperpolarised dissolution. By leveraging a deuterated dissolution buffer to extend the spin-lattice relaxation time of HP pyruvate, the authors aimed to analyze up to eight samples per dissolution. This setup was designed to reduce resource use, increase experimental reproducibility, and enable the study of multiple cell samples in a single experimental run.

Results demonstrated the utility of this system for studying the metabolic response of melanoma cells to BRAF inhibition. In BRAFV600E cells, treatment with vemurafenib significantly reduced the pyruvate-to-lactate flux, extracellular lactate, and glucose consumption, correlating with reduced cell proliferation. In contrast, BRAF wild-type cells showed no significant reduction in metabolic flux after 24 hours of treatment but displayed increased glycolytic activity after 48 hours, likely due to MAPK/ERK pathway activation. The use of the microcoil system improved experimental efficiency by 6–8 times compared to conventional methods.

Metabolism, like most biological processes, is in constant flux and most experiments only snap a single moment in time; however, real-time analysis can reveal the hidden between snapshots. Existing DNP-NMR methods require large cell quantities ($\sim 10^7$) for metabolic analysis due to their low sensitivity. This constraint makes it challenging to study mass-limited or rare cell populations, such as leukemia stem cells. The hyperpolarised micromagnetic resonance spectrometer (HMRS) platform designed by Jeong et al. addresses this gap by using a miniaturised microcoil integrated a microfluidic system that reduces sample requirements and plans for high-throughput scenarios [173].

The results demonstrate the HMRS platform's (Fig. 2.6c) ability to detect metabolic flux in as few as 10^4 cells, with a linear response to cell number. The system was validated by

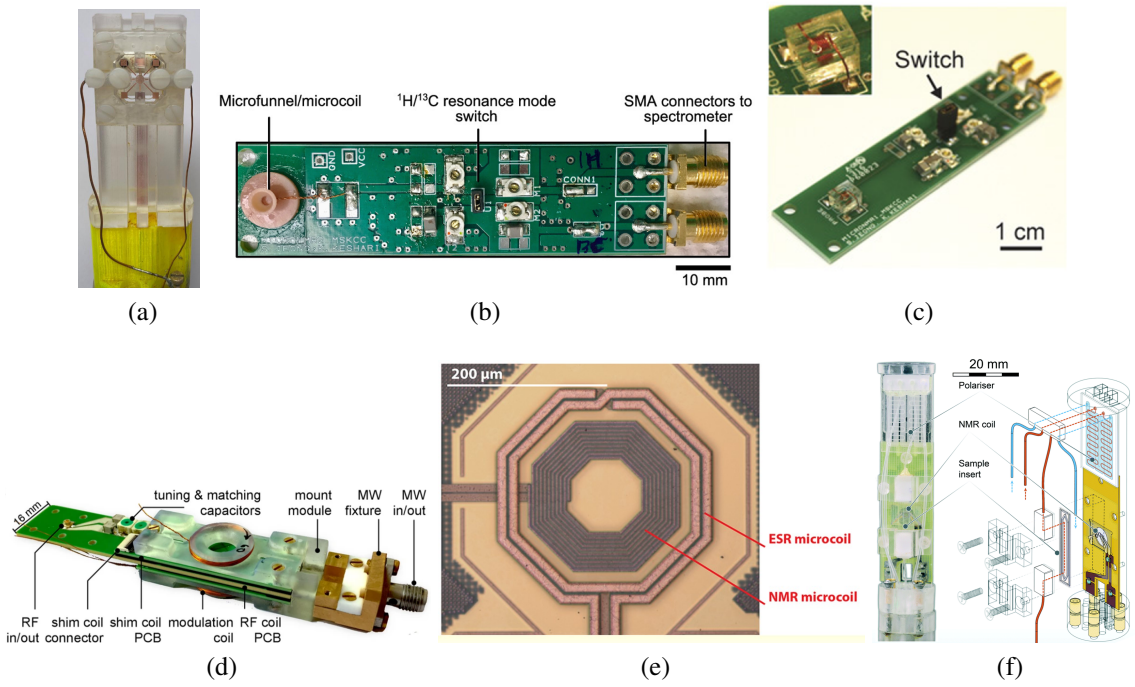

Figure 2.6: (a) Micro-SABRE NMR platform. Reproduced with permission from [171]. (b) Hyperpolarised NMR microcoil probe. Reproduced with permission from [172]. (c) Hyperpolarised micromagnetic resonance spectrometer probe. Reproduced with permission from [173]. (d) Overhauser DNP NMR probe. Reproduced with permission from [174]. (e) ESR and NMR coil structure within DNP-NMR chip. Reproduced with permission from [175]. (f) Microfluidic photo-CIDNP NMR probe. Reproduced with permission from [176].

profiling glycolytic flux in various cancer cell lines and comparing malignant and nonmalignant cells. In leukemia stem cells, the platform revealed nearly double the glycolytic flux compared to non-stem leukemia cells, correlating with high expression of the Myconcogene. Additionally, the platform was used to assess drug treatment efficacy, showing metabolic changes in cancer cells as early as three hours after treatment with imatinib, well before observable changes in cell viability.

Stronger, more homogeneous magnets inherently improve SNR but are usually bigger and/or require additional complexity. A way of sidestepping this limitation is to use techniques like Overhauser DNP (ODNP); however, that adds its own layer of hardware challenges. Kiss et al. designed an ODNP chip to enhancing signal sensitivity while enabling the NMR system to remain compact [174]. Their double-resonant probe head (Fig. 2.6d) that combines microwave and radiofrequency resonators within a microfluidic chip, enabling ODNP-enhanced spectroscopy of nanoliter-sized liquid samples. The system utilises a palm-sized, 0.5 T permanent magnet to create a compact and portable NMR platform.

The results showed substantial improvements in performance. ODNP-enhanced NMR achieved up to a 60-fold increase in SNR compared to thermal equilibrium signals, enabling the detection of 130 nL samples with high sensitivity. The system demonstrated a chemical shift

resolution of 0.7 ppm, comparable to much larger and more complex setups. Additionally, the probe head's modular design allowed for scalability and easy integration of components like shim coils and resonators. The experiments revealed minimal sample heating and consistent performance across varying sample volumes.

Further shrinking the apparatus for DNP, Sahin Solmaz et al. integrated NMR and electron spin resonance (ESR) detectors on a silicon chip of approximately 2 mm^2 [175]. The system reduced the footprint by making both both microcoils for ESR and NMR detection concentric.

Results showed that the single-chip microsystem (Fig. 2.6e) provided NMR signal enhancements of up to 50× for liquid samples of TEMPOL/H_2O with an effective volume of about 1 nL. The integrated ESR and NMR systems operated at 10.7 GHz and 16 MHz, respectively, demonstrating effective DNP capabilities. The system reduced power consumption and maintained high spectral resolution, despite the constraints of miniaturization. Additionally, the compact design opens possibilities for arrays of such chips for parallel spectroscopy, further increasing throughput for analytical applications.

In the realm of hyperpolarization techniques, parahydrogen-induced polarization (PHI-P) is another such method. Bordonali et al. incorporated Signal Amplification by Reversible Exchange (SABRE), a non-hydrogenative sub-class of PHIP, to address challenges related to the sensitivity and spectral crowding often encountered in NMR analysis of complex mixtures with low concentrations [176]. By combining SABRE with a microfluidic system (Fig. 2.6f), Bordonali et al. aimed to enhance NMR sensitivity while simplifying spectral complexity for precise identification of molecular components.

The platform includes a microfabricated polydimetilsiloxane (PDMS) membrane, serving as a gas–liquid contactor to facilitate parahydrogen transfer, and a compact microcoil NMR detector for efficient signal acquisition. The platform achieved significant signal enhancements, with up to 4.6-fold improvements for certain analytes and the detection of picomole quantities of material. The SABRE process generated clear, far-shifted dihydride peaks in the spectrum, enabling selective chemosensing. Experiments validated the system's ability to resolve signals in complex mixtures and provided linear sensing capabilities down to micromolar analyte concentrations. The results also highlighted the system's reproducibility and modularity, making it suitable for lab-on-a-chip applications.

Stripline Probes

Stripline probes have shown excellent sensitivity for volume-limited samples. Chen et al. showed even a simple designs work very well for compact and high-performance detectors suitable for applications like metabolomics and single-cell studies [177]. Two designs were explored: a flat-wire detector without a ground plane and a microstrip detector with a ground plane. First-generation detectors were manufactured with electroplated copper on substrates, and second-generation detectors used printed circuit board (PCB) techniques for batch fabrication (Fig.

2.7a). Improvements to copper surface finish and substrate smoothness significantly enhanced spectral resolution.

The presence of a ground plane improved RF sensitivity and homogeneity by confining residual RF fields, while optimised dimensions balanced sensitivity and homogeneity. Experimental results showed that the microstrip detector achieved RF homogeneity levels comparable to commercial NMR probes, with sensitivity metrics that enabled the detection of subnanoliter samples. For example, the microstrip detector demonstrated an LOD of 0.73 nmol $s^{1/2}$ for 0.13 nmol sucrose in 0.63 nL H_2O. Additionally, high-resolution 1D and 2D NMR spectroscopy was performed on nanoliter-scale samples, demonstrating the detector's capability for advanced NMR experiments.

Cheng et al. further improved on their previous work [177] by integrating a butterfly design into a stripline resonator design (Fig. 2.7b) aimed to further improve them [178]. The proposed design merges the advantages of each to enable a stronger and more focused RF magnetic field.

The design used a two-layer PCB with a flat capillary in between to deliver the sample underneath the coil. The butterfly-stripline and ground layers were separated by a PMMA spacer that also housed the capillary. Their study employed finite element method (FEM) simulations and experimental measurements to evaluate the performance of the butterfly stripline compared to a conventional stripline.

The results demonstrated that the butterfly stripline achieved a 7-fold increase in $\vec{B}_1$ field intensity and a 2-fold improvement in SNR compared to the regular stripline. The butterfly design also showed better RF shielding, with reduced signal coupling between adjacent coils, making it suitable for parallel NMR arrays. Experimental measurements revealed a shorter 90° pulse duration and higher sensitivity for the butterfly stripline, confirming the simulation predictions. The design flexibility of the butterfly structure allows for further optimization, such as tailoring $\vec{B}_1$ profiles for specific applications.

Planar Microcoils

Compared to traditional probes, planar microcoils are advantageous due to their compatibility with diverse sample sizes and shapes, but their inhomogeneous $\vec{B}_1$ field raises challenges for complex multi-pulse NMR sequences. Moxley-Paquette and colleagues evaluated the performance of double-tuned single-sided planar microcoils for heteronuclear 2D NMR spectroscopy, focusing on mass-limited samples enriched with ^{13}C, such as broccoli seeds and Daphnia magna [179]. They assessed whether planar microcoils could offer sensitivity and resolution improvements for localised sample regions (Fig. 2.8a).

They optimised and tested various ^{2}D ^{1}H–^{13}C NMR pulse sequences to determine the optimal experimental setup for planar microcoils. The microcoils' performance was then compared to a commercial 5 mm NMR probe, shown in Fig. 2.8b. This standard probe typically consists of a solenoidal RF coil wrapped around a 5 mm diameter sample tube, positioned at the center

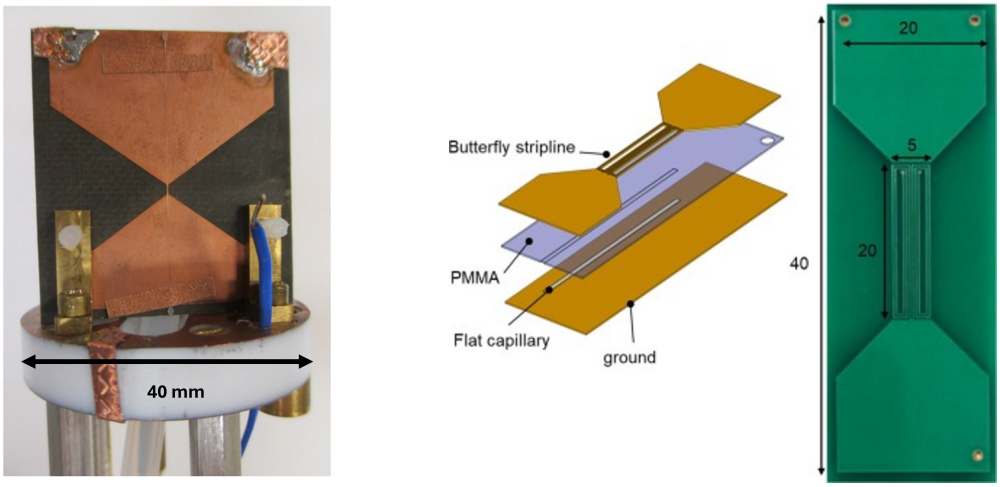

(a) (b)

Figure 2.7: (a) 1 mm x 0.15 mm microstrip NMR probe. Reproduced with permission from [177]. (b) Butterfly stripline design. Reproduced with permission from [178].

of a magnet bore [180]. The geometry is designed to achieve a high degree of magnetic field homogeneity and consistent $\vec{B}_1$ excitation across the entire sample volume. One of its main advantages is its ability to accommodate relatively large sample volumes (typically 600 µL), which increases absolute sensitivity and supports quantitative spectroscopy. However, this comes at the cost of a lower filling factor for mass-limited samples and higher hardware complexity.

In contrast, planar microcoils achieved a sixfold improvement in mass sensitivity over the conventional 5 mm probe, albeit for a much smaller detection volume localised within 0.7 mm of the coil surface. Optimised Heteronuclear Multiple-Quantum Correlation (HMQC) experiments using adiabatic pulses emerged as the best-performing sequence, balancing sensitivity and tolerance for $\vec{B}_1$ inhomogeneity. This setup enabled the identification of metabolites in a single Daphnia magna for the first time and revealed localised metabolite profiles in broccoli seeds and Daphnia. Despite these advantages, the highly localised detection volume posed challenges for larger or heterogeneous samples.

Planar microcoils provide open access for diverse sample sizes and flow systems but suffer from $\vec{B}_1$ field inhomogeneity, which impacts NMR performance. Helmholtz microcoils, on the other hand, offer superior $\vec{B}_1$ field homogeneity but impose size constraints on samples. By comparing these designs, it's possible to determine the suitability of each for different applications, particularly for metabolomics and environmental toxicity studies. Bastawrous et al. compared the performance of these two coil designs in terms of $\vec{B}_1$ field homogeneity, sensitivity, and their ability to handle complex biological samples, such as Daphnia magna eggs and chicken brain tissue [181]. They evaluated various NMR pulse sequences, including single and multi-pulse experiments, to assess the applicability of each coil type for metabolic and environmental research.

The results showed that Helmholtz microcoils outperformed planar microcoils (Fig. 2.8c) in

terms of $\vec{B}_1$ field homogeneity and sensitivity, achieving a doubling of SNR. They were particularly effective in multi-pulse and 2D experiments, which require precise RF performance. Planar microcoils, while less sensitive and prone to $\vec{B}_1$ inhomogeneity, performed adequately in single-pulse experiments and offered advantages in accommodating non-standard sample geometries and flow-based systems. Additionally, Helmholtz microcoils are better suited for complex pulse sequences and high-resolution biological studies, while planar microcoils remain valuable for specific applications requiring open-access designs or dynamic sample handling.

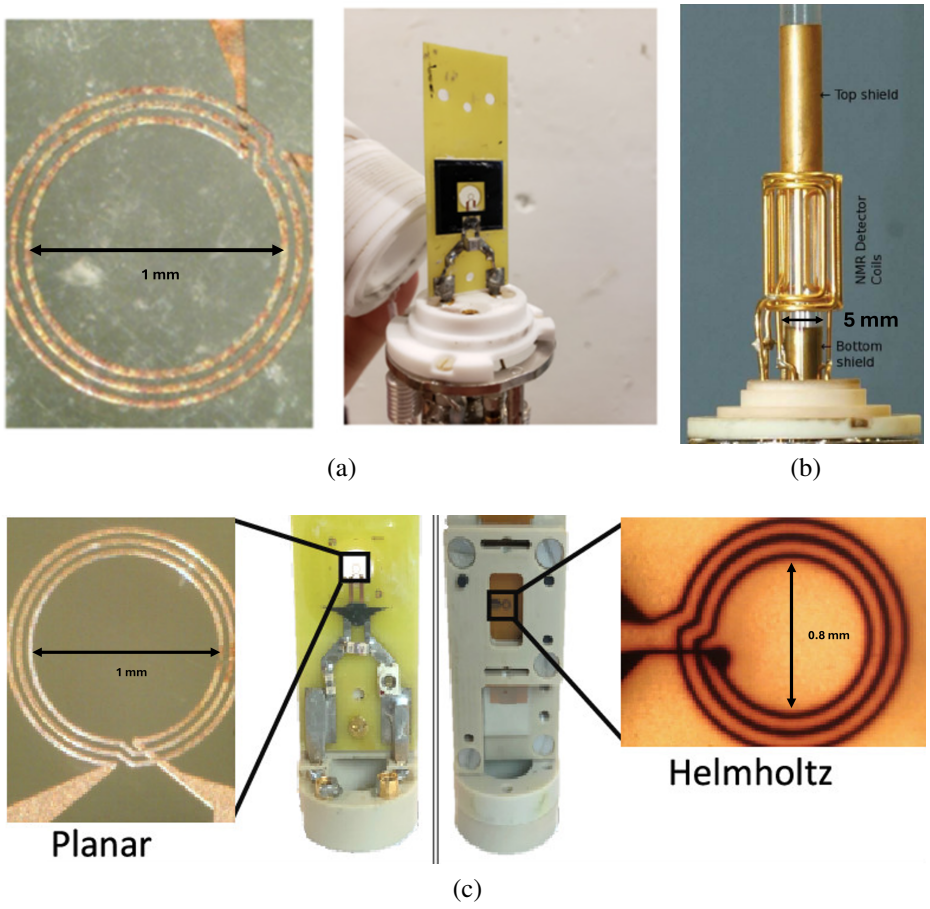

Figure 2.8: (a) Planar microcoil structure (left) placed inside probe housing (right). Reproduced with permission from [179]. (b) A standard 5 mm NMR probe. Reproduced with permission from [180] (c) Planar and Helmholtz microcoil configurations. Reproduced with permission from [181].

Large-Scale NMR Probe Production

In addition to the issues around mass-sensitivity, producing microcoils at scale is also a challenging task. To tackle these issues, Lepucki et al. introduced a self-assembled rolled-up microcoil integrated into a microfluidic system for nanoliter-scale samples [182]. Their design (Fig. 2.9a) leverages wafer-scale fabrication to create cylindrical geometries with nearly 100% filling factor,

encapsulated in PDMS to optimise analyte containment and eliminate parasitic signals. The microcoil architecture is engineered to minimise magnetic field inhomogeneities, which are further mitigated through intrinsic susceptibility matching and precise geometry tuning. By ensuring the inner winding of the coil directly interfaces with the analyte, the system aims to achieve enhanced sensitivity and spectral resolution.

The results demonstrate significant advancements in performance. The microcoils achieved an unprecedented spectral linewidth of 8 ppb with active shimming and 22 ppb without shimming, indicating exceptional resolution. The system's nLOD was calculated as 7.9 nmol/$\sqrt{\text{Hz}}$, placing it among the highest-performing microcoil-based NMR detectors. Comparative experiments showed that the microcoils outperformed conventional solenoid-based NMR setups by over an order of magnitude in resolution. The device's compact detection volume of 1.5 nL further highlights its suitability for high-resolution analyses of mass-limited samples.

At the sub-milliliter volume, glass capillaries are the most common type of sample container. Getting the microcoil on or around the capillary thus requires some creativity, especially if you need a low-cost scalable method. Wang et al. interestingly combined two-dimensional patterning of the coil with a rolling mechanism that enveloped it around the capillary [183].

The manufacturing process (Fig. 2.9b) begins with 2D patterning via inkjet printing and photolithography to define precise conductive paths on a flexible substrate. Electroplating then deposits a copper layer for low-resistance, high-frequency performance. The key innovation is rolling the patterned substrate into a cylindrical microtube, transforming the 2D layout into a 3D saddle-shaped coil. Controlled rolling ensures precise alignment and spacing, optimising magnetic field homogeneity and Q factors. The resulting microtubes, as small as 620 μm in diameter, remain structurally robust for high-frequency applications.

The results demonstrate the versatility and effectiveness of this process. The fabricated micro saddle coils, with diameters as small as 620 μm, achieved excellent electrical performance, including a Q factor of 60 at a resonance frequency of 500 MHz. NMR spectroscopy tests using these coils showed a SNR of 722.75 for an 82 nL sucrose solution sample, with a nLOD of 18.78 nmol/$\sqrt{\text{Hz}}$. High-resolution MRI experiments further validated the coil's performance, capturing detailed images of a grass stem sample with an in-plane resolution of 12 μm $\times$ 12 μm. The ability to fabricate exchangeable microfluidic sample channels also adds flexibility for various chemical and biological applications.

Traditional fabrication techniques for 3D microprobes often involve complex and time-consuming processes, which makes production at scale costly. However, microprobes that are sufficiently small can leverage existing methods like wafer-based processes. Karnaushenko et al. used strain-engineered ultrathin films to fabricate self-assembling Swiss-roll microcoils [184]. The self-assembly process allows for the transition of planar structures into three-dimensional architectures (Fig. 2.9c), significantly reducing device footprint while improving electromagnetic characteristics.

The results reveal that the self-assembled devices exhibit substantial performance improvements compared to their planar counterparts. The inductors demonstrated up to a fourfold increase in inductance and a 50-fold reduction in footprint. Additionally, the resonators achieved high quality factors of over 40,000, and the transformers showed enhanced mutual inductance and coupling coefficients. The devices served as LC resonators for NMR and ES experiments. The rolled-up NMR microcoils, for instance, successfully detected proton signals in glycerol, demonstrating their potential for high-sensitivity spectroscopy.

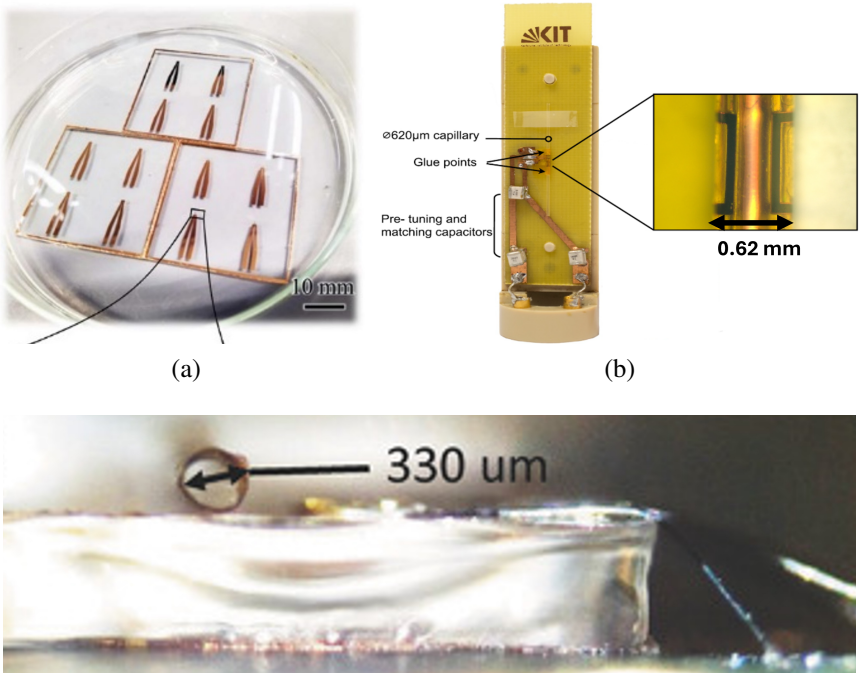

(a) (b)

(c)

Figure 2.9: (a) Self-assembled rolled microcoils. Reproduced with permission from [182]. (b) Rolled NMR saddle microcoil. Reproduced with permission from [183]. (c) Rolled-up NMR microcoil. Reproduced with permission from [184].

Electrochemistry and NMR

Electrochemistry is another powerful technique for studying the chemistry of samples. Normally, NMR and electrochemistry are seen as separate approaches, but in recent years they have been integrated to enable in situ electrochemical experiments. However, one of the major challenges is that the conductive electrodes that are necessary for electrochemical studies can introduce magnetic field distortions and degrade the quality of NMR signals. To combat this issue, Davoodi et al. aimed to identify electrode designs that mitigate these effects, enabling precise characterization of electrochemical reactions in microfluidic environment [185].

A combination of finite element simulations and experimental validation was used to test different metallic electrode configurations to minimise their impact on the homogeneity of the $\vec{B}_0$

and $\vec{B}_1$ fields. The results showed that specific electrode configurations, such as narrow-channel sidewall electrodes, significantly reduced magnetic field distortions and enhanced field homogeneity while preserving signal quality. Simulated and measured data demonstrated that these configurations improved sensitivity and spectral resolution compared to traditional designs. The researchers also conducted a proof-of-concept experiment on in situ chitosan electrodeposition (Fig. 2.10a), successfully monitoring the process using NMR. The experiment highlighted the platform's potential for non-invasive, real-time analysis of electrochemical reactions.

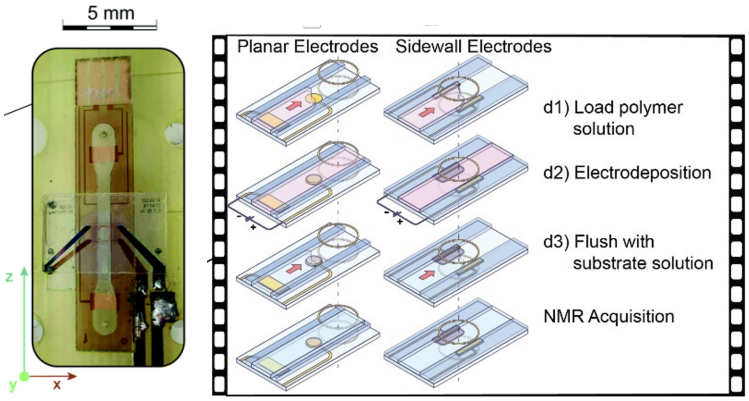

(a) (b)

Figure 2.10: (a) NMR electrochemistry probe. Reproduced with permission from [185]. (b) In situ electrodeposition process. Reproduced with permission from [186].

Nordin et al. demonstrated the use of microfluidic NMR for real-time monitoring of compartmentalised chemical reactions at microscale levels [186]. The study aimed to mimic biological environments by creating spatially separated reaction zones within hydrogels, enabling a controlled investigation of enzymatic processes. This approach provides insights into metabolic cascades and catalytic efficiency in complex systems.

They analysed the reactions in the multilayered hydrogel assemblies (Fig. 2.10b) using a custom NMR probe and a microfluidic device that incorporated the electrochemical functionalities to electrodeposit enzyme-loaded chitosan hydrogels. By functionalising each hydrogel layer with different enzymes, they monitored enzymatic activities both independently and in cascades within the same detection volume. The system enabled simultaneous monitoring of urea hydrolysis and glucose oxidation (GOx) reactions, with NMR data revealing clear differences in reaction kinetics depending on the hydrogel composition and assembly order. The device also facilitated high-resolution NMR spectra, confirming its capability for in situ biochemical analysis without compromising sensitivity or field homogeneity.

Digital Microfluidics

Samples in NMR experiment are very difficult to control or alter once the experiment has begun. However, as shown in the discussion above, it is possible to control the chemical reactions tak-

ing place. Swyer et al. introduced a digital microfluidics (DMF) system that operated within a high-field NMR spectrometer and allows for precise manipulation of microliter droplets directly within the system [187]. By integrating DMF with NMR (Fig. 2.11a), the team aimed to develop a flexible platform capable of overcoming these constraints while enabling high-resolution chemical analysis and in-situ reaction monitoring with minimal sample volumes.

The manufacturing process began with fabricating the DMF device on a glass substrate using photolithography and thin-film deposition techniques. The device consisted of a single-plate electrode array covered with a dielectric layer to ensure proper droplet actuation. A hydrophobic coating was applied to the top surface to reduce droplet adhesion and facilitate smooth movement. The electrode design was optimised to generate strong, localised electric fields capable of controlling microliter-scale droplets on the planar surface with high precision. For integration with the NMR system, a planar microcoil was positioned beneath the DMF device. The microcoil was fabricated through standard microfabrication techniques, such as electroplating copper onto a patterned substrate.

The results demonstrate that the DMF-NMR system successfully manipulates microliter droplets with no dead volumes, maintaining magnetic field homogeneity suitable for high-resolution spectroscopy. The researchers used the platform to monitor a borate–xylose and GOx reaction, showing clear spectral changes corresponding to reaction progress. Time-resolved reaction monitoring highlighted the system's ability to decouple reaction time from flow rate, reducing sample requirements. Additionally, the system achieved high reproducibility for both one-dimensional and two-dimensional NMR spectroscopy, validating its potential for microscale chemical analysis.

Swyer and colleagues created a two-plate DMF system integrated with NMR spectroscopy to enable droplet-scale manipulation of small sample volumes to enhance NMR spectral resolution [188] A microcoil was embedded within a DMF counter-electrode (Fig. 2.11b), allowing for controlled droplet movement, improved magnetic field homogeneity, and advanced chemical analysis. This builds on their previous one-plate DMF system which had restricted capabilities for droplet manipulation and poor spectral resolution [187].

The new two-plate system was designed to provide better control over droplet orientation and shape, which directly impacts the magnetic field homogeneity within the droplet and the quality of the resulting NMR spectra. This setup aimed to enable sophisticated applications such as diffusion-ordered spectroscopy (DOSY) and real-time reaction monitoring in a compact and efficient platform. The two-plate system allowed for precise droplet orientation along the magnetic field axis, resulting in enhanced spectral resolution. For example, elongated droplets oriented parallel to the magnetic field achieved superior field homogeneity and narrower spectral linewidths compared to other configurations. The system was successfully applied to measure diffusion coefficients using DOSY, yielding results consistent with literature values for model analytes. Additionally, the platform enabled real-time monitoring of rapid chemical reactions,

such as the decarboxylation of glycine, with time-resolved spectral data capturing reaction dynamics.

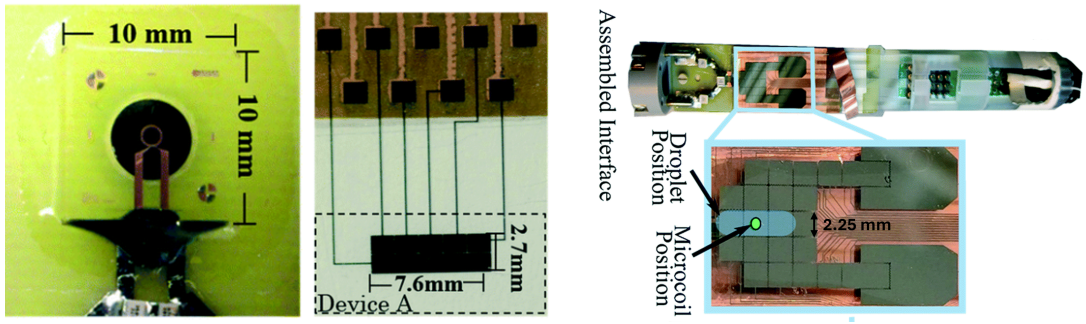

(a) (b)

Figure 2.11: (a) Microcoil (left) and electrodes (right) of one-plate DMF platform. Reproduced with permission from [187]. (b) Two-plate DMF-NMR probe. Reproduced with permission from [188].

Integrated Circuit-Based NMR Microcoils

In small animals MRI systems, image artifacts can be created by field and gradient imperfections. This can cause traditional MRI systems struggle to achieve the precision required for advanced imaging sequences and ultrashort echo times. One potential solution presented by Handwerker et al. was to development of a fully integrated field probe for real-time trajectory mapping during MRI experiments [189]. They proposed incorporating a custom application-specific integrated circuit (ASIC) with a microcoil and transceiver electronics on a single chip (Fig. 2.12a). The small form factor and low power consumption enable the deployment of arrays of probes to measure and correct higher-order field imperfections in MRI systems.

The microcoil, essential for detecting the NMR signal, was fabricated using lithographic techniques and electroplating to achieve precise geometric control. The coil was directly bonded to the ASIC, ensuring a compact design and reducing parasitic effects that could degrade performance. Special attention was given to minimising magnetic interference from the electronic components, as well as ensuring compatibility with the high-field MRI environment.

The results demonstrate that the field probes successfully measured and corrected gradient-induced imperfections in an 11.7 T small animal MRI scanner. The probe array, consisting of four spatially distributed sensors, achieved high spatial and temporal resolution, enabling the measurement of zero-order and first-order field imperfections. The proposed system reduced gradient trajectory errors by a factor of 20, significantly enhancing the accuracy of MRI trajectory mapping. Additionally, the compact probes operated independently of the MRI host system, allowing for flexible deployment in constrained environments.

NMR's non-invasive, real-time approach holds potential for applications like assisted reproductive technologies and developmental biology. Sivelli et al. used chip-based NMR spec-

troscopy to analyze single mammalian pre-implantation embryos [190]. By targeting single embryos, the study sought to establish a proof of concept for using NMR spectroscopy as a tool to investigate molecular compositions, particularly lipids, within individual samples.

The researchers developed a custom-designed microchip integrated with a microcoil and 3D-printed structures (Fig. 2.12b) for sample positioning that integrated into a 300 MHz Bruker system for experimentation. The system enabled non-invasive, in situ biochemical analysis of bovine embryos arrested at different developmental stages, such as 2-cell stages and morulae. Results showed that the system could successfully detect distinct NMR signals from single embryos, predominantly originating from their lipid content. The spectral linewidths were comparable to those observed in other small biological samples, such as microorganism eggs. The analysis revealed variations in lipid composition among embryos at similar developmental stages, suggesting that this method could provide insights into individual biochemical profiles. Additionally, the study demonstrated that the system maintained sample integrity, with no observable physical damage during or after the measurements.

Exploring the application of broadband complementary metal-oxide-semiconductor (CMOS) micro-coil NMR technology for environmental research, Lysak wanted to overcome sensitivity limits which are insufficient for samples like individual eggs or seeds [191]. Large sample volumes naturally improve SNR, however when volumes are unavailable then incorporating steady-state free precession and multi-nuclear NMR may overcome some of these issues.

The researchers here investigated various heteronuclei and evaluated the system's (Fig. 2.12c) performance in detecting fluorinated pollutants in single organisms, with the aim to demonstrate the potential of CMOS micro-coils to provide a scalable, cost-effective, and high-sensitivity solution for studying such complex experiments. The system achieved detection limits in the picomole range for various nuclei, including $^{1}3C$, $^{1}9F$, and $^{3}1P$. A steady-state free precession sequence enabled a six-fold improvement in signal-to-noise ratio for $^{1}3C$ NMR of a sprouting broccoli seed, revealing detailed metabolic profiles. Additionally, $^{1}9F$ NMR tracked fluorinated contaminants in Daphnia magna eggs, demonstrating the technology's capability to study pollutant interactions in single organisms. The study concluded that CMOS micro-coil NMR offers a promising platform for advancing environmental research, with future potential for scaling to multi-coil arrays for higher throughput.

High-Throughput NMR

Conventionally most NMR systems are restricted to single-sample measurements, but through methods like automated sample changers it's possible to increase throughput. These systems are designed to use standard NMR sample tubes, so methods leveraging microfluidics cannot leverage this approach. Nassar et al. sought to create a scalable and automated solution capable of both reducing sample preparation time and maximising throughput [192].

Their approach integrated a micro-saddle NMR detector with impedance-based flow sensing

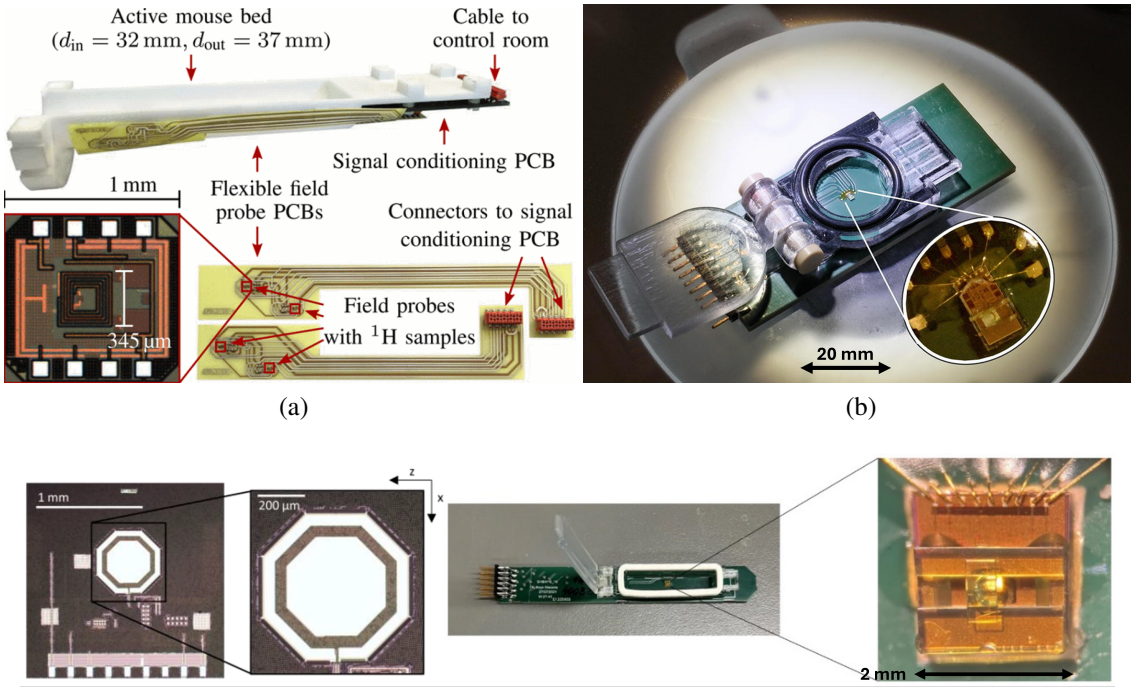

Figure 2.12: (a) CMOS-based array probe integrated into mouse bed for MRI trajectory mapping array. Reproduced with permission from [189]. (b) NMR embryo probe placed in a 3D-printed sample holder. Reproduced with permission from [190]. (c) Octagonal CMOS microcoil (left) integrated into PCB-based sample holder (right). Reproduced with permission from [191].

(Fig. 2.13a) for real-time sample tracking and synchronization. By employing a dual-phase flow approach, samples are arranged as plugs separated by immiscible fluids, transported through a capillary tube for measurement. The impedance sensors monitor the position and velocity of each sample, triggering the NMR data acquisition precisely when the sample enters the detector. Results demonstrated the system's capability for high-resolution and high-sensitivity NMR analysis. The automated triggering system reduced sample acquisition times to as little as 15.3 seconds per sample, achieving a sensitivity of 2.18 nmol/$\sqrt{\text{Hz}}$. The micro-saddle coil provided excellent spectral resolution with a linewidth of 1.25 Hz. Experiments on various aqueous solutions and commercial beverages validated the system's robustness, showing consistent sample detection and spectral quality. Notably, the system effectively differentiated chemical compositions without cross-contamination between samples.

High-throughput NMR in compact systems is an additional challenge on top the already difficult requirements. Lei et al. tested a solution that introduces parallel testing to enable higher throughput without significantly increasing the footprint [193]. They integrated a compact permanent magnet, a chip-based NMR spectrometer, and DC motors (Fig. 2.13b) to enable simultaneous analysis of multiple samples using time-interleaved scans and MRI techniques.

Using time-interleaved scans, the system analyzed two to four samples with separate NMR coils, achieving a 2-4x increase in throughput for 1D and 2D NMR spectroscopy, including two-

dimensional correlation spectroscopy (COSY) and relaxometry. Additionally, the MRI-based configuration analyzed up to 18 samples simultaneously in a single NMR coil, accelerating T_2relaxation measurements by 4.5 times. Field homogeneity optimization through shimming and motional averaging enabled sub-ppm resolution, critical for high-resolution spectroscopy. The system successfully identified chemical shifts and resolved fine J-coupling structures, validating its performance in various NMR applications.

One of the limitations of current multi-channel probes is that when tuned to a specific nucleus they cannot be repurposed mid-experiment for a different one. This is a result of their often-mechanical tuning mechanism. The software-defined radio (SDR) has enabled a wide range of frequencies to be used without the need for analogue devices. Huber et al. showed that SDR can be leveraged in NMR systems for the same purpose [194]. They introduced heteronuclear resonance multichannel electronic system (HERMES) (Fig. 2.13c), a scalable, multichannel NMR platform designed to improve throughput and versatility in NMR detection. The system uses virtual NMR consoles to perform parallel measurements on multiple samples across heteronuclear spins, and allow on-demand configuration of NMR modules without increasing system complexity.

The results highlight HERMES's effectiveness in performing multiplexed NMR analyses. The system demonstrated accurate parallel T_1 and T_2 relaxometry across multiple probes, significantly reducing assay times while maintaining high measurement reliability. Heteronuclear spectroscopy experiments successfully resolved chemical shifts for nuclei such as ^{1}H, ^{19}F, and ^{13}C, with high spectral resolution and sensitivity. Biosensing applications included the detection of dengue virus markers and profiling cancer cells with molecular-specific magnetic nanoparticles. HERMES achieved detection limits of 2 pg/μL for dengue virus NS1 protein and 25 cells for ovarian cancer cells, surpassing conventional diagnostic methods in sensitivity and efficiency.

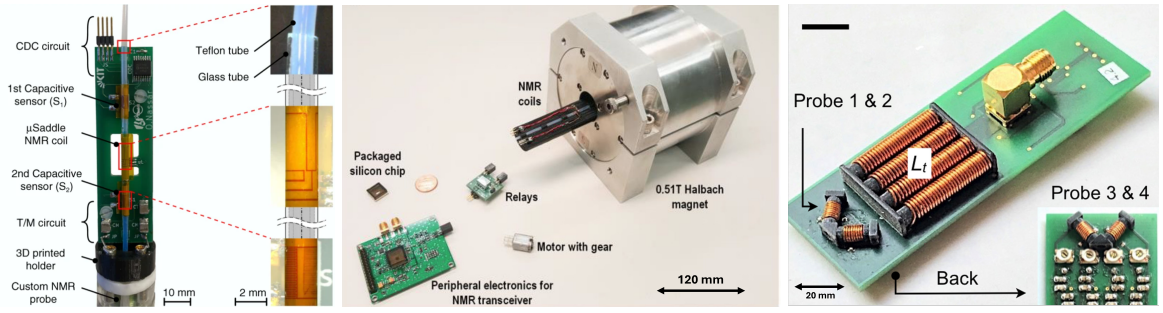

(a) (b) (c)

Figure 2.13: (a) High-throughput NMR probe. Reproduced with permission from [192]. (b) Motorised multi-sample NMR system. Reproduced with permission from [193]. (c) HERMES NMR platform. Reproduced with permission from [194].

Implantable NMR

Normally NMR is seen as a non-invasive technique, but certain cases require a degree of invasiveness. Intercranial spectroscopy is such a case, where an implanted device can achieve higher sensitivities and resolution that conventional methods. Fakri-Bouchet et al. developed an implantable microcoil for the detection of cerebral metabolites [195]. The microcoil (Fig. 2.14a) was developed to improve the limits of detection (LOD) and SNR for localised brain metabolite analysis, enabling high-resolution studies of cerebral metabolism in small animals. The work also aimed to assess the biocompatibility and practicality of implantable NMR devices for chronic use.

The microcoil was designed with a planar geometry, featuring dimensions of 500 μm $\times$ 1000 μm, and optimised to match the size of the region of interest in the brain. The study compares the performance of the microcoil to that of a commercial surface coil and evaluates its potential for in vivo applications in small animal models. Results from in vitro studies showed that the microcoil achieved a 2.5-fold improvement in sensitivity compared to the surface coil, with lower LOD for metabolites such as choline, N-acetylaspartate, lactate, and creatine. The microcoil outperformed the surface coil in detecting small metabolite concentrations, demonstrating superior performance for mass-limited samples. In vivo studies on Wistar rats validated the biocompatibility of the microcoil, with the animals surviving up to four months post-implantation. The implanted microcoil provided reproducible results under stereotaxic conditions and enabled high-resolution detection of cerebral metabolites with minimal damage to surrounding tissue.

Where Fakri-Bouchet only designed for the coil to enter the body [195], Handwerker et al. used CMOS technology to integrate both probe and electronics onto a needle spectrometer that can enter the body. Their approach aimed to push the limits of sensitivity to as high as possible [196].

The NMR needle (Fig. 2.14b) works by integrating an ultra-sensitive 300 μm microcoil and a complete NMR transceiver on a single silicon chip. This device enables localised NMR measurements in nanoliter volumes with a sampling rate of 200 Hz, providing insights into changes in blood oxygenation and cerebral blood flow (CBF) in small animals. The results demonstrated the needle's ability to achieve a 40-fold improvement in SNR compared to conventional surface coils. In vitro experiments showed a sensitive volume of 9.8 nanoliters with excellent spectral resolution of 12 Hz. In vivo experiments in rats revealed functional responses in the somatosensory cortex to forepaw stimulation, with detectable changes in CBF and blood oxygenation. The needle's temporal resolution enabled real-time monitoring of hemodynamic changes with a 150-fold improvement in volume-normalised temporal SNR compared to standard functional MRI.

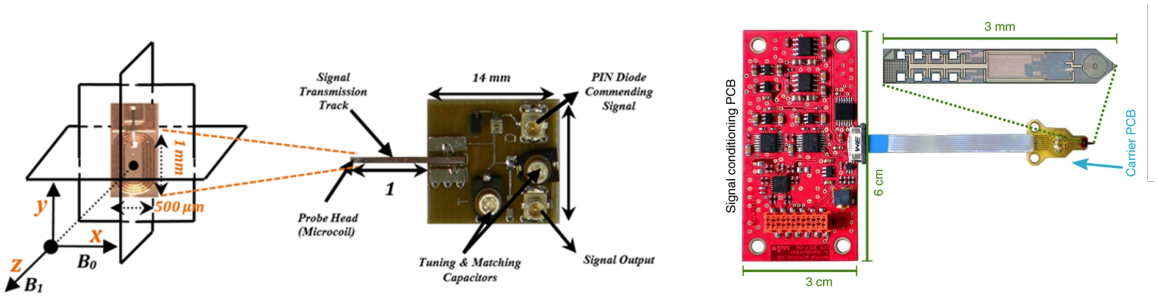

(a) (b)

Figure 2.14: (a) Implantable NMR microcoil. Reproduced with permission from [195]. (b) NMR CMOS needle probe. Reproduced with permission from [196].

Optically Polarised NMR

Diamond-based quantum sensors have become an alternative method of detecting NMR signals due to their submicrometer detection volumes and non-inductive detection capabilities. However, they struggled with spectral broadening and sensitivity issues. Smits et al. aimed to overcome these challenges and improve the resolution and applicability of nitrogen-vacancy (NV)-based NMR spectroscopy for mass-limited and single-cell biology applications [197]. They created a microfluidic diamond quantum sensor for two-dimensional NMR spectroscopy (Fig. 2.15a).

The authors designed a system that spatially separates polarization and detection phases, utilising NV centers in diamond as the quantum sensing mechanism. By leveraging this approach, they achieved high spectral resolution and sensitivity for analysing picoliter-scale liquid samples, enabling COSY for complex chemical analysis. Results demonstrated a significant improvement in spectral resolution, achieving 0.65 Hz, which is an order of magnitude better than previous studies. The system also exhibited a concentration sensitivity of 27 $M^{1/2}$ s, enabling the detection of chemical shifts and J-couplings in a 40-picoliter detection volume. Using the platform, the researchers successfully performed 2D COSY spectroscopy on trimethyl phosphate and 1,4-difluorobenzene, resolving complex spectral features with high precision. These experiments validated the platform's ability to analyze small molecules and highlighted its potential for single-cell metabolomics and in-line microfluidic chemical analysis.

Atomic vapour cells are a non-traditional type of NMR probe that use optically pumped alkali metal vapors to polarise spins, which then interact with external magnetic fields, allowing for highly sensitive detection of weak magnetic signals. Due to their use of gas, they are more complex to manufacture than traditional probes, and relaxation are greatly times in these sensors are affected by factors like wall collisions and spin-exchange interactions.

Noor and colleagues used a micro-glassblowing technique to fabricate spherical vapour cells (Fig. 2.15b), focusing on the effects of inner wall coatings and the construction materials on relaxation times, particularly for xenon isotopes [198]. They aimed to improve the performance

of NMR gyroscopes by reducing transverse relaxation rates, which directly impact the ARW and sensor precision. Their fabrication process involved etching cavities into silicon wafers, followed by anodic bonding of glass wafers to form spherical cells under high temperatures. To further optimise the cells, a 10 nm layer of aluminum oxide (Al_2O_3) was deposited on the inner walls using atomic layer deposition (ALD). Cells made from aluminosilicate glass (ASG) were also tested alongside conventional borosilicate glass (Pyrex). Experimental measurements of T_2relaxation times for ^{129}Xe and ^{131}Xe isotopes were conducted under controlled conditions to evaluate the effects of these modifications.

The results showed that ALD Al_2O_3 coatings increased the T_2 relaxation time of ^{131}Xe by a factor of 4.7 compared to uncoated Pyrex cells, while ASG cells provided a 3.2-fold increase. These improvements translated into significant reductions in ARW for NMR gyroscopes, with Al_2O_3-coated cells reducing ARW by fourfold. However, the coating reduced the T_2 of ^{129}Xe by twofold, while ASG had no notable impact on this isotope. The study confirmed that material and coating optimizations can significantly enhance NMR sensor performance by minimising relaxation losses.

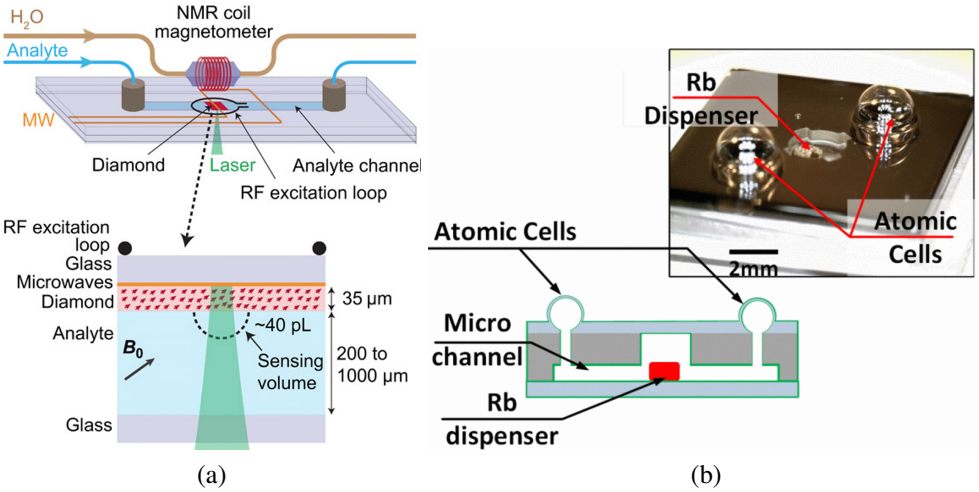

Figure 2.15: (a) Microfluidic prepolarization NMR probe. Reproduced with permission from [197]. (b) NMR atomic vapour cell. Reproduced with permission from [198].

Lenz lens NMR

Lenz lenses are passive electromagnetic structures used to enhance the detection sensitivity of NMR systems, particularly in cases where direct access to the detection site is limited or not feasible. They operate on the principle of magnetic flux conservation, derived from Lenz's Law, which states that an induced current in a closed loop opposes the change in magnetic flux that created it.

One of the key advantages of Lenz lenses is their simplicity. They are entirely passive structures that do not require any active electronics or power supply, which makes them easy

to fabricate and integrate into compact systems. When designed properly, they can concentrate magnetic flux into a small region, thereby improving the filling factor, which is the ratio of sample volume to coil volume. Since NMR sensitivity scales with the filling factor, even a modest improvement in this parameter can lead to significant gains in SNR. This is particularly beneficial in low-field or miniaturised NMR systems, where sensitivity is already limited by weak signal amplitude and broader line widths [199], [200].

In addition to their signal-focusing properties, Lenz lenses are especially useful in configurations where the detection coil cannot be placed in direct proximity to the sample. For instance, in microfluidic systems or in vivo applications, the geometry of the device or biological constraints may prevent the use of a conventional solenoid or surface coil at the detection site. In such cases, a Lenz lens can act as an intermediate coupler, transferring magnetic energy from the sample to a remotely located coil with minimal physical intrusion [201]. This approach has been demonstrated in lab-on-a-chip platforms and implantable biosensors, where access is limited but signal detection must still be performed with high fidelity. Moreover, their wireless nature can help reduce mechanical constraints in rotating systems or samples embedded in sealed environments [202].

However, Lenz lenses do have important limitations. Because they rely on mutual inductive coupling between loops, any misalignment or offset between the lens and the external detection coil can significantly reduce coupling efficiency. Their operation is also frequency-dependent: the geometry and spacing of the loops must be carefully tuned to the system's resonance frequency to avoid detuning or signal attenuation. Furthermore, while they improve local sensitivity, Lenz lenses inherently introduce insertion losses due to the additional reactive impedance they place between the sample and detection electronics. If the Q factor of the loops is not sufficiently high, these losses can offset the gains in filling factor. Additionally, because they are resonant structures, they typically offer narrow bandwidth operation, which may not be ideal in systems designed for broadband excitation or multi-nuclear detection. Despite these trade-offs, several studies have shown that when properly designed and aligned, Lenz lenses can increase the effective sensitivity of a detection system by up to an order of magnitude without any active signal conditioning [203].

It was shown by Liang in their novel stripline-based Lenz lens (S3L) [204]. Existing miniaturised NMR detectors often suffer from poor spectral resolution due to magnetic susceptibility mismatches and non-uniform RF fields. By integrating a Lenz lens (LL) into a stripline geometry (Fig. 2.16a), the authors aimed to provide a versatile tool for both NMR spectroscopy and in situ studies of complex systems, such as thin films and battery materials.

Their stripline LL leverages the principle of Lenz's law to focus and redirect the magnetic field, enhancing the SNR. The lens was a broadband device that can operate across a wide range of frequencies, from 125.76 MHz to 500 MHz, making it suitable for multiple nuclei in high-field NMR setups. The research combines the benefits of stripline and LL geometries, creating

a modular and effective solution for small sample volumes.

The results demonstrated significant improvements in performance. The S3L achieved up to an 11-fold enhancement in SNR at 500 MHz compared to traditional saddle coils. This enhancement allowed for reduced 90° pulse lengths and improved spectral resolution, with linewidths decreasing from 6 Hz to 3 Hz. The device showed strong broadband capabilities, successfully detecting signals from multiple nuclei, including ^{1}H, ^{13}C, ^{7}Li, and ^{31}P. Additionally, the S3L's ability to precisely focus the $\vec{B}_1$ field enabled better excitation localization, reducing interference from unwanted regions. The study concluded that the S3L is a promising innovation for advancing NMR technology, particularly in applications requiring high sensitivity and minimal sample volume.

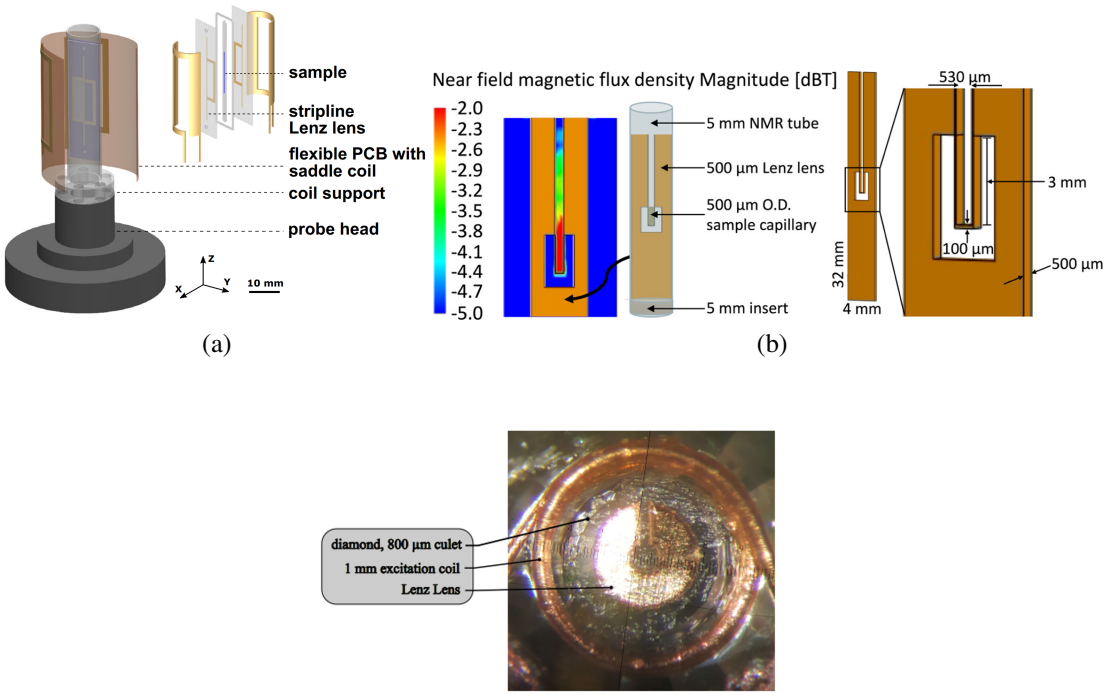

Figure 2.16: (a) Stripline-based Lenz lens sandwiched between saddle coils. Reproduced with permission from [204]. (b) Cryogrenic NMR probe with integrated Lenz lens. Reproduced with permission from [202]. (c) Lenz lens integrated into a diamond anvil for high pressure NMR experiments. Reproduced with permission from [201].

By combining cryogenic cooling with a paramagnetic LL, Bastawrous and colleagues aimed to improve the $\vec{B}_1$ field intensity at the sample location without compromising the advantages of cryoprobe technology [202]. Cryoprobes reduce thermal noise to enhance signal sensitivity, but their benefits diminish for microcoils due to reduced thermal mass. Similarly, miniaturised microcoils improve mass sensitivity but face challenges with field homogeneity and signal amplification. The LL offers a solution by focusing the $\vec{B}_1$ field from a larger coil onto a small sample volume, thereby enhancing sensitivity while maintaining cryogenic cooling benefits.

This approach (Fig. 2.16b) addressed the challenge of studying tiny samples, such as Daphnia magna eggs, that are require excellent sensitivity to analyze. Results demonstrated significant sensitivity gains. For ^{1}H and ^{13}C NMR, the integration of the LL improved sensitivity by factors of 2.8× and 3.5×, respectively, compared to a standard cryoprobe. This enhancement enabled high-resolution 2D heteronuclear experiments, including ^{1}H-^{13}C heteronuclear single quantum coherence spectroscopy (HSQC), which showed improved metabolite detection in hemolymph and eggs of D. magna. The LL reduced sample requirements, allowing the analysis of as little as 430 nL of hemolymph or eight eggs. Metabolites detected using the LL included key biomarkers related to stress and survival, such as amino acids, sugars, and neurotransmitters, which were undetectable with traditional setups.

Another way LLs were used was to experiment picoliter-sized samples under extreme pressures. Traditional high-pressure NMR techniques, which have historically struggled with signal quality due to the restricted sample volumes and challenging experimental conditions within diamond anvil cells (DACs). Meier aimed to fix that by introducing inductively coupled broadband electromagnetic lenses designed to amplify the magnetic field locally at the sample site (Fig. 2.16c), enabling in situ NMR measurements in DACs at pressures up to 72 GPa [201].

The study showed that the LL significantly improves sensitivity, with detection limits up to four orders of magnitude lower than conventional solenoidal microcoils. This enhancement allowed the successful acquisition of 1D and 2D NMR spectra, including nutation and homonuclear COSY experiments, at pressures ranging from ambient to 72 GPa. The method demonstrated high spectral resolution, with linewidths of approximately 2 parts per million, and maintained sensitivity with minimal deterioration across the superior stability compared to microcoils, which often degrade or fail at high pressures due to deformation. The authors demonstrate the feasibility of this method for analysing ultrahigh-pressure phenomena in chemistry, geoscience, and material science.

2.4 Conclusion

Here, we have discussed some of the key advancements in NMR technology, probe design, and signal enhancement techniques that have contributed to improving the sensitivity, accessibility, and applicability of NMR in diverse research and clinical settings. While this is not an exhaustive list, these developments represent significant progress in pushing the boundaries of what is possible in NMR spectroscopy. From microcoil technology and AI-driven optimization strategies to innovative approaches such as dynamic nuclear polarization, researchers have made notable strides in enhancing NMR efficiency and resolution. These innovations have not only improved performance but have also facilitated NMR's integration into point of care applications by addressing key challenges related to cost, portability, and ease of use.

Despite these advancements, several barriers remain that limit the widespread adoption of

NMR in routine diagnostics and real world applications. The high cost and complexity of conventional NMR systems, the need for specialised expertise, and the challenges associated with optimising RF coil geometries for diverse sample conditions all present obstacles that must be overcome. Emerging solutions such as microfluidic integration, planar coil designs, and AI-based optimization offer promising pathways to mitigate these challenges, yet further research and development are necessary to translate these innovations into practical, scalable solutions.

For NMR to become a widely adopted tool in point of care and resource limited settings, the field needs continued advancements in miniaturization, cost reduction, and automation. Developing low cost, high sensitivity detection systems that do not compromise performance is essential. Additionally, improving the robustness of hardware, reducing reliance on highly trained personnel, and integrating intelligent data processing methods will be key to making NMR more accessible. Further interdisciplinary collaboration between engineers, chemists, and clinicians is needed to design systems that align with real world clinical needs. By addressing these challenges, NMR has the potential to revolutionise diagnostics, enabling rapid, high resolution molecular analysis in a broad range of applications.

In this chapter, we looked at the the role of integrated technologies such as microfluidics, automated shimming, and broadband excitation schemes that aim to simplify NMR operation and reduce its cost and footprint. These are key prerequisites for moving the technique out of specialised laboratory environments and into point of care settings. While many of these advances are promising, each presents trade-offs in terms of complexity, fabrication challenges, or alignment with real-world diagnostic workflows.

In light of these considerations, and based on the specific requirements of our target application in early-stage prostate cancer diagnostics, we have chosen to adopt a Lenz lens based microcoil design as the basis for our detection probe. Prostate cancer is a condition where early detection through non-invasive metabolic profiling of urine or blood can significantly improve treatment outcomes. However, capturing weak NMR signals from small biofluid volumes presents a considerable challenge, particularly in low field systems.

The Lenz lens provides a compelling solution in this context. Its passive, wireless magnetic coupling mechanism enables enhanced local sensitivity without requiring direct electrical connections near the sample. This simplifies probe fabrication and integration into modular diagnostic platforms. It also supports high filling factors in restricted detection volumes and allows for more flexible probe geometries, which are important for systems intended for clinical use. Although this approach has limitations, the Lenz lens design offers an effective balance between performance, manufacturability, and suitability for integration into a compact and cost-effective NMR system tailored for prostate cancer screening.

Chapter 3

High Sensitivity NMR Probe Design

3.1 Introduction

Building on the advancements discussed in the previous chapter, we now turn our focus to the design and development of a high-sensitivity NMR probe. We explored various strategies for enhancing NMR sensitivity, emphasising the importance of optimising probe geometry and electromagnetic efficiency. An important takeaway was that while many approaches have demonstrated improvements in signal detection, practical implementation often requires balancing sensitivity, fabrication complexity, and compatibility with existing systems.

One particularly promising technique identified is the use of Lenz lenses, which have gained attention for their ability to concentrate magnetic flux and enhance inductive coupling. Compared to other sensitivity enhancement methods, LLs offer a passive and structurally simple way to improve signal detection without requiring additional power or complex system modifications. Many existing approaches to improving NMR sensitivity involve intricate fabrication processes, costly hardware, or trade-offs that limit their practical use in scalable applications. LLs, in contrast, achieve enhanced signal strength through efficient magnetic field redistribution, offering a straightforward solution that maintains simplicity while still delivering performance gains.

The inclusion of a Lenz lens in the detector was a deliberate design choice intended to increase the magnetic coupling between the sample region and the receiver coil, particularly within the constraints of our low-field, small-volume system. While it is true that LLs are often reserved for cases where direct electrical access to the detection region is not possible, we adopted this architecture to investigate the feasibility of passive field focusing in a modular system. Our system was designed for potential integration with microfluidic sample holders and other modular cartridges, where direct wiring might not be practical. Although inductive coupling inherently introduces signal loss, it also allows spatial separation between the coil and sample, which is advantageous in applications that require interchangeable sample modules or mechanical flexibility. The use of a Lenz lens in this context was not intended as a replacement for optimal

direct-wired detection but as a proof-of-concept strategy for integrating modular sensing units into compact, accessible diagnostic platforms. The trade-off between absolute sensitivity and mechanical adaptability was carefully evaluated, and although the signal loss associated with inductive coupling was acknowledged, the lens geometry was optimised to mitigate this loss and enhance local field concentration.

Given these advantages, we selected this approach for the design of our NMR probe. By incorporating a Lenz lens, we aimed to enhance sensitivity and signal detection while addressing key practical considerations such as fabrication, integration, and usability. This approach builds on existing research while focusing on real-world implementation, ensuring that the final design is both effective and feasible.

3.2 Theory

3.2.1 Lenz Lens Analytical Equations

Inductive coupling occurs when an alternating magnetic field generated by a primary coil induces a voltage in a nearby secondary coil, following Faraday's law of electromagnetic induction. This principle is fundamental in many resonant and transformer-based systems, where efficient energy transfer is required. The strength of the induced electromotive force (EMF) is influenced by the intensity of the primary magnetic field and the rate of change of this field over time.

Schoenmaker et al. [205] introduced the concept of LLs to enhance and focus alternating magnetic fields using inductive coupling principles. The LL consists of two nested loops with equal and opposite currents, creating a unique magnetic flux distribution that concentrates the field in a localised region. As shown in Fig. 3.1, this configuration modifies the magnetic field lines, increasing their density within the central region while reducing stray fields. This makes LLs particularly useful for applications requiring enhanced inductive coupling and efficient energy transfer, such as in NMR systems, wireless power transfer, and sensing applications.

When a Lenz Lens is inductively coupled to a magnetic field, an interesting phenomenon occurs: in addition to the current flowing through the primary coil (I_P), currents are also induced in both the inner loop (I_i) and the outer loop (I_o) of the lens structure. This interaction can be analyzed by treating the LL as two coupled circular loops, where each loop interacts not only with the primary coil but also with each other.

The excitation of both loops by the alternating magnetic field of the primary coil results in a redistribution of the magnetic flux, concentrating it within the focal region of the LL. The currents in the inner and outer loops flow in opposite directions, generating a field pattern that enhances the effective magnetic flux density in the detection region while reducing stray fields. This effect makes LLs particularly advantageous for applications requiring high magnetic field

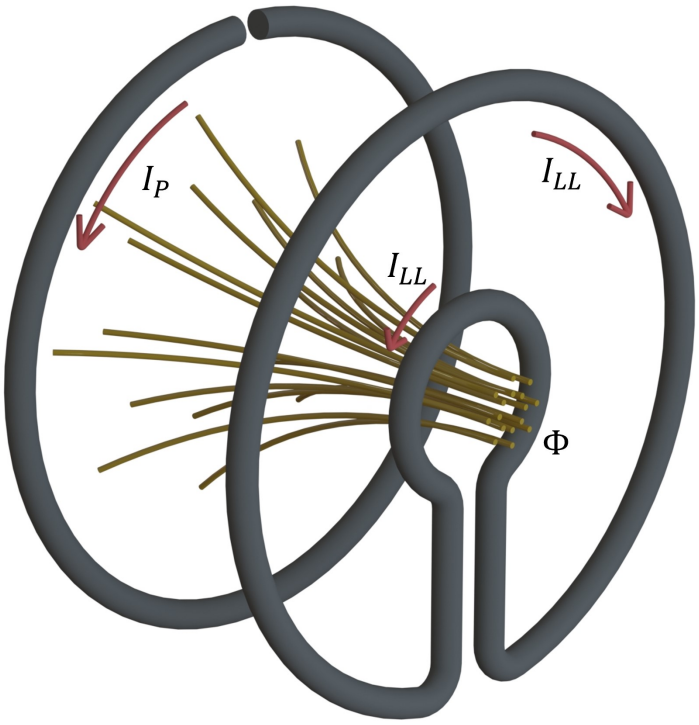

Figure 3.1: Lenz lens concept demonstrating the magnetic flux generated by the primary coil Φ_P being focused into the centre of the lens, through the action of the primary coil (I_P) and LL (I_{LL}) currents. Reproduced with permission from [206].

localisation, such as NMR, where increased inductive coupling improves signal sensitivity without additional power consumption.

As a result, the inner and outer loops share the same current, and their behaviour is governed by specific electromagnetic relationships that describe their interaction with both the external magnetic field and with each other. In essence, the LL can be regarded as two differentially coupled inductors [206] connected in series, both excited by the primary coil. Thus, they share the same current and follow the relationship:

$$V = I_{LL}R_{LL} + (L_o + L_i - 2M_{io})\frac{dI_{LL}}{dt}, \tag{3.1}$$

where I_{LL} is the current in the lens, R_{LL} is the lens' resistance, L_i and L_o are the self-inductances of the inner and outer loops of the lens, and M_{io} is the mutual inductance between the loops.

Given that the lens is inductively excited by the primary coil, it follows that the voltage across the lens must satisfy:

$$emf = M_{PLL}\frac{\mathrm{d}I_P}{\mathrm{d}t}. \tag{3.2}$$

Total emf can be expressed as

$$emf = emf_o - emf_i = M_{Po}\frac{\mathrm{d}I_P}{\mathrm{d}t} - M_{Pi}\frac{\mathrm{d}I_P}{\mathrm{d}t}, \tag{3.3}$$

where emf_i refers to the inner loop and emf_o to the outer loop EMFs. The introduction of a negative sign signifies that the EMF generated in the inner loop opposes the EMF in the outer loop, aligning with the structural arrangement of the LL. Combining these equations, we discern the relationship $M_{PLL} = M_{Po} - M_{Pi}$, which underscores the non-zero nature of the mutual inductance, M_{PLL}, between the primary coil and the LL. Consequently, this configuration gives rise to both EMF and an induced current within the lens.

Using the above equations, we can derive the relationship between the current in the primary coil and the current in the lens. After substituting and rearranging the terms, and assuming a sinusoidal primary coil current $I_P = I_0 e^{j\omega t}$, we arrive at Eq.3.4 for the expression detailing the relationship between these currents.

$$I_{LL} = \frac{j\omega\left(M_{Po} - M_{Pi}\right) I_P}{R_{LL} - j\omega\left(L_o + L_i - 2M_{io}\right)} \tag{3.4}$$

yields two noteworthy observations of considerable significance. The first pertains to the anticipated direction of currents within the LL configuration. Specifically, the current in the outer loop flows in the opposite direction to that of the primary coil. Consequently, the inner loop's current moves in the same direction as that of the primary coil. As a result, within the inner region of the LL, we observe the magnetic field generated to be in the same direction as that of the primary coil, hence creating an amplified zone. This phenomenon has been shown to enhance applications in magnetic resonance imaging [207], with recent studies comparing their performance to LC resonators and wired detector coils [202], [208]. The specific behaviour of the LL exhibits a high degree of dependence on its design and operating conditions [209]. Additionally, the lens demonstrates a remarkable capability for selective focusing, naturally suppressing signals beyond the region of focus, with the increase in signal-to-noise ratio greatly enhancing image resolution.

The second observation arising from this relationship delves into the intriguing interplay between the phases of currents within the lens-coil system. The geometry of the lens and the coil, factors that will be shown to determine the inductances in Eq. 3.4, plays a pivotal role in determining the phase shift between the currents and the resulting magnetic fields. However, a particularly noteworthy aspect is the possibility of achieving a zero phase shift condition should the resistance of the lens structure tend to zero. In such a scenario, the lens structure presents itself as exceptionally well-suited for cryogenic and superconductive applications, where the resistance can be effectively eliminated. This makes it suitable for high-field NMR systems as well, since they operate in cryogenic temperatures.

3.2.2 NMR Receiver Design Requirements

The induced NMR signal in the detection coil is a result of the interaction between the coil's B_1-field and the magnetisation $\mathbf{M}$ of the sample. According to the principle of reciprocity, the induced electromotive force (EMF) in the coil is given by:

$$\xi = -\frac{\partial}{\partial t}(\mathbf{B}_1 \cdot \mathbf{M}) \tag{3.5}$$

The equilibrium magnetisation M_0 of the sample, aligned with the external static magnetic field B_0, is given by:

$$M_0 = N\gamma^2\hbar^2 I(I+1)\frac{B_0}{3k_B T} \tag{3.6}$$

Where N is the number of spins per unit volume, γ is the gyromagnetic ratio of the nucleus, $\hbar$ is the reduced Planck's constant, I is the spin quantum number, B_0 is the external static magnetic field strength, k_B is the Boltzmann constant, T is the absolute temperature.

The precessing magnetisation M_0 generates an alternating magnetic flux, inducing a voltage in the coil. The RMS value of the induced NMR signal voltage (ξ_{rms}) is given by the expression:

$$\xi_{rms} = \eta k_0 \gamma^3 B_0^2 N_s \left(\frac{B_1}{i}\right) V_s \left(\frac{h}{2\pi}\right)^2 \frac{I(I+1)}{3\sqrt{2}k_B T} \tag{3.7}$$

Where η is the filling factor, representing the fraction of the coil volume occupied by the sample, k_0 is a constant that accounts for spatial inhomogeneities in the B_1-field, N_s is the number of spins per unit volume, $\frac{B_1}{i}$ is the magnetic flux density per unit current in the coil, V_s is the sample volume.

This equation provides the detailed expression for calculating the NMR signal induced in the detection coil based on the system parameters and sample properties.

The RMS noise voltage in the NMR detection system is primarily due to thermal noise generated in the coil's resistance. The RMS noise voltage is expressed as:

$$v_{\text{rms-noise}} = \sqrt{4k_B T R \Delta f} \tag{3.8}$$

Where R is the resistance of the coil, which includes contributions from the skin effect at high frequencies, Δf is the bandwidth of the receiver in Hz.

This equation describes the thermal noise voltage generated across a resistor due to the random motion of charge carriers, which depends on the coil's resistance and the receiver's bandwidth.

In the process of calculating the receiver specifications, we observe that several parameters in the signal equation are not constants but rather depend on the physical properties of the sample and the coil. Specifically, values such as the spin density, sample volume, and AC resistance of the coil are system-dependent and must be derived based on the experimental setup and

material properties. These parameters are crucial for accurately determining the NMR signal and noise levels, which, in turn, influence the receiver's specifications. Therefore, to proceed with the calculation, we first need to derive the values of these parameters using their respective formulas, which account for factors like the sample's physical dimensions, material properties, and the operating frequency of the NMR system.

The spin density N_s is defined as the number of resonating nuclei per unit volume of the sample and can be derived as:

$$N_s = \frac{\rho \times N_A}{M} \tag{3.9}$$

Where ρ is the density of the sample. N_A is Avogadro's number. M is the molar mass of the sample.

The sample volume V_s is calculated based on the physical dimensions of the sample holder (in this case, a cylindrical microcapillary tube). The formula for the volume of a cylinder is:

$$V_s = \pi \left(\frac{d}{2}\right)^2 h \tag{3.10}$$

Where d is the internal diameter of the sample holder. h is the length of the sample holder.

The AC resistance R_{AC} of the coil is influenced by the skin effect at high frequencies. The formula to calculate the AC resistance is:

$$R_{\mathrm{AC}} = R_{\mathrm{DC}} \times \frac{r_{\mathrm{external}}}{\delta} \tag{3.11}$$

Where R_{DC} is the DC resistance of the wire, given by:

$$R_{\mathrm{DC}} = \frac{\rho \times l_{\mathrm{wire}}}{A} \tag{3.12}$$

δ, the skin depth, is calculated as:

$$\delta = \sqrt{\frac{2\rho}{\omega\mu}} \tag{3.13}$$

The tables below list the physical constants, design parameters, and receiver specifications.

The performance of the NMR receiver is directly tied to its ability to accurately detect and amplify the decaying NMR signal over time. Since the NMR signal decays exponentially, the minimum signal that the receiver needs to detect is critical for accurate measurement of relaxation parameters such as the T_2 relaxation time and spectral line width. Additionally, to make the NMR signal observable, the receiver must be able to amplify this weak signal to a sufficient level, ensuring it can be processed and analyzed effectively.

The transverse magnetisation, which gives rise to the NMR signal, decays according to the following equation:

Table 3.1: Scientific Constants Used in Calculations

Constant	Value
γ	$2.675 \times 10^8\,\mathrm{rad/s/T}$
$\hbar$	$1.055 \times 10^{-34}\,\mathrm{J \cdot s}$
k_B	$1.38065 \times 10^{-23}\,\mathrm{J/K}$
N_A	$6.022 \times 10^{23}\,\mathrm{mol^{-1}}$
μ_0	$4\pi \times 10^{-7}\,\mathrm{H/m}$
ρ	$997\ \mathrm{kg/m^3}$
M	$0.018\ \mathrm{kg/mol}$
ρ_{copper}	$1.68 \times 10^{-8}\,\Omega \cdot \mathrm{m}$

Table 3.2: Design Parameters for the NMR System

Parameter	Value
B_0	0.67 T
d	1 mm
h	5 mm
l_{wire}	0.241 m
A	$3.12 \times 10^{-7}\,\mathrm{m^2}$
r_{external}	2.13 mm
ω	$2\pi \times 28.6 \times 10^6$ rad/s
T	298 K
Δf	20000 Hz

$$M_{xy}(t) = M_{xy}(0)\, e^{-t/T_2} \tag{3.14}$$

Where $M_{xy}(t)$ is the transverse magnetisation (or signal amplitude) at time t. $M_{xy}(0)$ is the initial magnetisation (initial signal amplitude). T_2 is the transverse relaxation time.

The signal amplitude $M_{xy}(t)$ decreases exponentially over time. Accurate measurement of the T_2 parameter requires detecting the signal until it reaches at least 37% of its initial value $M_{xy}(0)$. This is because, at $t = T_2$, the signal amplitude drops to $1/e$ (or approximately 37%) of its initial value:

$$M_{xy}(T_2) = M_{xy}(0) \times \frac{1}{e} \approx M_{xy}(0) \times 0.37 \tag{3.15}$$

Table 3.3: Calculated Parameters for NMR Receiver

Parameter	**Value**
N_s	$6.69 \times 10^{28}\,\text{nuclei}/\text{m}^3$
V_s	$3.92 \times 10^{-9}\,\text{m}^3$
δ	$43.2\ \mu\text{m}$
R_{DC}	$0.013\ \Omega$
R_{AC}	$2.27\ \Omega$
ξ_{rms}	$1.08 \times 10^{-6}\,\text{V}$
$v_{\text{rms}-\text{noise}}$	$2.73 \times 10^{-8}\,\text{V}$
SNR	39.5

This value serves as a reference point for determining T_2 accurately, as it captures the essence of the exponential decay behavior.

The transverse relaxation time T_2 is inversely related to the spectral line width $\Delta\nu$:

$$\Delta\nu = \frac{1}{\pi T_2} \tag{3.16}$$

A good estimate of T_2 requires capturing the signal up to at least 37% of its initial value. If the receiver cannot detect the signal accurately at this level, it will distort the measurement of T_2, leading to an incorrect estimate of the spectral line width.

Given that the RMS voltage of the NMR signal is $1.08 \times 10^{-6}\,\text{V}$, the minimum voltage that the receiver needs to detect can be calculated as:

$$\xi_{\text{min}} = \xi_{rms} \times 0.37\sqrt{2} \tag{3.17}$$

Substituting the values from table 3 shows that the receiver must be able to detect voltages as low as $5.651 \times 10^{-7}\,\text{V}$ to accurately measure the signal decay down to 37% of its initial amplitude. This level is essential for ensuring that the calculated T_2 and the corresponding spectral line width are accurate and reliable.

3.3 Lenz Lens Probe 1

3.3.1 Design

For our initial design, we opted for a planar geometry for both the receiver (Rx) microcoil and the first Lenz lens (LL_1). The key advantage of using two planar geometries is that they can be integrated onto a single flat substrate, which simplifies the fabrication process. The constraints in designing the Rx were mainly driven by the size of our magnet and the limitations of the

fabrication process. In this configuration, the microcoil and LL_1 serve as the NMR receiver, while the transmitter (Tx) is located on a separate PCB.

Although an RF switch was used to isolate the transmit and receive paths within the system, we chose to implement separate coils for excitation and acquisition. This design decision allowed for greater flexibility in optimising each coil independently for its intended function. The Tx coil could be positioned and sized to maximise uniformity across the sample region, while the Rx coil and Lenz lens could be tightly focused on sensitivity at the point of signal detection. Using separate coils also helped minimise the impact of mutual coupling and ring-down effects in the receiver, which are common challenges when rapidly switching a high-Q coil between transmit and receive modes. Additionally, the modularity of the separate-coil design simplified assembly and debugging during development, particularly when integrating new geometries or adjusting the spatial alignment between the probe and the sample.

The magnet used for the NMR experiments was the NMR7014-066 (Xiamen Dexing Magnet Tech. Co. Ltd., China), shown in Fig. 3.2, which features a 14 mm gap between its poles. This magnet was selected primarily for its portability and cost-effectiveness, making it suitable for the development of a modular, low-cost NMR system. It provided a stable field strength of 0.67 T, as specified in the manufacturer's performance test report, with a tested magnetic field uniformity of 0.0089% over a 5 mm × 5 mm volume. The system was tested at a magnet temperature of 18.0°C, confirming thermal stability under typical laboratory conditions. These characteristics were sufficient to support proof-of-concept metabolite detection in small sample volumes.

While this magnet met the requirements for early-stage development and laboratory testing, it does not offer the level of field homogeneity or mechanical integration needed for a deployable clinical system. For point-of-care prostate cancer diagnostics, a more advanced magnet such as the Metrolab PM1055 would be a more suitable alternative. This system offers compact, high-performance permanent magnets with field strengths up to 0.5 T, and is specifically engineered for integration into portable and cryogen-free NMR platforms. Its improved uniformity and mechanical design make it better suited for real-world clinical use, particularly where spectral resolution and robustness are essential.

The design and dimensions of the NMR probe are depicted in Fig. 3.3. The width of the square substrate, w_s, was set at 12 mm to provide adequate spacing between the edges of the board and the magnet poles. An outer lens loop diameter, D_{LLo}, of 10 mm was selected to maintain sufficient clearance between the loop and the edge of the substrate.

When designing the lens loop, the ratio of the outer to inner ring diameters is a critical parameter, as it influences the trade-off between magnetic flux amplification and available surface area for integration [207]. The inner Lenz lens diameter, D_{LLi}, was chosen to balance the need for strong magnetic coupling with the practical considerations of our in-house fabrication process. This was especially important because the receiver coil had to be placed within the inner loop without introducing electrical shorts or mechanical fragility.

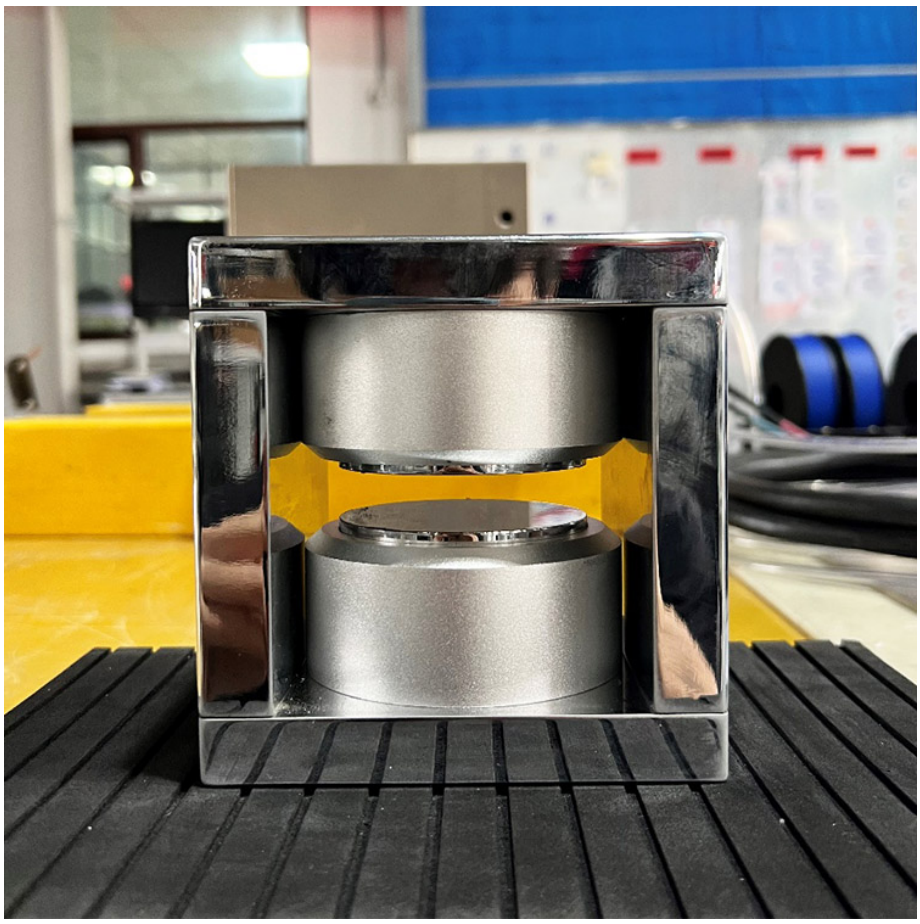

Figure 3.2: NMR7014-066 permanent magnet used for NMR experiments.

Although the photolithography and wet etching process we used, which employed an Elegoo Saturn 2 SLA printer for mask fabrication, could in principle achieve much finer feature sizes (approximately 100 micrometres with careful calibration), the actual fabricated structures were intentionally kept larger than this limit. This decision was made to improve yield, reduce alignment errors between printed masks and etched copper, and make manual handling of the receiver coils more reliable. In early trials, coils with smaller diameters or tighter spacing were prone to under-etching or shorting due to process variability.

As a result, we selected a circular receiver coil diameter of 2.9 mm (D_R), which provided a reliable balance between process yield, structural integrity, and ease of alignment within the lens loop. This dimension ensured consistent fabrication results while providing sufficient room within the inner lens loop for mechanical stability and electrical isolation. To accommodate this, the inner lens loop diameter (D_{LLi}) was set at 5 mm, providing both functional clearance and magnetic alignment.

The values for the gaps between the straight sections of LL_1 (w_{LLg_2}) were carefully chosen to balance two competing factors: maintaining effective magnetic field amplification while providing sufficient clearance for the Rx coil traces that would later pass through. Similarly, the gap on the outer loop of LL_1 (w_{LLg_1}) was designed to be wide enough to accommodate additional

traces without significantly compromising the field strength and homogeneity.

Additionally, the trace thickness of LL_1 and the Rx coil was selected to minimise resistive losses, ensuring efficient power transfer and signal integrity. The spacing between LL_1 and the Rx coil was also optimised to be large enough to mitigate capacitive coupling effects while maintaining strong inductive coupling. The finalised geometric parameters, presented in Table 3.4, reflect these considerations and were used as the foundation for subsequent simulations and fabrication steps.

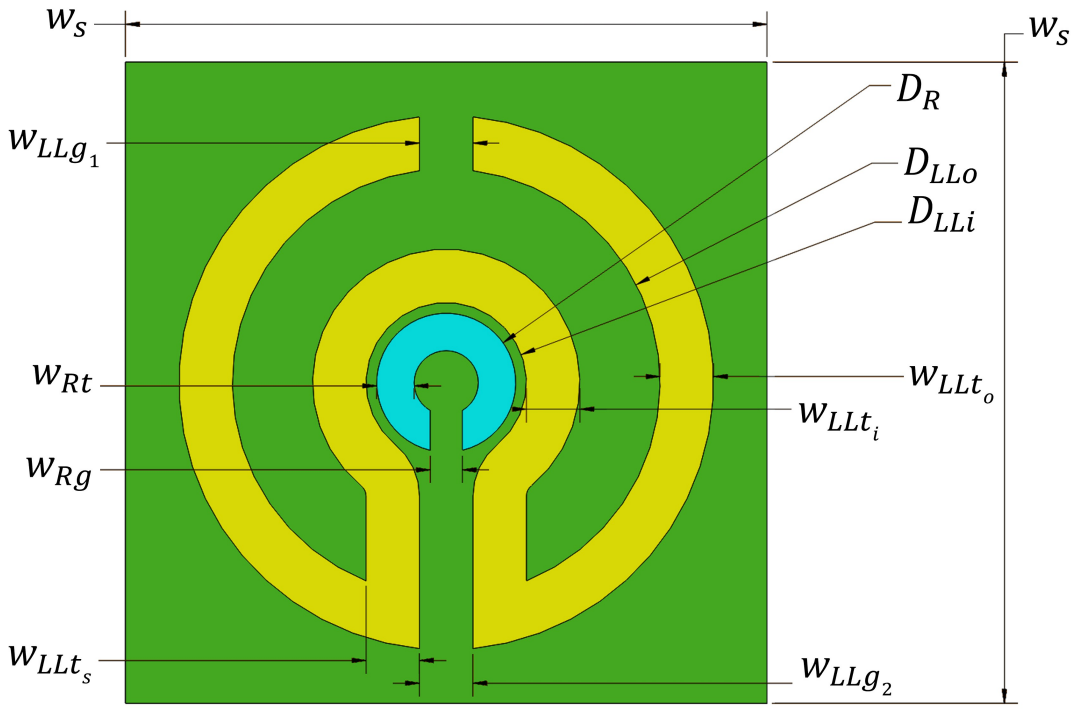

Figure 3.3: Design of the receiver microcoil (blue) and Lens lens (yellow) on the substrate (green). Reproduced with permission from [206].

Table 3.4: Dimensions of the Receiver Microcoil and Lenz Lenses (Units: mm). Reproduced with permission from [206].

Rx Microcoil Parameters	Value	LL_1 Parameters	Value
D_R	2.9	D_{LLo}	10
w_{Rt}	0.7	D_{LLi}	5
w_{Rg}	0.5	w_{LLt_o}	1
		w_{LLt_i}	1
		w_{LLt_s}	1
		w_{LLg_1}	1
		w_{LLg_2}	1

Both LL_1 and the microcoil function as inductors, and their impedance increases propor-

tionally with frequency. In the MHz and GHz ranges, this leads to high reactance, which can introduce signal non-linearities and degrade overall signal quality. To address this, it is essential to minimise or eliminate undesired reactance. To achieve this, we designed the LL_1 and the microcoil to work in a LC tank configuration by pairing them with appropriate capacitors [209]. The outer loop gap w_{LLg_1} provides this space for this capacitor placement. Although this configuration results in a narrowband frequency operation, it is an acceptable trade-off, as we are exclusively conducting proton NMR experiments and thus have a single centre frequency with a narrow bandwidth.

3.3.2 Simulation

The simulations were conducted using the frequency domain solver in CST Studio Suite 2019 (Dassault Systèmes SE, France) [210] to analyse and visualise the performance of the proposed design. These simulations were executed on a personal computer equipped with an 11th Gen Intel® Core™ i7-1185G7 processor and 16 GB of RAM. The signal source was modelled as a coil with an outer diameter matching D_{LLo} and a trace thickness of w_{LLo}, chosen to match the size of the NMR sample container used in the experiments. The trace width was optimised to minimise parasitic resistance and ensure efficient power delivery.

S-parameter ports were used to define the excitation and receiving interfaces in the model. Both ports were set to a reference impedance of 50 Ω, and the coil designs were impedance matched accordingly to maximise power transfer. The transmit port was driven with 0.5 W of input power to simulate realistic excitation conditions. Power-based excitation was used instead of a fixed current source because in real-world experiments, the input power to the coil can be precisely controlled using an RF amplifier, whereas the actual current through the coil varies depending on its impedance. Using a defined power level in the simulation ensures the results correspond to what is physically delivered to the coil during measurement.

All field evaluations were carried out using the magnetic field strength (H-field), which is directly computed by the solver. This field distribution was used to assess magnetic coupling, signal penetration, and uniformity across the sample region. The simulation frequency was centred at 28.6 MHz, consistent with the hydrogen-1 Larmor frequency under the applied magnetic field.

To reflect the experimental conditions accurately, the separation between the source coil and the receiver coil was set at 1 mm, corresponding to the wall thickness of the sample container. Capacitors were modelled as lumped elements strategically placed across designed gaps, allowing for impedance matching and resonance tuning. Tuning refers to adjusting the resonance frequency of the LC circuit formed by the coil and capacitor to align with the Larmor frequency, ensuring that the circuit responds most efficiently to the desired signal. Matching involves transforming the coil's complex impedance to match the 50 Ω input impedance of the measurement system, thereby maximising power transfer and minimising signal reflection. This

tuned and matched configuration results in passive amplification, where the narrowband resonance increases sensitivity by amplifying signals close to the resonance frequency. Although this enhances detection efficiency, it also affects the receiver's noise characteristics. A narrowband circuit reduces the bandwidth over which thermal and electronic noise is integrated, which can improve signal-to-noise ratio. However, it also increases susceptibility to detuning from parasitic elements or environmental changes. In our simulations, discrete face ports of the S-parameter type were applied to both the Tx and Rx coils to assess signal transmission characteristics under these tuned conditions. This setup enabled a detailed evaluation of power transfer efficiency and magnetic field distribution, as depicted in Fig. 3.4.

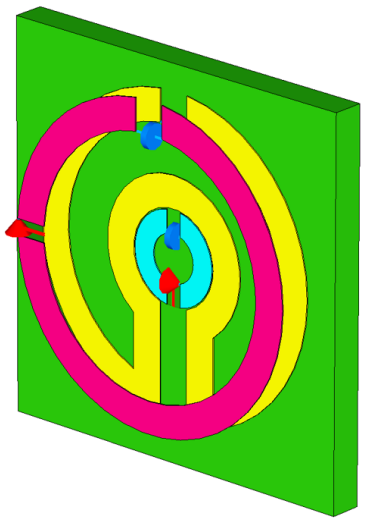

Figure 3.4: Simulation model of Rx microcoil (blue), LL_1 (yellow), and Tx coil (purple). Reproduced with permission from [206].

To analyze the proposed design, we examined the frequency-domain scattering parameters of LL_1, focusing specifically on the S_{21} parameter to assess the lens's effect. All designs were optimised to operate at 28.6 MHz, corresponding to the Larmor frequency for proton NMR [211]. Fig. 3.5a illustrates the impact of introducing LL_1 around the microcoil, when compared to no lens present as seen in Fig. 3.5b. It can be clearly seen that S_{21} parameter values with the addition of the lens is 25.925 dB higher. Similarly, the S_{11} parameter reveals that without the lens, nearly all input power is reflected back to the source, as shown in Fig. 3.5b, indicating a significant improvement in the receiver coil's performance when LL_1 is added.

The behaviour of the magnetic field component normal to the receiver coil plane (H_z) is displayed in Figs. 3.7a, 3.6a, 3.7b, and 3.6b . By comparing the one-dimensional field plots in Figs. 3.7a and 3.7b, we observe a magnetic field enhancement by a factor of 9.09 in the focusing region where the coil is placed. Along the x-axis, within the receiver coil, H_z peaks at approximately 165 A/m in the control simulation and 1500 A/m with LL_1, with center values of 75.6 A/m and 387.64 A/m, respectively. Furthermore, the introduction of LL_1 causes the magnetic field to decay sharply as one moves away from the center. The two-dimensional magnetic field

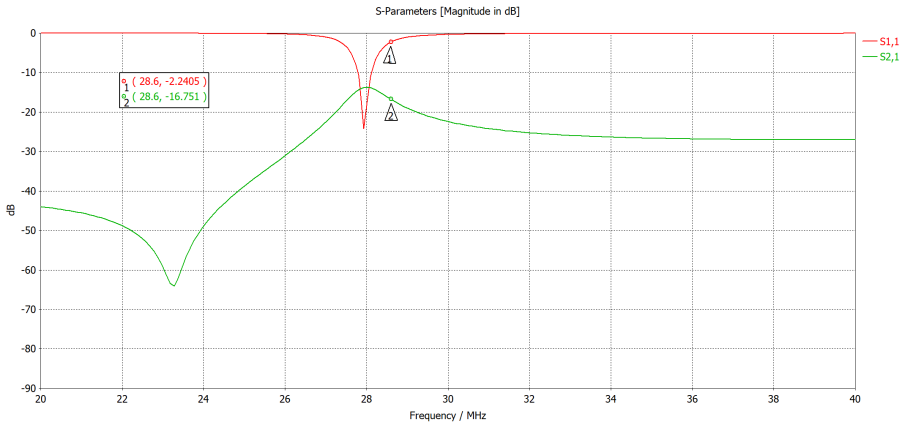

(a)

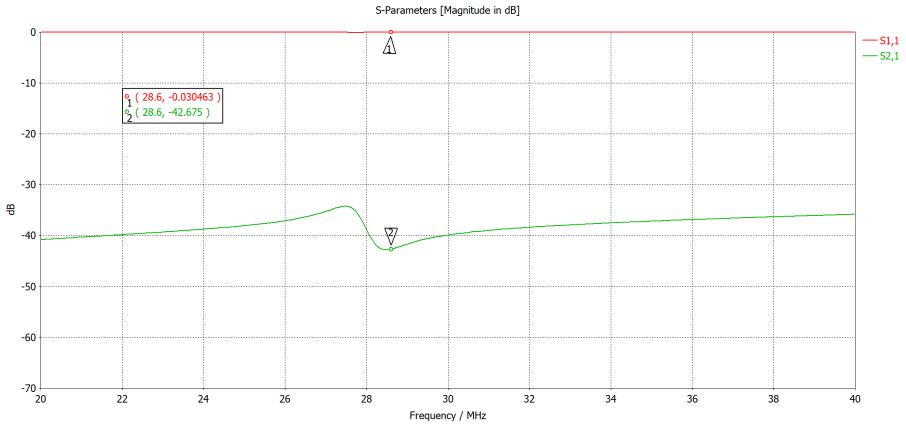

(b)

Figure 3.5: Simulated S-parameter of receiver board with (a) and without (b) the Lenz lens. Reproduced with permission from [206].

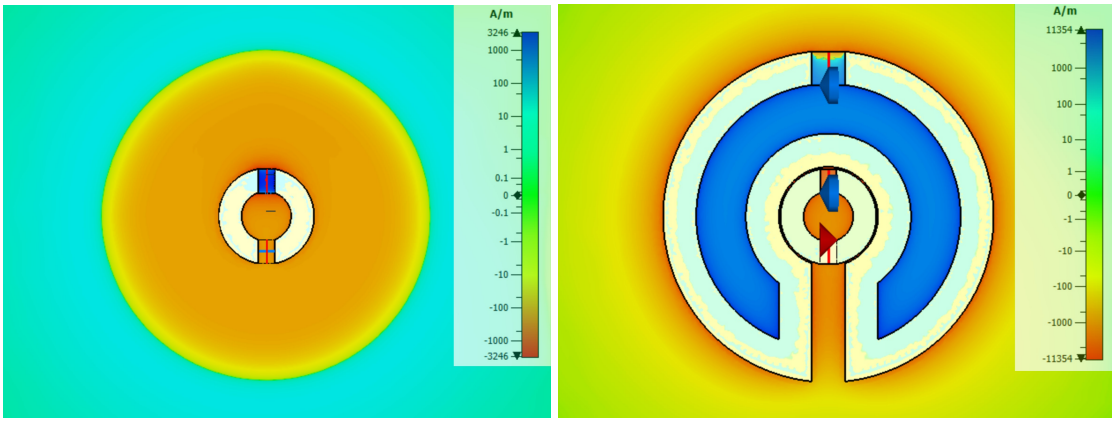

(a) (b)

Figure 3.6: Simulated 2D H-field at the surface of the receiver without (a) and with (b) LL_1. Reproduced with permission from [206].

plots in Figs. 3.6a and 3.6b clearly show that a field hotspot is created within the microcoil when

LL_1 is present.

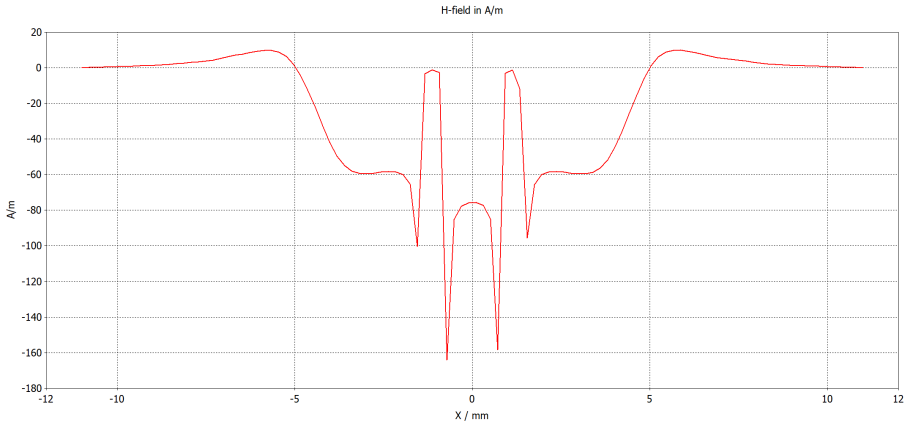

(a)

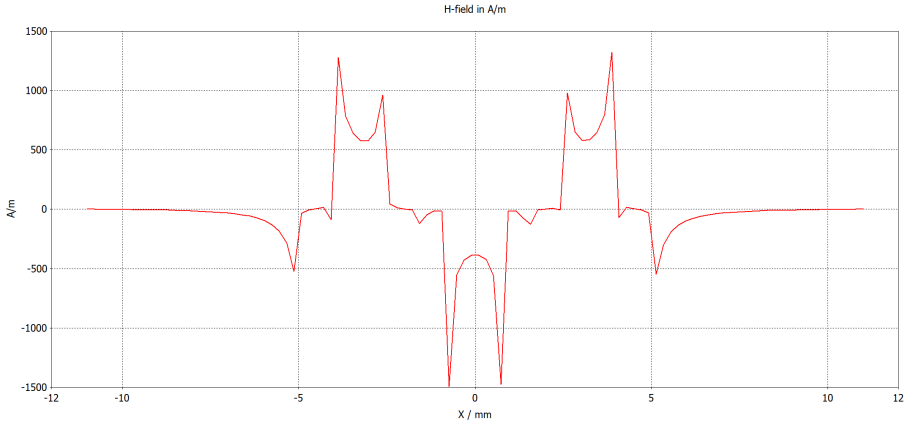

(b)

Figure 3.7: Simulated 1D H-field along the radius of the receiver coil without (a) and with (b) the Lenz lens. Reproduced with permission from [206].

Calculating the magnetic flux density at the center from LL_1 simulation results yields a value of 0.485 mT. In comparison to the findings of Schoenmaker et al. [205] and Spengler et al. [207], our design demonstrates an improvement of approximately 4.8 and 2.4 times in absolute magnetic flux density, respectively. While LL_1 is deployed under different conditions in our study compared to the aforementioned studies, our simulation results highlight the robustness and versatility of this approach.

3.3.3 Circuit Design

The next step was the fabrication of the design, where all components, including capacitors and other necessary accessories, were integrated onto a single board. We used EAGLE CAD (Autodesk Inc., United States) to design the PCB. At this stage, two additional considerations were crucial for ensuring optimal circuit performance. The first challenge was impedance matching between the receiver coil and the measuring equipment, which had a characteristic impedance

of 50Ω. Since the receiver coil did not naturally exhibit a 50 Ω impedance, a matching network was required. Among the various impedance matching topologies available, we selected the π match network due to its inherent ability to filter out higher order harmonics that could otherwise distort the signal. This network transformed the 50 Ω source impedance to a 2 Ω load, ensuring efficient signal transfer and minimal reflection losses.

The load impedance was determined by considering the total resistance of the receiver coil along with other circuit components. A value significantly higher than the sum of these resistances was chosen to minimise the influence of parasitics, such as those introduced by PCB traces, while still being small enough to limit thermal noise. This balance was essential for maintaining signal integrity and optimising sensitivity. The relationship between the components of a π network is described in Equation 3.18, where Z_{input} represents the total impedance of the matching circuit and $R_L + jX_L$ defines the load impedance. The components C_S, C_L, and L represent the source capacitor, load capacitor, and inductor, respectively.

$$Z_{input} = \left[\left((R_L + jX_L) \parallel \left(\frac{1}{jw \cdot C_L}\right)\right) + jw \cdot L\right] \parallel \left(\frac{1}{jw \cdot C_S}\right) \tag{3.18}$$

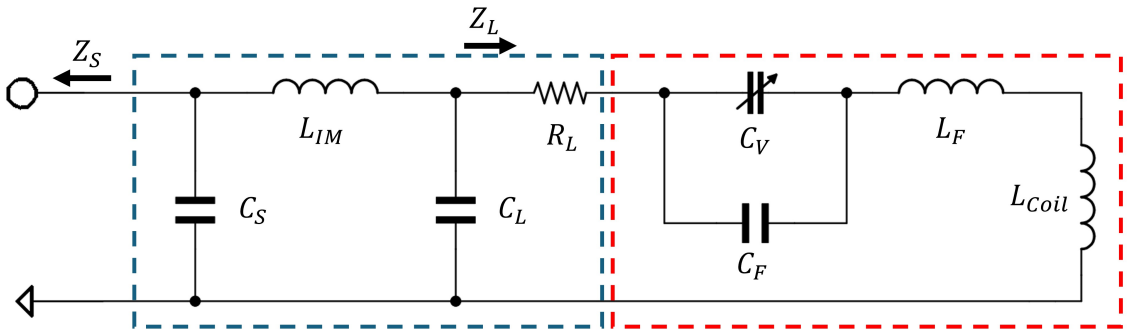

(a)

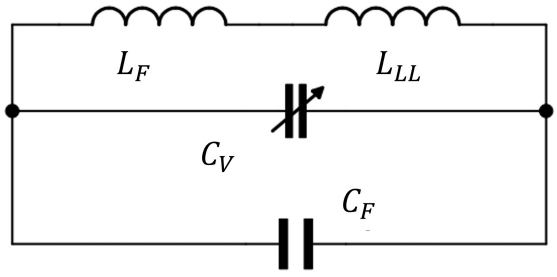

(b)

Figure 3.8: (a) Schematic for receiver coil resonance tuning (red box) and impedance matching (blue box) elements. (b) Schematic for resonant Lenz lens circuit. Reproduced with permission from [206].

The second key consideration was the inductance of the receiver coil, which was critical for calculating the capacitance required for the LC tank. Using the inductor design software Coil64

[212], we estimated the inductance to be on the order of a few nH. However, the stray inductance generated by the circuit traces and components was of a similar magnitude, potentially shifting the total inductance and impacting the resonant behavior of the system. To mitigate this issue, we added a fixed-value inductor with an inductance two orders of magnitude greater than that of the microcoil and its associated traces.

Table 3.5: Calculated Values of the Receiver's Electrical Parameters. Reproduced with permission from [206].

Electrical Parameters	Value
L_{Coil}	3 nH
L_F	150 nH
C_V	2x 50 pF
C_F	150 pF
R_L	2 Ω
C_L	5560 pF
L_{IM}	30 nH
C_S	1240 pF

Next, we selected a capacitor with a reactance equal and opposite to that of the inductor at the desired frequency, ensuring resonance in the LC tank circuit. Careful consideration was given to parasitic capacitances, which could affect the overall capacitor value. To account for any shifts caused by parasitics and to allow fine-tuning of the LC tank, we added a variable capacitor in parallel with a fixed-value capacitor. This configuration provided a means of manually adjusting the total capacitance. LL_1's LC tank was designed using the same approach.

The circuit schematic for both LL_1 and the microcoil is shown in Fig. 3.8, and the values of the components on the receiver board are provided in Table 3.5.

3.3.4 Fabrication

The board was fabricated using an in-house wet etching process on a double-sided FR-4 copper clad, with a copper thickness of 35μm and a substrate thickness of 0.8 mm. The fabrication process involved several steps. First, the blank copper clad board was cleaned using acetone and an abrasive pad to remove any contaminants that could interfere with the mask transfer process. Next, the mask was printed onto photo paper using a laser printer, and a solution composed of 3 parts acetone and 8 parts ethanol by volume was applied. After placing the mask onto the board and applying pressure for 90 seconds, the board was immersed in a water bath for 5 minutes to ensure the transfer process was complete.

Once the mask was successfully transferred, the third step involved etching the board in a ferric chloride solution until the exposed copper was fully dissolved. The board was then placed in a water bath for 5 minutes before proceeding to the final step, which involved removing the

mask using acetone. After fabrication, the individual components were soldered onto the board to form the tuning circuit for LL_1, as well as the tuning circuit and impedance matching circuit for the receiver coil. The fabricated LL_1 and assembled board are shown in Fig. 3.9a and Fig. 3.9b, respectively.

3.3.5 Measurement

Once the board was prepared, we set up an experimental apparatus (Fig. 3.10) to evaluate its performance. The experiment aimed to measure the power transfer from the transmitter to the receiver, allowing us to verify whether the board operates at the expected frequency and whether its SNR is sufficiently high for effective magnetic field amplification. The latter is particularly crucial, as LL_1 would be ineffective if it introduced substantial noise into the signal.

All measurements were performed using a single fabricated receiver board that incorporated the Lenz lens structure. This board included both the receiver coil and the concentric Lenz lens loops, as shown in Fig. 3.9a. No additional board was fabricated without the lens. To evaluate the performance of the receiver coil on its own, the lens structure was electrically disconnected from the circuit by opening the conductive path at one point in the outer loop. This effectively removed its inductive influence, allowing for a direct comparison without altering any other part of the setup. Using the same board for both configurations ensured consistency and eliminated fabrication variability.

A separate transmit coil (Fig. 3.9c) was used instead of a single coil for both transmission and reception. At this stage of the project, a complete NMR system was not yet available, and the goal was to evaluate whether introducing a Lenz lens would enhance the signal detected by the receiver. The transmit coil was therefore used to mimic the signal that would be produced by a real sample, allowing us to simulate the signal pathway and test the effect of the lens in a controlled, repeatable manner. Using a dedicated transmit coil also eliminated the need for RF switching circuitry, which can introduce noise, mismatched impedances, and transient artefacts that interfere with signal clarity. This approach enabled a cleaner experimental setup focused specifically on testing passive field amplification and the behaviour of the lens-receiver configuration.

To ensure the consistency of our results, we 3D printed assembly, shown in Fig. 3.11, with a holder that maintained a fixed relative position between the boards. The transmitter was connected via SMA cables to an AFG3151C signal generator (Tektronix Inc., United States), which produced a continuous 2 W sinusoidal wave at 28.6 MHz. The receiver was connected to a STEMlab 125-10 microcontroller (Red Pitaya d.o.o, Slovenia), acting as an oscilloscope with discrete Fourier transform (DFT) functionality. The transmitted signal appeared as a peak in the frequency domain using the DFT function on the oscilloscope.

Fig. 3.12 present the power spectra for the experiments conducted without and with LL_1, respectively. In both cases, a distinct peak is observed at the expected frequency of 28.6 MHz.

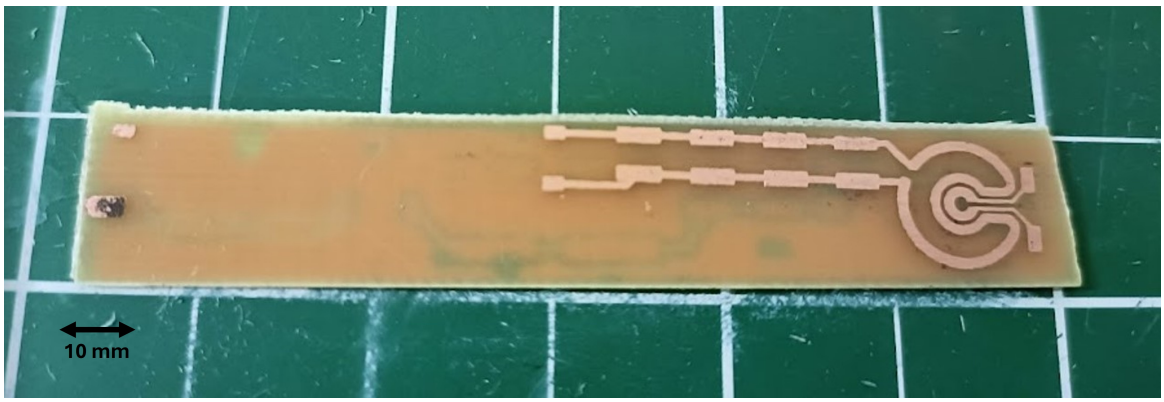

(a)

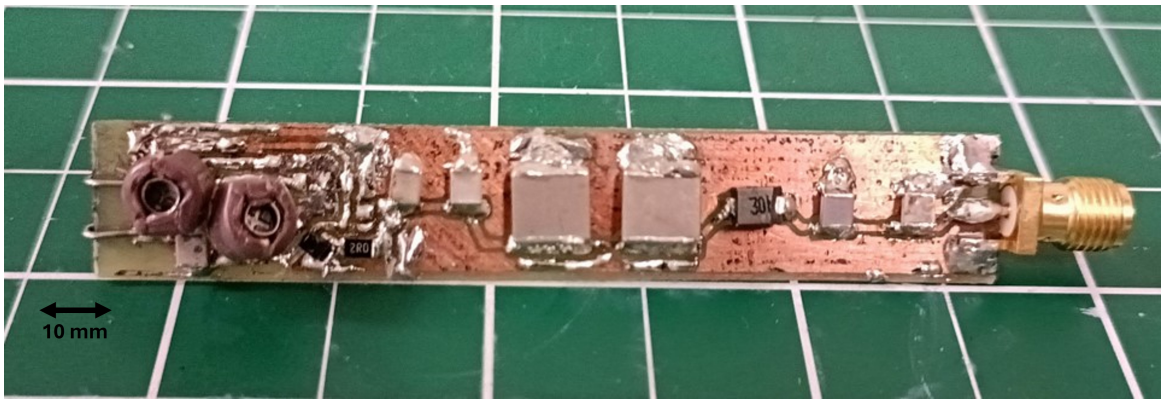

(b)

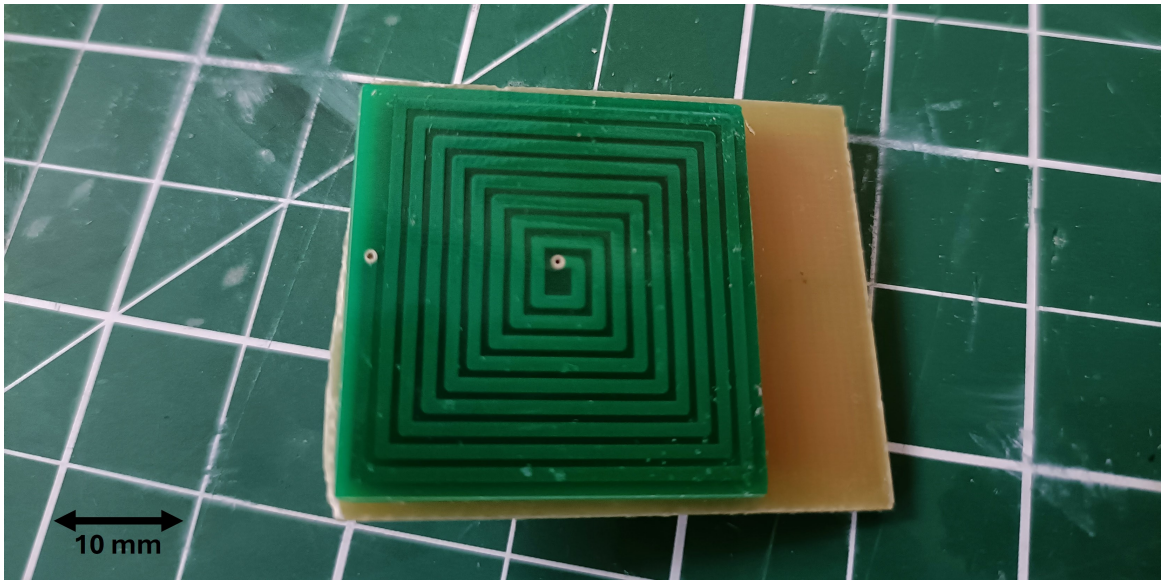

(c)

Figure 3.9: (a) The top side of the board with Lenz lens and receiver coil before components were added. (b) Bottom side of the receiver board with components. Reproduced with permission from [206]. (c) Transmitter coil used during testing.

With LL_1 present, the detected power was -2.770 dBm, equivalent to 0.528 mW. In contrast, without LL_1, the detected power was significantly lower at -18.854 dBm, or 0.0130 mW. The

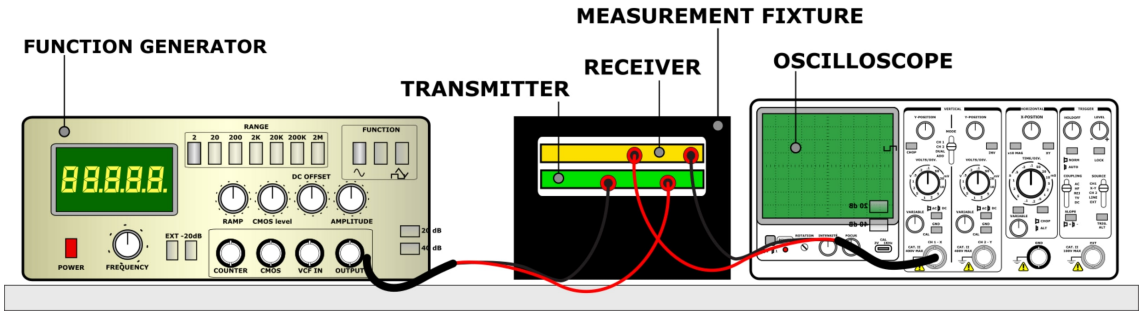

Figure 3.10: Diagram of experimental setup for testing the receiver board.

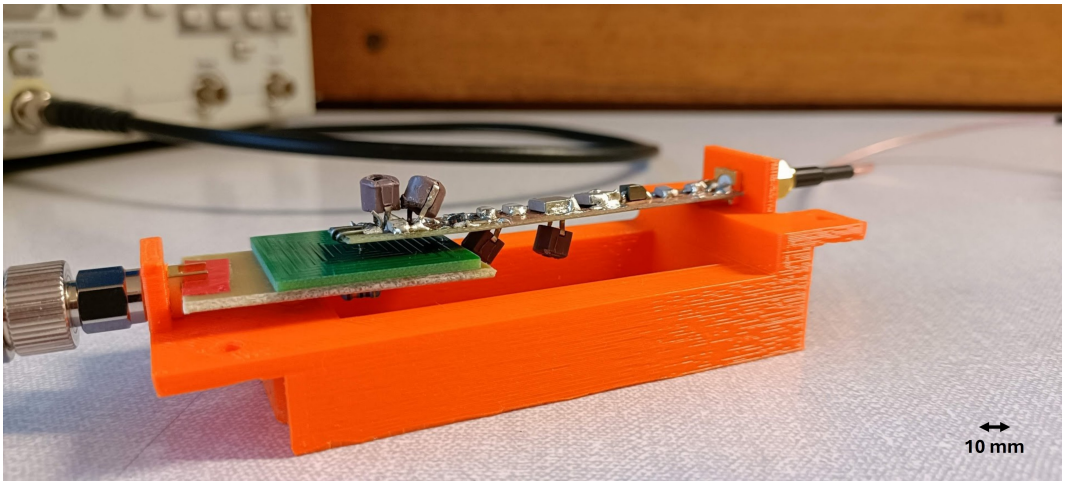

Figure 3.11: Experimental setup for testing the receiver board.

introduction of LL_1 resulted in over a 40-fold amplification of the received signal.

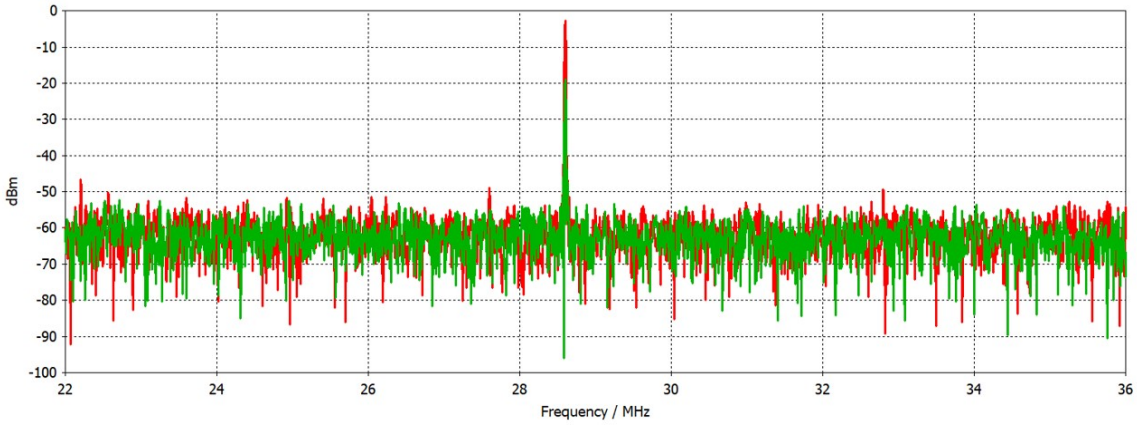

Figure 3.12: Measurement results for receiver board without (green) and with (red) the Lenz lens.

3.4 Lenz Lens Probe 2

3.4.1 Design

Our initial design served as a foundational step in understanding the behaviors and challenges associated with the Lenz lens probe. This iterative process provided critical insights that informed key refinements in the second version. One of the primary challenges we encountered was the precision required for fabricating the lens, which exceeded the capabilities of our in-house techniques. To address this, we outsourced the manufacturing to JLCPCB (Guangdong, China), a professional PCB supplier. This decision brought three major advantages: higher precision in fabrication, improved consistency between batches, and access to multi-layer PCB manufacturing, which was not feasible with our previous approach.

Another challenge was ensuring the precise alignment between the Tx and the lens. In the initial design, these components were placed on separate PCBs, making it difficult to maintain their relative positioning. Given that the alignment between the lens and transmitter is crucial for optimising magnetic field amplification, we revised our approach by integrating both components onto a single PCB. This change not only ensured a fixed relative position but also simplified the overall design, reducing complexity in both simulations and assembly. Additionally, we opted for smaller passive components in the second iteration, minimising parasitic effects that could distort the magnetic field distribution. These refinements collectively improved the system's reliability and performance, paving the way for a more robust and practical implementation of the Lenz lens probe.

After our initial design, LL_1, we learned that there are many variables that cannot be fully accounted for before designing the PCB. Factors such as connecting trace width, pad sizes, and component footprints must be carefully considered, as they can significantly impact performance. To address these challenges, our second design iteration prioritised a more systematic approach. We first designed the entire PCB with all necessary requirements and then simulated its behavior to achieve results as close as possible to the final implementation.

In this iteration, we adopted a round spiral geometry for the coil. This decision was based on its ability to generate a more uniform magnetic field, improving field homogeneity while maintaining a high fill factor on the PCB. The detailed coil dimensions are illustrated in Fig. 3.13a. To accommodate the sample more effectively, we introduced a hole through the center of the coil for a sample container to pass through. In the previous design, we intended for the sample was sandwiched between the Tx and Rx coils. However, integrating both coils onto a single board made this configuration unfeasible. Instead, a capillary tube was positioned through the central hole, allowing for more streamlined sample placement. This modification required widening the dimensions of the Rx coil and the inner lens loop. Compared our new design in Fig. 3.13b to the previous one in Fig. 3.3, we can see that this changes has also reduced the ratio between the inner and outer loops significantly. While this change may lead to a

Table 3.6: Dimensions of the primary coil and Lenz Lenses (Units: mm).

Tx Coil Parameters	Value	LL_1 Parameters	Value	Rx Coil Parameters	Value
w_t	0.40	w_t	1	w_g	0.6
w_g	0.20	w_{g_1}	1.75	D_o	3.50
s	0.60	w_{g_2}	0.25	D_i	2.2
R_i	0.95	r_f	0.88		
R_o	5.76	D_i	4.75		
		D_o	8		

slight reduction in amplification, it a reasonable trade-off for a more practical and streamlined fabrication process. The values for the individual geometric parameters of this design is listed in table 3.6.

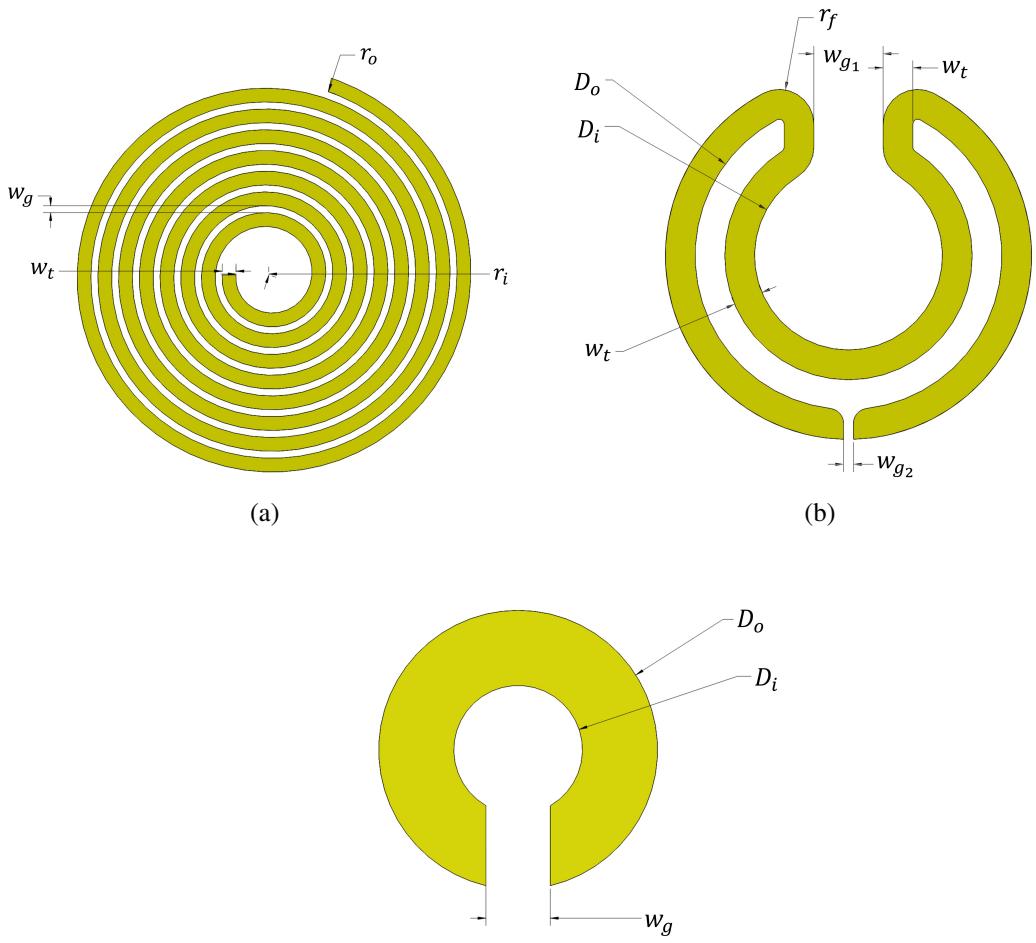

Figure 3.13: The designs and geometric parameters of the transmitter coil (a), Lenz lens (b), and receiver coil (c).

3.4.2 Circuit and PCB Design

To further ensure that our designs were planned as accurately as possible, before designing in the electrical components we first measured the static magnetic field $\vec{B}_0$, which was determined to be just under 0.671 T. Using this value, we calculated the corresponding Larmor frequency to be 28.566 MHz. All subsequent simulations were conducted at this frequency to ensure consistency with expected experimental conditions. This approach allowed us to fine-tune the lens design, optimise the system for maximum signal amplification, and enhance field homogeneity.

Our system consists of three separate inductors, all designed to operate at a single resonant frequency. In this configuration, the inductors are mutually coupled, meaning that each circuit is influenced not only by its own characteristics but also by the behaviour of the others. Additionally, since NMR systems switch between Rx and Tx modes, the external switches introduce impedance variations, dynamically altering the resonance conditions. To ensure proper operation, both the Rx and Tx coils must be matched to 50Ω.

The system can be represented using an impedance matrix, which accounts for the individual inductive reactances, mutual inductive reactances, capacitive reactance introduced to achieve resonance, and the additional impedance created by the switches in the Rx and Tx coils. If we denote the Rx coil, LL_2, and Tx coil as 1, 2, and 3 respectively, the system can be expressed as follows:

$$\mathbf{Z} = j\omega \begin{bmatrix} L_1 + Z_{\text{switch}_{Rx}} & M_{12} & M_{13} \\ M_{12} & L_2 & M_{23} \\ M_{13} & M_{23} & L_3 + Z_{\text{switch}_{Tx}} \end{bmatrix} + \frac{1}{j\omega} \begin{bmatrix} C_1^{-1} & 0 & 0 \\ 0 & C_2^{-1} & 0 \\ 0 & 0 & C_3^{-1} \end{bmatrix} \tag{3.19}$$

Due to mutual coupling effects, each inductor cannot be analyzed independently, requiring a more comprehensive approach. Determining circuit behaviour involves matrix inversion to establish voltage-current relationships; however, the switch-induced impedance variations introduce piecewise resonance conditions, leading to mode splitting and nonlinear transient effects. Since mutual inductance is impedance-dependent, the system must be analyzed separately for each switch state, often necessitating numerical eigenvalue analysis or circuit simulations to capture frequency shifts and transient responses accurately.

A more practical approach is to iteratively solve for each circuit component using established NMR probe tuning techniques. Traditional tuning and matching networks allow for impedance transformation, simplifying the design process. The equivalent electrical circuit representation is illustrated in Fig. 3.14. The tuning process begins by bringing LL_2 into resonance using C_{LL}, followed by identifying the remaining impedances Z^n.

The next step was to integrate all three elements onto a single PCB while incorporating the necessary traces and pads for proper connectivity. The design utilised a four-layer FR-4 board, with the top and bottom layers dedicated to the coil and Lenz Lens structures, while the inner

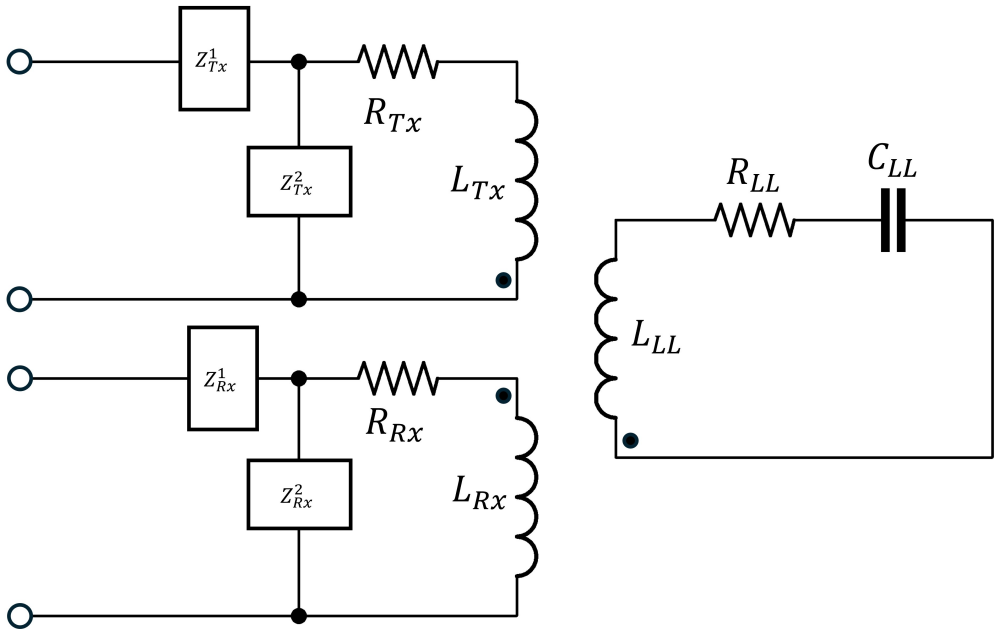

Figure 3.14: Equivalent electrical model of the NMR probe.

layers were used for grounding and signal routing. This multi-layer approach minimised interference and improved overall performance by maintaining a controlled impedance environment. To facilitate interfacing with measurement equipment, SMA connectors were integrated into the board design. Additionally, a 2 mm hole was cut at the center of the PCB to allow the sample tube to pass through, ensuring proper alignment and accessibility within the measurement setup. The layering of the PCB traces is shown in Fig. 3.15.

3.4.3 Simulation

Once the board layout was finalised, a 3D model was generated using ZofzPCB (ZofzPCB, Rafal Powierski, Germany), providing a detailed visualisation of the PCB, including traces, vias, pads, dielectrics, and component footprints. This model was then imported into CST Design Studio for simulation. Initially, lumped ports were used to represent the signal source and passive components. This approach leveraged CST's electrical schematic feature, allowing circuit elements to be substituted for their corresponding ports. Simulations were conducted for two probe configurations: one with only the Tx coil, as shown in Fig. 3.16a, and another with all components integrated, as depicted in Fig. 3.16b.

Once the initial simulation was completed, the impedances and inductances for each component were obtained, as summarised in Table 3.7. Additionally, the impedance variations over the 22 to 36 MHz frequency range are illustrated in Fig. 3.17b. One notable observation is that the inductance of the Rx coil is greater than that of LL_2, a result that may not have been imme-

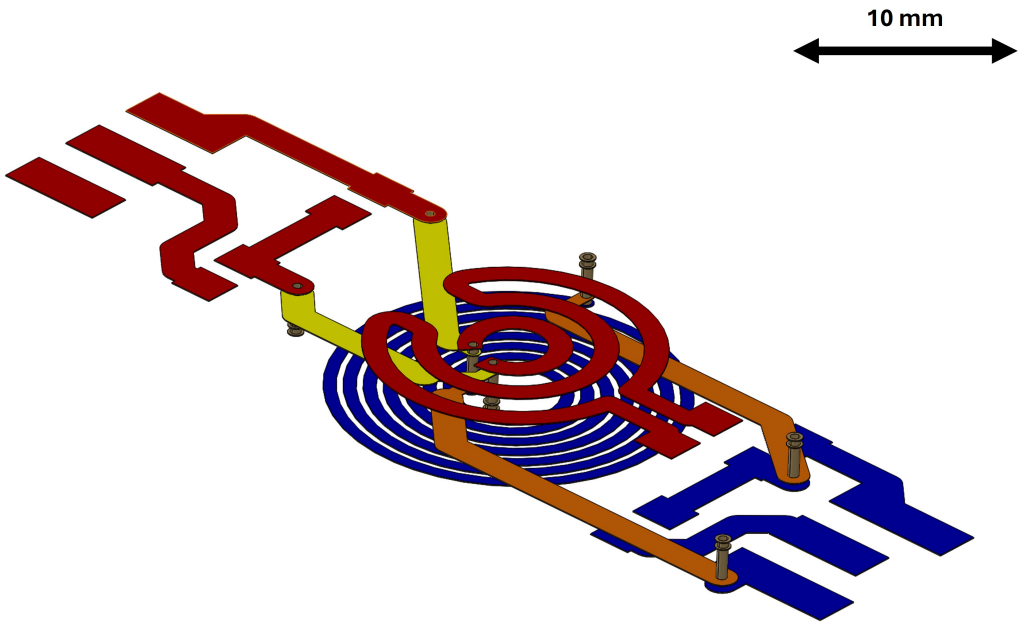

Figure 3.15: NMR probe PCB colour coded by layer.

diately apparent when considering only the active portion of the components. Furthermore, the S-parameter graph (Fig. 3.17a) indicates significant reflective losses, suggesting that the coils are losing a substantial portion of their power due to impedance mismatches.

Table 3.7: NMR Probe Simulated Values

Probe Element	**Impedance**	**Inductance**
Rx Coil	0.106 + 3.72j Ω	20.726 nH
LL_2	0.0799 + 2.823j Ω	15.728 nH
Tx Coil	2.21 + 71.1j Ω	395.6 nH

At this stage, we can begin the iterative process of transforming the impedances to achieve a configuration where both the Rx and Tx coils are matched to 50Ω while remaining unaffected by the switching dynamics. Since our model involves multiple coupled entities, any adjustment affects the impedance of all elements in the system. As a result, the matching process required systematically refining matching networks and component values to minimise reflective losses and optimise power transfer. This iterative approach ensures that the system remains stable and efficient across different operating conditions.

Table 3.8 presents the component values used for impedance matching, while Fig. 3.18a illustrates the impedance behaviour after matching. An interesting observation is the presence of a small dip near the desired frequency in the Rx coil's impedance response, along with a loop in the Tx coil's Smith Chart. The dip suggests weak coupling between LL_2 and the Rx coil, whereas the loop indicates stronger coupling, highlighting the differential interactions between these components within the system.

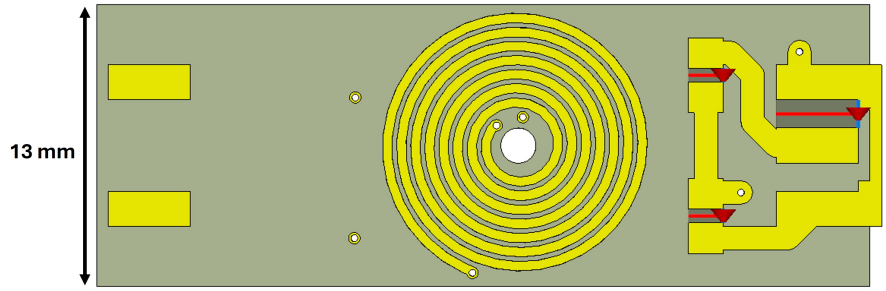

(a)

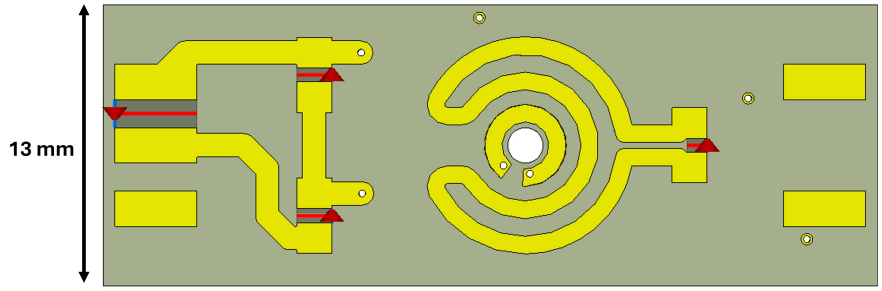

(b)

Figure 3.16: CST simulation port setup of Tx coil-only (a) and full probe (b) configurations. Red arrows represent lumped ports.

Table 3.8: NMR Probe Matching Values

Probe Element	**Matching Component**	**Value**
Rx Coil	Z^1	0 Ω
	Z^2	2.2 nF
LL_2	C_{LL}	2 nF
Tx Coil	Z^1	62 pF
	Z^2	1.5 uH

Once the matching component values were determined through the initial simulation, a second simulation was conducted with lumped elements replacing the ports. This simulation represents a fully matched board, ensuring that the maximum available power is efficiently utilised

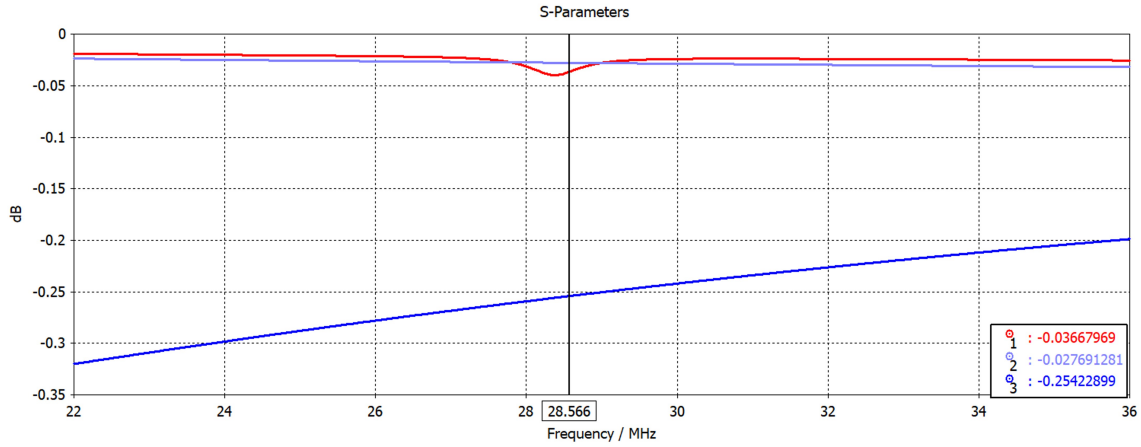

(a)

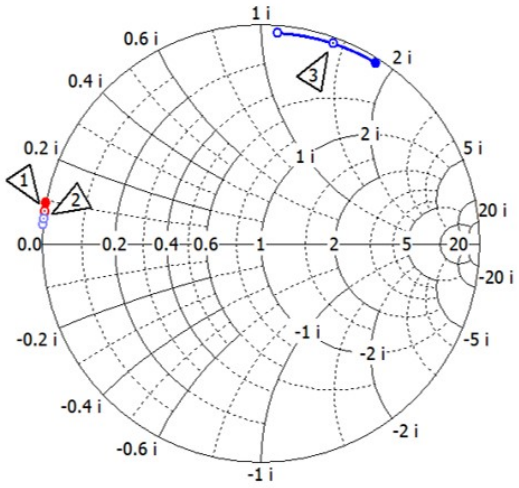

(b)

Figure 3.17: Simulated S-parameter bode plot (a) and Smith chart (b) showing impedances of the receiver (1), LL_2 (2), and transmitter (3).

to generate the magnetic field. By incorporating lumped elements directly into the model, the simulation more accurately reflects real world circuit behavior, capturing the effects of resonance and impedance matching. The results were analyzed by evaluating the magnetic field strength **H** at the center of the board using both one dimensional (Fig. 3.19a and 3.19b) and two dimensional (Fig. 3.20a and 3.20b) field distributions.

The 1D simulation results demonstrate the effect LL_2 on magnetic field distribution. While the coil-only configuration produced the highest magnetic field strength at 1528.5 A/m (1.92 mT), the LL_2 design achieved a lower value of 576.2 A/m (0.724 mT), indicating that the lens did not achieve an amplification similar to the previous LL_1 design. However, it did demonstrate a noticeably flat field distribution between -0.3 mm and 0.3 mm. In this region the magnetic field changed by only 12.63 A/m (15.9 μT) or at a rate of 21.05 A/m^2 (26.4 μT/m) while in the configuration without the lens it changed by 44.8 A/m or 74.7 A/m^2 (93.9 μT/m). Across this

region the homogeneity increased from 140 ppm to 36.7 ppm which is a 3.8-fold improvement. This shows that despite the much lower amplification, the lens still exhibited it's characteristic ability to focus the field and provide a better homogeneity than without it.

The 2D simulation results illustrate how the shaping effect is present on both the surface of the Tx coil (Fig. 3.20a) as well as the surface of LL_2 (Fig. 3.20b). A different interaction can be seen in here compared to the LL_1 design. Here we see that the field is contained within the Rx coil, which suggests that even though the simulation was setup to replicate our probe in Tx mode, there is still a significant coupling of the Rx coil to the lens in this state.

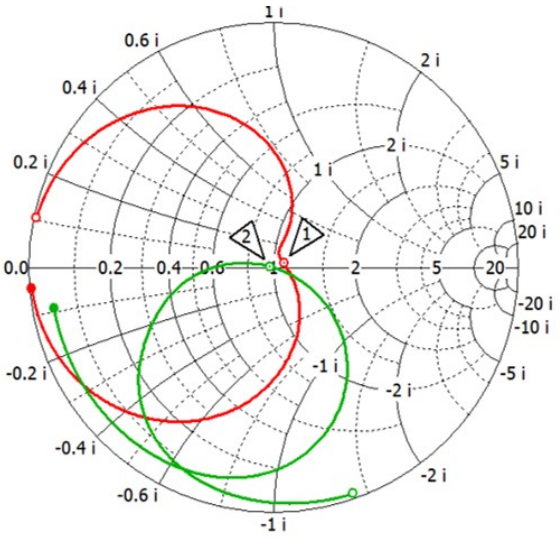

(a)

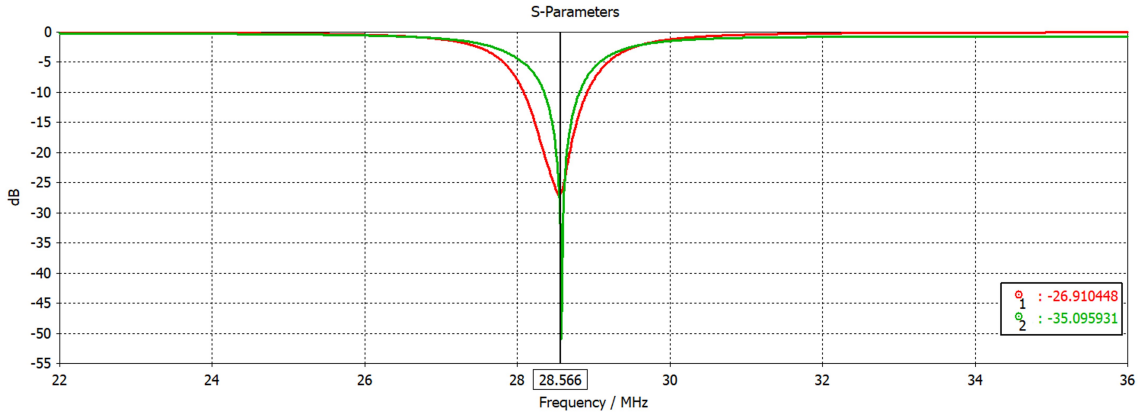

(b)

Figure 3.18: Simulated S-parameter Smith chart (a) and bode plot (b) showing matched impedances of the receiver (1) and and transmitter (2).

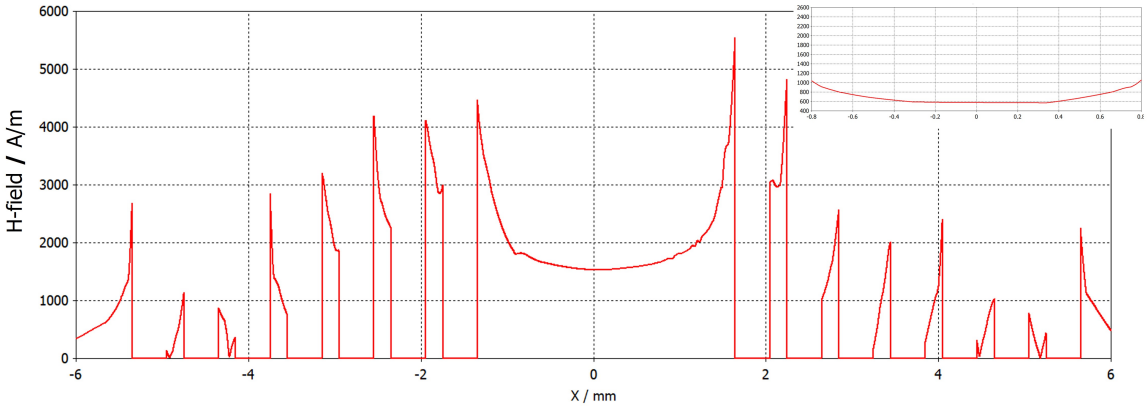

(a)

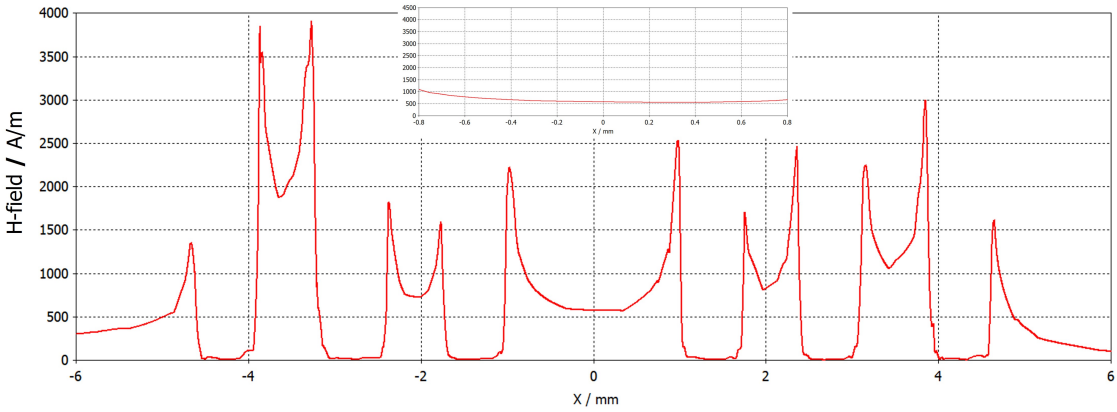

(b)

Figure 3.19: Simulated 1D H-field of the transmitter without (a) and with (b) LL_2.

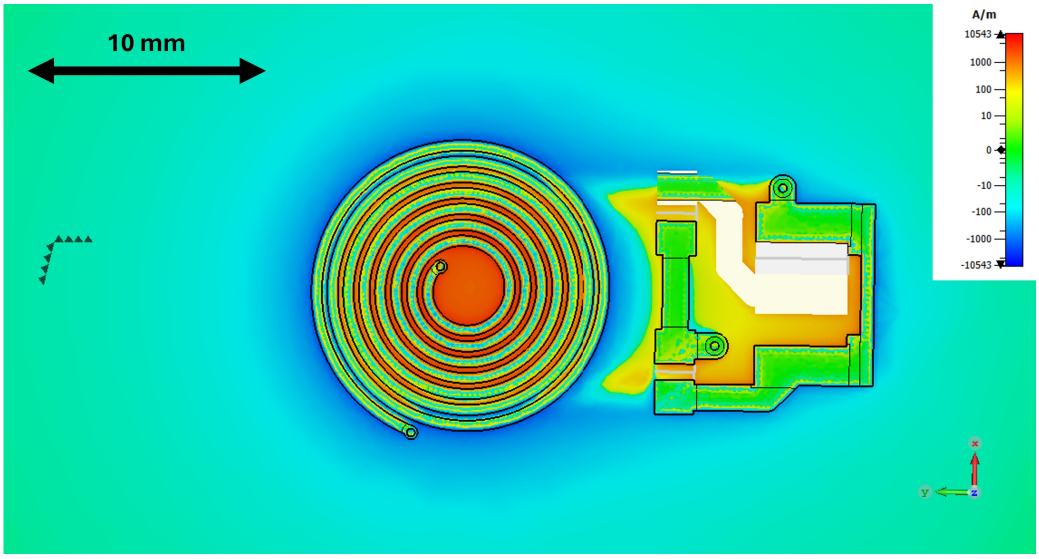

(a)

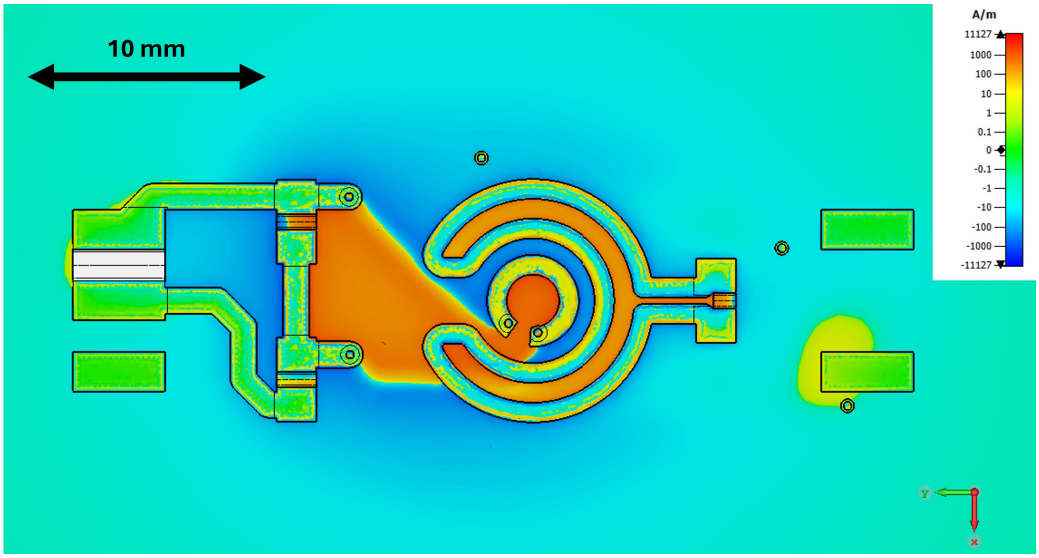

(b)

Figure 3.20: Simulated 2D H-field of the transmitter without (a) and with (b) LL_2.

3.5 Experimental Verification

After having fabricated our NMR probe based on the LL_2 design (Fig. 3.21), we can begin testing it to see if our simulations were accurate and if the probe behaves as we require it to. The first step is to perform all the impedance and S-parameter measurements for the individual probe elements to see how accurately the simulated predicted their inductances. Measuring the Rx coil, LL_2, and Tx coil separately using a vector network analyser (VNA) (CHELEGANCE JNCRADIO VNA 3G, Shenzhen, China) yielded values of 0.412 + 4.30j Ω, 0.0825 + 3.38j Ω, 1.504 + 73.1j Ω, and 1.504 + 73.1j Ω respectively. The Table 3.9 lists their impedance values, calculated inductances, and the difference between the simulated and measured results. The largest difference was 2.0j Ω so the simulation results were very accurate.

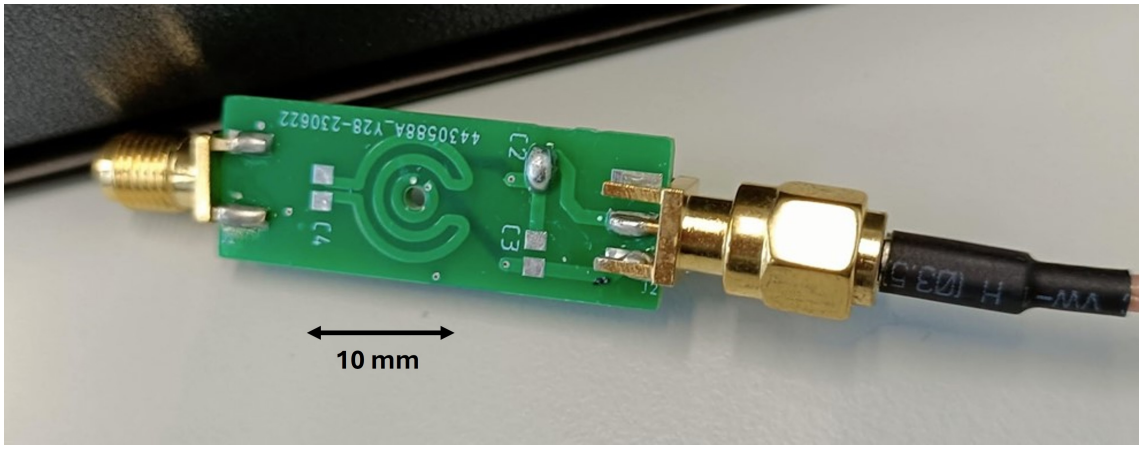

Figure 3.21: Fabricated LL_1 type board.

Table 3.9: NMR Probe Measured Values

Probe Element	**Impedance**	**Inductance**	**Impedance Difference**
Rx Coil	0.412 + 4.30j Ω	23.96 nH	0.306 + 0.58j Ω
LL_2	0.0825 + 3.38j Ω	18.83 nH	0.0026 + 0.557j Ω
Tx Coil	1.504 + 73.1j Ω	407.3 nH	-0.706 + 2.0j Ω

Table 3.10: NMR Probe Component Values

Probe Element	**Matching Component**	**Value**	**Percentage Difference**
Rx Coil	Z^1	0 Ω	0
	Z^2	1.5 nF	-31.8%
LL_2	C_{LL}	1.65 nF	-17.5%
Tx Coil	Z^1	150 pF	140%
	Z^2	1.5 uH	0

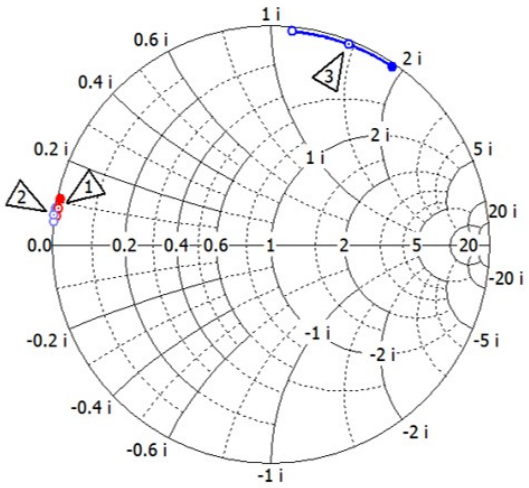

(a)

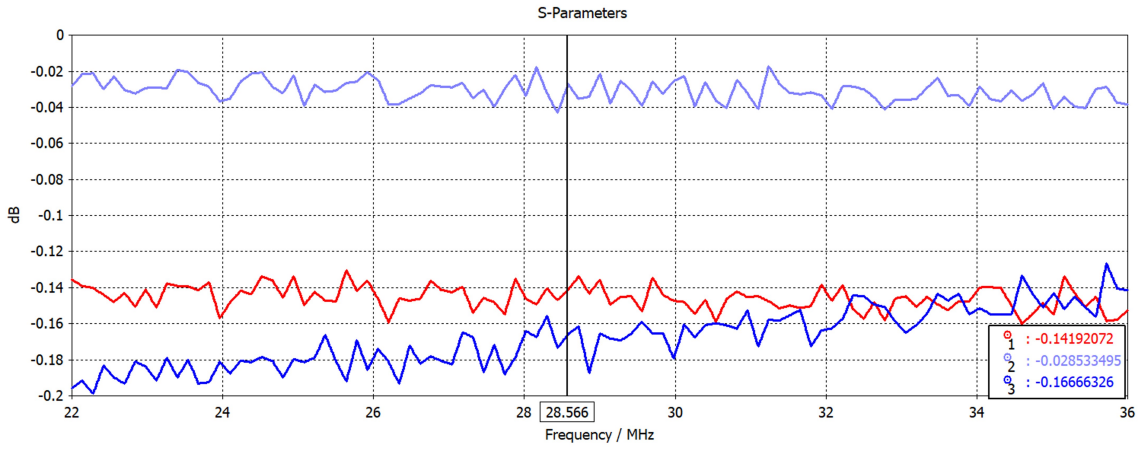

(b)

Figure 3.22: Measured S-parameter Smith chart (a) and bode plot (b) showing impedances of the receiver (1), LL_2 (2), and transmitter (3).

Matching was once again performed through an iterative process, and the final measured impedances were 30.78 - 0.68j Ω for the receiver coil and 50.94 - 6.60j Ω for the transmit coil. These results differed notably from the simulated values, particularly for the receiver coil, where the measured resistance was nearly three times higher than expected. This discrepancy led to a broader frequency response, as seen in Fig. 3.23a, and highlights a key limitation in the simulation process used.

The mismatch between simulated and measured results can be attributed to two main factors. First, the ports were not explicitly modelled in the simulations. This omission meant that transitions between PCB traces and coaxial connectors, which contribute both resistance and reactance, were not accounted for. These unmodelled elements directly affect impedance and return loss, especially in compact designs where the electrical length of connections is non-negligible. Second, practical implementation effects such as solder bridges and minor variations

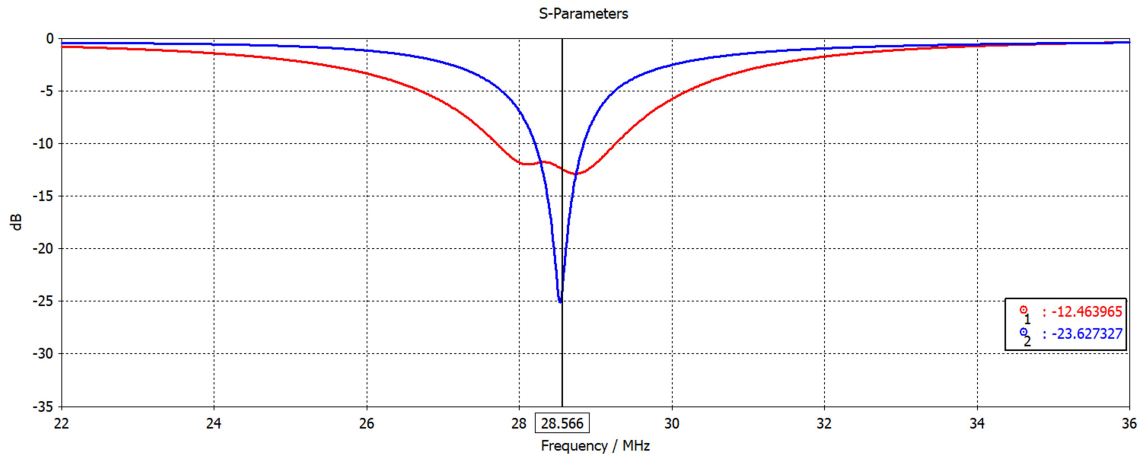

(a)

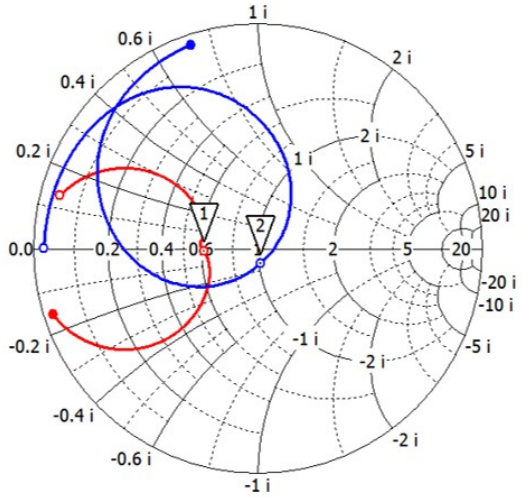

(b)

Figure 3.23: Measured S-parameter bode plot (a) and Smith chart (b) showing matched impedances of the receiver (1) and and transmitter (2).

in trace width introduced additional parasitic resistance and inductance. These factors, though difficult to simulate precisely, had a clear impact on the measured performance.

Despite these discrepancies, the return losses remained below 10 dB at the operating frequency, which was sufficient for the purposes of this study. Table 3.10 lists the components used, along with the percentage difference between the simulated and final implemented values. Due to space constraints, no tuning components were included, as their physical size could distort the magnetic field or interfere with the Lenz lens geometry. Although this increased the difficulty of achieving precise matching, it also ensured mechanical stability and avoided the need for re-tuning after assembly. This experience highlights the importance of accounting for real-world parasitics in future simulations and underscores the need for more robust designs that are less sensitive to small variations in component or layout parameters.

3.6 Conclusion

This chapter presented the development, simulation, and experimental validation of an NMR probe incorporating Lenz lenses to enhance signal sensitivity. By leveraging the ability of Lenz lenses to concentrate magnetic flux, we designed a passive approach to improving inductive coupling and maximising received signal strength without increasing power consumption or adding system complexity. The implementation of two probe iterations allowed for an iterative design process that addressed key challenges and progressively improved performance.

The first probe iteration demonstrated a 40.6-fold increase in received power, rising from 0.0130 mW without the lens to 0.528 mW with the lens. This amplification was a direct result of the Lenz lens's ability to focus the magnetic field, as shown by simulations that indicated a 9.09-fold increase in local magnetic field strength at the receiver coil. The maximum magnetic flux density at the probe center was measured at 0.485 mT, representing an improvement of up to 4.8 times compared to previous studies. However, practical challenges such as fabrication tolerances, sensitivity to parasitic capacitances, and alignment precision limited the robustness of the design, prompting the need for further optimisation.

To address these limitations, the second probe iteration introduced several key modifications, including a redesigned spiral geometry, improved field homogeneity, and an integrated PCB layout for better component alignment. Unlike the first iteration, which prioritised signal amplification, the second design was optimised for field uniformity, resulting in a 3.8-fold improvement in magnetic field homogeneity, reducing spatial variations in the field from 140 ppm to 36.7 ppm across the central detection region. However, this optimisation came at the cost of absolute signal amplification, with the second probe producing a peak field of 0.724 mT compared to the 1.92 mT of the coil-only configuration. Despite this reduction in peak field strength, the second probe demonstrated a more controlled and consistent field distribution, which is critical for maintaining signal integrity in practical NMR applications.

Experimental validation of the second probe generally confirmed the trends predicted by simulation, although discrepancies were observed in the measured impedance values. The receiver coil, Lenz lens, and transmitter coil exhibited measured impedances of $0.412 + 4.30j$ Ω, $0.0825 + 3.38j$ Ω, and $1.504 + 73.1j$ Ω, respectively. The largest deviation from simulated values occurred in the transmitter coil, with a difference of $2.0j$ Ω. Final impedance matching achieved return losses below 10 dB at 28.566 MHz, indicating acceptable power transfer and minimal reflection across the operating frequency. However, the receiver coil exhibited a higher resistance than anticipated, measuring 30.78 Ω instead of the expected 50 Ω, which led to a broader frequency response. This deviation, along with the adjustments required for the tuning and matching capacitors (from 2 nF to 1.65 nF and from 2.2 nF to 1.5 nF, respectively), highlights the impact of unmodelled parasitic elements and fabrication tolerances. These findings reinforce the limitations of the simulation process, particularly the omission of port losses and solder-related effects, and emphasise the importance of incorporating fabrication-aware design

strategies in future development.

While it would be ideal to compare the performance of the first and second Lenz lens designs using the same measurement parameters, a direct comparison is not possible due to the differing goals of each experiment. The first design focused on demonstrating the fundamental amplification potential of the Lenz lens. At that stage, we did not yet have an NMR sample or complete detection system, so we used a separate transmit coil to mimic the sample signal and measured the received power to determine whether the lens could increase signal strength. This approach allowed us to validate the basic concept.

In contrast, the second design was developed with the expectation of being used in an actual NMR experiment. Rather than measuring received power, the focus was on minimising return loss and ensuring efficient power transfer through careful impedance matching. The goal was to optimise the system for detecting real NMR signals with minimal reflection and maximum sensitivity. For this reason, we used S-parameter measurements to validate performance rather than power measurements.

The most consistent and reliable comparison between the two designs comes from simulation results of magnetic flux density at the sample region. The first design produced a simulated peak magnetic field of 0.485 mT, while the second design achieved a higher field of 0.724 mT. Although the second design did not surpass the 1.92 mT generated by the coil-only configuration used as a reference in that simulation, it still delivered a stronger field than the first lens design. This reinforces the effectiveness of the updated geometry and matching strategy in improving field strength at the detection region, even without a direct power-based comparison.

Overall, the use of Lenz lenses in NMR probe design has been shown to provide significant advantages in both signal enhancement and field shaping. The results of this study demonstrate that passive magnetic flux concentration can be effectively applied to improve NMR sensitivity while maintaining a compact and efficient design. With this in mind, the next chapter shifts focus to the electronic design of the NMR system, detailing how signal generation, amplification, and detection are integrated to support the performance of the probe. This discussion will examine how circuit-level considerations influence the overall sensitivity and functionality of the system, ensuring that the enhancements provided by the Lenz lens are fully realised in practical NMR measurements.

Chapter 4

Modular Electronics System

4.1 System Architecture and Modules

In the last chapter, we designed the front end of our NMR system, which directly interfaces with the sample. With the probe's expected performance defined, we can now design the supporting electronic system by working backwards to meet its requirements. The electronics serve two primary functions: transmitting signals into the probe and receiving signals from it. In developing this system, we aim to achieve two main criteria, high sensitivity and low cost. Experienced engineers will recognise that these two goals are often at odds with each other. Higher sensitivity typically demands higher quality components and careful design, both of which increase costs. In NMR, expenses tend to be particularly high, as many designs are bespoke.

Beyond cost, another major challenge in translating research into practical applications is reproducibility. Even when detailed designs are available, variations in parts and assembly techniques can lead to significant differences in performance, especially in complex instruments. Instead of creating a bespoke, fully custom solution, we took inspiration from Lego. Rather than focusing on fabrication, we focused on modular assembly.

When building a Lego set, one is given a set of standardised blocks, each with a defined shape and function, which can be pieced together in various ways to create different structures. These blocks are identical regardless of where they are purchased, ensuring that the same design can be replicated anywhere in the world. We applied this philosophy to NMR system design. The modular nature of NMR systems is already apparent, consisting of a magnet, probe, and electronics that come together to form a functional system. We took this idea one step further by breaking the electronics into modular components as well.

This concept has been previously explored by projects such as OPENCORE NMR [213], which has made open source designs available. However, these designs often require a level of electronics expertise that may be inaccessible to researchers without specialised training. Our approach builds on this idea by utilising commercially available modules that can be assembled like Lego blocks. As long as the necessary modules are available for purchase, users can con-

struct the system without needing to fabricate or modify individual components. Furthermore, if a particular module does not meet the desired performance, it can be easily replaced without affecting the rest of the system. This modular approach not only simplifies design and replication but also enhances flexibility, making NMR technology more accessible to a broader range of users.

The simplest NMR experiment consists of a single pulse followed by the detection of a signal. The pulse, typically described by the degree to which it tilts the magnetisation vector into the transverse plane, is a brief sinusoidal excitation oscillating at the Larmor frequency. The duration of this pulse determines the tilt angle and is proportional to the strength of the magnetic field. Consequently, the first requirement of the transmission chain is to generate a signal at the Larmor frequency, with the desired pulse duration and power level. For instance, a 1 mT field requires a 5 μs pulse to achieve a 90 degree tilt. From the previous chapter, we determined that the Lenz lens generated a field of 339.29 A/m, or 0.426 mT, necessitating a pulse duration of 11.7 μs. While these requirements apply to a simple single pulse experiment, more complex sequences demand different pulse shapes, making a programmable signal generator capable of outputting arbitrary waveforms ideal. One of the most effective methods for generating programmable high frequency signals is through the use of field programmable gate arrays (FPGAs). FPGAs offer several advantages, including high speed digital signal processing, flexibility in waveform design, and real time reconfigurability, making them well suited for the demanding requirements of NMR pulse sequences.

The Larmor frequency of our NMR system is expected to be around 28.6 MHz. However, to ensure compatibility with a wide range of magnetic field strengths, all components were selected to have as broad a bandwidth as possible. This approach provides flexibility, allowing the system to adapt to different experimental conditions without requiring major modifications. The only components that will require adjustment are the filters, which must be tuned to match the specific operating frequency of the system.

To determine the exact specifications required for each component, we used the simulation data from the previous chapter and worked backwards from the desired system performance. The PA's output powers the transmitter coil, which generates the magnetic field that is focused by the Lenz lens. In simulations, the Lenz lens achieved the desired results with 0.5 W, meaning the PA must be capable of delivering at least this power level. However, in practical implementations, losses due to impedance mismatches are inevitable. To account for these losses and provide sufficient operational headroom, selecting a PA with a slightly higher output power ensures consistent performance across different conditions.

Similarly, the switch in the system must not only handle the power passing through it but also maintain high isolation between the receiver and transmitter chains to prevent leakage that could degrade sensitivity. The specifications for the LNA chain can then be derived using fundamental NMR equations.

To ensure that the NMR signal can be observed and processed effectively, the receiver must amplify the signal from the minimum detectable value up to a higher voltage, such as 100 mV. This level is chosen because it provides a good balance between signal strength and manageable voltage for most data acquisition systems, allowing for clear and precise detection.

The amplification factor (or gain) G can be calculated using the ratio of the desired output voltage V_{out} to the minimum detectable input voltage V_{min}. The relationship is given by:

$$G = \frac{V_{\text{out}}}{\xi_{\text{min}}} \tag{4.1}$$

Where G is the amplification factor. V_{out} is the desired output voltage.

This amplification factor indicates that the receiver must provide a gain of approximately 176,960 (or 105 dB) to increase the signal from the minimum detectable value of 5.651×10^{-7} V up to 100 mV. This level of amplification is necessary to ensure that the NMR signal can be observed with high clarity and processed effectively by the data acquisition system. Such a high gain requires careful selection of low-noise amplifiers and consideration of stability to prevent additional noise from degrading the signal.

While this calculation represents the theoretical ideal gain, in practice, there will be losses along the receiver path due to impedance mismatches, attenuation, and component imperfections. To account for these losses and ensure reliable signal detection, an additional 15 dB of gain is recommended as a safety margin. This brings the total required gain to approximately 120 dB, providing extra headroom to accommodate any unexpected variations or losses in the signal path.

The SNR of the NMR system is an important indicator of the quality of the received signal. In this context, the SNR is normally defined as the ratio of the RMS NMR signal ξ_{rms} to the RMS noise voltage $v_{\text{rms-noise}}$. Since the SNR of interest depends on the minimum detectable signal, however, the expression can be adjusted as:

$$\text{SNR} = \frac{\xi_{\text{min}}}{F \times v_{\text{rms-noise}}} \tag{4.2}$$

The noise figure F is a measure of how much additional noise is introduced by the NMR receiver or detection electronics compared to an ideal, noiseless system. Substituting the calculated value of ξ_{min} and the previously determined $v_{\text{rms-noise}}$, we find that the minimum SNR is 20.7, assuming an ideal receiver with a noise factor of 1. However, in real-world systems, the receiver will introduce additional noise, reducing the SNR.

Rearranging the equation, we can express F in terms of the ideal SNR (i.e., when the noise factor is 1) and the minimum SNR:

$$F = \frac{SNR_{\max}}{SNR_{\min}} \tag{4.3}$$

An $SNR_{\min}$ of 5 ensures that the signal is sufficiently strong compared to the background noise, providing reliable detection and accurate measurements. Using this value, we find that the maximum allowable noise figure F is approximately 2.93. The noise figure can also be expressed in dB as:

$$F_{\mathrm{dB}} = 10\log_{10}(F) \tag{4.4}$$

This thus sets the upper limit on the amount of noise that can be introduced by the receiver electronics as 4.67 dB.

With these criteria in mind, we selected the components listed in Table 4.1. Each component was chosen to balance performance, cost, and flexibility, ensuring the system meets the required sensitivity while remaining adaptable for different system designs. Notably, in addition to functioning as the signal generator, the STEMLab 125-10 also controls the switch timings, synchronising the transmission and reception paths. This dual functionality simplifies the system architecture by reducing the number of independent control elements required, improving integration and overall system efficiency. The arrangement of the modules and overall system architecture is as described in section 2.1.

4.2 Impedance Analysis and Matching

Now that we have selected our components, we can begin assembling them. However, before doing so, it is crucial to consider the behaviour at the module interfaces for a moment. When a signal passes from one module to the next, three possible interactions can occur: transmission to the next module, reflection back to the current module, or absorption at the interface. The first scenario is ideal, ensuring efficient power transfer through the system, while the latter two introduce losses that must be minimised.

Absorption primarily depends on the internal efficiency of the modules themselves, which we mitigated by selecting high performance components suited to their respective tasks. Reflection, however, is determined by the impedance mismatch at the interface between modules. RF signals oscillate at high frequencies and require consistent impedance matching between connected components to ensure proper energy transfer. This is why most RF electronics adhere to a standardised 50 Ω impedance.

Despite manufacturers specifying RF compatibility, given the sensitivity of our instrumentation, it is essential to verify these impedance characteristics ourselves. Small variations in

Table 4.1: NMR System Modules

Module Name	**Part Number**	**Frequency Range**	**Key Specifications**
Power Amplifier	SBB2089Z, RD01MUS2B	1 – 930 MHz	Gain: 30 dB Noise Figure: 1.2 dB, Max Output Power: 2.0 W
Switch	HMC849A	DC – 6 GHz	Insertion Loss: 1.3 dB (2 GHz) Power Handling: +31 dBm (P1dB) Power Handling: +52 dBm (IP3) Input-Output Isolation: -60 dB Output-Output Isolation: -80 dB
Mixer	ADE-25MH	5 – 2500 MHz	Conversion Loss: 6.9 dB LO-RF Isolation: 34 dB LO-IF Isolation: 32 dB
Low-Noise Pre-Amplifier	Nooelec LaNA	10 – 3000 MHz	Noise Figure: 0.6 dB at 100 MHz Gain: 20 dB at 100 MHz
Low-Noise Amplifier	NXP BGA2869	1 – 1000 MHz	Noise Figure: 1.3 dB at 100 MHz Gain: 30 dB at 100 MHz
Signal Generator	STEMlab 125-10	DC - 50 MHz	Sampling Rate: 125 MS/s Amplitude: $\pm$ 1 V Output Waveform: Sine, Square, Sawtooth Pulse Shapes: Gaussian, Sinc, Rectangular

impedance mismatches can lead to significant signal loss, distortion, or standing waves that degrade system performance. Therefore, before full system assembly, we will characterise the impedance of each module and design appropriate matching networks where necessary to optimise signal transmission.

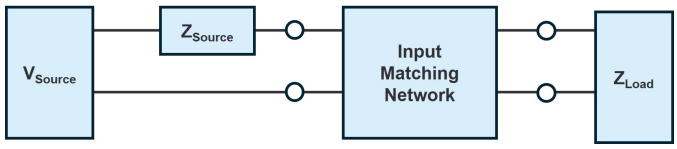

(a)

Figure 4.1: Impedance circuit matching network.

Table 4.2: Electronic Module Impedances

Module	**Impedance**
Bandpass Filter Input	47.2 - 7.12j Ω
PA Input	40.5 + 14.7j Ω
PA Output	80.1 - 126.6j Ω
Switch Input	55.0 - 6.08j Ω
Pre-LPF Input	84.30 - 148.8j Ω
Pre-LPF Output	30.1 + 23.1j Ω
LPF Input	172.8 - 8.55j Ω
LPF Output	34.0 + 8.49j Ω
Mixer RF Input	61.7 + 4.47j Ω

In high-frequency circuits such as NMR systems, efficient power transfer between components is crucial to minimising signal loss and preserving signal integrity. Impedance matching ensures that the source and load impedances are properly matched, allowing for maximum power transfer and reducing signal reflections. When impedances are mismatched, part of the signal is reflected back toward the source instead of being transmitted to the next stage, leading to inefficiencies and potential signal degradation.

A common approach to impedance matching is the use of matching networks, which consist of passive components such as inductors and capacitors arranged to transform the source impedance to match the load impedance. This is particularly important in RF applications, where mismatches can significantly affect system performance. Fig. 4.1a illustrates a general impedance matching network, where a source with impedance Z_{Source} is connected to a load with impedance Z_{Load} through an input matching network. The goal of this network is to adjust the impedance seen by the source to ensure maximum power transfer and minimal signal reflection.

We measured the S-parameters across a frequency range of 22 to 36 MHz at the input and

output of each module to characterise their signal transmission and reflection properties. S-parameters provide insight into how signals propagate through each stage, revealing key information about insertion loss, return loss, and impedance mismatches. By analysing these parameters, we can assess the efficiency of power transfer between modules and identify any potential mismatches that could degrade system performance.

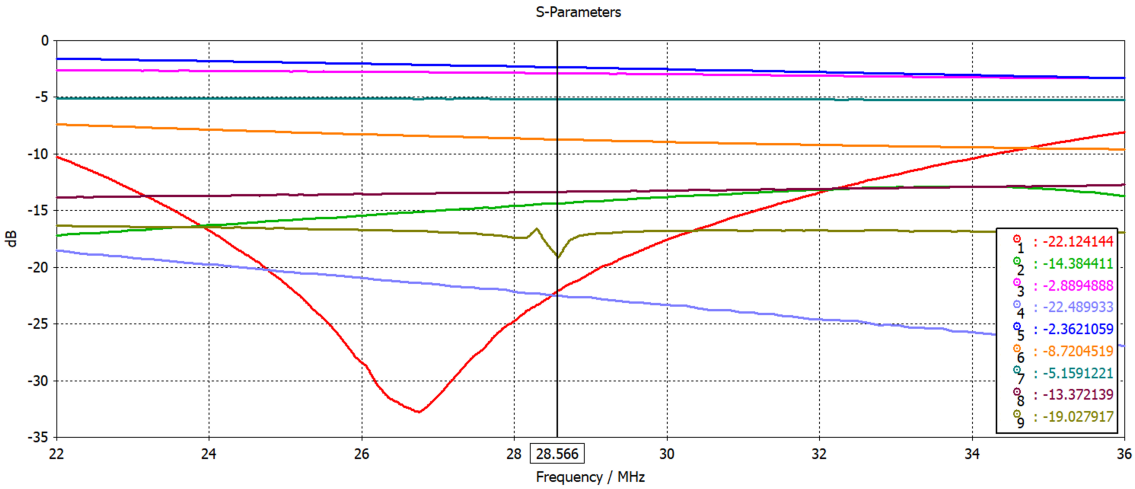

(a)

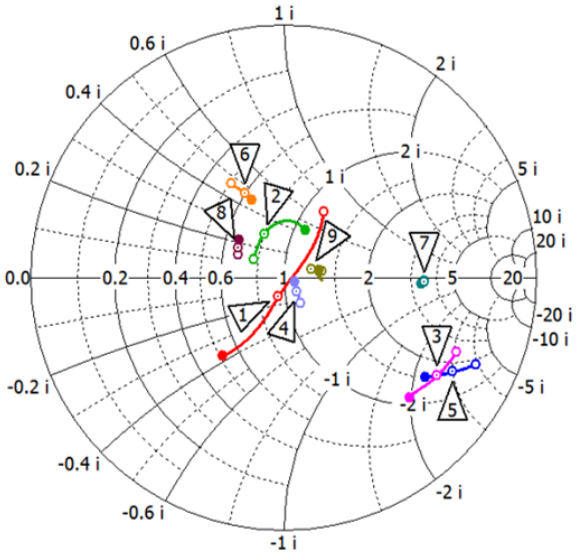

(b)

Figure 4.2: S-Parameter Bode plot and Smith Chart showing the measured input and output impedances of modules over the 22 (empty circle) to 36 (filled circle) MHz range. The markers indicate: (1) bandpass filter input, (2) power amplifier input, (3) power amplifier output, (4) switch in the closed state, (5) low-noise preamplifier input, (6) low-noise preamplifier output, (7) low-noise amplifier input, (8) low-noise amplifier output, and (9) mixer RF input.

Figure 4.2a shows the Bode plot of S_{11}, which represents the input reflection coefficient and indicates how much power is reflected rather than transmitted. From the figure, we can

see that the SG, PA output, pre-LNA input, and LNA input exhibit significant power loss due to reflection. To further investigate these losses, we examined the impedance values using the Smith chart in Figure 4.2b. The chart reveals that the observed reflections are caused by significant deviations from the standard 50 Ω impedance, which corresponds to the center of the normalised Smith chart. The farther the impedance values deviate from 50 Ω, the more complex the required impedance transformation becomes. Additionally, the width of the impedance trace indicates the extent of impedance variation across the measured frequency range. Most components exhibit relatively short traces, meaning their impedances remain stable, but the SG output shows considerable variability, suggesting the need for a more complex matching network, potentially requiring a second or third stage match.

The most critical impedance values, however, are those of the modules along the receiver chain, where signal integrity is most vulnerable. The signal at the probe is extremely weak, on the order of tens of nanovolts as previously discussed, making any losses particularly detrimental. To minimise these losses, impedance matching must be applied not only at the input and output of the amplification chain but also between individual amplification stages [214]. Our design goal is to ensure that no more than 10% or -10 dB of the signal is lost at any stage, preserving as much signal strength as possible throughout the receiver chain.

Table 4.3: Interfaces that Require Impedance Transformations

Output Module	**Output Impedance**	**Input Module**	**Input Impedance**
PA	79.9 - 126.5j Ω	Probe Tx	50.94 - 6.60j Ω
Probe Rx	30.78 - 0.68j Ω	Pre-LNA	84.28 - 148.69j Ω
Pre-LNA	30.07 + 23.12j Ω	LNA	172.83 - 8.50j Ω
LNA	33.99 + 8.51j Ω	LNA	172.83 - 8.50j Ω

Based on the circuit architecture in Fig. 2.2, Table 4.3 outlines the interfaces and impedance values that need to be matched. We designed the impedance matching networks by plotting the start and end impedance on a Smith chart and placing the necessary components to create a transformation path between them. To account for the effect of parasitics in our components, we designed our circuit to fit within Q-circles, with the Q value determined by the lowest Q among our components. This led to the design of the circuits shown in Fig. 4.3. Notably, in Fig. 4.3b, a two-stage matching network was required, while the others could be matched using a single stage which matches our expectation based on Fig. 4.2b.

In addition to parasitics, our inductors and capacitors also deviate from their intended values by a certain percentage, which can accumulate and cause significant shifts in the matching frequency range. The components we used had the standard 10% tolerance for most values. To evaluate the robustness of our matching networks against these deviations and to ensure that, regardless of the actual component values, we could achieve our matching goals, we ran Monte Carlo (MC) simulations on the networks.

MC simulations consider all possible combinations of component value variations and simulate the circuit's frequency response. Our aim was to ensure that our circuits maintained a 1.2 MHz bandwidth, meaning that from 28 to 29.2 MHz, the return loss remained below -10 dB. The simulation results, shown in Fig. 4.4, indicate that while the frequency peaks shift significantly, up to 1.5 MHz in some cases, the circuits consistently satisfy the -10 dB threshold across the target range, confirming their robustness for practical implementation.

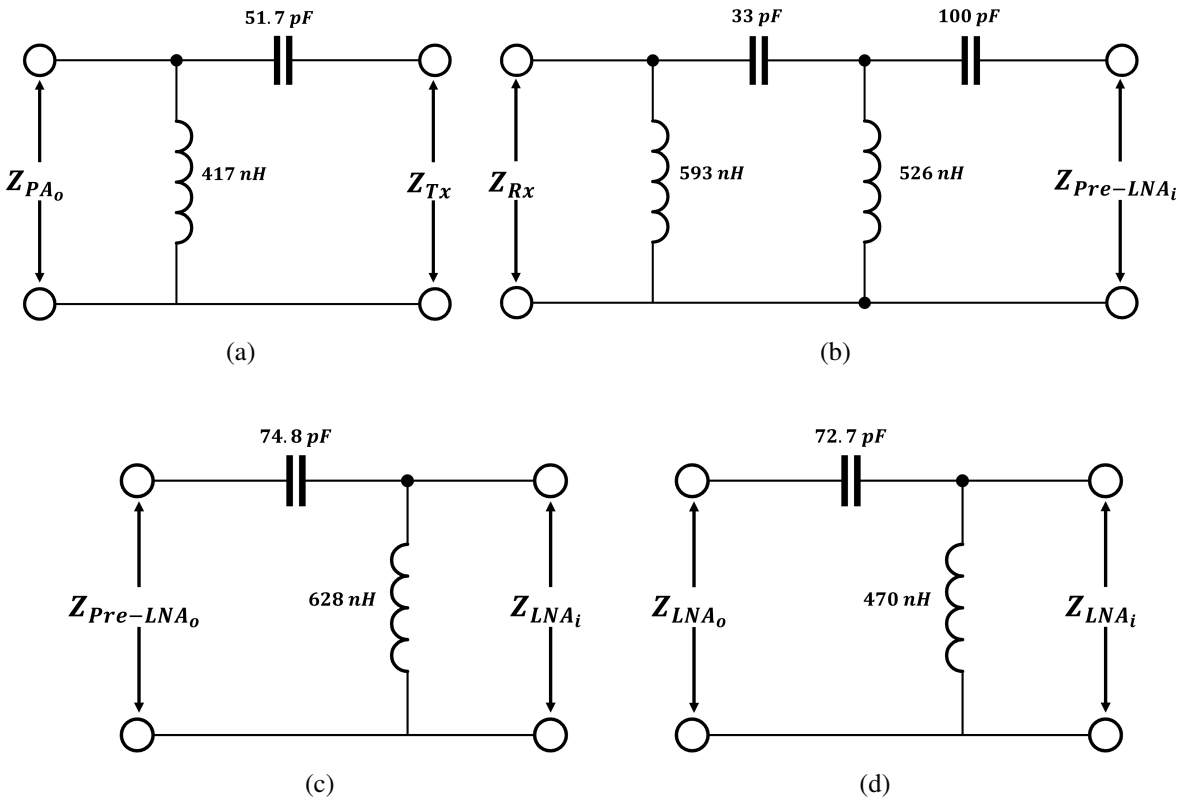

Figure 4.3: Impedance Matching Circuits

After confirming that the designed matching circuits met the expected outcomes from simulations, we proceeded with fabrication and measurement. The measured results indicate that the return loss, shown in Fig. 4.5a, remains below -10 dB, and the impedance values, shown in Fig. 4.5b, are at or near 50 Ω within our desired frequency range. These results confirm that the matching networks effectively minimised signal reflections and optimised power transfer between modules.

An interesting observation arises when comparing the impedance traces in Fig. 4.5b with those from the initial measurements in Fig. 4.2b. The impedance spread across the full frequency range of 22 to 36 MHz has increased following the addition of the matching circuits. This broadening of the frequency response is a direct consequence of the matching networks, which slightly extend the impedance variation beyond the originally measured range. In our case, this is not a concern, as our operational bandwidth is significantly smaller than 14 MHz.

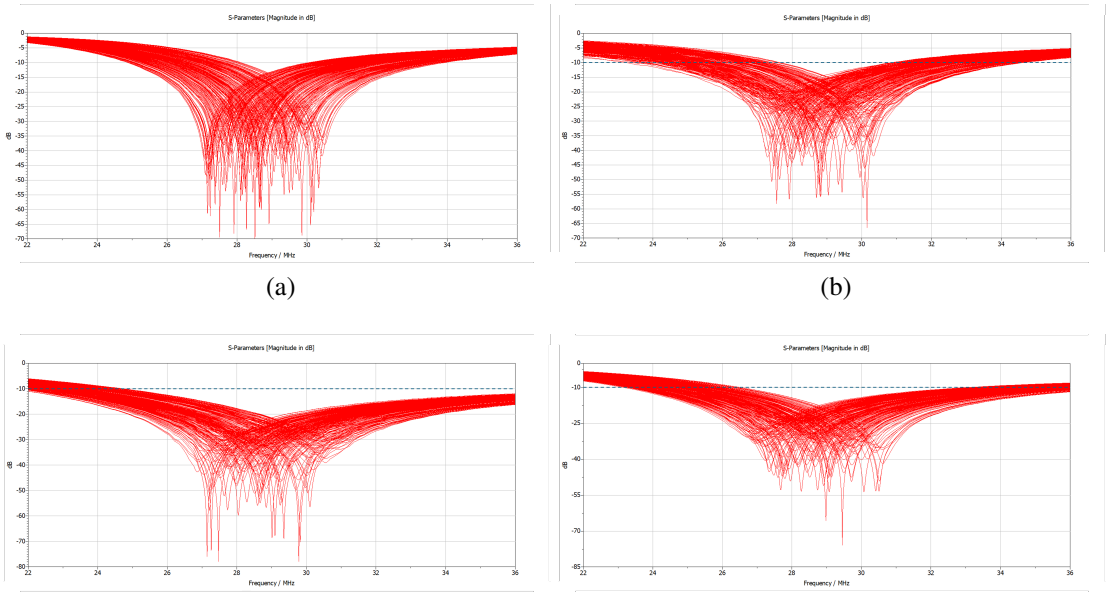

(a) (b)

(c) (d)

Figure 4.4: Monte Carlo simulation of impedance matching circuits with 10% component tolerances.

However, for applications requiring impedance matching over a larger bandwidth, a different matching strategy such as the use of wideband matching networks or multi-stage impedance transformation would be necessary to achieve consistently low return loss across the entire frequency range.

4.3 Electronic System Testing

With the modules matched, we proceeded with assembly and performance characterisation. The receiver electronics were mounted onto a large grounded aluminum plate to minimise interference from ambient signals and ensure stable operation. Beneath the plate, the impedance matching board was mounted, containing all previously discussed matching circuits. The aluminum plate also functioned as a shielding ground plane, reducing electromagnetic interference and providing a controlled environment for signal integrity testing. Fig. 4.6a illustrates the setup, showing the complete receiver chain integrated onto the aluminum plate.

At this stage, testing focused exclusively on the electronics without incorporating an actual NMR sample, allowing for an evaluation of system performance under controlled conditions. The transmission electronics were assembled separately, directly on the bench, as shown in Fig. 4.6b, with a gap maintained between the circuit boards and the table surface to reduce unwanted coupling and interference.

To simulate the NMR experiment, we used an oscilloscope (DSOX1204G, Keysight, USA) and a second signal generator (AFG13151C, Tektronix, USA). The excitation sequence was

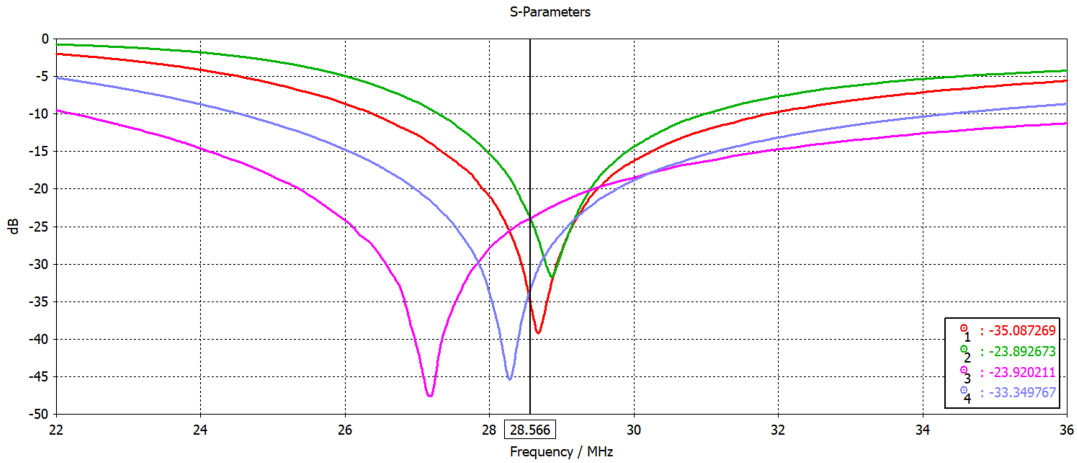

(a)

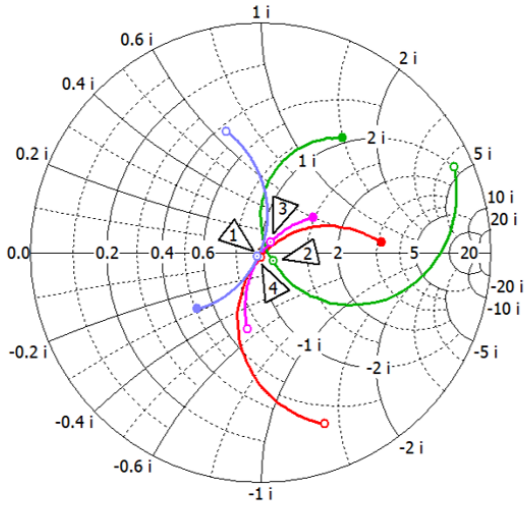

(b)

Figure 4.5: S-parameter Bode plot and Smith Chart showing the measured input and output impedances of modules over the 22 to 36 MHz range after matching. The markers indicate: (1) signal generator output, (2) power amplifier output, (3) low-noise preamplifier input, (4) low-noise preamplifier output, (5) low-noise amplifier input, (6) low-noise amplifier output.

simulated by sending a pulse from the signal generator, which was recorded on the oscilloscope to verify transmission accuracy. A second signal generator was then used to produce a test signal that passed through the receiver chain, allowing us to evaluate its amplification and filtering characteristics.

Although the SDRlab board used for signal generation includes onboard digital demodulators that could have been used for acquisition, we chose to use the oscilloscope for signal recording in this stage of development for several reasons. First, the analog nature of the receiver design meant that signal inspection during early testing benefited from the real-time, wide-band visibility provided by the oscilloscope. This allowed immediate observation of transient behaviour, gain stability, and any artefacts introduced by the analog stages. Second, the

oscilloscope's direct voltage readout made it easier to assess signal amplitude and verify linearity across the frequency response of the receiver. The Keysight DSOX1204G offers a sample rate of up to 2 GSa/s and a vertical resolution of 8 bits, which were sufficient to capture the low-frequency demodulated envelope of the test signals with high temporal precision. Once the analog front-end was validated, signal acquisition using the SDRlab board would be considered for future integration and automation.

Since NMR signals are inherently weak, an attenuation stage was introduced to replicate realistic input conditions. A series of attenuators were used to reduce the input signal by 126 dB before feeding it into the receiver chain. This significant reduction in signal strength approximated the power levels expected in a real NMR experiment, enabling a more accurate assessment of the receiver's sensitivity, noise performance, and overall amplification capabilities.

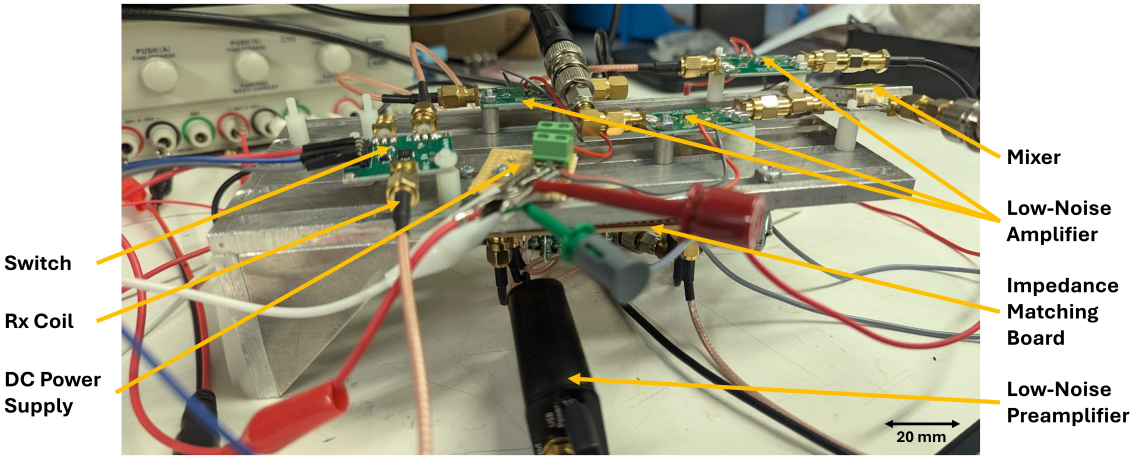

(a)

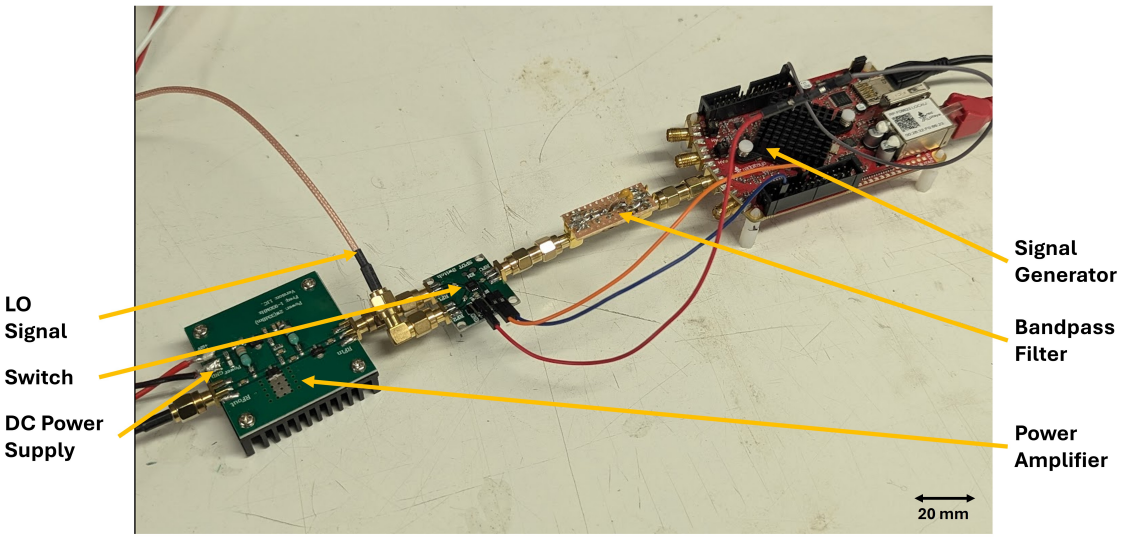

(b)

Figure 4.6: NMR receiver (a) and transmitter (b) chain electronic assembly.

Fig. 4.7b presents the results of our transmitter test, where a 0.5 μs pulse was applied to evaluate the behaviour of the transmitter chain. The pulse exhibits the expected sinusoidal waveform, confirming that the system is generating the desired RF excitation. However, a noticeable overshoot is present at the initial wave cycle, along with minor ringing towards the end of the pulse. The frequency analysis, shown in Fig. 4.7c, highlights a dominant peak at 28.6 MHz, corresponding to the expected excitation frequency. Additional smaller peaks appear due to the finite pulse duration, a natural consequence of the signal being time-limited, which results in spectral broadening. A small DC component is also observed, which appears in the time-domain signal as a slight offset.

During testing, the lowest input from the function generator that could be reliably detected was found to be 400 mV. After passing through the attenuators, this signal was reduced to an effective input level of 45 nV before being fed into the receiver for amplification. This ensured that the system was tested under conditions that closely mimic real-world NMR signal levels, allowing for an accurate assessment of its performance.

Fig. 4.7a shows the results of the receiver chain's amplification. Once again there is the notable observation if low-frequency noise in the output. This signal persisted even when no input was fed into the receiver, indicating that it was not originating from the transmitter or receiver electronics, but rather from the oscilloscope instrumentation.

To mitigate this issue, we introduced a 15 kHz offset between the LO and RF input signals. The excitation pulse was transmitted at 28.6 MHz, while the LO frequency during reception was set to 28.615 MHz. This offset was carefully chosen to minimise interference while maintaining compatibility with the system's filtering and signal processing capabilities. Lower offsets risked placing the signal within the range of power line harmonics and mechanical vibrations, introducing unwanted noise. Conversely, higher offsets would have increased susceptibility to the effects of parasitic capacitances and inductances, which become more pronounced at higher frequencies, leading to deviations from the desired filter response. Additionally, variations in component tolerances could further impact filter characteristics, affecting overall system stability [215]. By selecting 15 kHz, we achieved a balance that optimised signal integrity while minimising noise and distortion.

This frequency offset successfully shifted the detected signal away from the noise source, allowing for cleaner signal extraction. The amplified signal appears at 15 kHz with an approximate amplitude of -33 dB, while the surrounding noise floor is measured at -45 dB, yielding an SNR of 12 dB. This result confirms that the system successfully amplifies low-level signals while maintaining an SNR comparable to the previously calculated ideal value, demonstrating its effectiveness in handling weak NMR signals.

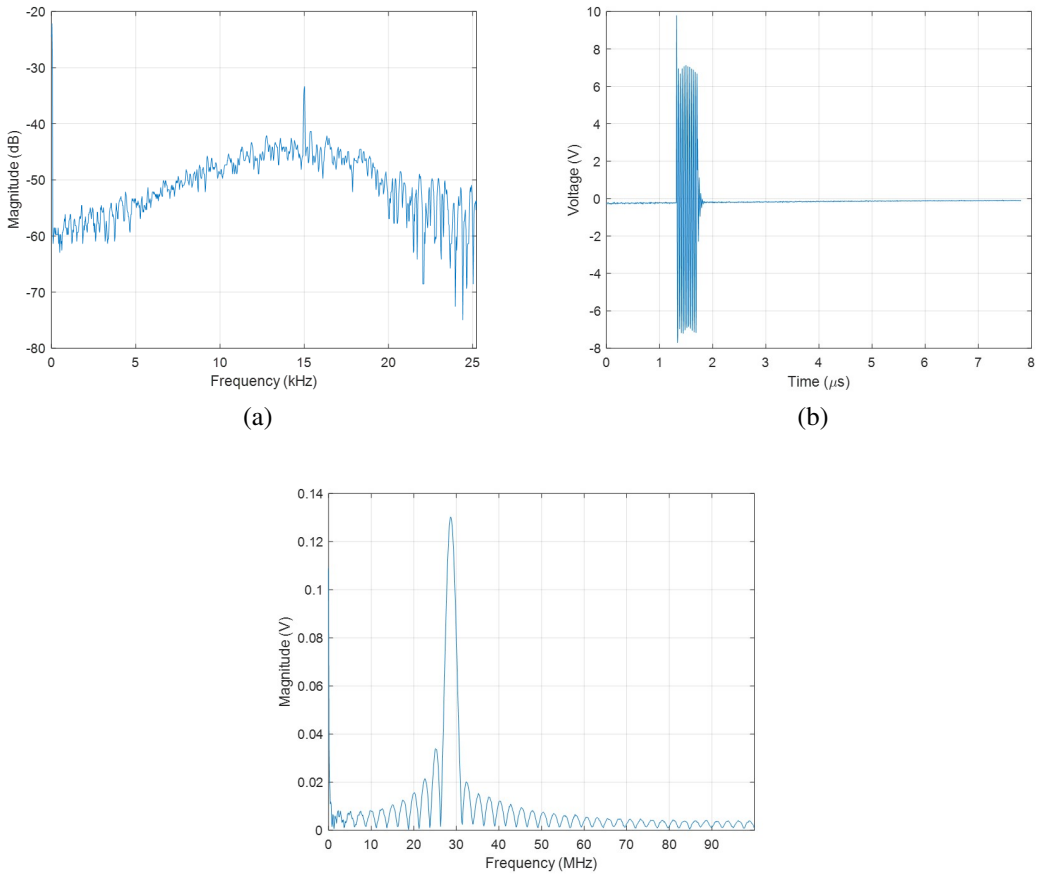

Figure 4.7: (a) Spectrum analysis of low-noise amplification output with 45 nV input. Transmitted NMR pulse in the time (b) and frequency (c) domains.

4.4 NMR Experiments

So far, we have focused on building and testing the individual components of the NMR system, including the electrical system and the performance of the Lenz lens. These steps were critical for validating the functionality of the key building blocks that make up the system. The electrical system was designed to generate and process signals with precision, while the Lenz lens was optimised to enhance sensitivity by efficiently detecting the weak signals emitted by the sample. Each component was carefully evaluated to ensure it met the requirements for signal generation, transmission, and detection.

Having verified the performance of these subsystems independently, the primary objective of these experiments is now to evaluate the performance of the NMR system under realistic conditions and to analyze the characteristics of the signals produced. By testing with various samples, including water and oil, the experiments aimed to assess the system's ability to generate FID signals and provide insight into the signal quality, sensitivity, and overall functionality of the setup. Additionally, these experiments offered an opportunity to identify potential limitations

in the system, such as field inhomogeneities or electronic noise, and to explore avenues for improvement.

4.4.1 Method

(a)

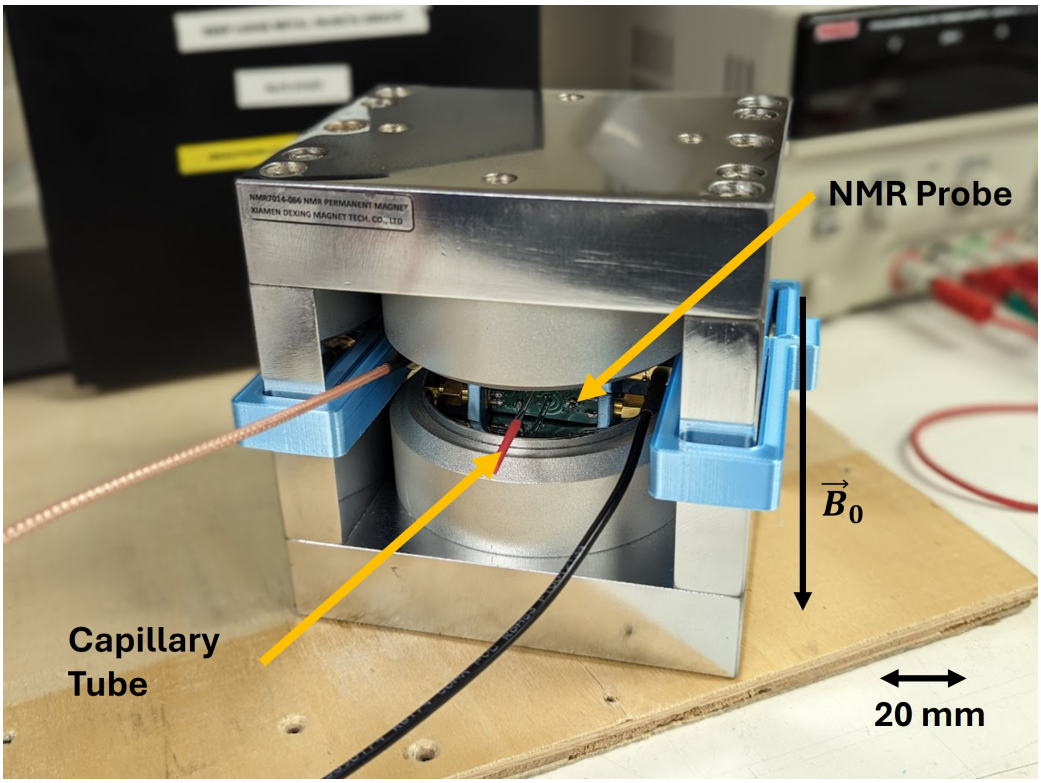

(b)

Figure 4.8: (a) Sealed glass capillary tube. (b) NMR experiment setup.

We tested our NMR system using two samples: deionised water and extra virgin olive oil. Their distinct chemical structures make them well-suited for evaluating the system's capabilities. The samples were contained in glass capillary tubes (Fig. 4.8a) with an outer diameter of 2 mm,

an internal diameter of 1.5 mm, and a length of 100 mm, resulting in a sample volume of 176.7 μL per tube. To prepare the samples, one end of each capillary tube was sealed by heating the glass until it melted and then pinching it closed with tweezers. The tubes were filled using a vacuum-assisted method: a syringe was first filled with the sample, and the open end of the capillary tube was placed against the syringe lip. Pulling back the plunger removed air from the tube, creating a vacuum, and upon releasing the plunger, the pressure difference drew the sample in, ensuring efficient filling without air bubbles. Once filled, the open end was sealed using heat shrink tubing to prevent evaporation and maintain sample stability, minimising potential compositional changes that could affect the NMR measurements.

As seen in Fig. 4.8b, the capillary tubes were positioned at the center of the probe to ensure optimal signal detection. The NMR probe itself was secured in place using a custom 3D-printed structure, designed to ensure that the detection coil was perfectly aligned with the center of the magnetic field. This precise positioning is critical to achieving the strongest and most uniform signal, as even slight deviations from the magnetic field's center can result in reduced sensitivity and increased field inhomogeneities.

The first step of the experiment involved determining the resonant frequency of the system, which is critical for accurately tuning the NMR apparatus to detect the precession of nuclear spins. This was achieved by programming the SG to perform a frequency sweep in small increments of 1000 Hz, covering the range from 28.5 MHz to 29.2 MHz. The chosen sweep range was based on prior estimations of the operating frequency of the system and ensured that the actual resonance frequency would be identified without missing significant peaks.

At each frequency step, a 90-degree RF pulse was applied to excite the nuclear spins, followed by a 1-second delay to allow the spins to relax back to their equilibrium state. This waiting period was sufficient to ensure that any residual magnetisation from the previous pulse had decayed, thereby avoiding overlap or distortion in the subsequent measurements. The systematic and controlled nature of this frequency sweep allowed for precise identification of the resonance frequency by observing the maximum signal amplitude in the acquired NMR response.The resonance frequency for this experimental setup was determined to be 28.621 MHz, reflecting the specific magnetic field strength and sample conditions used in the experiment.

4.4.2 Results

The raw signals received at the oscilloscope, seen in Fig. 4.9, presents the FID signals for tap water (Fig. 4.9a) and olive oil (Fig. 4.9c). In both cases, a sharp spike occurs just after 0.5 ms, marking the transition from excitation to signal acquisition. The signals then undergo a damped oscillation, gradually decaying as transverse relaxation progresses. Notably, instead of oscillating symmetrically around 0 V, both signals exhibit a DC and low-frequency transient that decays alongside the primary oscillation. This indicates that an additional unwanted low-frequency component is present, likely due to residual DC offsets in the system.

The oscillatory behaviour in both signals is the result of the 15 kHz offset introduced between the LO and the RF input, confirming the correct downconversion of the NMR signal. However, differences between the two samples are evident in the decay characteristics. The signal from the water sample reaches an initial peak of 6.5 mV and maintains visible oscillations for approximately 2.5 ms before merging with the noise floor. In contrast, the olive oil sample has a slightly lower peak amplitude of 5.5 mV and decays more rapidly, becoming indistinguishable from noise by 2 ms. This faster decay in oil suggests a shorter T_2^* relaxation time, consistent with its higher viscosity and stronger intermolecular interactions, which accelerate signal dephasing.

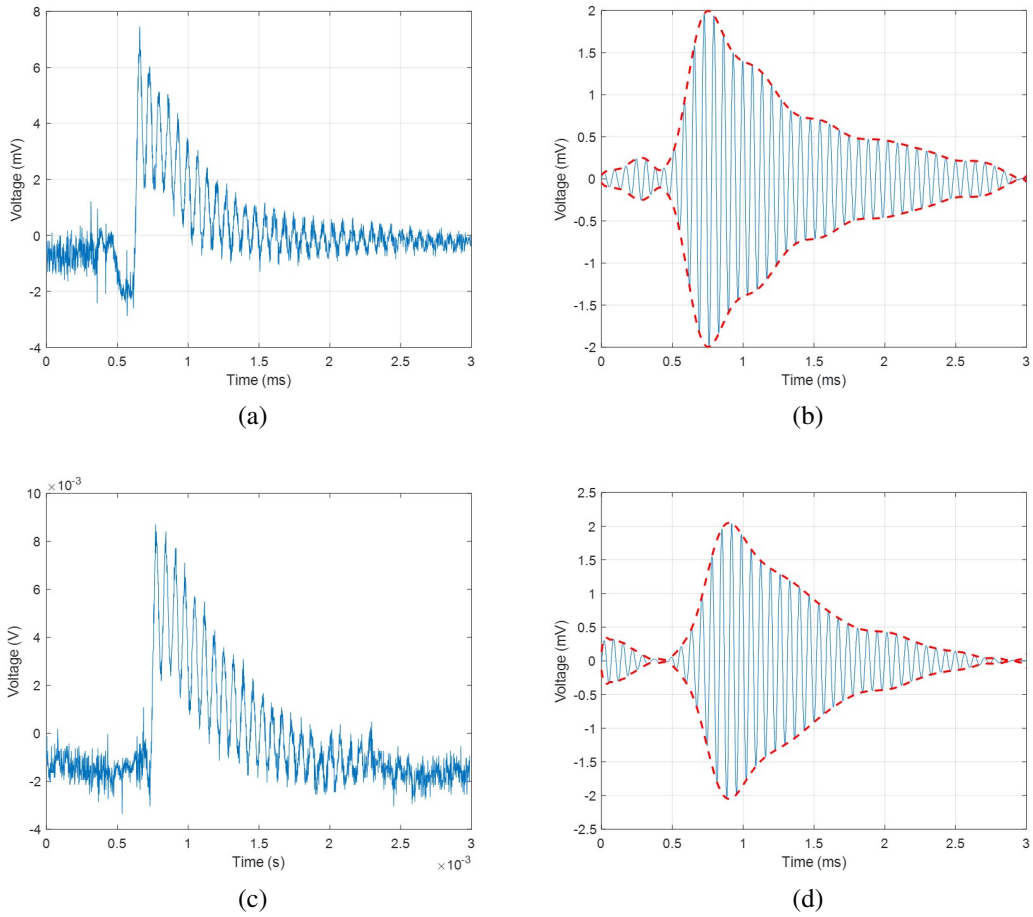

Figure 4.9: NMR time-domain signals from water (a-b) and oil (c-d) samples.

To process the signal, a 4th-order Butterworth bandpass filter was applied to the NMR signal to isolate the frequency components centered around 15 kHz while attenuating unwanted lower and higher frequencies. The filter was designed with a ± 2.5 kHz bandwidth, ensuring that only the relevant spectral content was preserved for further analysis. The Butterworth filter was selected for its maximally flat frequency response, which minimises passband distortions while effectively suppressing out-of-band noise.

Figures 4.9b and 4.9d illustrate the improvements in signal clarity and quality after filtering.

The removal of unwanted low-frequency components allows for a clearer view of the damped oscillation, making it easier to analyze signal decay characteristics. The red envelope overlaid on the filtered signals highlights the expected exponential decay of the FID, a fundamental feature of NMR signals that reflects transverse relaxation processes. The smooth decay envelope further confirms that the filtering process has preserved the intrinsic relaxation dynamics of the signals while removing extraneous noise.

We finally transformed the time-domain signal into the frequency domain creating a spectrum which showed a single broad peak for both the water (Fig. 4.10b) and oil (Fig. 4.10d). The frequency of the peaks for water and oil samples were 14641.12 Hz and 14539.44 Hz, which is close to the 15 kHz we were expecting.The low-frequency signal observed during the receiver chain tests is also present in the measurement data, as shown in the graph. From this spectrum, we can calculate the T_2^* values by measuring the full-width half-maximum (FWHM) of the resonance peak and using that value in the equation:

$$T_2^* = \frac{1}{\pi \cdot \Delta f_{\text{FWHM}}} \tag{4.5}$$

In high-field NMR systems with excellent magnetic field homogeneity, the T_2 of pure water at room temperature is typically reported to be around 3.6 seconds [216]. This value reflects the intrinsic relaxation behaviour of water under ideal conditions, where dephasing due to field variation is minimal. In contrast, the T_2^* value measured in this study for distilled water was 0.489 milliseconds, a value that is several orders of magnitude shorter. This discrepancy is primarily due to inhomogeneities in the B_0 field inherent to the permanent magnet used, which significantly accelerate dephasing and dominate the observed signal decay.

Similarly, literature values for olive oil report T_2 times in the range of 50 milliseconds when measured at low- field strengths such as 2 MHz and 100 MHz [217]. These values are consistent with the relatively restricted molecular motion in viscous oils and represent the intrinsic spin–spin relaxation under field-stable conditions. In our case, the measured T_2^* for the oil sample was 0.412 milliseconds, again much shorter than expected based on literature. The shortened T_2^* reflects the same limitations encountered in the water sample: poor field homogeneity, absence of active shimming, and the use of a single-pulse acquisition scheme. These conditions result in broadened spectral lines and faster signal decay, dominated by extrinsic dephasing effects.

These comparisons make it clear that the T_2^* values obtained here cannot be interpreted as reliable indicators of the samples' intrinsic relaxation times. A more accurate determination of T_2 would require the use of pulse sequences such as CPMG sequence, which refocuses dephasing effects caused by spatial field variation. Although such measurements were not performed in this study, they would be necessary for any future work involving quantitative comparison of sample relaxation properties.

The frequency-domain spectra confirmed the system's ability to detect the Larmor frequen-

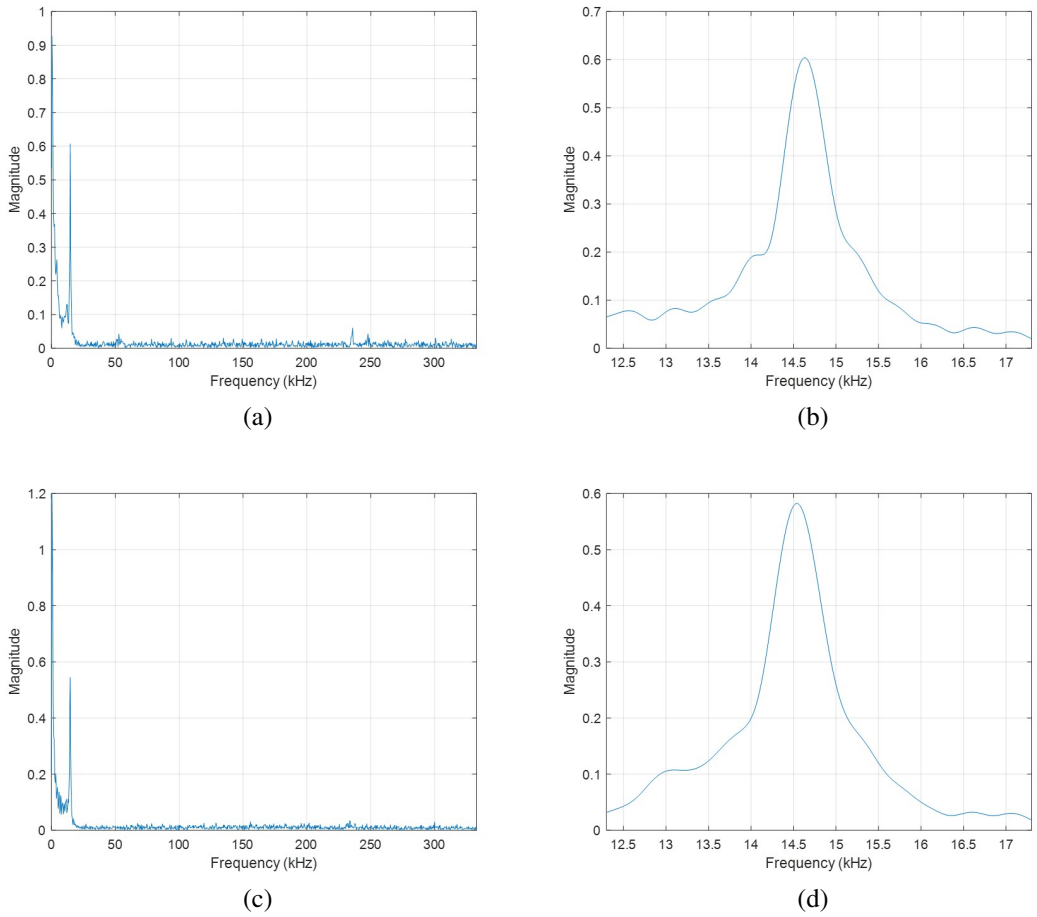

Figure 4.10: NMR frequency-domain spectrum from samples water (a-b) and oil (c-d) samples.

cies of the samples. However, the broad linewidths observed in the spectra, particularly for the oil sample, indicate the effects of magnetic field inhomogeneities and system noise. These broad linewidths reduce the spectral resolution, making it difficult to resolve the oil sample into its individual chemical groups.

Spin sensitivity in NMR quantifies the minimum number of nuclear spins required to produce a detectable signal within a given measurement bandwidth. It is a critical parameter for assessing the system's ability to detect weak signals, particularly in low-concentration samples. The spin and concentration sensitivity of the NMR system were determined based on the detected FID signal from the water sample contained in a capillary tube with an outer diameter of 2 mm, an internal diameter of 1.5 mm, and an effective length of 1 mm within the detection coil. The sample volume was recalculated as $1.77\,\mu$L.

The spin and concentration sensitivity of the system are given by

$$S_{\text{spin}} = \frac{C_H \cdot N_A \cdot V}{SNR \cdot \sqrt{\Delta f}} \tag{4.6}$$

$$S_{\text{conc}} = \frac{C_H \cdot N_A}{SNR \cdot \sqrt{\Delta f}} \tag{4.7}$$

where $C_H = 1.1 \times 10^5$ mol/m^3 is the molar density of nuclear spins, N_A is Avogadro's number (6.022×10^{23} spins/mol), and V is the sample volume = 1.77×10^{-9} m^3. The bandwidth is related to the spectrometer's sampling frequency $f_s = 666$ kHz, leading to an effective acquisition bandwidth of $\Delta f = f_s/2 = 333$ kHz. Since noise scales with the square root of bandwidth, the sensitivity equations normalise the spin detection limit per unit frequency. The spin sensitivity describes the minimum number of spins required to achieve an SNR of 1 per unit bandwidth, whereas the concentration sensitivity expresses this limit in terms of detectable molar concentration. Unlike spin sensitivity, which depends on sample volume, concentration sensitivity remains independent of volume but varies with the nuclear spin density of the medium. Using these definitions, the spin sensitivity was calculated as 5.07×10^{15} spins/$\sqrt{\text{Hz}}$, and the concentration sensitivity was determined to be 4.77 M/$\sqrt{\text{Hz}}$.

The spin and concentration sensitivity values presented in this study are specific to the measurements performed using distilled water, which was selected due to its high proton density, and well-characterised relaxation properties. While these results provide a useful benchmark for assessing the system's performance, they cannot be directly generalised to all samples containing hydrogen-1 nuclei. Sensitivity depends on several factors including proton concentration, relaxation times, and magnetic susceptibility, all of which vary across different substances. For example, biological fluids or organic solvents may have shorter transverse relaxation times or lower proton densities, both of which would influence the observed signal and thus the calculated sensitivity. Therefore, sensitivity measurements would need to be repeated for each new sample type to ensure accuracy under practical conditions.

4.4.3 Discussion

The system demonstrates significant promise as a pathway toward creating more accessible and cost-effective NMR systems, addressing the high costs and complexity associated with traditional setups. However, the current version of the system has limitations that must be addressed to achieve performance levels comparable to commercial NMR systems, particularly in performing reliable and precise spectrometry experiments. One major limitation observed was the rapid decay of the NMR signal. While the water sample exhibited a slower decay than the oil sample, both decayed significantly faster than expected. Typically, water samples maintain coherence for several seconds, whereas in our case, the signal lasted only 0.489 ms. This accelerated decay is likely due to magnetic field inhomogeneities inherent to the magnet, as well as those introduced by the PCB design and the use of a glass capillary tube. These inhomogeneities disrupt the coherence of the precessing spins, leading to faster signal dephasing and reduced T_2^* times. To mitigate this issue, a robust shimming mechanism is necessary to correct for magnetic field

imperfections and ensure more uniform resonance conditions across the sample volume. Implementing active or passive shimming techniques could help compensate for these variations, improving signal longevity and overall spectral resolution.

Additionally, the presence of sharp peaks in the acquired signal indicates a high level of noise, which affects the overall SNR and, consequently, the quality of the spectrometry data. This noise can be attributed to several factors, including electronic interference, environmental noise, and insufficient isolation of the system. Improvements can be achieved by averaging multiple acquisitions to enhance the SNR through noise reduction. Furthermore, implementing a shielded enclosure around the system would help minimise external electromagnetic interference, further improving signal clarity.

Beyond these immediate enhancements, other areas for improvement include refining the probe design to better match the sample's physical and magnetic properties, optimising the electronic circuitry to reduce signal distortion, and using higher-quality materials to reduce localised magnetic field distortions. These steps, combined with an iterative development approach, would move the system closer to the standards of commercial NMR platforms.

Despite these challenges, the current system provides a valuable proof-of-concept for a more accessible and modular approach to NMR system design. It lays the groundwork for applications in educational environments, low-resource laboratories, and emerging fields such as metabolomics, where affordability and simplicity are critical. As the system evolves, it has the potential to unlock NMR's analytical capabilities for a broader range of users and use cases, democratising access to this powerful technology.

A comparison of various low-cost NMR systems reveals significant differences in design choices, power efficiency, signal quality, and functional integration. Table 4.4 summarises key parameters across different implementations, highlighting the strengths and limitations of each system relative to the one presented in this work.

One of the most notable advantages of the present design is its exceptional power efficiency. While some systems, such as [219], require up to 4 kW of power, and others like [218] operate at 170 W, the system presented in this work achieves comparable functionality with only 0.5 W of power consumption. This dramatic reduction in power requirements is particularly advantageous for portability and integration into point-of-care and mobile diagnostic applications, where energy efficiency is a critical constraint.

Despite its lower power consumption, the system maintains an SNR of 16 dB, which is competitive given the power constraints. When evaluated in terms of SNR efficiency (dB/W), this design achieves 32 dB/W—an order of magnitude improvement over most existing systems. This efficiency ensures optimal signal quality without excessive power consumption, making the system well-suited for battery-operated or resource-limited applications.

The operating frequency of the system places it within a range suitable for a broad set of applications while maintaining compatibility with permanent magnets that provide moderate

Table 4.4: Comparison of Low-Cost NMR Systems. Tx: transmit, RX: receiver. Eff.: Efficiency

Parameter	[218]	[219]	[220]	[221]	[222]	[223]	This Work
Processor	STM32F745	LimeSDR	Altera Cyclone II	Teensy 4.1	NI PCIe-6363	Altera Cyclone V	Xilinx Zynq 7010
System Power (W)	170	4000	1	-	6.5	2.5/10.6	0.5
SNR (dB)	27	20	-	-	7.4	24.9	16
SNR Eff. (dB/W)	0.159	0.005	-	-	1.14	12.45/2.49	32
Frequency (MHz)	1–125 kHz	30 MHz	400 MHz	100 kHz	25 kHz	3.5–4.5 MHz	28-29.2 MHz
Magnetic Field (T)	3.6-3.9 mT	0.7 T	9.4 T	100 μT	0.6–3.5 mT	0.101 T	0.67 T
Tx Amplification	Yes	No	No	Yes	Yes	Yes	Yes
Rx Amplification	Yes	No	No	No	Yes	Yes	Yes
Mixing	No	Yes	Yes	No	Yes	Yes	Yes
Filtering	No	Yes	Yes	No	Yes	Yes	Yes
Switching	Yes	No	Yes	Yes	Yes	Yes	Yes

field strengths. In contrast, systems such as [220], which operates at 400 MHz, require a 9.4 T superconducting magnet, making them less practical for portable or cost-sensitive applications. Conversely, lower-frequency systems such as [218] and [222] operate in much weaker fields, limiting their resolution and overall applicability. By balancing frequency range, field strength compatibility, and power efficiency, this work offers a versatile and practical NMR solution.

Unlike previous designs that rely on discrete or less integrated solutions, this work leverages the Xilinx Zynq 7010, a system-on-chip (SoC) solution that integrates both FPGA and ARM processing capabilities. This choice enables real-time digital signal processing and flexible software-defined control, offering greater computational power and adaptability than alternatives such as the STM32F745 [218] and Teensy 4.1 [221], which are more limited in processing capability and flexibility.

In terms of RF front-end design, this system incorporates transmit and receive amplification, mixing, filtering, and switching, ensuring that all essential signal processing components are fully integrated. Many competing designs lack one or more of these critical elements. For example, [219] omits both amplification stages, while [220] lacks Rx amplification. The ability to handle all signal processing within a compact and modular architecture enhances the versatility of this system, making it more robust and adaptable for various NMR applications.

This work presents a system optimised for low power consumption, high SNR efficiency, and full integration of key RF functionalities, making it a strong candidate for practical and scalable applications. Unlike power-intensive or limited-functionality alternatives, this design enables a fully operational, low-cost NMR platform that balances performance, efficiency, and usability. Additionally, the modular architecture ensures that individual components can be easily replaced or upgraded, enhancing system adaptability and long-term flexibility.

4.5 Conclusion

In this chapter, we designed, assembled, and characterised the electronics required to support our NMR system. By working backwards from the known performance of our NMR probe, we determined the necessary specifications for each component, ensuring that the system achieved both high sensitivity and low cost. A modular design approach was adopted to enhance reproducibility and accessibility, allowing the system to be constructed from commercially available components.

Impedance matching was a critical aspect of the design, as efficient power transfer between modules is essential for minimising signal loss. Through careful analysis using Smith charts and *S*-parameter measurements, we identified the required matching networks and validated their performance through Monte Carlo simulations. The implemented matching circuits successfully maintained a return loss below -10 dB across the target frequency range of 28 to 29.2 MHz.

The transmitter chain was tested by generating a 0.5 μs RF pulse to evaluate the perfor-

mance of the power amplifier and overall signal transmission. The pulse exhibited the expected sinusoidal behavior, confirming that the system was producing the correct excitation signal. However, minor overshoot and ringing were observed, indicating transient effects likely due to amplifier response time or small impedance mismatches. Frequency analysis showed a dominant peak at 28.6 MHz, with smaller spectral components resulting from the finite pulse duration. A small DC offset was also detected, suggesting potential for further optimisation in filtering and biasing.

The receiver chain was tested using a simulated NMR signal to evaluate its ability to amplify weak inputs while maintaining signal integrity. Through controlled attenuation, input signals were reduced to levels comparable to real-world NMR experiments, allowing for a realistic assessment of system performance. The results confirmed that the receiver chain could detect and amplify signals as low as 45 nV while maintaining an SNR of 12 dB.

One challenge encountered during testing was the presence of low-frequency noise, which was effectively mitigated by introducing a 15 kHz offset between the transmitted and local oscillator frequencies. Additionally, a residual DC component was observed despite the use of DC-blocking networks, highlighting a potential area for further refinement.

Overall, the results demonstrate that the system meets the design requirements and is capable of handling the weak signals inherent to NMR experiments. The modular approach ensures flexibility and scalability, making the system adaptable to different experimental conditions. Moving forward, further improvements in signal stability, transient response, and noise reduction could enhance overall performance, paving the way for more robust and reproducible NMR measurements.

The experiments conducted validated the NMR system's ability to generate, acquire, and process free induction decay signals, confirming its fundamental functionality. By testing with both water and oil samples, we successfully demonstrated the system's capability to differentiate between materials based on their transverse relaxation properties. The distinct decay characteristics observed in the two samples aligned with their expected molecular dynamics, reinforcing the accuracy of the measurements. Additionally, the results confirmed that the system's resonance frequency was correctly identified and that the applied downconversion scheme functioned as intended, enabling clear signal detection in both the time and frequency domains.

Analysis of the NMR spectrum provided further quantitative insight into the system's performance. The frequency-domain spectra for both samples exhibited broad peaks, with full-width half-maximum values of 650.72 Hz for water and 772.73 Hz for oil. These values correspond to T_2^* relaxation times of 0.489 ms and 0.412 ms, respectively. The broader linewidth observed in the oil sample is consistent with its higher viscosity and stronger intermolecular interactions, which accelerate signal dephasing. However, the relatively large linewidths in both samples suggest that magnetic field inhomogeneities are significantly impacting spectral resolution. Addressing these inhomogeneities, potentially through improved magnet calibration or passive field

stabilisation techniques, could lead to sharper spectral peaks and more precise measurements.

The system's spin sensitivity was calculated as 5.07×10^{15} spins$/\sqrt{\text{Hz}}$, while the concentration sensitivity was determined to be 4.77 M$/\sqrt{\text{Hz}}$. These results indicate that the system is capable of detecting weak signals, though improvements in signal-to-noise ratio would further enhance its detection capabilities. The presence of low-frequency artifacts in the acquired signals, despite filtering, suggests residual DC offsets or noise sources within the receiver chain. Additional improvements, such as enhanced shielding, better grounding, and refined filtering techniques, could further increase signal clarity and reduce these unwanted signal components.

Despite these challenges, the system demonstrated significant advantages compared to existing low-cost NMR platforms. The power consumption of only 0.5 W, coupled with an SNR efficiency of 32 dB/W, highlights the system's strong performance with minimal energy requirements. This efficiency makes the system particularly well-suited for portable and resource-constrained applications, such as point-of-care diagnostics or remote sensing. Additionally, the modular architecture allows for incremental improvements in individual components, ensuring flexibility in future development.

While this work successfully demonstrates a low cost, modular NMR system with promising sensitivity for small volume samples, several technical limitations must be resolved before the system can be deployed for diagnostic purposes. Notably, discrepancies between simulated and measured results, particularly in impedance matching and magnetic field distribution, highlight the need for improved modeling and tighter control over fabrication tolerances. These mismatches affected both the signal uniformity and the power transfer efficiency, which in turn influence the quality of the acquired NMR signals. Additionally, the spectral resolution achieved is not yet sufficient for the detailed metabolic profiling required in real diagnostic scenarios. Narrower linewidths and reduced field inhomogeneities will be essential in order to resolve small chemical shifts and subtle biomarker differences, especially in early stage disease detection.

This limitation is particularly important given the system's intended application in detecting early signs of prostate cancer through metabolite profiling. While this work lays the groundwork by demonstrating detection capabilities in microlitre scale samples, the current signal quality and resolution are insufficient to distinguish diagnostically relevant compounds in complex biological fluids. Furthermore, while Lenz lenses were investigated as a method of passive signal enhancement, they may not offer the optimal tradeoff between amplification and homogeneity. Future iterations of the system should explore other strategies for improving sensitivity, such as cryogen free hyperpolarization techniques, optimized coil geometries, or active electronic amplification at the probe level. These refinements will be crucial to transforming this proof of concept system into a reliable diagnostic tool capable of supporting clinical workflows.

Chapter 5

Conclusion & Future Work

Conclusion

This thesis presented the design, development, and validation of a modular, low-cost NMR system specifically tailored for metabolomics applications. Metabolomics requires highly sensitive detection methods to analyze complex biochemical mixtures, making NMR an ideal technique due to its ability to provide quantitative and non-destructive molecular profiling. However, traditional NMR systems are often expensive, complex, and inaccessible to many research groups. This work aimed to address these challenges by developing an affordable and modular NMR platform that maintains high sensitivity while being adaptable to different metabolomic applications.

A key component of this work was the design of a high-sensitivity NMR probe that maximised signal detection while remaining cost-effective. The probe incorporated a Lenz lens to enhance magnetic flux concentration, improving sensitivity without increasing power consumption. The design process began with the integration of the LL with the primary coil on a single flat substrate, ensuring precise alignment and streamlined fabrication. The receiver circuit was carefully developed with impedance matching networks to optimise power transfer, employing a π-match network to transform the coil's impedance to 50 Ω while filtering out higher-order harmonics. Simulations using CST Studio Suite confirmed significant improvements in magnetic field strength and power transfer efficiency, with the LL increasing the magnetic flux density in the focusing region by a factor of 9.09. The S21 parameter showed an improvement of 25.925 dB with the LL, indicating enhanced power transfer and reduced signal reflection compared to setups without the lens. Experimental validation demonstrated that incorporating the LL increased the detected power from -18.854 dBm (0.0130 mW) to -2.770 dBm (0.528 mW), representing over a 40-fold amplification of received power.

In the second iteration of the design, fabrication limitations were addressed by outsourcing PCB manufacturing, allowing for greater precision and consistency. The transition from in-house techniques to a multi-layer PCB layout enabled the integration of the transmitter coil and

LL onto a single PCB, eliminating alignment issues and simplifying both design and assembly. To further enhance system performance, the coil geometry was refined by shifting from a square spiral to a round spiral transmitter coil, which provided a more uniform magnetic field. In contrast to the first iteration, which prioritised signal amplification, the second design focused on improving field uniformity. This led to a 3.8-fold enhancement in magnetic field homogeneity, reducing spatial variation from 140 ppm to 36.7 ppm within the central detection region. This improvement, however, came with a trade-off in peak signal strength. The second probe generated a maximum field of 0.724 mT, lower than the 1.92 mT produced by the coil-only setup. Nevertheless, the second design offered a more stable and uniform field distribution, which is essential for preserving signal quality in practical NMR measurements.

By working backwards from the probe's known performance, the necessary specifications for each component were determined to achieve both high sensitivity and low cost. A modular design approach was adopted, enabling reproducibility and accessibility by utilising commercially available components.

By systematically working backwards from the known performance requirements of the NMR probe, we established the necessary specifications for each electronic component, ensuring efficient power transfer, optimised signal amplification, and overall system reliability. Our focus was placed on using commercially available modules to enhance reproducibility, reduce fabrication complexity, and lower the barriers to adoption for researchers and engineers outside specialised NMR laboratories. A key aspect of the design was impedance matching, which was critical for efficient power transfer and minimal signal loss. Smith chart analysis and *S*-parameter measurements guided the development of matching networks, which were validated through Monte Carlo simulations. The implemented circuits successfully maintained a return loss below -10 dB across the operating frequency range of 28 to 29.2 MHz.

The transmitter chain was evaluated by generating a 0.5 μs RF pulse, confirming correct excitation signal generation. While the pulse exhibited the expected sinusoidal behavior, minor overshoot and ringing were observed, indicating transient effects that may require further optimisation. Frequency analysis revealed a dominant peak at 28.6 MHz, with smaller spectral components arising from the finite pulse duration. A small DC offset was also detected, suggesting areas for refinement in filtering and biasing.

The receiver chain was tested with a simulated NMR signal to evaluate its amplification capabilities. Input signals were attenuated to mimic real-world NMR conditions, and the system successfully detected and amplified signals as low as 45 nV while maintaining an SNR of 12 dB. One challenge encountered was the presence of low-frequency noise, which was mitigated by introducing a 15 kHz offset between the transmitted and local oscillator frequencies. Additionally, residual DC components were observed despite the use of DC-blocking networks, highlighting the need for further improvements in signal conditioning.

The system's performance was evaluated through experimental measurements of line width,

transverse relaxation times, and sensitivity for samples of tap water and grocery store olive oil. For the water sample, the FWHM of the resonance peak was measured as 650.72 Hz, yielding a T_2^* value of 0.489 ms. The oil sample exhibited a broader FWHM of 772.73 Hz, resulting in a shorter T_2^* of 0.412 ms, consistent with the expected differences in molecular mobility and dipole-dipole interactions between the two samples. These results align with the fact that water has a longer T_2^* due to its faster molecular motion and weaker intermolecular interactions, whereas the increased viscosity of oil restricts molecular motion, leading to faster dephasing and a shorter T_2^*.

Sensitivity analysis further demonstrated the system's ability to detect weak NMR signals. The spin sensitivity was determined to be 5.07×10^{15} spins/$\sqrt{\text{Hz}}$, while the concentration sensitivity was measured at 4.77 mM/$\sqrt{\text{Hz}}$. These values indicate that the system is capable of detecting nuclear spins at practical acquisition bandwidths, highlighting its potential for applications requiring low-concentration sample detection. Although improvements can still be made to further enhance sensitivity and reduce noise, these results validate the system's effectiveness in capturing and analysing weak NMR signals in a cost-effective and modular design.

This work demonstrates that a modular, low-cost approach to NMR system design is not only feasible but also provides a practical path toward making NMR technology more accessible for metabolomics research. By leveraging commercially available components and simplifying system assembly, this approach reduces the complexity of traditional NMR hardware while maintaining competitive performance. Future work could focus on further improving noise rejection, enhancing automation and control through software integration, and expanding the system's adaptability to different field strengths and sample types. With continued refinement, this modular framework has the potential to lower the entry barriers to NMR-based metabolomics, facilitating broader adoption in biomedical research, clinical diagnostics, and industrial applications.

Future Work

While the current NMR system demonstrates significant potential as a cost-effective and accessible alternative to traditional setups, several areas require further development to improve performance, enhance reliability, and expand its capabilities. These improvements will focus on addressing the fundamental limitations of the current design and optimising the system for broader applications.

A primary focus for future work will be addressing magnetic field inhomogeneities, which significantly affect the accuracy and reliability of the NMR signal. The current system lacks a robust mechanism to ensure field uniformity, leading to broadened spectral lines and rapid signal decay. This limits the spectral resolution of the system, which is currently on the order of several hundred hertz, far from the sub-hertz resolution required to distinguish narrow spectral features

in complex samples. Improving spectral resolution will require both enhanced field homogeneity and reduced susceptibility to external perturbations. Introducing shimming, particularly active shimming, would allow for dynamic correction of magnetic field variations across the sample volume, enabling more uniform precession and sharper spectral peaks.

In addition to inhomogeneity, field drift presents another significant challenge in systems that use portable permanent magnets. Even small variations in the field over time can shift the resonance frequency during data acquisition, making it difficult to coherently average multiple scans. This is particularly problematic in low-field systems where the SNR is inherently low and signal averaging is essential to extract usable data. Without field stability, the accumulated signal averages destructively, negating the benefits of extended acquisition. Bridging this gap will require the integration of drift compensation mechanisms, either through temperature regulation of the magnet or real-time frequency tracking and correction during acquisition. Addressing both field homogeneity and drift will be essential for advancing this platform toward high-resolution, quantitative NMR measurements in small volumes.

Noise reduction remains a significant challenge in the current system, directly impacting the SNR and the clarity of the NMR output. Future iterations of the system will incorporate a shielded enclosure to minimise electromagnetic interference from external sources. This shielding will be essential for isolating the sensitive NMR electronics from environmental noise, especially in low-resource or shared laboratory environments. Additionally, the integration of higher-quality components, such as low-noise amplifiers and more precise analog-to-digital converters, will be explored to further reduce noise. Signal averaging techniques, which combine multiple acquisitions to enhance SNR, will also be a key area of investigation, particularly for applications involving weak signals or low-concentration samples.

The current system relies on multiple discrete components, which introduces inefficiencies and potential sources of signal distortion. A key step in future development will involve integrating these components into a PCB. This integration will streamline the system, reduce signal loss due to interconnects, and improve overall performance. Moreover, integrating all essential elements into a single PCB will enhance the system's robustness and make it more suitable for deployment in various environments.

Addressing the differences in magnetic permeability between the PCB, glass tube, and magnet will also be crucial for minimising field distortions and improving signal uniformity. Developing a method to match these differences, either through material selection or structural design, will help ensure that the magnetic environment within the sample region remains consistent. Such improvements could involve using specialised coatings, engineered materials, or adjustments to the probe design to better align the magnetic properties of the various components.

Refining the probe design remains a critical area of focus. While this work investigated the use of Lenz lenses to enhance magnetic flux concentration and signal pickup, the results showed

that this approach does not offer a universally optimal solution. Although some configurations improved field homogeneity, others introduced signal loss or inconsistent amplification, suggesting that passive magnetic focusing through Lenz lenses may not scale effectively across all applications. Future work should therefore explore alternative strategies, such as reconfigurable coil geometries, active amplification circuits placed closer to the detection region, or novel resonator structures that balance field uniformity and signal strength. Additionally, optimising the physical geometry of the probe to reduce field distortions and improve signal consistency remains essential. Exploring different construction materials with low magnetic susceptibility and high thermal stability could also help minimise inhomogeneities caused by susceptibility mismatches. Together, these improvements would enhance signal quality, increase experimental reproducibility, and push the system closer to meeting the demands of reliable clinical diagnostics.

Beyond addressing these technical challenges, future work will also focus on expanding the system's application space. For instance, incorporating advanced pulse sequences and enabling multi-dimensional NMR experiments would extend its utility for more complex analyses. The system's modular design philosophy makes it well-suited for these upgrades, allowing for the addition of new functionalities without significant redesign.

Finally, validation of the system in real-world scenarios will be a key step. This includes testing the device with a wider variety of samples and benchmarking its performance against commercially available NMR systems. Collaborations with external laboratories and researchers could provide valuable insights into the system's performance and guide its refinement for specific use cases. These efforts will not only improve the system's reliability but also establish its potential for broader adoption in educational, research, and clinical settings. By addressing these areas, the system can evolve into a versatile, robust platform capable of meeting the demands of modern NMR applications while maintaining its focus on affordability and accessibility.

Chapter 6

Appendix

6.1 Appendix A: NMR Signal Theoretical Analysis

6.1.1 Introduction and NMR Spectroscopy

The goal of this section is to derive the expressions for the RMS NMR signal and RMS noise, which are critical parameters for evaluating the sensitivity of the NMR receiver. These derivations will provide a foundation for understanding how different system parameters influence the signal quality and noise characteristics. This analysis is based on the fundamental principles of NMR signal generation and the relationship between the sample's magnetisation and the magnetic field of the detection coil, as derived by Hoult and Richards [224].

In addition to studying the FID time-domain characteristics, the Fourier Transform can be applied signal to a one-dimensional NMR frequency spectrum [160] . This spectrum consists of a series of peaks, each corresponding to specific resonance frequencies of the nuclei in the sample. Interpreting this spectrum provides a wealth of information about the molecular structure, including details on the types and quantities of nuclei present, their chemical environments, and their spatial relationships with neighboring atoms.

Chemical Shifts and Molecular Environment

One of the most fundamental aspects of an NMR spectrum is the chemical shift, which is indicated by the position of each peak along the horizontal axis of the spectrum. Chemical shift values are measured in parts per million (ppm) and are relative to a standard reference compound, such as tetramethylsilane (TMS) in ^{1}H and ^{13}C NMR. TMS is chosen as a reference because its protons and carbons are highly shielded and typically produce a signal at 0 ppm, serving as a baseline for comparison [225].

Chemical shifts provide insights into the local electronic environment surrounding each nucleus. The exact position of each peak on the ppm scale reflects how "shielded" or "deshielded" a nucleus is by surrounding electrons:

- **Shielded Nuclei**: Nuclei surrounded by higher electron density experience a reduced effective magnetic field because the electrons produce a counteracting local magnetic field. This shielding effect reduces the Larmor frequency and moves the resonance signal upfield, or to lower ppm values. For example, protons in nonpolar environments, such as in methyl ($-CH_3$) or methylene ($-CH_2$) groups, tend to be more shielded and exhibit chemical shifts in the range of 0-3 ppm in ^{1}H NMR [226].

- **Deshielded Nuclei**: Nuclei near electronegative atoms (such as oxygen, nitrogen, or halogens) or in electron-poor environments experience less shielding, resulting in a higher effective magnetic field at the nucleus. This deshielding effect increases the Larmor frequency and shifts the resonance signal downfield, or to higher ppm values. For instance, protons attached to carbons adjacent to electronegative atoms typically show shifts in the range of 3-5 ppm, while protons in aldehydes can appear as far downfield as 9-10 ppm [226].

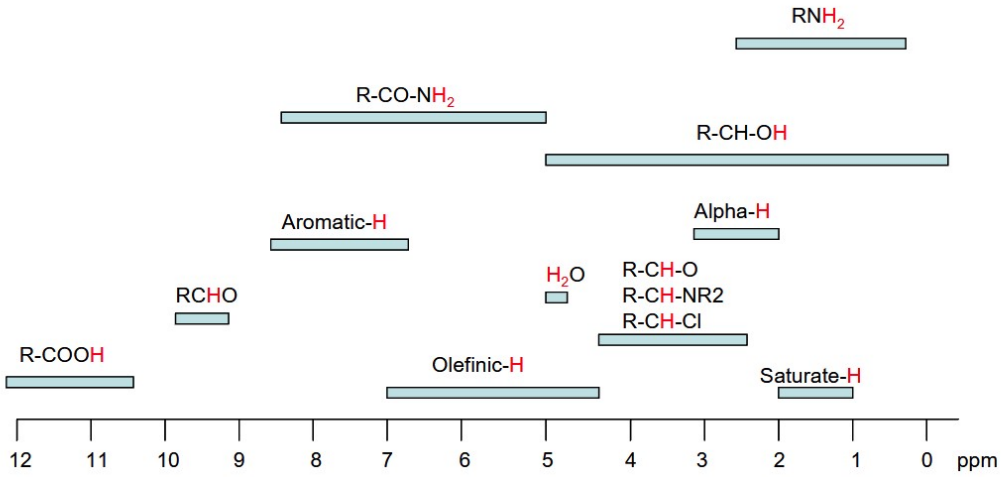

Figure 6.1: Chemical shifts of different groups in ^{1}H NMR [227].

Chemical shifts are invaluable for identifying functional groups and assessing the electronic characteristics of the sample. By comparing observed chemical shifts to known values in reference tables, researchers can identify specific chemical environments, infer the presence of functional groups, and distinguish between different molecular regions.

Spin-Spin Coupling and Peak Splitting

Another defining feature of NMR spectra is spin-spin coupling, or J-coupling, which results in the splitting of peaks into multiplets. Spin-spin coupling occurs when magnetic nuclei are close enough that the spin state of one nucleus affects the local magnetic field experienced by a neighboring nucleus. This interaction creates additional sub-levels in the energy states of the nuclei, leading to the splitting of each resonance signal [228].

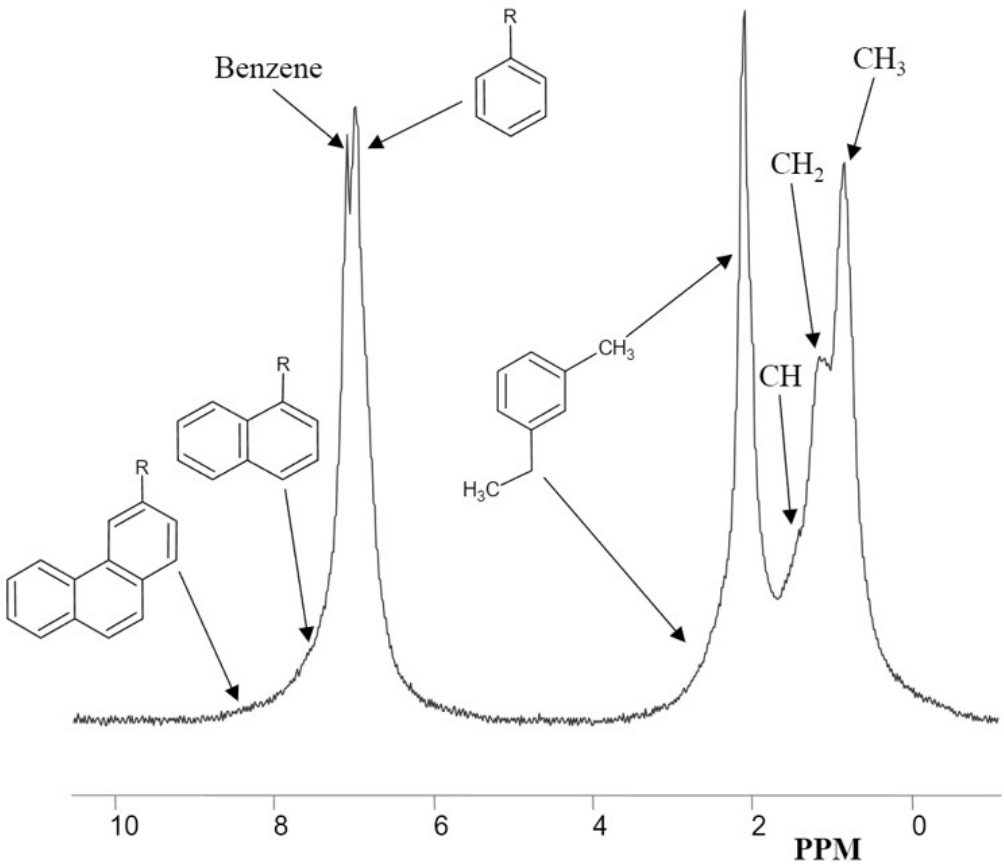

Figure 6.2: ^{1}H NMR spectrum of Reformate revealing peaks associated with different groups [227].

The coupling pattern provides detailed connectivity information, allowing researchers to identify the number and spatial arrangement of neighboring nuclei. In 1D ^{1}H NMR, common splitting patterns include:

- **Doublet**: Indicates one neighboring proton (spin-1/2 nucleus) causing a single split, with an intensity ratio of 1:1.
- **Triplet**: Indicates two equivalent neighboring protons, with an intensity ratio of 1:2:1.
- **Quartet**: Indicates three equivalent neighboring protons, with an intensity ratio of 1:3:3:1.

The spacing between these split peaks is defined by the coupling constant J, measured in Hertz (Hz), which provides information about the strength of the interaction. For example, the coupling constant for protons on adjacent carbons in a simple alkyl chain typically ranges from 6 to 8 Hz [229]. The value of J depends on the bonding and distance between coupled nuclei; larger J-values often indicate stronger coupling or proximity within the molecular structure [230].

The specific coupling pattern reveals the number of neighboring nuclei, making it possible to deduce how atoms are connected within the molecule. For instance, in an ethyl group (-CH_3-CH_2), the -CH_3 protons will appear as a triplet (due to two neighboring -CH_2 protons), while the -CH_2 protons appear as a quartet (due to three neighboring -CH_3 protons). Such coupling patterns are essential for mapping out molecular connectivity, particularly in organic chemistry, where they aid in determining structure and stereochemistry [231].

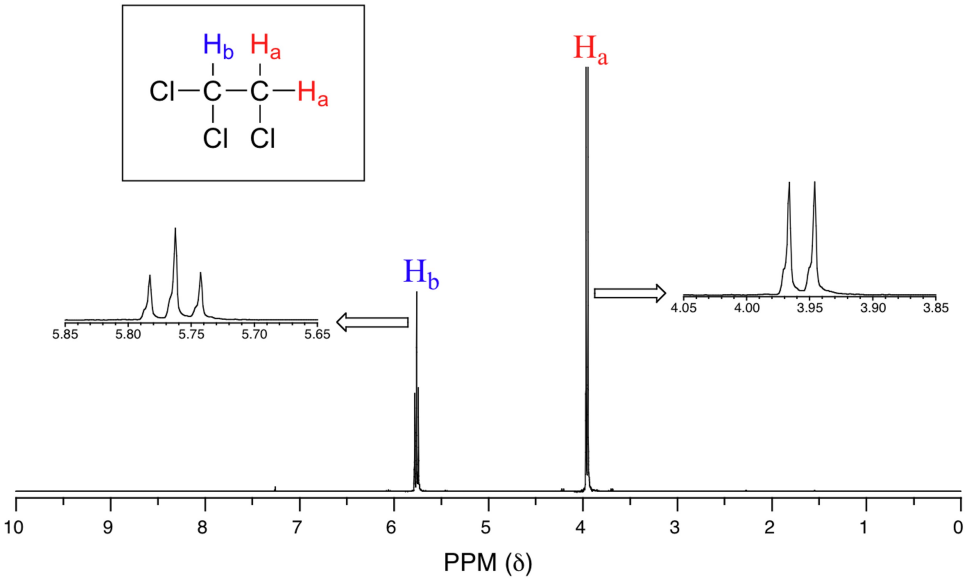

Figure 6.3: Peak splitting in a ^{1}H NMR spectrum of 1,1,2-trichloroethane [232].

Peak Integration and Quantitative Analysis

In a 1D NMR spectrum, each peak's integration (or area under the peak) is directly proportional to the number of equivalent nuclei contributing to that signal [233]. Integration provides quantitative information, particularly in ^{1}H NMR, where the number of protons associated with each peak can be deduced by comparing the relative peak areas.

For example, if a spectrum shows two peaks with integration values in a 3:1 ratio, this suggests that one peak corresponds to a group of three equivalent protons (such as a methyl group, -CH_3), while the other corresponds to a single proton (such as in a methine group, -CH). Integration allows for detailed quantitative analysis, aiding in the confirmation of molecular formulas, relative ratios of different functional groups, and even the purity of the sample [234].

In practice, the spectrometer software calculates and displays integration values as either absolute or relative units [235]. Analysts often use these values to assign specific peaks to known atomic groups within the molecule. For instance, in an unknown organic compound, peaks with integration ratios of 3:2:2:1 might suggest the presence of a methyl group (3 protons), two methylene groups (2 protons each), and a single methine or hydroxyl group (1 proton). This

quantitative aspect of NMR is especially useful in compound verification and purity assessment, as well as in characterising mixtures or unknown compounds.

Interpreting an NMR spectrum involves a synthesis of information from chemical shifts, integration, and coupling patterns to construct a coherent picture of the molecular structure. Analysts often begin by examining the chemical shifts to identify functional groups or specific structural motifs. Integration values then provide quantitative information, verifying the number of nuclei within each environment and confirming molecular ratios. Finally, coupling patterns establish connectivity, enabling researchers to map out atomic arrangements and infer spatial relationships [236]. By combining these aspects, a 1D NMR spectrum can reveal intricate details about a molecule's framework, symmetry, and electronic distribution [237]. The combination of peak positions, intensities, and splitting patterns enables chemists to accurately determine not only the presence of specific functional groups but also their exact arrangement within the molecule, providing a comprehensive view of molecular structure.

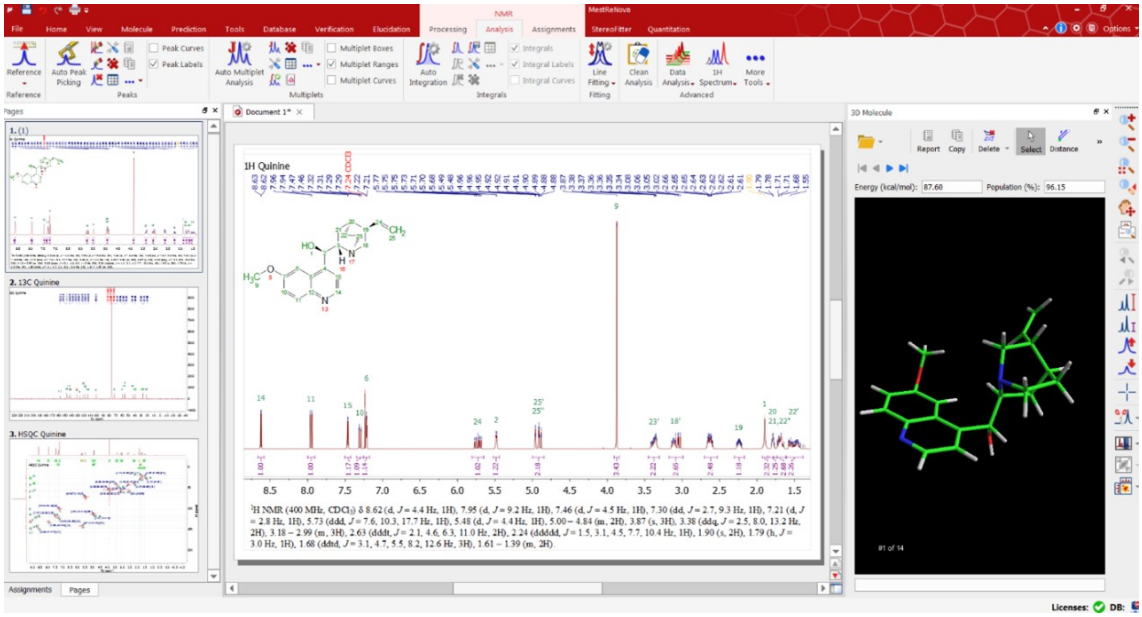

Figure 6.4: Automated NMR spectral analysis in MnoVa NMR (Mestrelab Research S.L.).

6.2 Appendix B: Theoretical Basis for Impedance Matching

6.2.1 Introduction and RF Theory

Impedance matching is a foundational principle in RF system design that ensures efficient power transfer between components. Without proper matching, significant portions of the transmitted power are reflected back toward the source, leading to inefficiencies and degraded system performance. This becomes particularly important in high-frequency systems, such as those used in Nuclear Magnetic Resonance (NMR), where signal integrity is paramount. In this section, we

will explore the theoretical concepts that underpin impedance matching, starting with the maximum power transfer theorem and moving through key factors like the reflection coefficient and quality factor. We will also touch on the differences between theory and practice, highlighting potential challenges faced in real-world applications.

The Maximum Power Transfer Theorem

The concept of impedance matching begins with the maximum power transfer theorem. This theorem states that to achieve the greatest possible transfer of power from a source to a load, the load impedance (Z_L) should be equal to the complex conjugate of the source impedance (Z_S):

$$Z_L = Z_S^* \tag{6.1}$$

In simpler terms, this means that both the resistive and reactive parts of the impedances should be appropriately matched. For example, if the source has a resistive component of 50 Ω and an inductive component (which contributes reactance), the load should mirror this, with an impedance that cancels out the reactance and matches the resistance.

This theorem is particularly useful in RF systems like NMR, where power transfer efficiency directly impacts the signal strength reaching the detection coil. However, while the maximum power transfer theorem provides a solid theoretical basis, it is important to remember that in practical situations, achieving perfect matching isn't always the primary objective. For instance, in some systems, noise minimisation or bandwidth maximisation may take precedence over maximum power transfer.

Reflection Coefficient and Standing Wave Ratio

When there is a mismatch between the source and load impedances, some of the signal gets reflected back to the source, rather than being fully transmitted to the load. This reflection can be quantified using the reflection coefficient (Γ), which is a measure of the amplitude of the reflected signal relative to the incident signal:

$$\Gamma = \frac{Z_L - Z_S}{Z_L + Z_S} \tag{6.2}$$

A reflection coefficient of zero ($\Gamma = 0$) indicates perfect matching—none of the signal is reflected back, and all the power is delivered to the load. However, as the reflection coefficient increases, so does the inefficiency of power transfer, and more power is reflected. The Voltage Standing Wave Ratio (VSWR), which is derived from the reflection coefficient, offers another way to measure this inefficiency:

$$\text{VSWR} = \frac{1 + |\Gamma|}{1 - |\Gamma|} \tag{6.3}$$

A VSWR of 1:1 represents perfect impedance matching. Higher VSWR values suggest greater mismatch and, consequently, more signal loss. In practical applications, including NMR systems, a VSWR below 1.5 is typically acceptable, though precise requirements can vary based on system design goals.

Impedance Transformation and Matching Networks

In practice, source and load impedances rarely match by default, which is where impedance matching networks come into play. These networks are designed to adjust the impedance of either the source or the load so that they match, allowing for optimal power transfer. Various matching network topologies exist, each suited to specific applications and impedance transformation requirements. Common types include L-networks, Pi-networks, and T-networks, which differ in complexity and bandwidth performance.

For instance, an L-network consists of two reactive elements, typically a capacitor and an inductor, configured to provide a simple, narrowband impedance match. The relationship between the Q factor and impedance transformation in an L-network is given by:

$$\frac{Z_L}{Z_S} = Q^2 + 1 \tag{6.4}$$

Here, the quality factor Q represents the sharpness of the impedance transformation. Higher-Q networks provide excellent impedance matching over narrow frequency ranges but can be sensitive to small changes in component values. Lower-Q networks offer broader bandwidth but may compromise the precision of the match.

Quality Factor and Bandwidth

One of the key trade-offs in designing impedance matching networks is between the quality factor (Q) and bandwidth. A high-Q network is capable of transforming impedance with great accuracy but only over a limited range of frequencies. In contrast, a low-Q network can match impedances over a broader frequency range, albeit with reduced precision. The relationship between Q and bandwidth is defined by:

$$\text{Bandwidth} = \frac{f_0}{Q} \tag{6.5}$$

where f_0 is the center frequency. For NMR systems, this trade-off must be carefully balanced. A high-Q network might offer the precise matching required for maximum signal sensitivity but at the cost of being highly sensitive to component variations. This makes it necessary to consider practical factors like the tolerance of components, which we will discuss shortly.

The Smith Chart: A Practical Tool for Matching

Designing impedance matching networks often relies on the use of the Smith Chart, a powerful graphical tool that simplifies the visualisation of complex impedance transformations. By plotting the normalised source and load impedances on the Smith Chart, engineers can quickly determine the necessary reactive components to achieve a match. Each point on the Smith Chart represents a specific impedance value, and movements on the chart correspond to adding capacitive or inductive elements.

For example, starting from the normalised impedance of the load, the engineer can trace a path along the Smith Chart toward the source impedance by sequentially adding reactive components. This process allows for an intuitive and visual method of designing matching networks. Importantly, the Smith Chart also displays Q-circles, which represent constant-Q paths, providing insight into how different matching network designs impact bandwidth and efficiency.

Practical Considerations and Real-World Challenges

While the theoretical foundation of impedance matching provides clear guidelines, real-world designs must contend with several practical limitations. Two of the most significant factors that can affect the performance of an impedance matching network are parasitics and component tolerances.

- Parasitics: At RF frequencies, even the most well-designed components can exhibit parasitic behaviors. Inductors, for example, may have unintended capacitive effects, while capacitors might possess inductive parasitics. These parasitics alter the impedance of the components and can cause deviations from the intended design. As a result, adjustments are often necessary to account for these effects, particularly when working with high-frequency circuits like NMR systems.

- Component Tolerances: Real-world components are rarely manufactured to exact specifications. Even small deviations in component values, due to manufacturing tolerances, can lead to significant mismatches in high-Q networks. To ensure robust performance despite these variations, Monte Carlo simulations are often employed. These simulations allow designers to analyze how the matching network will perform under a range of possible component values, ensuring that it remains effective within the required tolerances.

Conclusion

Impedance matching forms the cornerstone of efficient RF circuit design, with its theoretical basis grounded in the maximum power transfer theorem, reflection coefficient, and quality factor. However, transitioning from theory to practice introduces new challenges, including parasitics

and component tolerances, that must be carefully managed to achieve the desired system performance. In the next section, we will explore how these principles are applied in the context of NMR system design, with a focus on practical tools, methodologies, and real-world examples drawn from academic research.

6.2.2 Design Process for Impedance Matching Networks in the NMR System

The design of impedance matching networks for the NMR system follows a structured, step-by-step process. This section provides a detailed walkthrough of each phase, focusing on practical applications, challenges, and the solutions applied. We will also cover S-parameters in more detail, presenting them in matrix form, and explore how Q-circles guide decisions around bandwidth and impedance matching.

Step 1: Initial Impedance Measurements Using the VNA

The process begins by obtaining precise impedance measurements using a VNA. The VNA measures the reflection and transmission properties of RF components within the desired frequency range (28 to 29.2 MHz for the NMR system), providing critical S-parameters that describe how signals interact with the network.

Understanding S-Parameters

In RF system analysis, S-parameters (scattering parameters) are essential because they quantify how signals reflect and transmit through each port of the network. For a typical two-port device, the S-parameters are represented by a 2x2 matrix:

$$\mathbf{S} = \begin{bmatrix} S_{11} & S_{12} \\ S_{21} & S_{22} \end{bmatrix} \tag{6.6}$$

Where:

- S_{11} represents the input reflection coefficient (how much of the signal is reflected back at port 1),
- S_{12} represents the reverse transmission (how much signal travels from port 2 to port 1),
- S_{21} represents the forward transmission coefficient (how much of the signal travels from port 1 to port 2),
- S_{22} represents the output reflection coefficient (how much of the signal is reflected back at port 2).

In impedance matching, the most crucial parameter is S_{11}, which measures how much of the input signal is reflected back. Ideally, we aim to minimis S_{11} to achieve efficient power transfer between the source and load. A value of S_{11} below -10 dB is typically acceptable in RF systems, meaning that less than 10% of the signal is reflected.

The relationship between S_{11} and the reflection coefficient Γ is defined as:

$$S_{11} = 20\log(|\Gamma|) \tag{6.7}$$

Initial Measurement Challenges

In this design, we used a NanoVNA (CHELEGANCE JNCRADIO VNA 3G, Chelegance Co. Ltd, Shenzhen, China) instead of a traditional, larger VNA. The NanoVNA was chosen due to its compact size, affordability, and sufficient frequency coverage for the system's needs. Despite its smaller form factor, the NanoVNA provides accurate S-parameter measurements, making it ideal for field work or environments where larger VNAs are impractical.

While traditional VNAs often offer a wider frequency range and additional features, the NanoVNA's portability and cost-effectiveness make it particularly suitable for targeted, lower-frequency applications like NMR systems operating around 28.6 MHz. Additionally, the device's ease of use and robust software interface allow for real-time impedance analysis, which was a key factor in choosing it for this project.

Parameter	**Specification**	**Conditions**
Frequency range	50 kHz – 3 GHz	
RF output power	-10 dBm	50 kHz – 140 MHz
	-9 dBm	140 MHz – 1 GHz
	-12 dBm	1 GHz – 2 GHz
	-14 dBm	2 GHz – 3 GHz
Frequency accuracy	$< \pm 0.5$ ppm	
S21 dynamic range	80 dB	50 kHz – 1.5 GHz
	70 dB	1.5 GHz – 3 GHz
S11 dynamic range	50 dB	50 kHz – 1.5 GHz
	40 dB	1.5 GHz – 3 GHz
Sweep points	501	11 – 501 configurable

Table 6.1: NanoVNA Specifications

This table highlights the key features of the NanoVNA that made it suitable for the impedance measurements in this project. The device's wide frequency range and portability allowed for flexible and accurate testing, while its compatibility with PC software facilitated smooth data export and integration into the design and simulation workflow.

As with any VNA, proper calibration is essential to ensure accurate impedance data. Using short-open-load-through calibration standards, we accounted for the effects of cables, connectors, and other components in the measurement setup. This ensures that the impedance data

reflects the actual behaviour of the system, free from distortions introduced by the measurement setup itself.

Step 2: Designing the Matching Network Using the Smith Chart in ADS

Once the impedance data has been measured, the next step involves importing this data into Advanced Design System (ADS) for analysis. The Smith Chart in ADS provides a visual representation of the measured impedance and is used to design the impedance matching network.

Using the Smith Chart and Q-Circles for Impedance Matching

The Smith Chart is an indispensable tool for designing RF matching networks, as it allows designers to map the measured load impedance and navigate toward the desired source impedance. By plotting the impedance values on the Smith Chart, reactive components, such as inductors and capacitors, can be added to the circuit to shift the impedance to a matched condition.

A key concept in the Smith Chart is the use of Q-circles. These circles represent constant-Q paths, with higher Q-circles indicating sharper impedance matches that are effective over a narrower bandwidth. Conversely, lower Q-circles allow for broader bandwidths but with less precise matching.

For NMR systems operating within a narrow frequency range, the goal is to use the smallest Q-circle possible. This ensures a tight match within the desired bandwidth (28 to 29.2 MHz) without making the network too sensitive to component variations. The placement of inductors and capacitors is guided by the position on the Q-circle, balancing the trade-off between bandwidth and the precision of the match.

Challenges in Balancing Q-Factor and Bandwidth

A practical challenge in this phase is selecting components that maintain an acceptable bandwidth while still achieving a precise impedance match. Higher-Q networks, while excellent for narrowband matching, can be sensitive to component variations. By staying within the appropriate Q-circle on the Smith Chart, the network is designed to maintain sufficient bandwidth for the NMR system's operation while minimising reflection and loss.

Step 3: Running S-Parameter Simulations in ADS

Once the matching network has been designed, S-parameter simulations are run in ADS to validate the design's performance. These simulations use the impedance data obtained from the VNA and the designed matching network to predict how well the system will perform across the operational frequency range.

Analysing S_{11} for Matching Quality

The focus of these simulations is primarily on S_{11}, which quantifies how well the network matches the impedance of the source and load. Ideally, the simulation will show S_{11} values below -10 dB across the frequency range of 28–29.2 MHz. If the simulation results show excessive reflection (i.e., high S_{11}), further adjustments can be made to the network's components to improve the match.

At this stage, real-world issues such as parasitics (unwanted inductance or capacitance in components) become significant. By including parasitic models in the simulation, ADS can more accurately reflect the behaviour of the components, ensuring that the matching network performs well even when these imperfections are considered.

Step 4: Monte Carlo Simulations for Component Tolerances

After optimising the network through S-parameter simulations, it's important to ensure that the design is robust against variations in component values. Real-world components come with manufacturing tolerance, —typically 5% or 10%, which can affect the matching network's performance. To address this, Monte Carlo simulations are performed in ADS.

Ensuring Robustness with Monte Carlo Simulations

Monte Carlo simulations vary the component values within their specified tolerance ranges and simulate the network's performance for each variation. This provides a statistical view of how the matching network will perform in real-world conditions.

The objective is to confirm that the network maintains acceptable performance, even with component variability. For instance, the simulation should show that S_{11} remains below -10 dB for all potential component values. If the network proves too sensitive to tolerances, higher-precision components can be selected, or adjustments to the design can be made to improve robustness.

Step 5: PCB Fabrication and Testing with the VNA

Once the network has been validated through simulations, the design is fabricated on a PCB. During PCB design, care must be taken to minimis parasitic inductance and capacitance, which can arise from the PCB traces and layout. Short, wide traces are used to reduce inductance, and ground planes are incorporated to maintain signal integrity and reduce electromagnetic interference.

After fabrication, the matching network is tested once again using the VNA. This final step confirms that the network performs as expected under real-world conditions. If any deviations are observed, minor adjustments can be made to fine-tune the performance.

6.2.3 Red Pitaya STEMlab 125-10

In the development of our NMR system, selecting the right signal generation, processing, and control platform was crucial. The Red Pitaya STEMlab 125-10 emerged as the optimal choice for fulfilling multiple roles due to its flexibility, performance, and cost-effectiveness, making it an excellent fit for the unique demands of an NMR system. Unlike traditional RF instruments, which often require separate devices for signal generation, data acquisition, and timing control, the Red Pitaya integrates these capabilities into one compact, reconfigurable platform. This versatility allows it to handle the distinct tasks required in the NMR system, from generating precise RF excitation pulses to acting as a local oscillator and managing timing synchronisation across components.

The primary reason the Red Pitaya is so well-suited to our NMR system is its FPGA-based architecture, which enables real-time signal processing and reconfiguration. In an NMR system, where precise control over RF pulses and timing is essential, the ability to program and modify the Red Pitaya through software without needing hardware modifications is a significant advantage. This reconfigurability allows the Red Pitaya to serve multiple roles in the system without requiring dedicated hardware for each function. For instance, it can be easily reprogrammed to switch between generating the RF signal and handling synchronisation tasks, reducing both complexity and cost.

Another critical factor is the Red Pitaya's high sampling rate and dual-channel capability. With a sampling rate of up to 125 MS/s, the Red Pitaya can generate and process signals within the required frequency range of 28 to 29.2 MHz, which is crucial for the Larmor frequency in our NMR experiments. Its dual-channel operation allows simultaneous signal generation and data acquisition, ensuring that the system can not only excite the nuclear spins with the correct RF frequency but also capture the resulting signals without needing separate devices. This ability to manage both tasks within one unit simplifies system design and enhances synchronisation between components.

Additionally, the open-source nature of the Red Pitaya was a major advantage for this project. The flexibility to customise the device's behaviour to suit the specific needs of the NMR system was invaluable. Rather than being limited to a rigid, pre-configured set of features, the Red Pitaya's open-source platform enabled the rapid development of tailored control scripts and configurations for tasks such as pulse shaping, precise frequency control, and timing coordination. This open-source ecosystem also provided access to a wide range of pre-built applications and software tools that could be adapted for our use, accelerating the development process.

Cost efficiency was another significant consideration in choosing the Red Pitaya. NMR systems traditionally rely on specialised, high-end signal generators, oscillators, and timing controllers, which are often expensive and bulky. In contrast, the Red Pitaya offers a cost-effective alternative that integrates these capabilities into a single device without compromising performance. Its compact form factor allowed us to reduce the system's footprint while maintaining

the necessary functionality, making it ideal for research environments where budget and space are often constrained.

In summary, the Red Pitaya STEMlab 125-10 offers a combination of flexibility, reconfigurability, and cost-efficiency that makes it exceptionally well-suited for our NMR system. Its ability to fulfill multiple roles—serving as a signal generator, local oscillator, and timing controller—without requiring separate hardware for each task allows us to maintain a compact, integrated system without sacrificing performance. In the following sections, we will explore how the Red Pitaya is specifically used in each of these roles, highlighting the ways in which it meets the technical demands of our NMR setup.

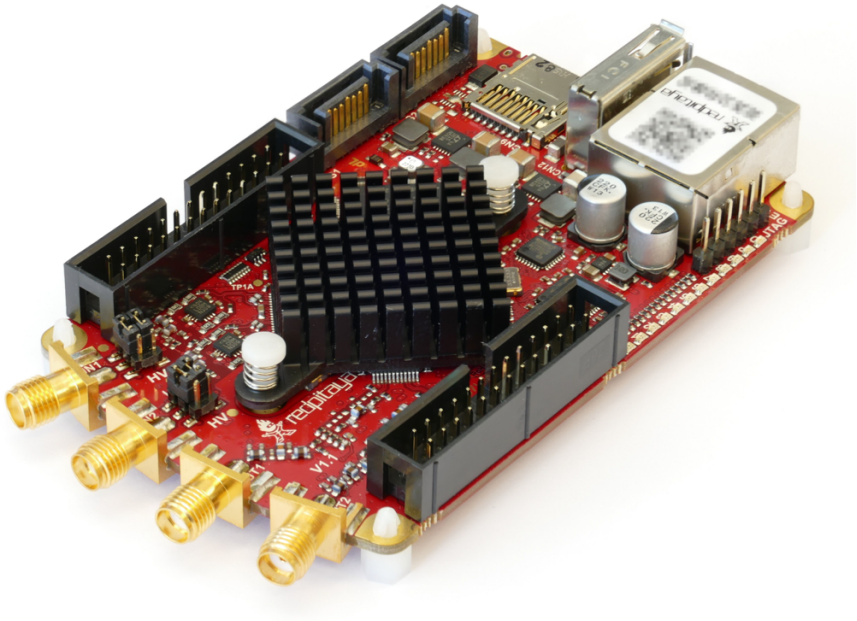

Figure 6.5: Red Pitaya board.

Feature	Specification
Processor	DUAL CORE ARM CORTEX A9
FPGA	FPGA Xilinx Zynq 7010 SOC
RAM	256 MB (2 Gb)
System memory	Micro SD up to 32 GB
Console connection	Micro USB
Power connector	Micro USB
Power consumption	5 V, 1.5 A max
RF Outputs	
RF output channels	2
Sample rate	125 MS/s
DAC resolution	10 bit
Load impedance	50 Ω
Voltage range	±1 V
Short circuit protection	Yes
Connector type	SMA
Output slew rate	2 V / 10 ns
Bandwidth	DC - 50 MHz

Table 6.2: Red Pitaya STEMlab 125-10 Specifications

Bibliography

[1] T. Crnogorac-Jurcevic, "A brief history of urine examination - From ancient uroscopy to 21st century urinomics," *Advances in Biomarker Sciences and Technology*, vol. 6, pp. 83–90, Jan. 2024. DOI: 10.1016/j.abst.2024.06.001.

[2] G. Eknoyan, "Looking at the Urine: The Renaissance of an Unbroken Tradition," *American Journal of Kidney Diseases*, vol. 49, no. 6, pp. 865–872, Jun. 2007. DOI: 10.1053/j.ajkd.2007.04.003.

[3] B. Bynum and H. Bynum, "The matula," *The Lancet*, vol. 387, no. 10019, p. 638, Feb. 2016. DOI: 10.1016/S0140-6736(16)00289-0.

[4] X. Liu, X. Zhu, G. J. Kost, J. Liu, J. Huang, and X. Liu, "The Creation of Point-of-Careology," *Point of Care*, vol. 18, no. 3, p. 77, Sep. 2019. DOI: 10.1097/POC.0000000000000191.

[5] J. Büttner, "The Origin of Clinical Laboratories," vol. 30, no. 10, pp. 585–594, Jan. 1992. DOI: 10.1515/cclm.1992.30.10.585.

[6] J. E. Szalados, "Clinical Labs: CLIA and Other Evolving Challenges," in *The Medical-Legal Aspects of Acute Care Medicine: A Resource for Clinicians, Administrators, and Risk Managers*, J. E. Szalados, Ed., Cham: Springer International Publishing, 2021, pp. 463–477, ISBN: 978-3-030-68570-6. DOI: 10.1007/978-3-030-68570-6_22.

[7] N.-E. Drenck, "Point of care testing in Critical Care Medicine: The clinician's view," *Clinica Chimica Acta*, Critical Care Testing in the New Millennium: The Integration of Point of Care Testing, vol. 307, no. 1, pp. 3–7, May 2001. DOI: 10.1016/S0009-8981(01)00448-X.

[8] B. C. Ozaki, A. Mix, and P. Vivanco, "A-005 Comparison of Performance of High Sensitive Troponin I (cTNIH) by "Point of care" (POC) and Automated cTNIH Immunoassays in Patients at Low Risk of Heart Attack in a Chilean Emergency Unit; Impact on E.R Department Efficiency," *Clinical Chemistry*, vol. 70, no. Supplement_1, hvae106.005, Oct. 2024. DOI: 10.1093/clinchem/hvae106.005.

[9] N. M. Sumita, C. E. S. Ferreira, M. D. V. Martino, *et al.*, *Clinical Applications of Point-of-Care Testing in Different Conditions. — EBSCOhost*, https://openurl.ebsco.com/contentitem/do Jul. 2018. DOI: 10.7754/Clin.Lab.2018.171021.

[10] J. Howick, J. W. L. Cals, C. Jones, *et al.*, "Current and future use of point-of-care tests in primary care: An international survey in Australia, Belgium, The Netherlands, the UK and the USA," *BMJ Open*, vol. 4, no. 8, e005611, Aug. 2014. DOI: 10.1136/bmjopen-2014-005611.

[11] M. Mor and Y. Waisman, "Point-of-care testing: A critical review," *Pediatric Emergency Care*, vol. 16, no. 1, p. 45, Feb. 2000.

[12] P. K. Drain, E. P. Hyle, F. Noubary, *et al.*, "Diagnostic point-of-care tests in resource-limited settings," *The Lancet Infectious Diseases*, vol. 14, no. 3, pp. 239–249, Mar. 2014. DOI: 10.1016/S1473-3099(13)70250-0.

[13] L. Cullen, P. O. Collinson, and E. Giannitsis, "Point-of-care testing with high-sensitivity cardiac troponin assays: The challenges and opportunities," *Emergency Medicine Journal*, vol. 39, no. 11, pp. 861–866, Nov. 2022. DOI: 10.1136/emermed-2021-211907.

[14] G. Meyer-Rath, K. Schnippel, L. Long, *et al.*, "The Impact and Cost of Scaling up GeneXpert MTB/RIF in South Africa," *PLOS ONE*, vol. 7, no. 5, e36966, May 2012. DOI: 10.1371/journal.pone.0036966.

[15] Z. Rong, Z. Bai, J. Li, *et al.*, "Dual-color magnetic-quantum dot nanobeads as versatile fluorescent probes in test strip for simultaneous point-of-care detection of free and complexed prostate-specific antigen," *Biosensors and Bioelectronics*, vol. 145, p. 111 719, Dec. 2019. DOI: 10.1016/j.bios.2019.111719.

[16] K. Yun, J. Choi, I.-U. Song, and Y.-A. Chung, "Smartphone-Based Point-of-Care Cholesterol Blood Test Performance Evaluation Compared with a Clinical Diagnostic Laboratory Method," *Applied Sciences*, vol. 9, no. 16, p. 3334, Jan. 2019. DOI: 10.3390/app9163334.

[17] C. D. Chin, V. Linder, and S. K. Sia, "Commercialization of microfluidic point-of-care diagnostic devices," *Lab on a Chip*, vol. 12, no. 12, pp. 2118–2134, 2012. DOI: 10.1039/C2LC21204H.

[18] N. T. Darwish, S. D. Sekaran, and S. M. Khor, "Point-of-care tests: A review of advances in the emerging diagnostic tools for dengue virus infection," *Sensors and Actuators B: Chemical*, vol. 255, pp. 3316–3331, Feb. 2018. DOI: 10.1016/j.snb.2017.09.159.

[19] K. Hsieh, B. S. Ferguson, M. Eisenstein, K. W. Plaxco, and H. T. Soh, "Integrated Electrochemical Microsystems for Genetic Detection of Pathogens at the Point of Care," *Accounts of Chemical Research*, vol. 48, no. 4, pp. 911–920, Apr. 2015. DOI: 10.1021/ar500456w.

[20] L. Huang, D. Zhang, L. Jiao, E. Su, and N. He, "A new quality control method for lateral flow assay," *Chinese Chemical Letters*, vol. 29, no. 12, pp. 1853–1856, Dec. 2018. DOI: 10.1016/j.cclet.2018.11.028.

[21] H. Khan, A. Khan, Y. Liu, *et al.*, "CRISPR-Cas13a mediated nanosystem for attomolar detection of canine parvovirus type 2," *Chinese Chemical Letters*, vol. 30, no. 12, pp. 2201–2204, Dec. 2019. DOI: 10.1016/j.cclet.2019.10.032.

[22] C. C. Boehme, P. Nabeta, D. Hillemann, *et al.*, "Rapid Molecular Detection of Tuberculosis and Rifampin Resistance," *New England Journal of Medicine*, vol. 363, no. 11, pp. 1005–1015, Sep. 2010. DOI: 10.1056/NEJMoa0907847.

[23] Z. Chen, Y. Wu, M. Kang, *et al.*, "Research on Automated Nucleic Acid Extraction Instrument Based on Magnetic Nanoparticles Separation," *Nanoscience and Nanotechnology Letters*, vol. 10, no. 1, pp. 60–68, Jan. 2018. DOI: 10.1166/nnl.2018.2595.

[24] M. Hussain, M. Lv, X. Dong, *et al.*, "Design of Rapid Bacterial Identification System Based on Scattering of Laser Light and Classification of Binned Plots," *Journal of Nanoscience and Nanotechnology*, vol. 20, no. 7, pp. 4047–4056, Jul. 2020. DOI: 10.1166/jnn.2020.17491.

[25] C. Wang, Z. Guo, H. Zhu, N. He, Z. Chen, and Z. Wang, "Mechanical Gripper Design and Force Analysis of Microplates for Automated High-Throughput Nucleic Acid Detection System," *Journal of Nanoscience and Nanotechnology*, vol. 20, no. 3, pp. 1401–1408, Mar. 2020. DOI: 10.1166/jnn.2020.17355.

[26] H. Chen, Y. Wu, Y. Fang, *et al.*, "Integrated and Automated, Sample-In to Result-Out, System for Nanotechnology-Based Detection of Infectious Pathogens," *Nanoscience and Nanotechnology Letters*, vol. 10, no. 10, pp. 1423–1428, Oct. 2018. DOI: 10.1166/nnl.2018.2802.

[27] Z. Chen, H. Yang, J. Peng, *et al.*, "Highly Precise and Fast Polymerase Chain Reaction Thermal Cycling Module with a Novel Integrated Temperature Control Strategy," *Nanoscience and Nanotechnology Letters*, vol. 10, no. 1, pp. 23–31, Jan. 2018. DOI: 10.1166/nnl.2018.2597.

[28] H. He, Y. Wu, N. He, and Y. Deng, "The Latest Progress of On-Site Pathogens Detection Techniques and Instruments Based on Nucleic Acid," *Journal of Nanoscience and Nanotechnology*, vol. 15, no. 9, pp. 6342–6356, Sep. 2015. DOI: 10.1166/jnn.2015.10710.

[29] Y. Fang, P. Liao, Z. Chen, *et al.*, "Improvement and application of qPCR data processing method for home-made integrated nucleic acid detection system," *Journal of Nanoscience and Nanotechnology*, vol. 20, no. 12, pp. 7375–7381, 2020.

[30] C. Wang, Y. Huang, H. Zhu, *et al.*, "Design and Implementation of High-Throughput Magnetic Separation Module for Automated Nucleic Acid Detection System Based on Magnetic Nano-Beads," *Journal of Nanoscience and Nanotechnology*, vol. 20, no. 4, pp. 2138–2143, Apr. 2020. DOI: 10.1166/jnn.2020.17327.

[31] C. E. Kennedy, P. T. Yeh, K. Gholbzouri, and M. Narasimhan, "Self-testing for pregnancy: A systematic review and meta-analysis," *BMJ Open*, vol. 12, no. 2, e054120, Feb. 2022. DOI: 10.1136/bmjopen-2021-054120.

[32] F. Sanchis-Gomar, J. Cortell-Ballester, H. Pareja-Galeano, G. Banfi, and G. Lippi, "Hemoglobin Point-of-Care Testing: The HemoCue System," *Journal of Laboratory Automation*, vol. 18, no. 3, pp. 198–205, Jun. 2013. DOI: 10.1177/2211068212457560.

[33] K. Kaur, M. Zubair, and J. J. Adamski, "Fecal Occult Blood Test," in *StatPearls*, Treasure Island (FL): StatPearls Publishing, 2025.

[34] W. L. Lean, S. Arnup, M. Danchin, and A. C. Steer, "Rapid Diagnostic Tests for Group A Streptococcal Pharyngitis: A Meta-analysis," *Pediatrics*, vol. 134, no. 4, pp. 771–781, Oct. 2014. DOI: 10.1542/peds.2014-1094.

[35] A. Niemz, T. M. Ferguson, and D. S. Boyle, "Point-of-care nucleic acid testing for infectious diseases," *Trends in Biotechnology*, vol. 29, no. 5, pp. 240–250, May 2011. DOI: 10.1016/j.tibtech.2011.01.007.

[36] R. Sista, Z. Hua, P. Thwar, *et al.*, "Development of a digital microfluidic platform for point of care testing," *Lab on a Chip*, vol. 8, no. 12, pp. 2091–2104, 2008. DOI: 10.1039/B814922D.

[37] C. Junot, F. Fenaille, B. Colsch, and F. Bécher, "High resolution mass spectrometry based techniques at the crossroads of metabolic pathways," *Mass Spectrometry Reviews*, vol. 33, no. 6, pp. 471–500, 2014. DOI: 10.1002/mas.21401.

[38] S. G. Oliver, M. K. Winson, D. B. Kell, and F. Baganz, "Systematic functional analysis of the yeast genome," *Trends in Biotechnology*, vol. 16, no. 9, pp. 373–378, Sep. 1998. DOI: 10.1016/s0167-7799(98)01214-1.

[39] O. Fiehn, "Metabolomics — the link between genotypes and phenotypes," in *Functional Genomics*, C. Town, Ed., Dordrecht: Springer Netherlands, 2002, pp. 155–171, ISBN: 978-94-010-0448-0. DOI: 10.1007/978-94-010-0448-0_11.

[40] J. L. Griffin, H. Atherton, J. Shockcor, and L. Atzori, "Metabolomics as a tool for cardiac research," *Nature Reviews Cardiology*, vol. 8, no. 11, pp. 630–643, Nov. 2011. DOI: 10.1038/nrcardio.2011.138.

[41] A. D. Patterson, O. Maurhofer, D. Beyoğlu, *et al.*, "Aberrant Lipid Metabolism in Hepatocellular Carcinoma Revealed by Plasma Metabolomics and Lipid Profiling," *Cancer research*, vol. 71, no. 21, pp. 6590–6600, Nov. 2011. DOI: 10.1158/0008-5472.CAN-11-0885.

[42] P. Rinaudo, S. Boudah, C. Junot, and E. A. Thévenot, "Biosigner: A New Method for the Discovery of Significant Molecular Signatures from Omics Data," *Frontiers in Molecular Biosciences*, vol. 3, Jun. 2016. DOI: 10.3389/fmolb.2016.00026.

[43] I. Dudka, A. Chachaj, A. Sebastian, *et al.*, "Metabolomic profiling reveals plasma GlycA and GlycB as a potential biomarkers for treatment efficiency in rheumatoid arthritis," *Journal of Pharmaceutical and Biomedical Analysis*, vol. 197, p. 113 971, Apr. 2021. DOI: 10.1016/j.jpba.2021.113971.

[44] S. Takahashi, J. Saegusa, A. Onishi, and A. Morinobu, "Biomarkers identified by serum metabolomic analysis to predict biologic treatment response in rheumatoid arthritis patients," *Rheumatology*, vol. 58, no. 12, pp. 2153–2161, Dec. 2019. DOI: 10.1093/rheumatology/kez199.

[45] A. K. Carlson, R. A. Rawle, E. Adams, M. C. Greenwood, B. Bothner, and R. K. June, "Application of global metabolomic profiling of synovial fluid for osteoarthritis biomarkers," *Biochemical and Biophysical Research Communications*, vol. 499, no. 2, pp. 182–188, May 2018. DOI: 10.1016/j.bbrc.2018.03.117.

[46] A. Zhang, H. Sun, and X. Wang, "Emerging role and recent applications of metabolomics biomarkers in obesity disease research," *RSC Advances*, vol. 7, no. 25, pp. 14 966–14 973, 2017. DOI: 10.1039/C6RA28715H.

[47] Z. Wang, L. Bian, C. Mo, *et al.*, "Quantification of aminobutyric acids and their clinical applications as biomarkers for osteoporosis," *Communications Biology*, vol. 3, no. 1, pp. 1–14, Jan. 2020. DOI: 10.1038/s42003-020-0766-y.

[48] X. S. Li, Z. Wang, T. Cajka, *et al.*, "Untargeted metabolomics identifies trimethyllysine, a TMAO-producing nutrient precursor, as a predictor of incident cardiovascular disease risk," *JCI Insight*, vol. 3, no. 6, e99096, DOI: 10.1172/jci.insight.99096.

[49] J. M. Wilkins and E. Trushina, "Application of Metabolomics in Alzheimer's Disease," *Frontiers in Neurology*, vol. 8, Jan. 2018. DOI: 10.3389/fneur.2017.00719.

[50] A. Yilmaz, T. Geddes, B. Han, *et al.*, "Diagnostic Biomarkers of Alzheimer's Disease as Identified in Saliva using 1H NMR-Based Metabolomics," *Journal of Alzheimer's Disease*, vol. 58, no. 2, pp. 355–359, Jan. 2017. DOI: 10.3233/JAD-161226.

[51] J. Xu, Y. Chen, R. Zhang, *et al.*, "Global and Targeted Metabolomics of Esophageal Squamous Cell Carcinoma Discovers Potential Diagnostic and Therapeutic Biomarkers *," *Molecular & Cellular Proteomics*, vol. 12, no. 5, pp. 1306–1318, May 2013. DOI: 10.1074/mcp.M112.022830.

[52] W. B. Dunn, W. Lin, D. Broadhurst, *et al.*, "Molecular phenotyping of a UK population: Defining the human serum metabolome," *Metabolomics*, vol. 11, no. 1, pp. 9–26, Feb. 2015. DOI: 10.1007/s11306-014-0707-1.

[53] M. A. Schmidt and T. J. Goodwin, "Personalized medicine in human space flight: Using Omics based analyses to develop individualized countermeasures that enhance astronaut safety and performance," *Metabolomics*, vol. 9, no. 6, pp. 1134–1156, Dec. 2013. DOI: 10.1007/s11306-013-0556-3.

[54] S. M. C. Lee, B. K. Rana, M. B. Stenger, *et al.*, *Metabolomic and Genomic Markers of Atherosclerosis as Related to Oxidative Stress, Inflammation, and Vascular Function in Twin Astronauts*, Feb. 2016.

[55] D. R. Schmidt, R. Patel, D. G. Kirsch, C. A. Lewis, M. G. Vander Heiden, and J. W. Locasale, "Metabolomics in Cancer Research and Emerging Applications in Clinical Oncology," *CA: a cancer journal for clinicians*, vol. 71, no. 4, pp. 333–358, Jul. 2021. DOI: 10.3322/caac.21670.

[56] O. P. Trifonova, D. L. Maslov, E. E. Balashova, and P. G. Lokhov, "Current State and Future Perspectives on Personalized Metabolomics," *Metabolites*, vol. 13, no. 1, p. 67, Jan. 2023. DOI: 10.3390/metabo13010067.

[57] M. Gogiashvili, J. Nowacki, R. Hergenröder, J. G. Hengstler, J. Lambert, and K. Edlund, "HR-MAS NMR Based Quantitative Metabolomics in Breast Cancer," *Metabolites*, vol. 9, no. 2, p. 19, Feb. 2019. DOI: 10.3390/metabo9020019.

[58] T. J. Wang, M. G. Larson, R. S. Vasan, *et al.*, "Metabolite profiles and the risk of developing diabetes," *Nature Medicine*, vol. 17, no. 4, pp. 448–453, Apr. 2011. DOI: 10.1038/nm.2307.

[59] V. Bodi, J. Sanchis, J. M. Morales, *et al.*, "Metabolomic Profile of Human Myocardial Ischemia by Nuclear Magnetic Resonance Spectroscopy of Peripheral Blood Serum," *Journal of the American College of Cardiology*, vol. 59, no. 18, pp. 1629–1641, May 2012. DOI: 10.1016/j.jacc.2011.09.083.

[60] H. Chen, Z. Pan, N. Talaty, D. Raftery, and R. G. Cooks, "Combining desorption electrospray ionization mass spectrometry and nuclear magnetic resonance for differential metabolomics without sample preparation," *Rapid Communications in Mass Spectrometry*, vol. 20, no. 10, pp. 1577–1584, 2006. DOI: 10.1002/rcm.2474.

[61] C. Deng, N. Li, and X. Zhang, "Development of headspace solid-phase microextraction with on-fiber derivatization for determination of hexanal and heptanal in human blood," *Journal of Chromatography B*, vol. 813, no. 1, pp. 47–52, Dec. 2004. DOI: 10.1016/j.jchromb.2004.09.007.

[62] D. S. Wishart, "Emerging applications of metabolomics in drug discovery and precision medicine," *Nature Reviews Drug Discovery*, vol. 15, no. 7, pp. 473–484, Jul. 2016. DOI: 10.1038/nrd.2016.32.

[63] L. Dang, D. W. White, S. Gross, *et al.*, "Cancer-associated IDH1 mutations produce 2-hydroxyglutarate," *Nature*, vol. 462, no. 7274, pp. 739–744, Dec. 2009. DOI: 10.1038/nature08617.

[64] P. S. Ward, J. Patel, D. R. Wise, *et al.*, "The Common Feature of Leukemia-Associated IDH1 and IDH2 Mutations Is a Neomorphic Enzyme Activity Converting α-Ketoglutarate to 2-Hydroxyglutarate," *Cancer Cell*, vol. 17, no. 3, pp. 225–234, Mar. 2010. DOI: 10.1016/j.ccr.2010.01.020.

[65] C. P. Wild, A. Scalbert, and Z. Herceg, "Measuring the exposome: A powerful basis for evaluating environmental exposures and cancer risk," *Environmental and Molecular Mutagenesis*, vol. 54, no. 7, pp. 480–499, 2013. DOI: 10.1002/em.21777.

[66] T. Suna, A. Salminen, P. Soininen, *et al.*, "1H NMR metabonomics of plasma lipoprotein subclasses: Elucidation of metabolic clustering by self-organising maps," *NMR in Biomedicine*, vol. 20, no. 7, pp. 658–672, 2007. DOI: 10.1002/nbm.1123.

[67] K. K. Pasikanti, K. Esuvaranathan, Y. Hong, *et al.*, "Urinary Metabotyping of Bladder Cancer Using Two-Dimensional Gas Chromatography Time-of-Flight Mass Spectrometry," *Journal of Proteome Research*, vol. 12, no. 9, pp. 3865–3873, Sep. 2013. DOI: 10.1021/pr4000448.

[68] X. Zhang, X. Zhu, C. Wang, H. Zhang, and Z. Cai, "Non-targeted and targeted metabolomics approaches to diagnosing lung cancer and predicting patient prognosis," *Oncotarget*, vol. 7, no. 39, pp. 63 437–63 448, Aug. 2016. DOI: 10.18632/oncotarget.11521.

[69] G. K. Alderton, "Feeding the TCA cycle in vivo," *Nature Reviews Cancer*, vol. 16, no. 4, pp. 198–198, Apr. 2016. DOI: 10.1038/nrc.2016.29.

[70] S. Furumoto, R. Shinbo, R. Iwata, *et al.*, "In Vitro and In Vivo Characterization of 2-Deoxy-2-18F-Fluoro-d-Mannose as a Tumor-Imaging Agent for PET," *Journal of Nuclear Medicine*, vol. 54, no. 8, pp. 1354–1361, Aug. 2013. DOI: 10.2967/jnumed.112.113571.

[71] P. Som, H. L. Atkins, D. Bandoypadhyay, *et al.*, "A Fluorinated Glucose Analog, 2-fluoro-2-deoxy-D-glucose (F-18): Nontoxic Tracer for Rapid Tumor Detection," *Journal of Nuclear Medicine*, vol. 21, no. 7, pp. 670–675, Jul. 1980.

[72] J. W. Fletcher, B. Djulbegovic, H. P. Soares, *et al.*, "Recommendations on the Use of 18F-FDG PET in Oncology," *Journal of Nuclear Medicine*, vol. 49, no. 3, pp. 480–508, Mar. 2008. DOI: 10.2967/jnumed.107.047787.

[73] T. Arumugam, V. Paolillo, D. Young, *et al.*, "Preliminary evaluation of 1′-[18F]fluoroethyl-β-D-lactose ([18F]FEL) for detection of pancreatic cancer in nude mouse orthotopic xenografts," *Nuclear Medicine and Biology*, vol. 41, no. 10, pp. 833–840, Nov. 2014. DOI: 10.1016/j.nucmedbio.2014.08.001.

[74] A. Babic, M. H. Rosenthal, W. R. Bamlet, *et al.*, "Postdiagnosis Loss of Skeletal Muscle, but Not Adipose Tissue, Is Associated with Shorter Survival of Patients with Advanced Pancreatic Cancer," *Cancer Epidemiology, Biomarkers & Prevention*, vol. 28, no. 12, pp. 2062–2069, Dec. 2019. DOI: 10.1158/1055-9965.EPI-19-0370.

[75] Z. Zhang, Y. Qiu, Y. Hua, *et al.*, "Serum and Urinary Metabonomic Study of Human Osteosarcoma," *Journal of Proteome Research*, vol. 9, no. 9, pp. 4861–4868, Sep. 2010. DOI: 10.1021/pr100480r.

[76] V. M. Asiago, L. Z. Alvarado, N. Shanaiah, *et al.*, "Early Detection of Recurrent Breast Cancer Using Metabolite Profiling," *Cancer Research*, vol. 70, no. 21, pp. 8309–8318, Oct. 2010. DOI: 10.1158/0008-5472.CAN-10-1319.

[77] K. K. Pasikanti, K. Esuvaranathan, P. C. Ho, *et al.*, "Noninvasive Urinary Metabonomic Diagnosis of Human Bladder Cancer," *Journal of Proteome Research*, vol. 9, no. 6, pp. 2988–2995, Jun. 2010. DOI: 10.1021/pr901173v.

[78] K. Odunsi, R. M. Wollman, C. B. Ambrosone, *et al.*, "Detection of epithelial ovarian cancer using 1H-NMR-based metabonomics," *International Journal of Cancer*, vol. 113, no. 5, pp. 782–788, 2005. DOI: 10.1002/ijc.20651.

[79] M. D. Cao, G. F. Giskeødegård, T. F. Bathen, *et al.*, "Prognostic value of metabolic response in breast cancer patients receiving neoadjuvant chemotherapy," *BMC Cancer*, vol. 12, no. 1, p. 39, Jan. 2012. DOI: 10.1186/1471-2407-12-39.

[80] S. M. Wolahan, D. Hirt, D. Braas, and T. C. Glenn, "Role of Metabolomics in Traumatic Brain Injury Research," *Neurosurgery Clinics*, vol. 27, no. 4, pp. 465–472, Oct. 2016. DOI: 10.1016/j.nec.2016.05.006.

[81] N. R. Stein, D. L. McArthur, M. Etchepare, and P. M. Vespa, "Early Cerebral Metabolic Crisis After TBI Influences Outcome Despite Adequate Hemodynamic Resuscitation," *Neurocritical Care*, vol. 17, no. 1, pp. 49–57, Aug. 2012. DOI: 10.1007/s12028-012-9708-y.

[82] M. R. Viant, B. G. Lyeth, M. G. Miller, and R. F. Berman, "An NMR metabolomic investigation of early metabolic disturbances following traumatic brain injury in a mammalian model," *NMR in Biomedicine*, vol. 18, no. 8, pp. 507–516, 2005. DOI: 10.1002/nbm.980.

[83] R. M. Adibhatla and J. F. Hatcher, "Role of Lipids in Brain Injury and Diseases," *Future lipidology*, vol. 2, no. 4, pp. 403–422, Aug. 2007.

[84] P. M. Kochanek, R. P. Berger, H. Bayr, A. K. Wagner, L. W. Jenkins, and R. S. Clark, "Biomarkers of primary and evolving damage in traumatic and ischemic brain injury: Diagnosis, prognosis, probing mechanisms, and therapeutic decision making," *Current Opinion in Critical Care*, vol. 14, no. 2, p. 135, Apr. 2008. DOI: 10.1097/MCC.0b013e3282f57564.

[85] G. T. Manley, R. Diaz-Arrastia, M. Brophy, *et al.*, "Common Data Elements for Traumatic Brain Injury: Recommendations From the Biospecimens and Biomarkers Working Group," *Archives of Physical Medicine and Rehabilitation*, vol. 91, no. 11, pp. 1667–1672, Nov. 2010. DOI: 10.1016/j.apmr.2010.05.018.

[86] A. Pitkänen and K. Lukasiuk, "Molecular Biomarkers of Epileptogenesis," *Biomarkers in Medicine*, vol. 5, no. 5, pp. 629–633, Oct. 2011. DOI: 10.2217/bmm.11.67.

[87] L. J. Sparvero, A. A. Amoscato, P. M. Kochanek, B. R. Pitt, V. E. Kagan, and H. Bayır, "Mass-spectrometry based oxidative lipidomics and lipid imaging: Applications in traumatic brain injury," *Journal of Neurochemistry*, vol. 115, no. 6, pp. 1322–1336, 2010. DOI: 10.1111/j.1471-4159.2010.07055.x.

[88] A. K. Ottens, J. E. Stafflinger, H. E. Griffin, R. D. Kunz, D. X. Cifu, and J. P. Niemeier, "Post-Acute Brain Injury Urinary Signature: A New Resource for Molecular Diagnostics," *Journal of Neurotrauma*, vol. 31, no. 8, pp. 782–788, Apr. 2014. DOI: 10.1089/neu.2013.3116.

[89] S. M. Wolahan, D. Hirt, and T. C. Glenn, "Translational Metabolomics of Head Injury: Exploring Dysfunctional Cerebral Metabolism with Ex Vivo NMR Spectroscopy-Based Metabolite Quantification," in *Brain Neurotrauma: Molecular, Neuropsychological, and Rehabilitation Aspects*, ser. Frontiers in Neuroengineering, F. H. Kobeissy, Ed., Boca Raton (FL): CRC Press/Taylor & Francis, 2015, ISBN: 978-1-4665-6598-2.

[90] R. Yang, G. Fredman, S. Krishnamoorthy, *et al.*, "Decoding Functional Metabolomics with Docosahexaenoyl Ethanolamide (DHEA) Identifies Novel Bioactive Signals *," *Journal of Biological Chemistry*, vol. 286, no. 36, pp. 31 532–31 541, Sep. 2011. DOI: 10.1074/jbc.M111.237990.

[91] S. A. Sheth, A. T. Iavarone, D. S. Liebeskind, S. J. Won, and R. A. Swanson, "Targeted Lipid Profiling Discovers Plasma Biomarkers of Acute Brain Injury," *PLOS ONE*, vol. 10, no. 6, e0129735, Jun. 2015. DOI: 10.1371/journal.pone.0129735.

[92] T. C. Glenn, D. Hirt, G. Mendez, *et al.*, "Metabolomic Analysis of Cerebral Spinal Fluid from Patients with Severe Brain Injury," in *Brain Edema XV*, Y. Katayama, T. Maeda, and T. Kuroiwa, Eds., Vienna: Springer, 2013, pp. 115–119, ISBN: 978-3-7091-1434-6. DOI: 10.1007/978-3-7091-1434-6_20.

[93] H. Abou-El-Hassan, F. Sukhon, E. J. Assaf, *et al.*, "Degradomics in Neurotrauma: Profiling Traumatic Brain Injury," in *Neuroproteomics: Methods and Protocols*, F. H. Kobeissy and J. Stevens Stanley M., Eds., New York, NY: Springer, 2017, pp. 65–99, ISBN: 978-1-4939-6952-4. DOI: 10.1007/978-1-4939-6952-4_4.

[94] R. Tzekov, C. Dawson, M. Orlando, *et al.*, "Sub-Chronic Neuropathological and Biochemical Changes in Mouse Visual System after Repetitive Mild Traumatic Brain Injury," *PLOS ONE*, vol. 11, no. 4, e0153608, Apr. 2016. DOI: 10.1371/journal.pone.0153608.

[95] P. K. Dash, G. W. Hergenroeder, C. B. Jeter, H. A. Choi, N. Kobori, and A. N. Moore, "Traumatic Brain Injury Alters Methionine Metabolism: Implications for Pathophysiology," *Frontiers in Systems Neuroscience*, vol. 10, Apr. 2016. DOI: 10.3389/fnsys.2016.00036.

[96] T. Emmerich, L. Abdullah, G. Crynen, *et al.*, "Plasma Lipidomic Profiling in a Military Population of Mild Traumatic Brain Injury and Post-Traumatic Stress Disorder with Apolipoprotein E 4–Dependent Effect," *Journal of Neurotrauma*, vol. 33, no. 14, pp. 1331–1348, Jul. 2016. DOI: 10.1089/neu.2015.4061.

[97] L. Abdullah, J. E. Evans, S. Ferguson, *et al.*, "Lipidomic analyses identify injury-specific phospholipid changes 3 mo after traumatic brain injury," *The FASEB Journal*, vol. 28, no. 12, pp. 5311–5321, 2014. DOI: 10.1096/fj.14-258228.

[98] T. Emmerich, L. Abdullah, J. Ojo, *et al.*, "Mild TBI Results in a Long-Term Decrease in Circulating Phospholipids in a Mouse Model of Injury," *NeuroMolecular Medicine*, vol. 19, no. 1, pp. 122–135, Mar. 2017. DOI: 10.1007/s12017-016-8436-4.

[99] M. Orešič, J. P. Posti, M. H. Kamstrup-Nielsen, *et al.*, "Human Serum Metabolites Associate With Severity and Patient Outcomes in Traumatic Brain Injury," *eBioMedicine*, vol. 12, pp. 118–126, Oct. 2016. DOI: 10.1016/j.ebiom.2016.07.015.

[100] L. Yi, S. Shi, Y. Wang, *et al.*, "Serum Metabolic Profiling Reveals Altered Metabolic Pathways in Patients with Post-traumatic Cognitive Impairments," *Scientific Reports*, vol. 6, no. 1, p. 21 320, Feb. 2016. DOI: 10.1038/srep21320.

[101] A. D'Alessandro, T. Nemkov, H. B. Moore, *et al.*, "Metabolomics of trauma-associated death: Shared and fluid-specific features of human plasma vs lymph," *Blood Transfusion*, vol. 14, no. 3, pp. 185–194, May 2016. DOI: 10.2450/2016.0208-15.

[102] D. R. Lexcen, E. R. Lusczek, N. E. Witowski, K. E. Mulier, and G. J. Beilman, "Metabolomics classifies phase of care and identifies risk for mortality in a porcine model of multiple injuries and hemorrhagic shock," *Journal of Trauma and Acute Care Surgery*, vol. 73, no. 2, S147, Aug. 2012. DOI: 10.1097/TA.0b013e3182609821.

[103] E. D. Peltz, A. D'Alessandro, E. E. Moore, *et al.*, "Pathologic metabolism: An exploratory study of the plasma metabolome of critical injury," *Journal of Trauma and Acute Care Surgery*, vol. 78, no. 4, p. 742, Apr. 2015. DOI: 10.1097/TA.0000000000000058

[104] B. J. Blaise, A. Gouel-Chéron, B. Floccard, G. Monneret, and B. Allaouchiche, "Metabolic Phenotyping of Traumatized Patients Reveals a Susceptibility to Sepsis," *Analytical Chemistry*, vol. 85, no. 22, pp. 10 850–10 855, Nov. 2013. DOI: 10.1021/ac402235q.

[105] C. C. Finnerty, M. G. Jeschke, W.-J. Qian, *et al.*, "Determination of Burn Patient Outcome by Large-Scale Quantitative Discovery Proteomics," *Critical Care Medicine*, vol. 41, no. 6, p. 1421, Jun. 2013. DOI: 10.1097/CCM.0b013e31827c072e.

[106] J. Hazeldine, P. Hampson, and J. M. Lord, "The diagnostic and prognostic value of systems biology research in major traumatic and thermal injury: A review," *Burns & Trauma*, vol. 4, s41038-016-0059–3, Dec. 2016. DOI: 10.1186/s41038-016-0059-3.

[107] C. S. Davis, S. E. Janus, M. J. Mosier, *et al.*, "Inhalation Injury Severity and Systemic Immune Perturbations in Burned Adults," *Annals of Surgery*, vol. 257, no. 6, p. 1137, Jun. 2013. DOI: 10.1097/SLA.0b013e318275f424.

[108] C. C. Finnerty, H. Ju, H. Spratt, *et al.*, "Proteomics Improves the Prediction of Burns Mortality: Results from Regression Spline Modeling," *Clinical and Translational Science*, vol. 5, no. 3, pp. 243–249, 2012. DOI: 10.1111/j.1752-8062.2012.00412.x.

[109] Y. Zhang, B. Cai, H. Jiang, *et al.*, "Use of 1H-nuclear magnetic resonance to screen a set of biomarkers for monitoring metabolic disturbances in severe burn patients," *Critical Care*, vol. 18, no. 4, R159, Jul. 2014. DOI: 10.1186/cc13999.

[110] X.-R. Liu, X.-F. Zheng, S.-Z. Ji, *et al.*, "Metabolomic analysis of thermally injured and/or septic rats," *Burns*, vol. 36, no. 7, pp. 992–998, Nov. 2010. DOI: 10.1016/j.burns.2010.03.015.

[111] G. A. N. Gowda and D. Djukovic, "Overview of Mass Spectrometry-Based Metabolomics: Opportunities and Challenges," in *Mass Spectrometry in Metabolomics: Methods and Protocols*, D. Raftery, Ed., New York, NY: Springer, 2014, pp. 3–12, ISBN: 978-1-4939-1258-2. DOI: 10.1007/978-1-4939-1258-2_1.

[112] W. J. Griffiths and Y. Wang, "Mass spectrometry : From proteomics to metabolomics and lipidomics," *Chemical Society Reviews*, vol. 38, no. 7, pp. 1882–1896, 2009. DOI: 10.1039/B618553N.

[113] R. Ramautar, G. W. Somsen, and G. J. de Jong, "CE-MS for metabolomics: Developments and applications in the period 2016–2018," *ELECTROPHORESIS*, vol. 40, no. 1, pp. 165–179, 2019. DOI: 10.1002/elps.201800323.

[114] Q. Ma, Y. Li, M. Wang, *et al.*, "Progress in Metabonomics of Type 2 Diabetes Mellitus," *Molecules*, vol. 23, no. 7, p. 1834, Jul. 2018. DOI: 10.3390/molecules23071834.

[115] D. S. Wishart, "Metabolomics for Investigating Physiological and Pathophysiological Processes," *Physiological Reviews*, vol. 99, no. 4, pp. 1819–1875, Oct. 2019. DOI: 10.1152/physrev.00035.2018.

[116] Z. A. Al-Talla, S. H. Akrawi, and A.-H. M. Emwas, "Solid state NMR and bioequivalence comparison of the pharmacokinetic parameters of two formulations of clindamycin," *International journal of clinical pharmacology and therapeutics*, vol. 49, no. 7, pp. 469–476, Jul. 2011. DOI: 10.5414/cp201478.

[117] Z. A. Al-Talla, S. H. Akrawi, L. T. Tolley, S. H. Sioud, M. F. Zaater, and A.-H. M. Emwas, "Bioequivalence assessment of two formulations of ibuprofen," *Drug Design, Development and Therapy*, vol. 5, no. null, pp. 427–433, Oct. 2011. DOI: 10.2147/DDDT.S24504.

[118] J. Li, S. Wang, M. Wang, W. Shi, X. Du, and C. Sun, "The toxicity of 3-chloropropane-1,2-dipalmitate in Wistar rats and a metabonomics analysis of rat urine by ultra-performance liquid chromatography–mass spectrometry," *Chemico-Biological Interactions*, vol. 206, no. 2, pp. 337–345, Nov. 2013. DOI: 10.1016/j.cbi.2013.10.004.

[119] P. Molz, J. H. Ellwanger, C. Eliete Iochims dos Santos, *et al.*, "A metabolomics approach to evaluate the effects of shiitake mushroom (*Lentinula edodes*) treatment in undernourished young rats," *Nuclear Instruments and Methods in Physics Research Section B: Beam Interactions with Materials and Atoms*, The 13th International Conference on Particle Induced X-ray Emission (PIXE 2013), vol. 318, pp. 194–197, Jan. 2014. DOI: 10.1016/j.nimb.2013.05.108.

[120] M. Szultka, R. Krzeminski, J. Walczak, M. Jackowski, and B. Buszewski, "Pharmacokinetic study of amoxicillin in human plasma by solid-phase microextraction followed by high-performance liquid chromatography–triple quadrupole mass spectrometry," *Biomedical Chromatography*, vol. 28, no. 2, pp. 255–264, 2014. DOI: 10.1002/bmc.3014.

[121] K. Lan, Y. Zhang, J. Yang, and L. Xu, "Simple quality assessment approach for herbal extracts using high performance liquid chromatography-UV based metabolomics platform," *Journal of Chromatography A*, vol. 1217, no. 8, pp. 1414–1418, Feb. 2010. DOI: 10.1016/j.chroma.2009.12.031.

[122] X. Liang, L. Zhang, X. Zhang, *et al.*, "Qualitative and quantitative analysis of traditional Chinese medicine Niu Huang Jie Du Pill using ultra performance liquid chromatography coupled with tunable UV detector and rapid resolution liquid chromatography coupled with time-of-flight tandem mass spectrometry," *Journal of Pharmaceutical and Biomedical Analysis*, vol. 51, no. 3, pp. 565–571, Feb. 2010. DOI: 10.1016/j.jpba.2009.09.015.

[123] S. Zheng, M. Yu, X. Lu, *et al.*, "Urinary metabonomic study on biochemical changes in chronic unpredictable mild stress model of depression," *Clinica Chimica Acta*, vol. 411, no. 3, pp. 204–209, Feb. 2010. DOI: 10.1016/j.cca.2009.11.003.

[124] F. R. Pinu, D. J. Beale, A. M. Paten, *et al.*, "Systems Biology and Multi-Omics Integration: Viewpoints from the Metabolomics Research Community," *Metabolites*, vol. 9, no. 4, p. 76, Apr. 2019. DOI: 10.3390/metabo9040076.

[125] V. Pirro, C. M. Alfaro, A. K. Jarmusch, E. M. Hattab, A. A. Cohen-Gadol, and R. G. Cooks, "Intraoperative assessment of tumor margins during glioma resection by desorption electrospray ionization-mass spectrometry," *Proceedings of the National Academy of Sciences*, vol. 114, no. 26, pp. 6700–6705, Jun. 2017. DOI: 10.1073/pnas.1706459114.

[126] H. M. Brown, C. M. Alfaro, V. Pirro, *et al.*, "Intraoperative Mass Spectrometry Platform for IDH Mutation Status Prediction, Glioma Diagnosis, and Estimation of Tumor Cell Infiltration," *The Journal of Applied Laboratory Medicine*, vol. 6, no. 4, pp. 902–916, Jul. 2021. DOI: 10.1093/jalm/jfaa233.

[127] A.-H. Emwas, R. Roy, R. T. McKay, *et al.*, "NMR Spectroscopy for Metabolomics Research," *Metabolites*, vol. 9, no. 7, p. 123, Jul. 2019. DOI: 10.3390/metabo9070123.

[128] R. R. da Silva, P. C. Dorrestein, and R. A. Quinn, "Illuminating the dark matter in metabolomics," *Proceedings of the National Academy of Sciences*, vol. 112, no. 41, pp. 12 549–12 550, Oct. 2015. DOI: 10.1073/pnas.1516878112.

[129] O. P. Trifonova, D. L. Maslov, E. E. Balashova, and P. G. Lokhov, "Mass spectrometry-based metabolomics diagnostics – myth or reality?" *Expert Review of Proteomics*, vol. 18, no. 1, pp. 7–12, Jan. 2021. DOI: 10.1080/14789450.2021.1893695.

[130] L. Corte, M. Tiecco, L. Roscini, *et al.*, "FTIR Metabolomic Fingerprint Reveals Different Modes of Action Exerted by Structural Variants of N-Alkyltropinium Bromide Surfactants on Escherichia coli and Listeria innocua Cells," *PLOS ONE*, vol. 10, no. 1, e0115275, Jan. 14, 2015, ISSN: 1932-6203. DOI: 10.1371/journal.pone.0115275. (visited on 05/31/2025).

[131] N. Cebi, H. Bekiroglu, and A. Erarslan, "Nondestructive Metabolomic Fingerprinting: FTIR, NIR and Raman Spectroscopy in Food Screening," *Molecules*, vol. 28, no. 23, p. 7933, 23 Jan. 2023, ISSN: 1420-3049. DOI: 10.3390/molecules28237933. (visited on 05/31/2025).

[132] Q. Teng, D. R. Ekman, W. Huang, and T. W. Collette, "Push-through direct injection NMR: An optimized automation method applied to metabolomics," *The Analyst*, vol. 137, no. 9, p. 2226, 2012, ISSN: 0003-2654, 1364-5528. DOI: 10.1039/c2an16251b. (visited on 06/01/2025).

[133] S. E. G. Porter, D. R. Stoll, S. C. Rutan, P. W. Carr, and J. D. Cohen, "Analysis of Four-Way Two-Dimensional Liquid Chromatography-Diode Array Data: Application to Metabolomics," *Analytical Chemistry*, vol. 78, no. 15, pp. 5559–5569, Aug. 1, 2006, ISSN: 0003-2700. DOI: 10.1021/ac0606195. (visited on 06/01/2025).

[134] L. Shintu, R. Baudoin, V. Navratil, *et al.*, "Metabolomics-on-a-Chip and Predictive Systems Toxicology in Microfluidic Bioartificial Organs," *Analytical Chemistry*, vol. 84, no. 4, pp. 1840–1848, Feb. 21, 2012, ISSN: 0003-2700. DOI: 10.1021/ac2011075. (visited on 06/01/2025).

[135] H. Chen, Z. Pan, N. Talaty, D. Raftery, and R. G. Cooks, "Combining desorption electrospray ionization mass spectrometry and nuclear magnetic resonance for differential metabolomics without sample preparation," *Rapid Communications in Mass Spectrometry*, vol. 20, no. 10, pp. 1577–1584, 2006, ISSN: 1097-0231. DOI: 10.1002/rcm.2474. (visited on 06/01/2025).

[136] M. Zhou, J. F. McDonald, and F. M. Fernández, "Optimization of a direct analysis in real time/time-of-flight mass spectrometry method for rapid serum metabolomic fingerprinting," *Journal of the American Society for Mass Spectrometry*, vol. 21, no. 1, pp. 68–75, Jan. 1, 2010. DOI: 10.1016/j.jasms.2009.09.004. (visited on 06/01/2025).

[137] P. Miggiels, B. Wouters, G. J. P. van Westen, A.-C. Dubbelman, and T. Hankemeier, "Novel technologies for metabolomics: More for less," *TrAC Trends in Analytical Chemistry*, vol. 120, p. 115 323, Nov. 1, 2019, ISSN: 0165-9936. DOI: 10.1016/j.trac.2018.11.021. (visited on 05/20/2025).

[138] D. Damborska, T. Bertok, E. Dosekova, *et al.*, "Nanomaterial-based biosensors for detection of prostate specific antigen," *Microchimica Acta*, vol. 184, no. 9, pp. 3049–3067, Sep. 2017. DOI: 10.1007/s00604-017-2410-1.

[139] T. Zhang, Y. He, J. Wei, and L. Que, "Nanostructured optical microchips for cancer biomarker detection," *Biosensors and Bioelectronics*, vol. 38, no. 1, pp. 382–388, Oct. 2012. DOI: 10.1016/j.bios.2012.06.029.

[140] T. B. Salisbury and S. Arthur, "The Regulation and Function of the L-Type Amino Acid Transporter 1 (LAT1) in Cancer," *International Journal of Molecular Sciences*, vol. 19, no. 8, p. 2373, Aug. 2018. DOI: 10.3390/ijms19082373.

[141] J. Huang, A. M. Mondul, S. J. Weinstein, *et al.*, "Serum metabolomic profiling of prostate cancer risk in the prostate, lung, colorectal, and ovarian cancer screening trial," *British Journal of Cancer*, vol. 115, no. 9, pp. 1087–1095, Oct. 2016. DOI: 10.1038/bjc.2016.305.

[142] M. Johansson, B. Van Guelpen, S. E. Vollset, *et al.*, "One-Carbon Metabolism and Prostate Cancer Risk: Prospective Investigation of Seven Circulating B Vitamins and Metabolites," *Cancer Epidemiology, Biomarkers & Prevention*, vol. 18, no. 5, pp. 1538–1543, May 2009. DOI: 10.1158/1055-9965.EPI-08-1193.

[143] K. Glunde, M.-F. Penet, L. Jiang, M. A. Jacobs, and Z. M. Bhujwalla, "Choline metabolism-based molecular diagnosis of cancer: An update," *Expert Review of Molecular Diagnostics*, vol. 15, no. 6, pp. 735–747, Jun. 2015. DOI: 10.1586/14737159.2015.1039515.

[144] B. J. Trock, "Application of metabolomics to prostate cancer," *Urologic Oncology: Seminars and Original Investigations*, Metabolomics, vol. 29, no. 5, pp. 572–581, Sep. 2011. DOI: 10.1016/j.urolonc.2011.08.002.

[145] R. S. Kelly, M. G. Vander Heiden, E. Giovannucci, and L. A. Mucci, "Metabolomic Biomarkers of Prostate Cancer: Prediction, Diagnosis, Progression, Prognosis, and Recurrence," *Cancer Epidemiology, Biomarkers & Prevention*, vol. 25, no. 6, pp. 887–906, May 2016. DOI: 10.1158/1055-9965.EPI-15-1223.

[146] A. Sreekumar, L. M. Poisson, T. M. Rajendiran, *et al.*, "Metabolomic profiles delineate potential role for sarcosine in prostate cancer progression," *Nature*, vol. 457, no. 7231, pp. 910–914, Feb. 2009. DOI: 10.1038/nature07762.

[147] J. W. Locasale, "Serine, glycine and one-carbon units: Cancer metabolism in full circle," *Nature Reviews Cancer*, vol. 13, no. 8, pp. 572–583, Aug. 2013. DOI: 10.1038/nrc3557.

[148] L. C. Soliman, Y. Hui, A. K. Hewavitharana, and D. D. Y. Chen, "Monitoring potential prostate cancer biomarkers in urine by capillary electrophoresis–tandem mass spectrometry," *Journal of Chromatography A*, Capillary Electromigration Techniques, vol. 1267, pp. 162–169, Dec. 2012. DOI: 10.1016/j.chroma.2012.07.021.

[149] M. Kobayashi, S. Kurokawa, and A. Tokue, "Intraindividual Variation in Total and Percent Free Prostate-Specific Antigen Levels in Prostate Cancer Suspects," *Urologia Internationalis*, vol. 74, no. 3, pp. 198–202, Apr. 2005. DOI: 10.1159/000083548.

[150] "Prostate cancer statistics," World Cancer Research Fund. (), (visited on 05/20/2025).

[151] G. S. Sandhu and G. L. Andriole, "Overdiagnosis of Prostate Cancer," *JNCI Monographs*, vol. 2012, no. 45, pp. 146–151, Dec. 1, 2012, ISSN: 1052-6773. DOI: 10.1093/jncimonographs/lgs031. (visited on 05/20/2025).

[152] M. J. Roberts, H. J. Schirra, M. F. Lavin, and R. A. Gardiner, "Metabolomics: A Novel Approach to Early and Noninvasive Prostate Cancer Detection," *Korean Journal of Urology*, vol. 52, no. 2, pp. 79–89, Feb. 1, 2011, ISSN: 2005-6737. DOI: 10.4111/kju.2011.52.2.79. (visited on 05/20/2025).

[153] B. Faubert, A. Solmonson, and R. J. DeBerardinis, "Metabolic reprogramming and cancer progression," *Science*, vol. 368, no. 6487, eaaw5473, Apr. 10, 2020. DOI: 10.1126/science.aaw5473. (visited on 05/20/2025).

[154] M. Pujana-Vaquerizo, L. Bozal-Basterra, and A. Carracedo, "Metabolic adaptations in prostate cancer," *British Journal of Cancer*, vol. 131, no. 8, pp. 1250–1262, Nov. 2024, ISSN: 1532-1827. DOI: 10.1038/s41416-024-02762-z. (visited on 05/20/2025).

[155] N. Cernei, Z. Heger, J. Gumulec, *et al.*, "Sarcosine as a Potential Prostate Cancer Biomarker—A Review," *International Journal of Molecular Sciences*, vol. 14, no. 7, pp. 13 893–13 908, 7 Jul. 2013, ISSN: 1422-0067. DOI: 10.3390/ijms140713893. (visited on 05/20/2025).

[156] E. Benedetti, K. Chetnik, T. Flynn, *et al.*, "Plasma metabolomics profiling of 580 patients from an Early Detection Research Network prostate cancer cohort," *Scientific Data*, vol. 10, no. 1, p. 830, Nov. 25, 2023, ISSN: 2052-4463. DOI: 10.1038/s41597-023-02750-7. (visited on 05/20/2025).

[157] A. P. Siskos, P. Jain, W. Römisch-Margl, *et al.*, "Interlaboratory Reproducibility of a Targeted Metabolomics Platform for Analysis of Human Serum and Plasma," *Analytical Chemistry*, vol. 89, no. 1, pp. 656–665, Jan. 2017. DOI: 10.1021/acs.analchem.6b02930.

[158] S. Ravanbakhsh, P. Liu, T. C. Bjorndahl, *et al.*, "Correction: Accurate, Fully-Automated NMR Spectral Profiling for Metabolomics," *PLOS ONE*, vol. 10, no. 7, e0132873, Jul. 2015. DOI: 10.1371/journal.pone.0132873.

[159] A. Furukawa, T. Konuma, S. Yanaka, and K. Sugase, "Quantitative analysis of protein–ligand interactions by NMR," *Progress in Nuclear Magnetic Resonance Spectroscopy*, vol. 96, pp. 47–57, Aug. 1, 2016, ISSN: 0079-6565. DOI: 10.1016/j.pnmrs.2016.02.002. (visited on 12/28/2024).

[160] A. G. Marshall and F. R. Verdun, *Fourier Transforms in NMR, Optical, and Mass Spectrometry: A User's Handbook*. Elsevier, Feb. 25, 2016, 470 pp., ISBN: 978-1-4832-9384-4. Google Books: F_nJCgAAQBAJ.

[161] M. H. Levitt, *Spin Dynamics: Basics of Nuclear Magnetic Resonance*. John Wiley & Sons, Apr. 2008, ISBN: 978-0-470-51118-3.

[162] D. L. Olson, T. L. Peck, A. G. Webb, R. L. Magin, and J. V. Sweedler, "High-Resolution Microcoil $ˆ1$H-NMR for Mass-Limited, Nanoliter-Volume Samples," *Science*, vol. 270, no. 5244, pp. 1967–1970, 1995, ISSN: 0036-8075. JSTOR: 2888822. (visited on 12/22/2024).

[163] N. Wu, T. L. Peck, A. G. Webb, R. L. Magin, and J. V. Sweedler, "Nanoliter Volume Sample cells for 1H NMR: Application to Online Detection in Capillary Electrophoresis," *Journal of the American Chemical Society*, vol. 116, no. 17, pp. 7929–7930, Aug. 1994, ISSN: 0002-7863, 1520-5126. DOI: 10.1021/ja00096a073. (visited on 12/23/2024).

[164] P. Lepucki, A. P. Dioguardi, D. Karnaushenko, O. G. Schmidt, and H.-J. Grafe, "The normalized limit of detection in NMR spectroscopy," *Journal of Magnetic Resonance*, vol. 332, p. 107 077, Nov. 1, 2021, ISSN: 1090-7807. DOI: 10.1016/j.jmr.2021.107077. (visited on 01/24/2025).

[165] T. Dohi and Y. Yokoyama, "A Low-resistance and Low-parasitic Capacitance Micro Coil for MRI Fabricated by Selective Deposition on 3D Stepped Helical Structures," *IEEJ Transactions on Sensors and Micromachines*, vol. 137, no. 1, pp. 2–7, 2017. DOI: 10.1541/ieejsmas.137.2.

[166] J. Xie, X. You, Y. Huang, *et al.*, "3D-printed integrative probeheads for magnetic resonance," *Nature Communications*, vol. 11, no. 1, p. 5793, Nov. 13, 2020, ISSN: 2041-1723. DOI: 10.1038/s41467-020-19711-y. (visited on 01/26/2025).

[167] V. Moxley-Paquette, J. Pellizzari, D. Lane, *et al.*, "Exploration of Materials for Three-Dimensional NMR Microcoil Production via CNC Micromilling and Laser Etching," *Analytical Chemistry*, vol. 96, no. 33, pp. 13 588–13 597, Aug. 20, 2024, ISSN: 0003-2700. DOI: 10.1021/acs.analchem.4c02373. (visited on 01/24/2025).

[168] R. M. Noor and A. M. Shkel, "MEMS Components for NMR Atomic Sensors," *Journal of Microelectromechanical Systems*, vol. 27, no. 6, pp. 1148–1159, Dec. 2018, ISSN: 1941-0158. DOI: 10.1109/JMEMS.2018.2874451. (visited on 01/28/2025).

[169] J. A. Bernardo, "A new approach for the optimization of Implantable NMR micro-probe for In-vivo Application : Alzheimer's disease," Ph.D. dissertation, Université de Lyon, Mar. 25, 2022. (visited on 01/26/2025).

[170] T. Tritrakarn, M. Takahashi, and T. Okamura, "Optimization of RF coil geometry for NMR/MRI applications using a genetic algorithm," *Journal of Magnetic Resonance*, vol. 362, p. 107 685, May 1, 2024, ISSN: 1090-7807. DOI: 10.1016/j.jmr.2024.107685. (visited on 01/24/2025).

[171] M. V. Gomez, S. Baas, and A. H. Velders, "Multinuclear 1D and 2D NMR with 19F-Photo-CIDNP hyperpolarization in a microfluidic chip with untuned microcoil," *Nature Communications*, vol. 14, no. 1, p. 3885, Jun. 30, 2023, ISSN: 2041-1723. DOI: 10.1038/s41467-023-39537-8. (visited on 01/24/2025).

[172] H. Lees, M. Millan, F. Ahamed, *et al.*, "Multi-sample measurement of hyperpolarized pyruvate-to-lactate flux in melanoma cells," *NMR in Biomedicine*, vol. 34, no. 3, e4447, 2021, ISSN: 1099-1492. DOI: 10.1002/nbm.4447. (visited on 01/26/2025).

[173] S. Jeong, R. Eskandari, S. M. Park, *et al.*, "Real-time quantitative analysis of metabolic flux in live cells using a hyperpolarized micromagnetic resonance spectrometer," *Science Advances*, vol. 3, no. 6, e1700341, Jun. 16, 2017. DOI: 10.1126/sciadv.1700341. (visited on 01/28/2025).

[174] S. Z. Kiss, N. MacKinnon, and J. G. Korvink, "Microfluidic Overhauser DNP chip for signal-enhanced compact NMR," *Scientific Reports*, vol. 11, no. 1, p. 4671, Feb. 25, 2021, ISSN: 2045-2322. DOI: 10.1038/s41598-021-83625-y. (visited on 01/26/2025).

[175] N. Sahin Solmaz, M. Grisi, A. V. Matheoud, G. Gualco, and G. Boero, "Single-Chip Dynamic Nuclear Polarization Microsystem," *Analytical Chemistry*, vol. 92, no. 14, pp. 9782–9789, Jul. 21, 2020, ISSN: 0003-2700. DOI: 10.1021/acs.analchem.0c01221. (visited on 01/26/2025).

[176] L. Bordonali, N. Nordin, E. Fuhrer, N. MacKinnon, and J. G. Korvink, "Parahydrogen based NMR hyperpolarisation goes micro: An alveolus for small molecule chemosensing," *Lab on a Chip*, vol. 19, no. 3, pp. 503–512, 2019. DOI: 10.1039/C8LC01259H. (visited on 01/26/2025).

[177] Y. Chen, H. S. Mehta, M. C. Butler, *et al.*, "High-resolution microstrip NMR detectors for subnanoliter samples," *Physical Chemistry Chemical Physics*, vol. 19, no. 41, pp. 28 163–28 174, Oct. 25, 2017, ISSN: 1463-9084. DOI: 10.1039/C7CP03933F. (visited on 01/28/2025).

[178] Y.-T. Cheng, J. G. Korvink, and M. Jouda, "A field focusing butterfly stripline detects NMR at higher signal-to-noise ratio," *Journal of Magnetic Resonance*, vol. 353, p. 107 517, Aug. 1, 2023, ISSN: 1090-7807. DOI: 10.1016/j.jmr.2023.107517. (visited on 01/24/2025).

[179] V. Moxley-Paquette, B. Wu, D. Lane, *et al.*, "Evaluation of double-tuned single-sided planar microcoils for the analysis of small 13C enriched biological samples using 1H-13C 2D heteronuclear correlation NMR spectroscopy," *Magnetic Resonance in Chemistry*, vol. 60, no. 3, pp. 386–397, 2022, ISSN: 1097-458X. DOI: 10.1002/mrc.5227. (visited on 01/24/2025).

[180] N. V. Orlov and V. P. Ananikov, "NMR analysis of chiral alcohols and amines: Development of an environmentally benign "in tube" procedure with high efficiency and improved detection limit," *Green Chemistry*, vol. 13, no. 7, pp. 1735–1744, Jul. 2011. DOI: 10.1039/C1GC15191F.

[181] M. Bastawrous, O. Gruschke, R. Soong, *et al.*, "Comparing the Potential of Helmholtz and Planar NMR Microcoils for Analysis of Intact Biological Samples," *Analytical Chemistry*, vol. 94, no. 23, pp. 8523–8532, Jun. 14, 2022, ISSN: 0003-2700. DOI: 10.1021/acs.analchem.2c01560. (visited on 01/24/2025).

[182] P. Lepucki, A. I. Egunov, M. Rosenkranz, *et al.*, "Self-Assembled Rolled-Up Microcoils for nL Microfluidics NMR Spectroscopy," *Advanced Materials Technologies*, vol. 6, no. 1, p. 2 000 679, 2021, ISSN: 2365-709X. DOI: 10.1002/admt.202000679. (visited on 01/26/2025).

[183] N. Wang, M. V. Meissner, N. MacKinnon, V. Luchnikov, D. Mager, and J. G. Korvink, "Fast prototyping of microtubes with embedded sensing elements made possible with an inkjet printing and rolling process," *Journal of Micromechanics and Microengineering*, vol. 28, no. 2, p. 025 003, Dec. 2017, ISSN: 0960-1317. DOI: 10.1088/1361-6439/aa7a61. (visited on 01/28/2025).

[184] D. D. Karnaushenko, D. Karnaushenko, H.-J. Grafe, V. Kataev, B. Büchner, and O. G. Schmidt, "Rolled-Up Self-Assembly of Compact Magnetic Inductors, Transformers, and Resonators," *Advanced Electronic Materials*, vol. 4, no. 11, p. 1 800 298, 2018, ISSN: 2199-160X. DOI: 10.1002/aelm.201800298. (visited on 01/26/2025).

[185] H. Davoodi, N. Nordin, L. Bordonali, J. G. Korvink, N. MacKinnon, and V. Badilita, "An NMR-compatible microfluidic platform enabling in situ electrochemistry," *Lab on a Chip*, vol. 20, no. 17, pp. 3202–3212, 2020. DOI: 10.1039/D0LC00364F. (visited on 01/26/2025).

[186] N. Nordin, L. Bordonali, H. Davoodi, *et al.*, "Real-Time NMR Monitoring of Spatially Segregated Enzymatic Reactions in Multilayered Hydrogel Assemblies," *Angewandte Chemie International Edition*, vol. 60, no. 35, pp. 19 176–19 182, 2021, ISSN: 1521-3773. DOI: 10.1002/anie.202103585. (visited on 01/26/2025).

[187] I. Swyer, R. Soong, M. D. M. Dryden, *et al.*, "Interfacing digital microfluidics with high-field nuclear magnetic resonance spectroscopy," *Lab on a Chip*, vol. 16, no. 22, pp. 4424–4435, 2016. DOI: 10.1039/C6LC01073C. (visited on 01/28/2025).

[188] I. Swyer, S. von der Ecken, B. Wu, *et al.*, "Digital microfluidics and nuclear magnetic resonance spectroscopy for in situ diffusion measurements and reaction monitoring," *Lab on a Chip*, vol. 19, no. 4, pp. 641–653, Feb. 12, 2019, ISSN: 1473-0189. DOI: 10.1039/C8LC01214H. (visited on 01/26/2025).

[189] J. Handwerker, M. Eder, M. Tibiletti, *et al.*, "An array of fully-integrated quadrature TX/RX NMR field probes for MRI trajectory mapping," in *ESSCIRC Conference 2016: 42nd European Solid-State Circuits Conference*, Sep. 2016, pp. 217–220. DOI: 10.1109/ESSCIRC.2016.7598281. (visited on 01/28/2025).

[190] G. Sivelli, G. M. Conley, C. Herrera, *et al.*, "NMR spectroscopy of a single mammalian early stage embryo," *Journal of Magnetic Resonance*, vol. 335, p. 107 142, Feb. 1, 2022, ISSN: 1090-7807. DOI: 10.1016/j.jmr.2021.107142. (visited on 01/26/2025).

[191] D. H. Lysak, M. Grisi, K. Marable, *et al.*, "Exploring the Potential of Broadband Complementary Metal Oxide Semiconductor Micro-Coil Nuclear Magnetic Resonance for Environmental Research," *Molecules*, vol. 28, no. 13, p. 5080, 13 Jan. 2023, ISSN: 1420-3049. DOI: 10.3390/molecules28135080. (visited on 01/24/2025).

[192] O. Nassar, M. Jouda, M. Rapp, D. Mager, J. G. Korvink, and N. MacKinnon, "Integrated impedance sensing of liquid sample plug flow enables automated high throughput NMR spectroscopy," *Microsystems & Nanoengineering*, vol. 7, no. 1, pp. 1–17, Apr. 14, 2021, ISSN: 2055-7434. DOI: 10.1038/s41378-021-00253-2. (visited on 01/26/2025).

[193] K.-M. Lei, D. Ha, Y.-Q. Song, *et al.*, "Portable NMR with Parallelism," *Analytical Chemistry*, vol. 92, no. 2, pp. 2112–2120, Jan. 21, 2020, ISSN: 0003-2700. DOI: 10.1021/acs.analchem.9b04633. (visited on 01/26/2025).

[194] S. Huber, C. Min, C. Staat, *et al.*, "Multichannel digital heteronuclear magnetic resonance biosensor," *Biosensors and Bioelectronics*, vol. 126, pp. 240–248, Feb. 1, 2019, ISSN: 0956-5663. DOI: 10.1016/j.bios.2018.10.052. (visited on 01/26/2025).

[195] L. Fakri-Bouchet, "Implantable Microcoil for In-vivo Magnetic Resonance Spectroscopy," *International Journal of Biosensors & Bioelectronics*, vol. 3, no. 2, Sep. 15, 2017, ISSN: 25732838. DOI: 10.15406/ijbsbe.2017.03.00056. (visited on 01/28/2025).

[196] J. Handwerker, M. Pérez-Rodas, M. Beyerlein, *et al.*, "A CMOS NMR needle for probing brain physiology with high spatial and temporal resolution," *Nature Methods*, vol. 17, no. 1, pp. 64–67, Jan. 2020, ISSN: 1548-7105. DOI: 10.1038/s41592-019-0640-3. (visited on 01/26/2025).

[197] J. Smits, J. T. Damron, P. Kehayias, *et al.*, "Two-dimensional nuclear magnetic resonance spectroscopy with a microfluidic diamond quantum sensor," *Science Advances*, vol. 5, no. 7, eaaw7895, Jul. 26, 2019. DOI: 10.1126/sciadv.aaw7895. (visited on 01/26/2025).

[198] R. M. Noor, N. Kulachenkov, M. H. Asadian, and A. M. Shkel, "Study on Mems Glass-blown Cells for NMR Sensors," in *2019 IEEE International Symposium on Inertial Sensors and Systems (INERTIAL)*, Apr. 2019, pp. 1–4. DOI: 10.1109/ISISS.2019.8739655. (visited on 01/28/2025).

[199] S. G. Hyberts, S. A. Robson, and G. Wagner, "Exploring Signal-to-noise Ratio and Sensitivity in Non-Uniformly Sampled Multi-Dimensional NMR Spectra," *Journal of biomolecular NMR*, vol. 55, no. 2, pp. 167–178, Feb. 2013. DOI: 10.1007/s10858-012-9698-2.

[200] N. Spengler, P. T. While, M. V. Meissner, U. Wallrabe, and J. G. Korvink, "Magnetic Lenz lenses improve the limit-of-detection in nuclear magnetic resonance," *PLOS ONE*, vol. 12, no. 8, e0182779, Aug. 2017. DOI: 10.1371/journal.pone.0182779.

[201] T. Meier, N. Wang, D. Mager, J. G. Korvink, S. Petitgirard, and L. Dubrovinsky, "Magnetic flux tailoring through Lenz lenses for ultrasmall samples: A new pathway to high-pressure nuclear magnetic resonance," *Science Advances*, vol. 3, no. 12, eaao5242, Dec. 8, 2017. DOI: 10.1126/sciadv.aao5242. (visited on 01/28/2025).

[202] M. Bastawrous, R. Ghosh Biswas, R. Soong, *et al.*, "Lenz Lenses in a Cryoprobe: Boosting NMR Sensitivity Toward Environmental Monitoring of Mass-Limited Samples," *Analytical Chemistry*, vol. 95, no. 2, pp. 1327–1334, Jan. 17, 2023, ISSN: 0003-2700. DOI: 10.1021/acs.analchem.2c04203. (visited on 01/24/2025).

[203] J. Liang, H. Davoodi, S. Wadhwa, V. Badilita, and J. G. Korvink, "Broadband stripline Lenz lens achieves 11 × NMR signal enhancement," *Scientific Reports*, vol. 14, no. 1, p. 1645, Jan. 2024. DOI: 10.1038/s41598-023-50616-0.

[204] J. Liang, H. Davoodi, S. Wadhwa, V. Badilita, and J. G. Korvink, "Broadband stripline Lenz lens achieves 11 × NMR signal enhancement," *Scientific Reports*, vol. 14, no. 1, p. 1645, Jan. 18, 2024, ISSN: 2045-2322. DOI: 10.1038/s41598-023-50616-0. (visited on 01/24/2025).

[205] J. Schoenmaker, K. R. Pirota, and J. C. Teixeira, "Magnetic flux amplification by Lenz lenses," *Review of Scientific Instruments*, vol. 84, no. 8, p. 085 120, Aug. 2013, ISSN: 0034-6748, 1089-7623. DOI: 10.1063/1.4819234. (visited on 10/17/2022).

[206] A. M. A. A. S. Tajabadi, P. Dehghani, D. S. Assi, *et al.*, "Compact Magnetic Field Amplification by Tuned Lenz Lens," *IEEE Sensors Journal*, vol. 23, no. 22, pp. 27 154–27 160, Nov. 2023, ISSN: 1558-1748. DOI: 10.1109/JSEN.2023.3297254. (visited on 02/09/2025).

[207] N. Spengler, P. T. While, M. V. Meissner, U. Wallrabe, and J. G. Korvink, "Magnetic Lenz lenses improve the limit-of-detection in nuclear magnetic resonance," *PLOS ONE*, vol. 12, no. 8, e0182779, Aug. 15, 2017, ISSN: 1932-6203. DOI: 10.1371/journal.pone.0182779. (visited on 10/28/2022).

[208] M. Jouda, R. Kamberger, J. Leupold, *et al.*, "A comparison of Lenz lenses and LC resonators for NMR signal enhancement," *Concepts in Magnetic Resonance Part B: Magnetic Resonance Engineering*, vol. 47B, no. 3, e21357, 2017, ISSN: 1552-504X. DOI: 10.1002/cmr.b.21357. (visited on 11/12/2022).

[209] R. Kamberger, K. Göbel-Guéniot, J. Gerlach, *et al.*, "Improved method for MR microscopy of brain tissue cultured with the interface method combined with Lenz lenses," *Magnetic Resonance Imaging*, vol. 52, pp. 24–32, Oct. 2018, ISSN: 0730725X. DOI: 10.1016/j.mri.2018.05.010. (visited on 01/17/2023).

[210] "CST Studio Suite & Opera Recommended Hardware." (), (visited on 12/20/2022).

[211] "CODATA Value: Proton gyromagnetic ratio in MHz/T." (), (visited on 02/01/2023).

[212] "Coil32 - Coil64 for 64-bit Windows - Coil64 for 64-bit Windows." (), (visited on 12/20/2022).

[213] K. Takeda, "OPENCORE NMR: Open-source core modules for implementing an integrated FPGA-based NMR spectrometer," *Journal of Magnetic Resonance*, vol. 192, no. 2, pp. 218–229, Jun. 1, 2008, ISSN: 1090-7807. DOI: 10.1016/j.jmr.2008.02.019. (visited on 12/23/2024).

[214] M. Sabzi and A. Medi, "Analysis and design of multi-stage wideband LNA using simultaneously noise and impedance matching method," *Microelectronics Journal*, vol. 86, pp. 97–104, Apr. 2019. DOI: 10.1016/j.mejo.2019.03.004.

[215] A. D. I. A. D. I. Engineeri, *Linear Circuit Design Handbook*. Newnes, Aug. 2011, ISBN: 978-0-08-055915-5.

[216] D. G. Gadian, *NMR and Its Applications to Living Systems* (Oxford Science Publications), 2nd ed. Oxford University Press, 1995. (visited on 05/23/2025).

[217] A. Gradišek, M. Cifelli, D. Ancora, *et al.*, "Analysis of Extra Virgin Olive Oils from Two Italian Regions by Means of Proton Nuclear Magnetic Resonance Relaxation and Relaxometry Measurements," *Journal of Agricultural and Food Chemistry*, vol. 69, no. 41, pp. 12 073–12 080, Oct. 20, 2021, ISSN: 0021-8561. DOI: 10.1021/acs.jafc.1c00622. pmid: 33847493. (visited on 05/23/2025).

[218] M. R. H. Chowdhury, F. Ahmed, C. Oladun, *et al.*, "Low-Cost Purpose-Built Ultra-Low-Field NMR Spectrometer," *Analytical Chemistry*, vol. 96, no. 42, pp. 16 724–16 734, Oct. 2024. DOI: 10.1021/acs.analchem.4c03149.

[219] A. Doll, "Pulsed and continuous-wave magnetic resonance spectroscopy using a low-cost software-defined radio," *AIP Advances*, vol. 9, no. 11, p. 115 110, Nov. 2019. DOI: 10.1063/1.5127746.

[220] K. Takeda, "A highly integrated FPGA-based nuclear magnetic resonance spectrometer," *Review of Scientific Instruments*, vol. 78, no. 3, p. 033 103, Mar. 2007. DOI: 10.1063/1.2712940.

[221] M. C. D. Tayler and S. Bodenstedt, "NMRduino: A modular, open-source, low-field magnetic resonance platform," *Journal of Magnetic Resonance*, vol. 362, p. 107 665, May 2024. DOI: 10.1016/j.jmr.2024.107665.

[222] N. Bryden, M. Antonacci, M. Kelley, and R. T. Branca, "An open-source, low-cost NMR spectrometer operating in the mT field regime," *Journal of Magnetic Resonance*, vol. 332, p. 107 076, Nov. 2021. DOI: 10.1016/j.jmr.2021.107076.

[223] D. Ariando, C. Chen, M. Greer, and S. Mandal, "An autonomous, highly portable NMR spectrometer based on a low-cost System-on-Chip (SoC)," *Journal of Magnetic Resonance*, vol. 299, pp. 74–92, Feb. 2019. DOI: 10.1016/j.jmr.2018.12.007.

[224] D. I. Hoult and R. E. Richards, "The signal-to-noise ratio of the nuclear magnetic resonance experiment," *Journal of Magnetic Resonance (1969)*, vol. 24, no. 1, pp. 71–85, Oct. 1976. DOI: 10.1016/0022-2364(76)90233-X.

[225] R. E. Hoffman, "Standardization of chemical shifts of TMS and solvent signals in NMR solvents," *Magnetic Resonance in Chemistry*, vol. 44, no. 6, pp. 606–616, 2006, ISSN: 1097-458X. DOI: 10.1002/mrc.1801. (visited on 12/28/2024).

[226] e-PG Pathshala, *1H NMR chemical shifts for common functional groups*.

[227] J. C. Edwards, "Principles of NMR," *Process NMR Associates LLC, 87A Sand Pit Rd, Danbury CT*, vol. 6810, 2009.

[228] A. Bainbridge, "NUCLEAR MAGNETIC RESONANCE SPECTROSCOPY — Overview," in *Encyclopedia of Analytical Science (Second Edition)*, P. Worsfold, A. Townshend, and C. Poole, Eds., Oxford: Elsevier, Jan. 1, 2005, pp. 203–211, ISBN: 978-0-12-369397-6. DOI: 10.1016/B0-12-369397-7/00404-0. (visited on 12/28/2024).

[229] Heriot-Watt University, *1H NMR spectroscopy handout*, 2015.

[230] T. R. Hoye, P. R. Hanson, and J. R. Vyvyan, "A Practical Guide to First-Order Multiplet Analysis in 1H NMR Spectroscopy," *The Journal of Organic Chemistry*, vol. 59, no. 15, pp. 4096–4103, Jul. 1, 1994, ISSN: 0022-3263. DOI: 10.1021/jo00094a018. (visited on 12/28/2024).

[231] R. J. Ouellette and J. D. Rawn, "14 - Methods for Structure Determination Nuclear Magnetic Resonance and Mass Spectrometry," in *Organic Chemistry Study Guide*, R. J. Ouellette and J. D. Rawn, Eds., Boston: Elsevier, Jan. 1, 2015, pp. 229–242, ISBN: 978-0-12-801889-7. DOI: 10.1016/B978-0-12-801889-7.00014-5. (visited on 12/28/2024).

[232] "5.7: Spin-Spin Splitting in Proton NMR Spectra," Chemistry LibreTexts. (Feb. 11, 2023), (visited on 12/31/2024).

[233] C. H. R. I. S. T. I. A. N. Rischel, "Fundamentals of Peak Integration," *Journal of Magnetic Resonance, Series A*, vol. 116, no. 2, pp. 255–258, Oct. 1, 1995, ISSN: 1064-1858. DOI: 10.1006/jmra.1995.0016. (visited on 12/28/2024).

[234] M. Weber, C. Hellriegel, A. Rück, R. Sauermoser, and J. Wüthrich, "Using high-performance quantitative NMR (HP-qNMR®) for certifying traceable and highly accurate purity values of organic reference materials with uncertainties <0.1 %," *Accreditation and Quality Assurance*, vol. 18, no. 2, pp. 91–98, Apr. 1, 2013, ISSN: 1432-0517. DOI: 10.1007/s00769-012-0944-9. (visited on 12/28/2024).

[235] Bruker BioSpin GmbH, *TopSpin 4.0 user manual*, manual, 2017.

[236] M. Dračínský, M. Buchta, M. Buděšínský, *et al.*, "Dihydrogen contacts observed by through-space indirect NMR coupling †Electronic supplementary information (ESI) available: Experimental procedures, spectroscopic data of all new compounds, and NMR and calculation details. See DOI: 10.1039/c8sc02859a," *Chemical Science*, vol. 9, no. 38, pp. 7437–7446, Aug. 13, 2018, ISSN: 2041-6520. DOI: 10.1039/c8sc02859a. pmid: 30319744. (visited on 12/28/2024).

[237] University of Oxford, NMR Facility, *NMR techniques in organic chemistry: A quick guide*, 2016.